UNIVERSITY OF SOUTHAMPTON

FACULTY OF PHYSICAL SCIENCES AND ENGINEERING

Optoelectronics Research Centre

Speciality Optical Fibre Fabricated by Outside Vapour Deposition Process

by

Martín Miguel Ángel Núñez Velázquez

Thesis for the degree of Doctor of Philosophy

June 2018

UNIVERSITY OF SOUTHAMPTON

ABSTRACT

FACULTY OF PHYSICAL SCIENCES AND ENGINEERING

Optoelectronics

Thesis for the degree of Doctor of Philosophy

SPECIALITY OPTICAL FIBRE FABRICATED BY OUTSIDE VAPOUR DEPOSITION PROCESS

Martín Miguel Ángel Núñez Velázquez

Outside Vapour Deposition process was used to demonstrate transparent and defect-free optical preforms on a wide range of glass compositions. Fabrication parameters were established for deposition, dehydration and consolidation of optical preforms using a thermodynamic analysis. Also, the drawing conditions for canes and fibres were stablished. Silica depositions were demonstrated for applications on high quality substrates or jacketing material. Fluorine-doped silica glass was fabricated with a refractive index of -6X10^{-3} below pure silica level. A wide range of germanium-doped silica preforms were fabricated from 5 - 95%. Optical fibres ranging from SMF-like profile to a high NA and small core fibre were fabricated. 100% Germania deposition was successfully achieved and consolidated. 100% germania core rods were inserted into pure silica substrate and an ultra-high NA preform and fibre was achieved. A fibre Bragg grating was inscribed showing the multimode properties of this high NA fibre. Crystallisation study was carried out for Germanosilicate glasses. Aluminosilicate glass preforms were achieved via traditional and modified solution doping. Concentrations of ~20,000ppm or rare-earth ions were achieved. Large core fibres were fabricated with a small NA. Phosphosilicate glass was successfully demonstrated on passive and active preforms. Refractive index shows an ultra large core with a refractive index difference of 0.01. Co-doped germanium and phosphorous glass was successfully achieved on preforms with refractive index difference of ~0.01. Stimulated emission measurements demonstrate the successful incorporation of RE-ions into both aluminosilicate and phosphosilicate preforms showing the distribution of the dopant.

List of Contents

List of Figures

List of Equations

List of Graphs

List of Images

List of Tables

Academic Thesis: Declaration Of Authorship

I, Martín Miguel Ángel Núñez Velázquez declare that this thesis and the work presented in it are my own and has been generated by me as the result of my own original research.

Speciality Optical Fibre Fabricated by Outside Vapour Deposition Process

I confirm that:

1. This work was done wholly or mainly while in candidature for a research degree at this University;
2. Where any part of this thesis has previously been submitted for a degree or any other qualification at this University or any other institution, this has been clearly stated;
3. Where I have consulted the published work of others, this is always clearly attributed;
4. Where I have quoted from the work of others, the source is always given. With the exception of such quotations, this thesis is entirely my own work;
5. I have acknowledged all main sources of help;
6. Where the thesis is based on work done by myself jointly with others, I have made clear exactly what was done by others and what I have contributed myself;
7. Parts of this work have been published as:
8. [1] N.J. Ramirez-Martinez, M. Nunez Velazquez, A.A. Umnikov and J.K. Sahu, Efficient Thulium-doped Fiber Laser Operating in the 1890 – 2080nm Wavelength Band, Advanced Photonics Congress, Zurich, Switzerland, 2018.

   [2] N.J. Ramirez-Martinez, M. Nunez Velazquez, A.A. Umnikov and J.K. Sahu, Novel Fabrication Technique for Highly Efficient Tm-doped Fibres, Conference on Lasers and Electro-Optics, San Jose California, United States, 2018.

   [3] Donko, M. Nuñez-Velazquez, P. Barua, F. Guzman Cruz, R. Ismaeel, T. Lee, J.K. Sahu, M. Beresna, and G. Brambilla, Femtosecond inscription and thermal testing of Bragg gratings in high concentration (40 mol%) Germania-doped optical fibre, Optics Express 25, 32879-32886, 2017.

   [4] Donko, A., Nuñez Velazquez, M., Barua, P., Sahu, J., Beresna, M. and Brambilla, G., Point-by-point femtosecond laser inscription of Bragg gratings in high NA (>0.4) germania-doped optical fibre At WSOF 2017, Limassol, Cyprus. 11 - 13 Oct 2017. 3 pp.

[5] Tománek, Pavel, Senderáková, Dagmar, Páta, Petr, Cajzl, Jakub, Peterka, Pavel, Honzátko, Pavel, Mrázek, Jan, Podrazký, Ondřej, Todorov, Filip, Gladkov, Petar, Sahu, Jayanta, Nuñez Velazquez, Martin, Nekvindová, Pavla and Kašík, Ivan, Characterization of fluorescence lifetime of Tm-doped fibers with increased quantum conversion efficiency at SPIE Photonics, Devices, and Systems VI, Czech Republic. 27 - 29 Aug 2014. (doi:10.1117/12.2070425).

Signed:

Date:

Acknowledgements

The following institutions are gratefully acknowledged for the support received during this research project.

- National Council of Science and Technology (CONACyT; Consejo Nacional de Ciencia y Tecnología) Fellowship 216085, CVU 377962.
- Central Bank of Mexico (BANXICO; Banco Nacional de México) as Mexican federal government's trustee in the fund for the development of human resources (FIDERH; Fondo para el Desarrollo de Recursos Humanos). Fellowship 1311110126.
- State of Mexico Council of Science and Technology (COMECyT; Consejo Mexiquense de Ciencia y Tecnología). Fellowships 12BEA052; 13BAE082.
- Faculty of Physical Sciences and Engineering, University of Southampton
- Engineering and Physical Sciences Research Council.
- Centre for Innovative Manufacturing in Photonics
- UK National Crystallography Centre
- The μ-VIS X-Ray Imaging Centre

To my beloved wife Angeles, thank you for always being by my side and supporting me under any circumstances. I know that this has not been an easy endeavour for you since the beginning. Nonetheless, I am sure you share the reasons behind this adventure. It is not possible for me to express how grateful I am for having you in my life.

To Daniel; I would like to share this achievement with you because I know this journey has been difficult for many reason, and I promise to you that it can and will be worst at sometimes. I can only excuse myself on the instructions provided with that little-cracked egg coming from outer space that landed years ago in my garden. Regardless of the stressful, complicated and difficult situations that you can face along your life, I am convinced that you can, and you will handle them. Remember that sometimes you only need to remove all the light-coloured hairs that appear on your head from time to time. Remember that there is always a reward for putting an additional effort into all your activities and keep challenging yourself to make things better and then, better.

To Carlos; I am sharing this success with you to let you know a little secret. Indeed you were born different, and you must be proud to be born with a very unique skills. A rather rare greatness lay beneath the surface, which will help you to shape the world in a better way. The next time you feel that you are different, embrace that thought and make it work towards your success. Allow this world to enjoy your creativity because you can make this world better. I understand that trying new things can be difficult sometimes, but remember that the greatest ideas always come from thinking out of the box. Never forget that you are so cool that I want to be like you when I grow up.

To my dad Eduardo Núñez and my mom Gabriela Velázquez for imprinting on me the desire to achieve more than what is expected. For always being an example of hard work and for all the support and trust that you put on me along all these years. I expect this achievement exceeds the goal you confide me long, long time back: 'go beyond; go where nobody else has been before, not even us'.

To my sister Minerva because with hard work and persistence, it is possible to reach unimaginable achievements; and because despite the distance you have been always there and I will be always there.

To all my friends; because distance has proven that friendship is a conviction and not a circumstance. To all those friends that I left behind following this dream. For the new friendships; for the treasured ones; the good ones; the not so bad ones and for the sour ones as well, because every moment has been worth.

To Prof. Peter Schultz, special thanks for the invaluable discussions and incomparable experience. It was a pleasure working together.

Finally, I would like to express my immense gratitude to Prof. Jayanta Sahu for the opportunity and for the trust you put on me. For all the fruitful conversations and invaluable support during this research. I had perhaps one of the better experiences working with you.

Definitions and Abbreviations

All the units in this document are given under the International System of Units, its derived units, multiple and sub-multiples.

The preforms and fibres refractive index are given at a wavelength of 633nm unless it is specified a different wavelength in the graph.

The data on the thermochemical and thermophysical properties of the elements and compounds used in this thesis has been obtained from the Chemistry WebBook of The National Institute of Standards and Technology which is an agency of the U.S. Department of Commerce, unless other specified.

AOM: Acusto-Optic Modulator.

CDS: Chelate Deposition System, also referred as MCVD-CDS.

CFQ: Crucible Fused Quartz.

CH: Channel.

EDFA: Erbium-doped Fibre Amplifier.

EDX: Energy Dispersive X-ray spectroscopy.

FBG: Fibre Bragg grating; it can also be referred as FBG-fs when the grating was inscribed by femtosecond laser, or FBG-UV when the grating was inscribed by exposure to Ultra-violet radiation.

FEG-SEM: Field Emission and Gentle beam – Scanning Electron Microscopy.

F300: Refers to a high-quality quartz substrate; model of Heraeus Group.

F-L: Füchtbauer–Ladenburg.

FRIP: Fibre Refractive Index Profile.

FUT: Fibre Under Test.

H: Height of the external ring of the burner, measured from the base plate of the chamber.

h: Height of the internal rings of the burner, measured from the base plate of the chamber.

HOM: High Order Mode, also referred in the plural as HOM's.

IFA: Refers to a multiwavelength fibre refractive index profiler, a model from Inter-fiber analysis, LLC

IR: Infra-red.

Layer: In this report, the term layer means the soot deposited by a round-trip of the burner.

L: Separation length.

MCF: Multi-Core Fibre

MCVD: Modified Chemical Vapour Deposition. It can also be found as MCVD-CDS or MCVD-SD when emphasising the process for dopant incorporation.

MEF: Multi-Element Fibre

MeOH: Methanol (CH_3OH).

MFC: Mass Flow Controller.

MIMO: Multiple-input and Multiple-Output is a method of multiplying the capacity of communication links using multiple transmitters and receptors to exploit multi-mode propagation.

MSD: Modified Solution Doping

N: This letter is used to specify the number nines in the percentage of purity on a chemical; for instance, 3N specify a 99.9% purity on a given chemical; whereas 6N means 99.9999% purity of the chemical or precursor.

NA: Numerical Aperture.

NIR: Near Infra-red.

OFS: Optical Fiber Solutions; trademark of Furukawa Electric Co, Ltd. (FEC).

OH: Hydroxyl functional group.

OM: Optical Microscopy.

ORC: Optoelectronics Research Centre.

OSA: Optical Spectrum Analyser.

OVD: Outside Vapour Deposition.

PK2600: Refers to a preform refractive index profiler; model of Photon Kinetics, Inc.

PTFE: Refers to the synthetic fluoropolymer known as Polytetrafluoroethylene.

RE: Rare earth, referring to the series of lanthanides on the periodic table.

RF: Radio Frequency.

RIP: Refractive Index Profile.

S14: Refers to a fibre refractive index profiler; model of Photon Kinetics, Inc.

SC: Supercontinuum source

SDM: Space Division Multiplexing

SD: Solution Doping, also referred as MCVD-SD

SEM: Scanning Electron Microscopy usually an image referred as micrograph. It can also refer to Stimulated Emission Measurement; this last one is performed on the IFA and it is represented on an X-Y plot.

SM: Single Mode.

SMF: Single Mode Fibre.

T: Temperature.

TDFA: Thulium-doped Fibre Amplifier.

TLS: Tuneable Laser Source.

UV: Ultra-violet.

VAD: Vapour Axial Deposition.

VOC: Volatile Organic Compounds.

WDM: Wavelength Division Multiplexer.

WLS: White Light Source.

XRD: X-Ray Diffraction.

Chapter 1 Introduction

Speciality optical fibres that can offer low loss are of great interest to the telecommunications industry as they can lead to longer unrepeated distances for long-haul transmission systems. Low loss silica fibres operating at 1.55 microns have a theoretical limitation of 0.16 $dB \cdot km^{-1}$. At longer wavelengths, the attenuation from Rayleigh scattering reduces. However; in silica, the infra-red (IR) absorption starts to increase and impacts directly on the losses of the system. Laser sources at longer wavelengths are currently not easy to obtain, but there are different techniques to generate optical signals at 2-microns, such as optical amplification using TDFA.

Low loss transmission at 2-microns is prevented due to limited material availability which sets the challenge of developing a new glass host. The development of a novel speciality glass is required to be targeting primarily on transmission in the 2-micron region with low attenuation and reduced IR absorption. Germanium oxide has been investigated as a potential candidate to overcome the current limitations. The high purity of the precursors used during the deposition process is a crucial factor that enhances the performance of the resulting optical fibres.

The research project presented in this thesis includes the fabrication of germanium-doped silica glass and pure germania glass. Chapter 6 provides detailed information about the germanosilicate glass preforms fabricated by OVD and the resulted fibres. Chapters 7 describes the fabrication of pure germania glass using OVD and the development of these glass into optical fibres.

Alternative approaches for the utilisation of the 2-micron laser technology have captured the attention of many research areas, such as biomedical applications, defence systems, and the manufacturing industry. This particular region of the IR spectrum, in which silica glass has strong IR absorption, also has particular interest due to the hard absorption of some organic molecules. The applications above have yielded interest in the field of sensing by companies which use detection technologies as their business model.

Extensive characterisations of the equipment were performed as part of this research and are reported in Chapter 2 of this dissertation. Critical components, such as the burner, had paramount importance since it governs the reaction and the deposition conditions.

An exhaustive study on the OVD process is reported in Chapter 3. Thermodynamic calculations were also obtained to understand the boundaries in which the depositions occur. Secondary processes, such as dehydration and consolidation of the porous soot preforms, were also analysed.

The development of the glass fabricated by OVD deposition process started using a single material. Minimising the number of variables during the initial development was essential. Therefore, pure silica was the first OVD deposition process developed, and it is outlined in Chapter 4. Having a well-established process for pure silica depositions was a fundamental goal that enabled the developing of further glass compositions.

The incorporation of fluorine into the silica glass lower the refractive index of the glass. In Chapter 5 it is described a process for fluorine incorporation that does not change the soot deposition conditions. Adding dopants maintaining the deposition conditions helped to preserve the reliability of the process at the initial stages of the process development.

Novel routes to fabricate optical fibres with large cores for laser applications are also desirable. The current fabrication techniques are mainly limited by the way the glass host is built-up. The research presented in this thesis demonstrate that the OVD fabrication technique has the required capabilities for manufacturing large volumes of the preform core materials.

Speciality optical fibres for laser applications require the development of different types of glass host. The incorporation of rare-earth (RE) ions into the glass is essential for the development of fibre laser applications. Network modifiers into the glass matrix are required to enhance the laser performance and reduce the undesirable clustering of the RE-ions.

Aluminosilicate and phosphosilicate are among the most common glass host used in the photonics industry for laser applications. The refractive index of silica glass raises when it is doped with aluminium oxide (Al_2O_3) or phosphorous pentoxide (P_2O_5). Both dopants act as network modifiers in the silica glass matrix allowing a better distribution of additional dopants such as rare-earths RE. Aluminosilicate glass preforms and optical fibres are reported in Chapter 8. Experiments targeting only a refractive index change and RE-ion incorporation are described. Correspondingly, phosphosilicate glass preforms and optical fibres had been outlined in Chapter 9.

A selection of additional projects carried out during the PhD programme had been included in Chapter 10. Motivated by the scientific and industrial significance of the 2-micron laser technologies, spectroscopic studies of thulium-doped silica fibres were performed. Samples made in-house by MCVD using solution doping, and gas phase deposition techniques are reported in Section 10.1.

The analysis was made to provide a better understanding of the dopant behaviour and the dependence of its performance changing the characteristics of the glass host. The information obtained in this study will be used as a foundation for further developments using the OVD process for Tm-doped optical preforms.

Alternative routes to incorporate dopants into the OVD preforms were explored during the development process. An underlying condition for dopant incorporation is to minimise the handling and post-processing of the soot preform. Otherwise, the soot can be damaged, and the characteristics of the glass will be compromised. The use of gas phase deposition for Al_2O_3 and RE incorporation is a procedure that has been explored for fabrication of preforms using the MCVD process and has been described in section 10.2.

The potential impact of the gas phase deposition translated into the OVD system has promising economic interest from the photonics industry. Therefore, the study of the gas delivery system, its advantages and limitations, allow defining the requirements for its further implementation in the OVD process.

The significance of the OVD deposition system lays in the possibility to produce novel glass compositions for speciality optical fibre application. Accordingly, an application that requires unusual glass compositions is reported in section 10.3. A barrier with high concentrations of Al_2O_3 is proposed to reduce the molecular hydrogen intake of optical fibres exposed to high temperatures and pressures in the oil and gas industry. Although this experimental work was not made using OVD process, it stresses that the OVD process could be utilised for research challenges that conventional techniques face limitations.

Optical fibres can have undesirable features on the refractive index profile (RIP). Particularly the fibres fabricated for laser applications having core compositions that include phosphorous present an undesirable central depth in the RIP. Analysis and an approach on how to tailor the central depth on the RIP are proposed in Section 10.4. The section mentioned before was included as an example of the

demand for novel processes that can satisfy the requirements of the photonics industry. Optical preforms made by OVD process can overcome the current drawbacks from current fabrication processes.

Complementary to the development of germanosilicate glass and pure germania glass described in Chapter 6 and Chapter 7 correspondingly, a study on fibre Bragg gratings is reported in section 10.5. The motivation of this study was to establish a starting point for the further development of OVD based fibres. A germanium-doped silica fibre fabricated by MCVD was used to establish the grating inscription process based on a femtosecond laser source. The characterisation of the thermal behaviour of this gratings is also described in the section mentioned above.

The accelerated growth of Internet users and applications had put the installed capacity to the limit. New approaches based on space division multiplexing (SDM) are currently in development with the aim to meet the demand for data traffic over the Internet. Section 10.6 reports the activities carried out within a project based on the SDM approach. The use of OVD in SDM is underexploited, preform fabrication for multi-element and multi-core optical fibres would be desirable for further developments in SDM technologies.

1.1 Passive Fibres

The SiO_2/GeO_2 system is essential within the optical fibre industry. It has been the primary platform of fibre fabrication for at least the past 35 years. This glass system has improved with the availability of precursors with higher purity, and the increment in the demand for glass preforms[1,2].

Fundamental limitations such as Rayleigh scattering and OH incorporation pushed the telecommunications industry to base its development in the NIR[2,3]. Nowadays, the lowest losses are around the wavelength of 1550 nm. Theoretically, longer wavelengths can reduce the Rayleigh scattering, leading to reductions in the signal loss. However, the nature of the main component of the system, the SiO_2, has a multi-phonon absorption of its Si – OH bond in the 2-micron wavelength region which increases the losses significantly of the transmission systems[3].

Research groups around the world have studied the utilisation of additional dopants to improve the performance of the current telecommunications systems[4].

Also, investigations using highly doped GeO_2 fibres have been tried. However, the mechanical and thermal properties mismatch between the components make the processing of these particular preforms difficult[5].

Other types of hosts such as calcium-aluminate glass and the calcium-aluminate-germanate glass have been studied due to their transparency in the infrared. However, the available fabrication processes do not permit low loss fibres, mainly owing to the lack of purity of the precursors and the processes themselves[6-10].

Different approaches to the existing processes have been tried to improve the properties of the glass, for example using network modifiers; the use of ceramics and different oxides also form part of recent investigations[11,12].

2-micron fibre lasers have been noted as another potential application of the pursued low loss fibres. The advantages of 2-micron technology are well known, such as the feasibility of increasing the core sizes of the single mode fibres, which reduces the energy density allowing an increase of output power, overcoming the current limits of 1.5-micron technology.

The eye-safe characteristics of the 2-micron radiation is another positive characteristic which could allow increased power in free-space communications, reducing the impact of attenuation during adverse weather. Finally, within the biomedical application field, the potential of 2-micron lasers as part of the development of less invasive medical procedures, or more precise surgeries, builds a unique attractiveness for this technology.

Owing to the capabilities of 2-micron technology, research groups around the world have been making progress in this area. Commonly, the development of thulium-doped fibres has been considered one of the leading routes to achieving 2-micron fibre lasers. Several studies around the thulium-doped fibres and investigations about how to obtain the most effective energy conversion have captured the attention of specialists around the world[13-18]. However, even though the 2-micron technology is already available in devices such as TDFA, low loss transmission fibres at this wavelength are still not available, mainly because of the fundamental limitations mentioned above.

1.2 Active Fibres

The preform fabrication for fibre lasers is also an important research area to explore since large core diameter fibres are mostly limited by the amount of porous soot in which the dopant solution can penetrate. Alternative fabrication processes such as powder-in-tube are commonly used. However, the limitation of this technique is mainly due to the available purity and particle size distribution of the chemical powders that can be obtained.

Soot characterisations have been performed to provide the optimum conditions for the preparation of the soot and correlating their effects to the impact on the final dopant distribution[19-21]. Alternative precursors and their impact on the refractive index has also been studied[22]. Optimisation of the processes, such as repeated immersions and thermal treatments during the rare-earth incorporation, and utilisation of different solvents, has attracted the attention of research groups[23,24].

The in-situ solution doping technique has been successfully applied for the fabrication of preforms with up to 2.6mm core diameter[25]. This technique has demonstrated better results than conventional solution doping; nevertheless, by the nature of the technique, there is a limited number of soot layers that can be deposited as a host for the dopants.

All the research efforts mentioned before have mainly focussed on the obtainment of sizeable doped preform cores. The principal problem of the solution doping techniques is the control of the soot characteristics. The repeated deposition of soot layers in the substrate can lead to the partial sintering of the initial layers deposited, reducing the potential dopant incorporation.

The nature of the manufacturing process of OVD preforms, position them as ideal candidates to achieve large doped cores. Since the whole preform could be immersed into the desired rare-earth solution; the soot characteristics are homogeneous along the preform and over the cross section area.

Also, an external soot deposition can be performed and treated with the same technique, using the same solution, or a different one. Furthermore, an opposite effect dopant could be used, such as fluorine, to depress the refractive index and increase the numerical aperture of the preform design.

1.3 Outside Vapour Deposition (OVD)

OVD is one of the three widely adopted processes used to manufacture glass preforms for optical fibres. Due to the capability to manufacture passive, active and also special preforms for optical fibre manufacturing, this process has unique attractiveness for industrial and research industries[3,26].

Experimental conditions used with the OVD process are not commonly detailed in the literature because of industrial and intellectual property rights[8,27-34]. For that reason, this research project had the particular interest of developing the research and fabrication capabilities for the Optoelectronics Research Centre (ORC).

The OVD deposition involves a complex gas delivery system which supplies the reactants, fuel, oxidiser and additional gases to the burner. Figure 1 illustrates a general scheme of the OVD deposition process. Alternative configurations are available, depending on the design and specific purpose of the manufacturing facilities. Variations on burner design are one of the significant attributes of each OVD system since it governs the conditions of the reactions and their effects on the final preform.

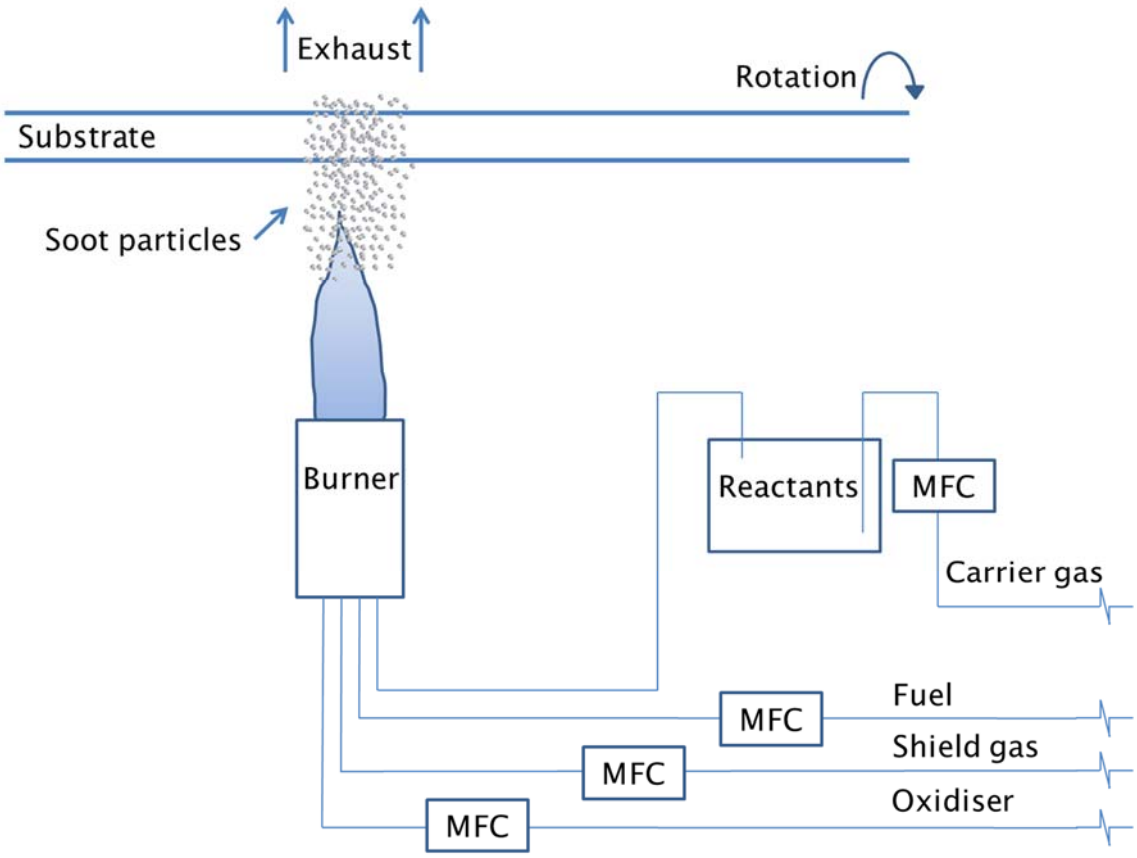

Figure 1. Schematic of the OVD deposition process.

The OVD process starts when a carrier gas flow passes through a container with a preheated halide precursor in liquid form. Slight differences can exist for systems having more than one precursor or having the reactants in gas phase from the beginning. The flow of carrier gas and the vaporised precursor mixture is then directed to the burner via a permanent heated umbilical line. Heaters are used to prevent condensation of the precursor before it reaches the reaction zone in the burner. Depending on the burner design and carrier gas, the vapour mixture undergoes oxidation, combustion or hydrolysis reactions, and, in most cases, a complex combination of all three. As a result of any of the three reaction mechanisms, the halide precursor is oxidised and forms small soot particles which coalesce into more significant aggregates that are finally deposited on the substrate. Combining the soot formation of the deposition with the movement of the torch along the substrate, it leads to the evolution of a multilayer soot porous preform.

After the deposition is concluded, the porous soot preform is usually treated by a dehydration process at high temperatures using a desiccant agent to remove all the OH content trapped during the deposition. Finally, the dehydrated porous preform is taken to the final stage which is the consolidation. At this stage, the soot is processed at a higher temperature than the dehydration process to reach enough energy and allow the sintering of the soot. However, this temperature should not be too high, preventing the glass viscosity being reduced to the point where the glass starts to flow and precipitates[35].

One of the significant advantages of the process is the capability to repeat the depositions as many times as necessary, substituting the precursors or the gas treatments, making it possible to fabricate preforms with multilayers of different dopants.

Extended characterisation of the Optoelectronics Research Centre OVD equipment is detailed in Chapter 2. Also, an exhaustive analysis of the OVD process; deposition conditions; dehydration and consolidation conditions had been reported in Chapter 3.

1.3.1 Passive preforms

Preforms that lack of an active gain medium (i.e. RE-ions) are known as passive preforms. Germanium-doped silica preforms had a particular attraction because it is not possible to make highly doped preforms with large core by alternative techniques. Finally, the pure germania fibre has a high attractiveness due to diverse

applications such as optical fibres, couplers and WDMs, among others[7,36]. Also, the low loss transmission fibres at 2-micron wavelength are highly attractive.

Every $SiCl_4/GeCl_4$ ratio requires reconsidering the thermodynamic analysis. The change in the molar composition of the precursors in the reaction evolves into different solutions. Caution has to be taken preventing that the thermodynamic parameters do not shift to unfavourable conditions for the reaction.

Additionally, the GeO_2 is not as stable as SiO_2. Particular conditions can produce alternative forms of GeO_2 such as Ge/GeO_2, GeO_2 (hexagonal), GeO_2 (tetragonal), GeO_2 (glass), GeO_2 (Solid Solution)[37], or it can even return into a halide[38]. Fabrication conditions and experimental results for germanosilicate glass and pure germania glass are described in Chapter 6 and Chapter 7 respectively.

Other types of passive preforms were fabricated, and their experimental results are shown in the following chapters. Pure silica preforms are described in Chapter 4, and fluorine-doped silica preforms are described in Chapter 5. From the active performs development, there is also a section dedicated to the development of the glass host, those types of glass can be used to fabricate passive preforms as well.

Preform development for aluminosilicate glass is reported in Chapter 8, and phosphosilicate glass is outlined in Chapter 9. Phosphosilicate was also doped with germanosilicate to demonstrate the capability to fabricate the glass composition. This glass is commonly used in the section of the preform known as the pedestal. The pedestal in optical preforms is a region surrounding the core that helps to reduce the numerical aperture between the core and the cladding. The pedestal acts as a cladding structure in the waveguides, and it is commonly used in the active preforms designs.

1.3.2 Active preforms

Extending the capabilities of the OVD process is driven by the particular interest of fabricating active preforms. There are different techniques to add dopants into the preforms, such as gas phase, sol-gel, conventional solution doping, or in-situ solution doping. Solution doping is widely utilised to fabricate RE-doped optical fibres. The low vapour pressure of the RE compounds makes the solution doping a valuable technique for the fabrication of active preforms. Extensive studies have been carried out to optimise the incorporation of dopants[19-24,31,39,40].

The nature of the OVD porous soot preforms enables the incorporation of a significant amount of dopants inside the silica matrix. The techniques used in MCVD preforms consist in soaking the inner porous soot layer with the solution. The dopants penetrate the porous soot body attached to the substrate tube. However, no substrate supports the OVD soot preforms, which requires significant modifications to the existing techniques.

The solution is contained in a tailored vessel where the preform is immersed. There is also a particularity of the OVD soot porous preforms, the penetration of the dopants in the solution may happen in a bidirectional manner; via the inner hole left by the bait rod removal, and via the outside surface of the soot body.

The soot preforms produced for the solution doping process require a particular porosity. Depositions too loose tend to crack and precipitate during solution doping. Contrarily, depositions too compact may prevent the solution from penetrating in the soot preform, leading to a low dopant concentration or an unexpected RIP in the final preform.

Incorporation of Al_2O_3 into the porous soot preforms has a particular interest; it has been reported that it helps to minimise clustering of RE-ions[41]. Preventing the interaction between RE-ions in the glass network and reducing the unwanted short fluorescence lifetimes[42]. Rapid fluorescent decays happen due to the quenching effect of the lasing process. There are extensive studies in the literature about the aluminium incorporation in MCVD preforms using a thin soot layer. Also, the effects of multiple doping and alternative dopants have been reported[21,23,24].

Phosphosilicate is also used as a glass host for RE doping. Its use is widely adopted in the fibre lasers industry. The phosphosilicate glass matrix enhances the core of the fibres tackling the unwanted photodarkening which is an undesirable consequence in high power applications. More complex glass hosts for active preforms can be achieved, for instance mixing aluminosilicate and phosphosilicate.

The photonics industry and primarily the high power laser sector, have a particular interest in optical fibres with a large core and reduced numerical apertures. The OVD process can be developed to satisfy this demand. It is described in Chapter 8 the experimental work towards the development of aluminosilicate glass fabricated by OVD. Also, in Chapter 9 it is reported the set of experiments carried out in the development of the OVD process for fabrication of phosphosilicate glass.

Chapter 2 OVD Equipment Characterisation

The OVD equipment was designed, delivered and installed before the starting date of the research work presented in this thesis. According to available records, the equipment was delivered to the Optoelectronics Research Centre in the second half of the year 2011. It was installed in the first half of the year 2012. After few initial operational tests, the commissioning activities started in the last quarter of the year 2012, which coincides in time with the starting date of the research reported in this document.

Initial deposition trials were performed by the supplier commissioning team to demonstrate the deposition of pure silica soot. Depositions resulted in the top layer partially sintered; this was corrected by reducing the flame flows to reduce the deposition temperature. Unfortunately, the corrected deposition temperature was unsuitable for large diameter preforms with the deposited soot detaching or cracking.

The commissioning activities also proposed a handle with a tapered bait rod for the substrate removal procedure. However, the soot preforms were not successfully detached from the substrate rod without breaking them. Therefore, consolidation furnace demonstrations were carried out using depositions made on top of CFQ glass rods. After the initial samples were sintered, it was identified that the samples contain defects. The defects were apparent bubbles that appear on the surface and embedded in the glass preform.

Further depositions were carried out to demonstrate the silica soot doped with germanium. The use of germanium precursor in the flow started to present additional challenges for the commissioning team. The deposition conditions established for pure silica soot were not suitable for the new flow composition.

During the commissioning stage, the author contribution was towards the identification of the defects. Close analysis showed there was a metallic composition. Particles were found to be encapsulated in a bubble formed during the consolidation process due to evaporation of the chloride form present in the particle. These particles were later identified as iron dichloride ($FeCl_2$) falling from the top hood of the deposition chamber. The particles were the result of the chlorides released during the process in contact with the stainless steel of the deposition chamber.

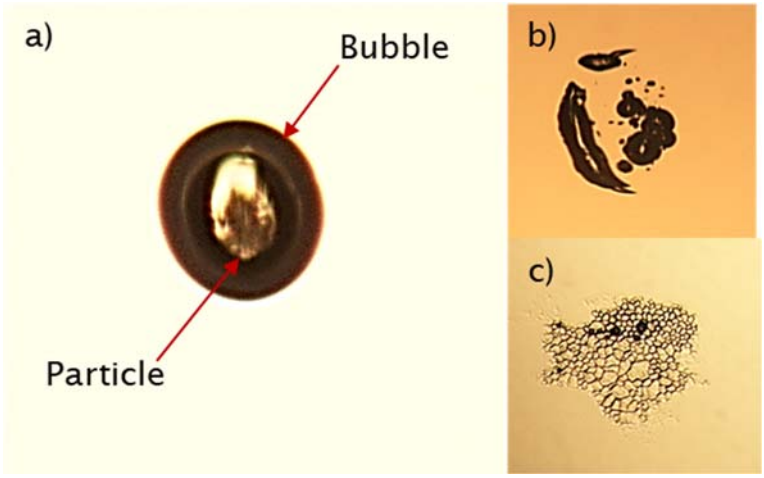

Image 1. Defects found in sintered preforms. a) Particle inside a bubble; b) Cluster of particles with surrounding bubbles; c) Surface defect.

An optical microscope was used to identify the defects observed in the preforms made during commissioning activities. Image 1 shows the most common types of defects found after the preforms were consolidated. After identifying the source of the particles, the supplier modified the chamber extract design to allow more efficient removal of the by-products. The modifications to the extract solved the problem of particles falling from the top hood of the chamber into the deposited soot.

Final attempts from the commissioning team were carried out looking to demonstrate the substrate removal and germanium-doped silica soot preforms. However, different approaches proved unsuccessful and the commissioning period for the equipment had been already exceeded. Therefore, a proposal to limit the commissioning activities to the demonstration of pure silica soot depositions and sintering process into a bubble-free transparent glass was agreed. The supplier decided to retire its commissioning team and leave the system for further process development by the ORC.

This chapter describes the comprehensive analysis and the characterisations made to the OVD system to develop the process. A thorough literature review was carried out to find, that due to its commercial application, there is limited information available on the OVD process. Hence, the majority of the deposition conditions were obtained experimentally using the commissioning trial conditions and the limited literature data as a starting point.

2.1 Preliminary Analysis

It was fundamental for this project to understand the OVD process and its differences with other preform fabrication processes. The following section gives an overview of the main parameter that drives the deposition process.

2.1.1 Temperatures

The OVD process involves the reaction of at least one halide precursor and an oxidising agent. The temperature dependence of the reaction has been widely studied previously[43-48]. Therefore, it is quite essential to know the temperature profiles of the flame region and their dependence on the H_2/O_2 ratio.

The temperature of the deposition is affected by the amount of heat produced by the oxidation reactions and the exposure time of the burner. Tanden, P. et al.[45], K. H. Hong and S. H. Kang[49], and Cho, J. et al.[44] studied the effects of burner speed on substrate and surface deposition temperature, growth rate and deposition efficiency. Also, Petit, V. et al.[32] correlated the influence of the translation/rotation ratio on the substrate temperature.

The particular mechanism of the OVD deposition is entirely different to other processes used to fabricate glass preforms for optical fibres. The VAD deposition process has a static burner and a moving preform which is retracted at a specific ratio allowing the desired deposition; however, the temperature conditions of the deposition zone are assumed to be stable.

The MCVD process has a moving burner and a lengthwise static preform; the deposition process is performed as the burner moves. The soot particles are deposited on the substrate glass after the precursors react in the hot zone. Figure 2 illustrates the MCVD process. It is possible to appreciate how the reaction occurs in the hot zone and the soot aggregates are deposited on the inner surface of the substrate.

It is also important to mention that the MCVD process uses a temperature gradient to produce the reaction and then make the deposition, for MCVD the hottest zone is the reaction zone, see Figure 2. Usually, due to the carriage movement, a gap is noticeable between the centre of the burner and the hottest zone. However, the resulted temperature difference is easily corrected by increasing the flows of the burner.

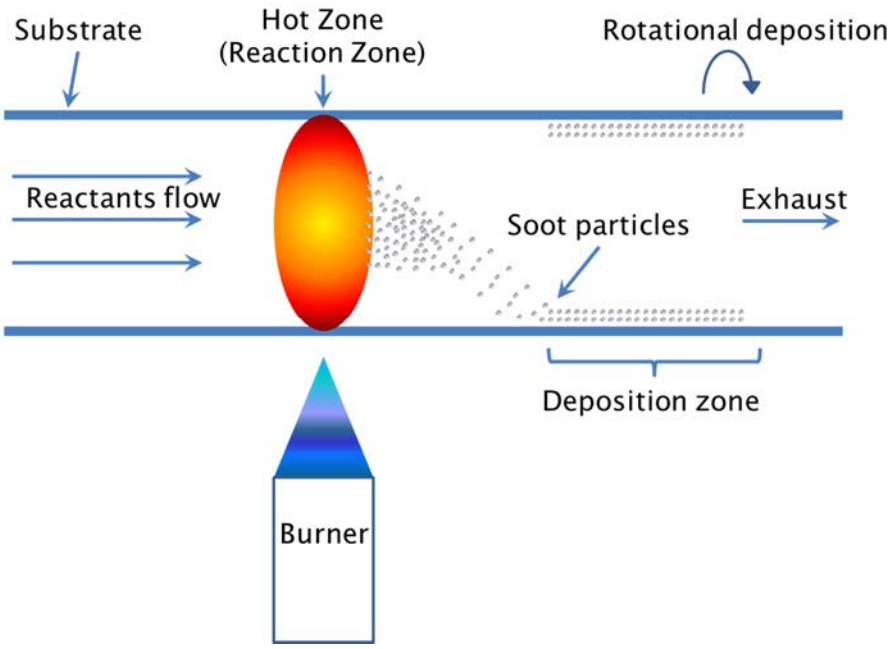

Figure 2. Schematic of the MCVD process.

Alternatively, the OVD deposition process occurs in both directions lengthwise. Figure 3 shows a schematic of the OVD soot preform deposition. The reaction happens in the flame, and the soot aggregates are deposited on top of a rotating substrate as the flame traverses in both directions. In this process, it is essential to minimise the gap between the hottest zone and the burner position due to the carriage movement.

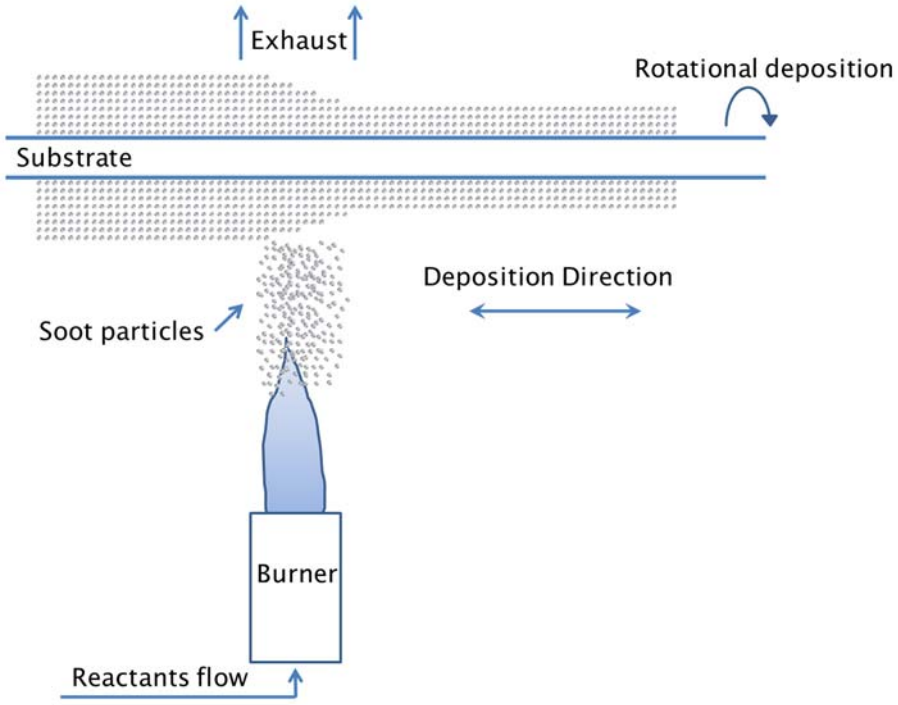

Figure 3. Schematic of OVD.

An excess of temperature after the deposition can have disastrous consequences for the soot preform. The excess heat sinters the outer layers of the soot body modifying the interface between the deposited layers. For $SiCl_4/GeCl_4$ mixtures, the consequences are even worse because an overexposure of the deposition to the heat can lead to the reduction of the GeO_2 content due to evaporation or secondary reactions.

Ideally, the hottest zone should match with the burner position even when the carriage is moving. No difference in temperature is expected in the deposition between moving and stationary conditions. If the carriage speed requires being reduced or stopped; the only side effect will be the increase in the deposition thickness. Otherwise, if the burner is stopped the preform will sinter by overheating and the soot prefrom will be damaged.

2.2 OVD system

2.2.1 Thermal characterisation of burner flows

Temperature measurements were performed in the flame at an equidistant point between the substrate and the burner using an R-type thermocouple, and processing the signal into a data logger thermometer, model YC-717UD made by YCT. Experiments were performed for different combinations of oxidiser, fuel, shield gas and carrier gas.

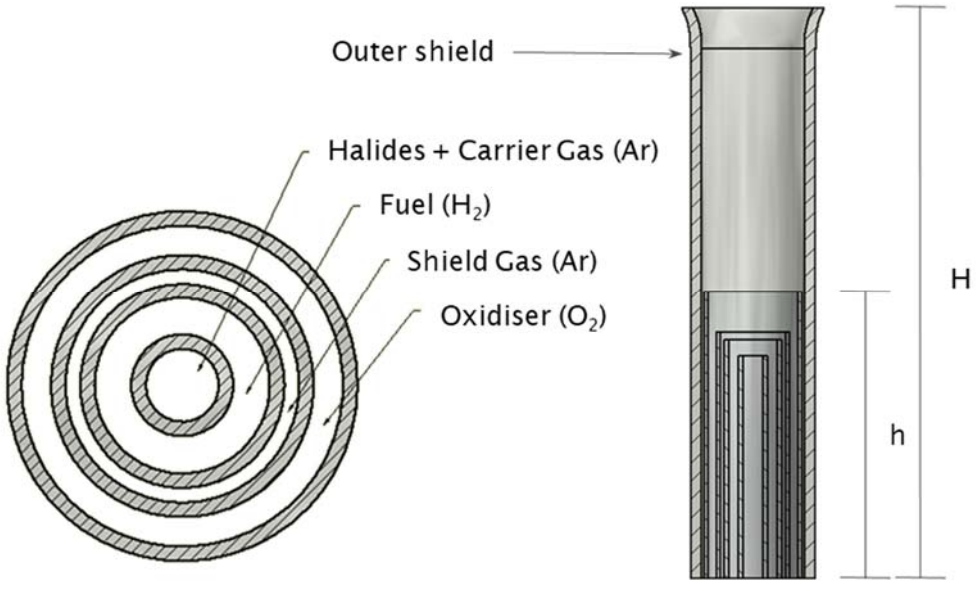

Figure 4. OVD burner schematic.

The burner consisted of five concentric tubes, as shown in Figure 4. A carrier gas, Ar for this study, was passed through a liquid halide precursor(s) heated and contained in a bubbler. The common halides are $SiCl_4$ or $GeCl_4$, among others making a vapour mixture which then passes through the central tube. Hydrogen and oxygen flows were separated by a shield gas flow (Ar), which prevented the premature mixing of the fuel and oxidiser.

The burner also has an outer shield, shown in Figure 4, which helps to maintain the shape of the flame flow. The outer shield produces the conditions that confines reaction before the total flow surrounds the substrate. Thus, the reaction is completed before the flow reaches the substrate. From our experiments, this burner design has experimentally improved deposition efficiency. Also, it seems to be essential for low-temperature depositions allowing to control deposition efficiency and soot density.

The thermocouple was set on the same rotational axis where the substrate was clamped during the deposition. Precursor flow was suppressed for these measurements to avoid deposition on the thermocouple probe. It also avoided the differences in temperature due to the heat transfer across the thickness of the soot layer. Image 2 shows the experimental setup used for the temperature measurements.

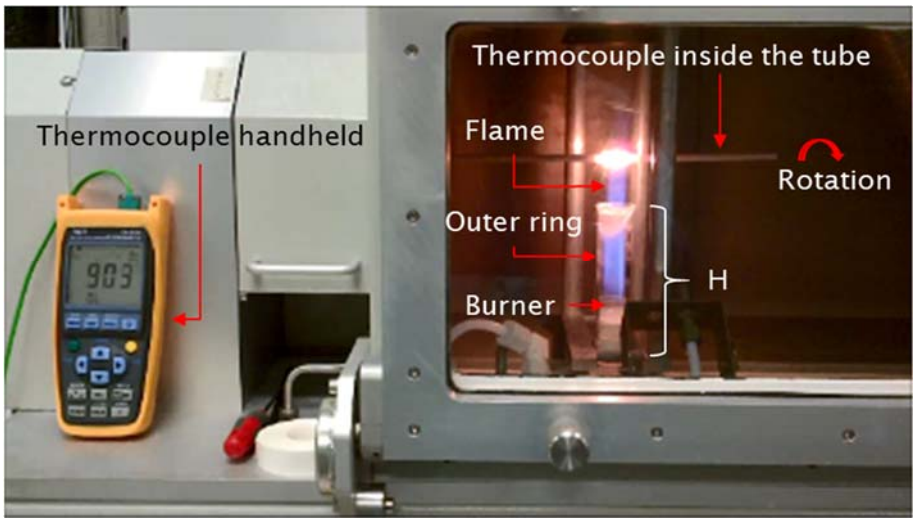

Image 2. Experimental setup used for burner temperatures characterisation.

Since the aim of this experiment was to measure the temperature in the flame and the corresponding dependence of the H_2/O_2 ratio, the corresponding flow of precursor was replaced by adding the same amount of carrier gas only. These conditions were used as a guide only because the equipment lacks temperature monitoring system.

The real temperatures in the flame vary with the heat exchange of the chemical reactions that lead to the soot formation. Other parameters, such as extract flow, traverse speed and distance from the burner to the substrate remained constant.

Temperatures of H_2/O_2 flames in a stoichiometric ratio were performed using an R-type thermocouple inserted directly into the flame and set on the same rotational axis where the substrate is clamped during the deposition.

Graph 1 shows the flame temperature affected by varying the H_2 flows. Since the flame was in a stoichiometric ratio, an increment of the temperature was observed as the flows were increased.

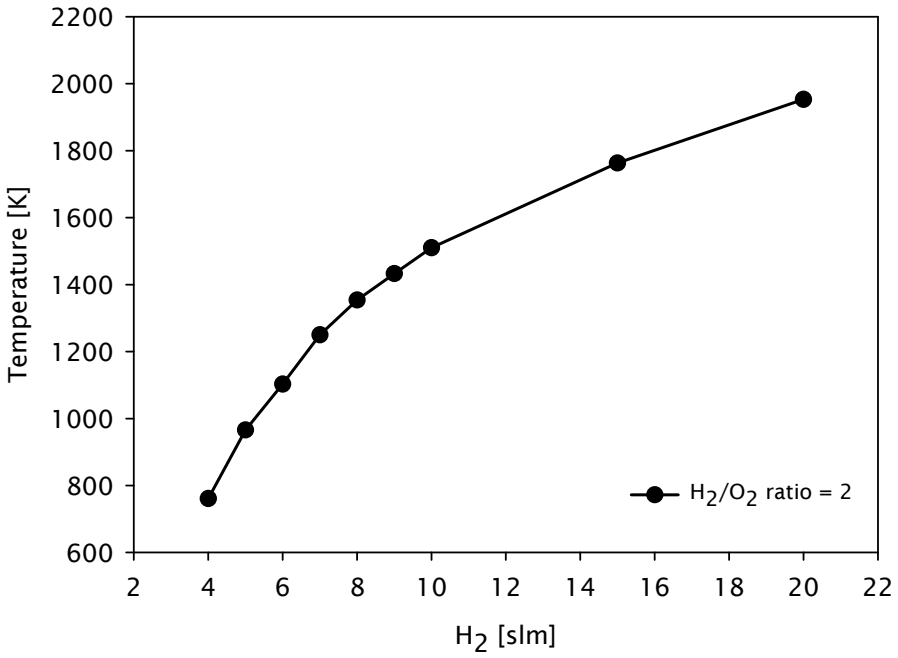

Graph 1. Hydrogen flow effect on flame temperature with stoichiometric ratio.

Temperatures of the H_2/O_2 flame using different ratios were also determined using the same setup previously described. The effect in temperature by varying the H_2/O_2 ratio are presented in two graphs. The previous stoichiometric results were added as a reference. Graph 2 shows the changes in temperature as the O_2 flow is modified, using fixed amounts of H_2.

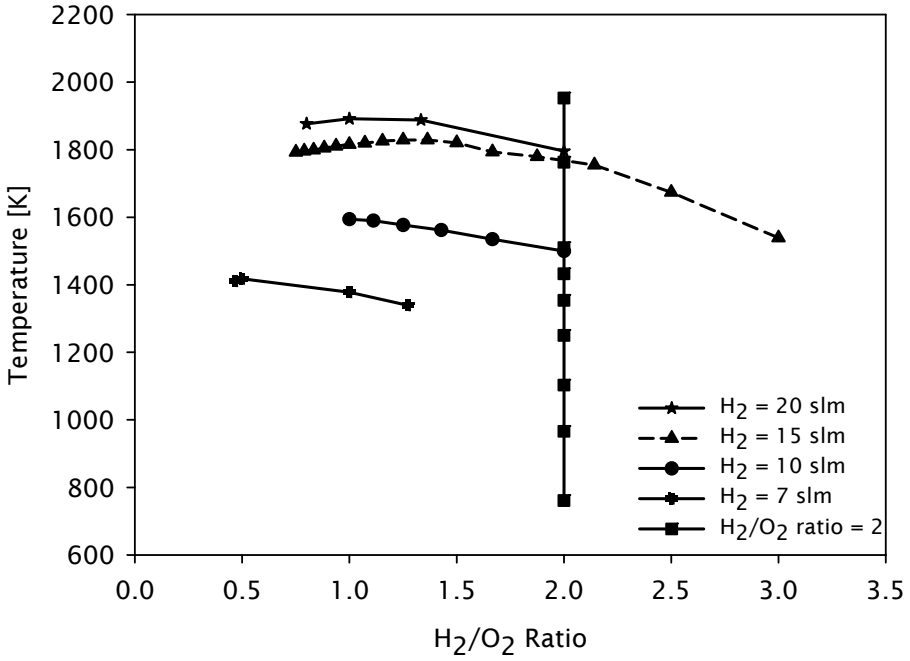

Graph 2. Effect of varying the O_2 flows with fixed flows of H_2.

Likewise, Graph 3 shows the changes in temperature as the H_2 flow is modified, using fixed amounts of O_2. The slopes of the plots in the previous Graph 2 indicate a reduction of the temperature as the O_2 flow increases, whereas the slopes in Graph 3 indicate an increase in temperature as H_2 flow increases.

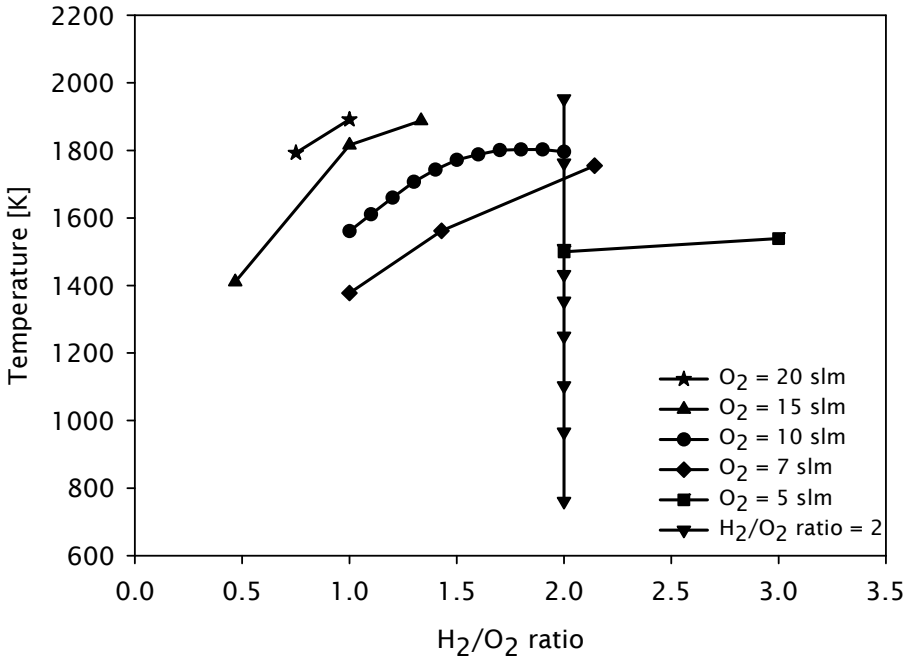

Graph 3. Effect of changing H_2 flows with fixed flows of O_2.

By experimentation it was found that a H_2/O_2 ratio of 0.466 yielded the amount of oxygen required for the reactions of combustion and oxidation during the deposition process. Different glass compositions used different total flows but the ratio was consistently 0.466 for the reasons above.

Using fixed flows and an H_2/O_2 ratio = 0.466, temperatures of the flame were measured while modifying the flow of the shield gas. Argon is the gas for the protective curtain and the carrier gas used in the system.

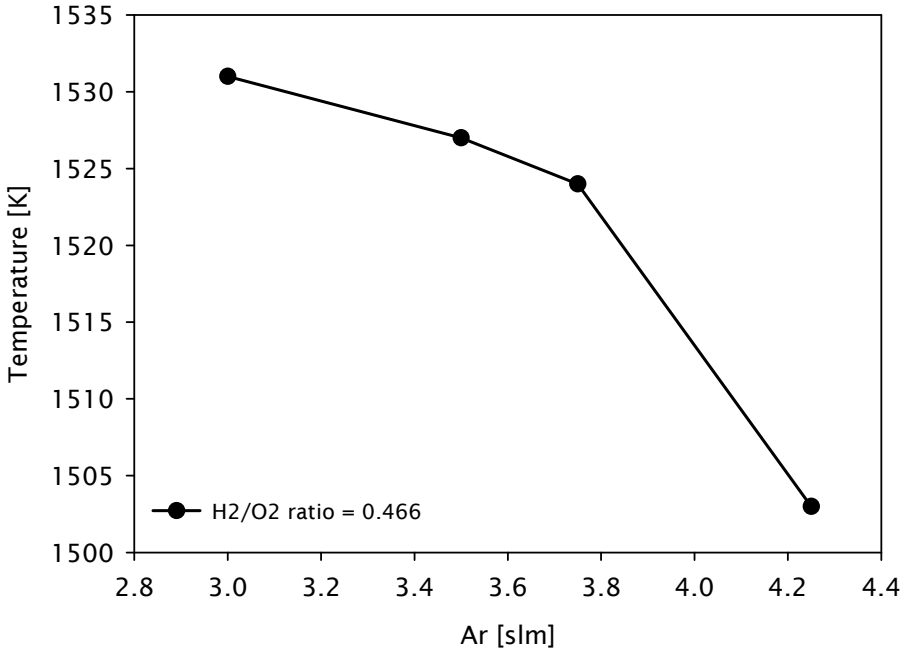

Graph 4. Shield/Carrier gas flow effect on flame temperature.

A reduction in temperature is shown in Graph 4 as the flow of the shield gas increases. The particular design of the OVD burner develops a stream mixture as follows. The carrier gas flow with the reactants mix with the fuel gas first; then, it mixes again with the shield gas; and finally, all the gases react with the outer oxidiser reagent flow.

Temperatures of the flame were measured using fixed flows of H_2, O_2, and Ar, with an H_2/O_2 ratio = 0.466; temperatures of the flame were taken while modifying the height of the external ring of the burner - measured from the base plate of the chamber. The increment in the flame temperature as the distance H was increased is presented in Graph 5.

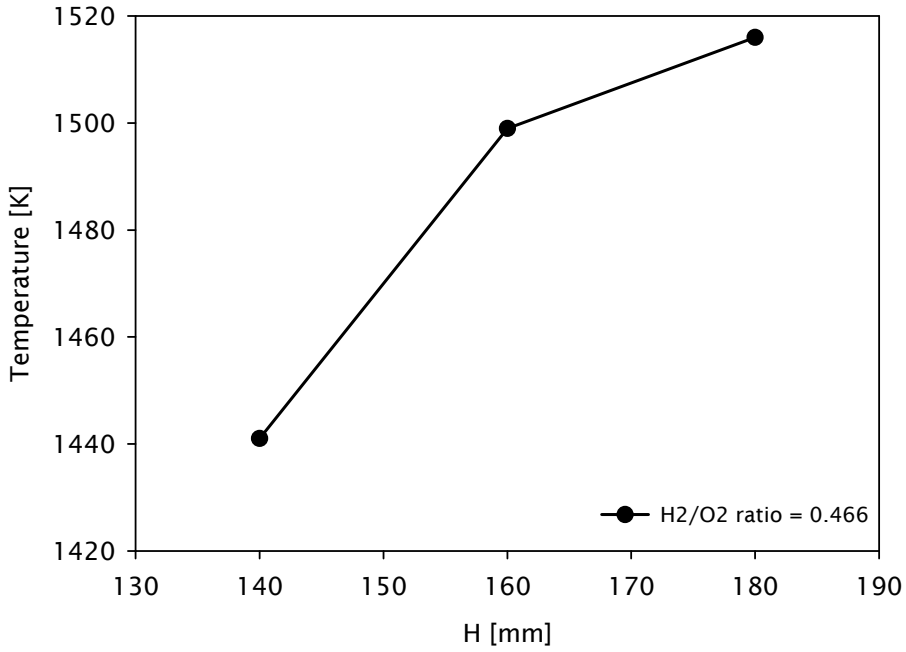

Graph 5. Temperature change by varying the height of the outer burner ring.

The temperature rise observed as the distance was increased, is explained by the fact that the flame remained confined at a closer distance from the substrate position. An additional consideration regarding the hot zone position in the burner flame is described below. Deposition flame changes were observed with the addition of the precursors to the flow. The flame changes were recorded and analysed frame-by-frame.

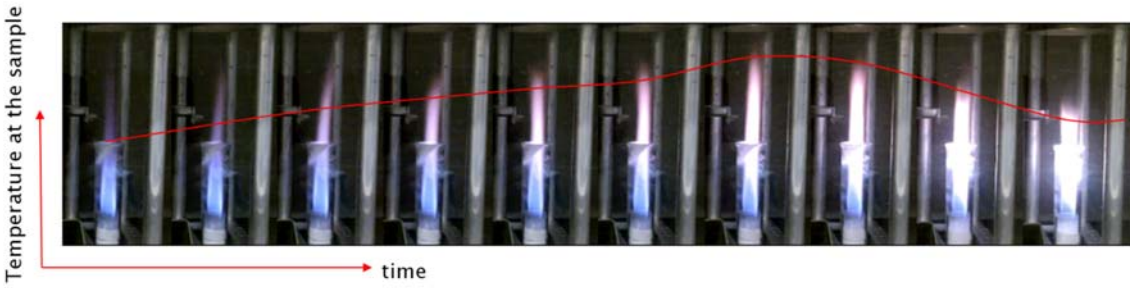

Image 3. Flame changes with the addition of precursors to the flow.

The initial frame shown in Image 3 represents the pure H_2/O_2 flame, subsequent frames show the evolution of the flame as the reactants are incorporated in the flame after the MFC's were switched on by the recipe commands. The red line of Image 3 shows the change in temperature at the sample level measured during the flame changes

An initial low brightness is perceptible at the top of the flame; as it starts to become more intense, the luminous zone moves down into a lower reaction zone until it reaches a minimum position. It is essential to notice that also a change in flame height occurs during this stabilisation process.

Experiments using the initial established conditions show signs of low-temperature depositions. The changes in the flame led to a change in the reaction zone. Therefore, the temperature of the deposition changes during this process of flame stabilisation. The temperatures obtained in the burner characterisations had to be adjusted to compensate the changes in the flame height; but, also to compensate the changes in the reaction zone position.

2.2.1.1 Discussion and Conclusion

Increasing a stoichiometric flow of the H_2/O_2 flame has, as a result, a rise in temperature of the flame. Increasing the flow of O_2, using a fixed flow of H_2, reduced the temperature of the flame. Because the system is not sealed, when the H_2/O_2 ratio < 1 the combustion of H_2 uses the flow of O_2 and complements with oxygen available from the surrounding atmosphere. Thus, any increase in O_2 flow results in an excess that tends to cool down the flame.

Conversely, increasing the flow of H_2 using a fixed flow of O_2 tends to increase the temperature of the flame. Any increase of fuel is going to burn in the presence of oxygen and, as the flow of fuel increases, the energy released from the combustion increases.

Increasing the inert gas flow reduces the temperature of the flame, but that is due to the extra volume of the flow absorbing the energy from the combustion. An increase of the temperature is evident when the outer ring of the burner is closer to the substrate. The outer ring preserves the flame confined closer to the target, and subsequently, the heat transfer is more efficient.

The experiments carried out with the initial established conditions resulted in cold depositions. Parameters had to be adjusted to consider the fact that the flame changes affect the reaction zone position and subsequently the temperature at the sample level. After the flame behaviour was analysed, and the correspondent corrections were made to the temperatures; it was possible to obtain a suitable soot deposition for the following stages of the process.

2.2.2 Burner traverse speed

During the process, it was noticed that the hot zone had a gap or a delay concerning the position of the burner or the deposition zone. Thus, the initial traverse speed condition of 0.100 $m \cdot min^{-1}$ was reduced until no gap between the hot zone and burner position was observed.

A difference in the temperature of at least 63% compared with the stagnation point was recorded when the burner reached the probe position. Temperatures of an H_2/O_2 flame using fixed flows and ratio were measured using an R-type thermocouple.

The probe was inserted directly into the flame and set on the rotational axis of the substrate as shown in Image 2 from the previous section. An example of the delay or gap that occurs between the burner position and the hottest zone is shown in Image 4.

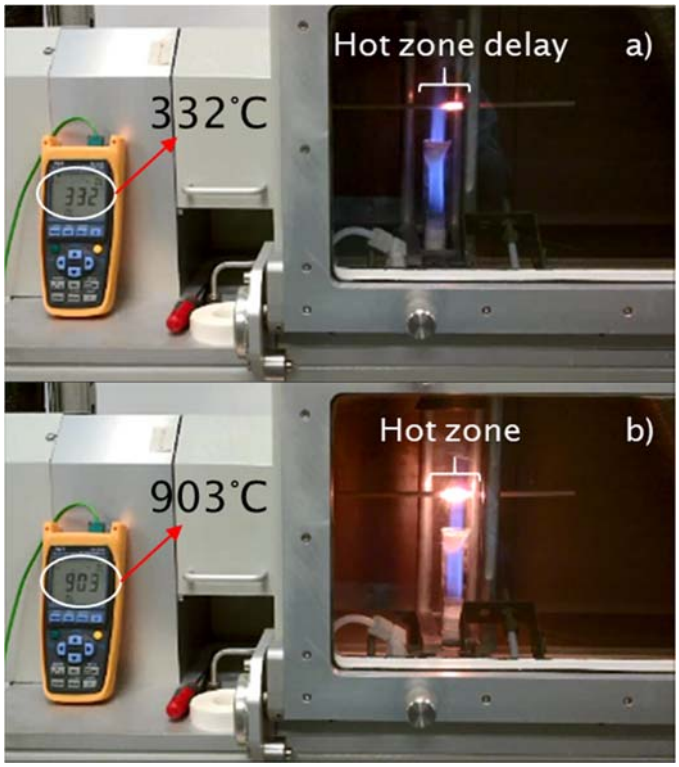

Image 4. Effect of carriage traverse speed in target temperature. a) Delay of the hottest zone with relation to the burner position for moving carriage, and b) stationary point.

Analysis of the traverse speeds of the burner was performed to match the burner position with the hottest zone. During the experiments the speed of the traverse carriage was established for different compositions to minimise the delay in the hot zone. Table 1 lists the burner speeds determined according to the deposition required.

Deposition	Traverse speed [mm·min^{-1}]
SiO_2	Up to 0.020
$SiO_2/GeO_2 > 5$	Up to 0.020
$SiO_2/GeO_2 < 5$	Up to 0.015
GeO_2	Up to 0.015

Table 1.Traverse speed for OVD depositions with different flow compositions.

2.2.2.1 Discussion and Conclusion

It is noticeable that a slight reduction of the traverse speed is needed for the highly doped germanium-doped silica preforms and pure germania preforms. The difference of the heat capacity between the SiO_2 and GeO_2 may explain this experimental result. This assumption is based on the fact that the heat capacity of the GeO_2 is higher than that of SiO_2, which means that the amount of energy to raise the temperature in a determined volume of GeO_2 is higher than in the case of the same volume of SiO_2.

That explains why the traverse speed needs to be lower allowing the same amount of heat from the flame be transferred to the preform, matching the hottest point with the burner position.

The difference in position between the hottest point and the burner position could provoke an excess of temperature which leads to non-desirable evaporation of the GeO_2. Also, physical modification of the soot due to the high temperature could worsen the physical properties mismatch, increasing the likelihood of cracks in the soot.

An alternative solution to avoid the overheating of the deposition could be the reduction of fuel flow; however, reducing the energy in the system will impact directly in the chemical reaction, making the soot fragile and liable to crack.

2.2.3 Bait rod as a detachable substrate

Particular consideration had to be analysed for the use of a detachable substrate. Characteristics of the substrate; the design of the handle; consolidation furnace length, diameter and thickness of the deposition were among the parameters evaluated. Finally, thorough analysis of deposition conditions was conducted to obtain the soot characteristics preventing cracking or fractures during the bait rod removal. Chapter 3 and Chapter 4 discuss this analysis extensively. In this section, the requirements and design of the detachable substrate is discussed.

Two separate detachable tapered bait rods were investigated. A silica glass rod was made in-house and an alumina rod that was bought from a commercial supplier. Both bait rods were used with the same handle support/seal accessory shown in Image 5. The seal prevents the escape of deposition fumes through the handle tube. The construction of the seal includes a PTFE compression ferrule that relies on its deformation by longitudinal compression; it also incorporates an O-ring to provide better sealing.

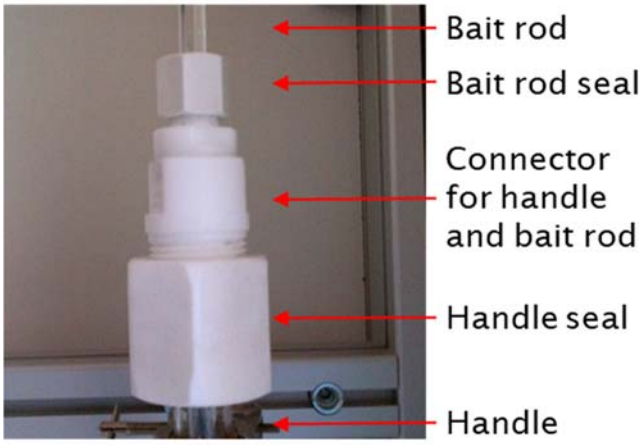

Image 5. Support/seal accessory including a top seal for the bait rod and a bottom seal for the handle.

The use of the alumina bait rod was found to perform better for the detachment procedure; it also reduces the damage to the inner surface. The silica glass bait rod was less reliable as it was more likely to jam. The silica substrate is no longer useful when the deposition has more than 5 mol% of germania. However, the use of the alumina bait rod required substantial modifications to the handle design.

The first problem is that the tight fit used on the silica glass bait rod cannot be used with the alumina bait rod. The thermal expansion coefficient of the alumina is about 14 times larger than the silica; this causes the silica handle to break by

the expansion of the inserted alumina rod. The breakage occurs as soon as the burner starts the preheating pass in the recipe. The assembly requires a gap between the bait rod and the handle to avoid the rupture of the handle. Nevertheless, an intersection between the bait rod and the handle is required. Otherwise, the resulting loose bait rod makes the preform joint brittle.

The difference between the diameters of the bait rod and the inner diameter of the handle was another adverse factor. It was not possible to achieve a correct transition of the deposition from the bait rod to the handle. The overlap on top of the handle is critical since it becomes the only support of the preform once the bait rod is detached. An inadequate joint between the preform and the handle may cause the preform to separate from the handle. That would compromise the preform since there is no way to recover the deposition at this stage. Image 6 shows the typical problems on the joint between the handle and the bait rod.

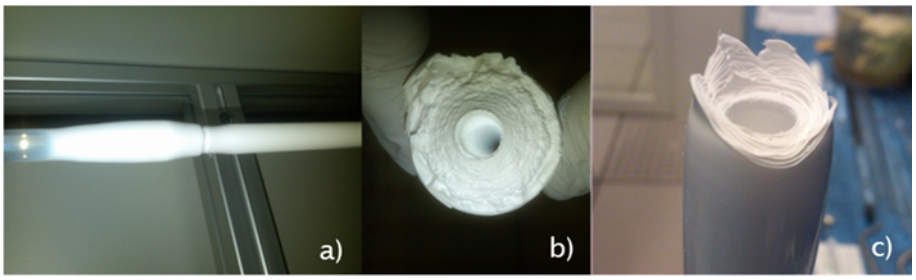

Image 6. Defects on preform/handle joint; a) Preform joint not deposited; b) Preform with too low temperature detached from the joint; c) Preform with too high temperature detached from the joint.

A new handle design shown in Figure 5 was introduced to overcome the problems when using the alumina bait rod. A detailed fabrication process is described in Appendix A; the main feature of this design is that the wall thickness of the joint end was reduced. A simple stretching tube process usually does not work correctly. The critical internal diameter is easy to collapse in excess, preventing the bait rod from sliding inside fully.

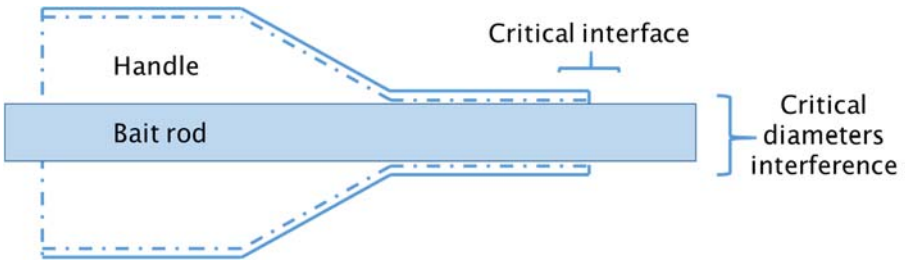

Figure 5. Schematic of new handle design.

After the implementation of the new handle; successful removal of the alumina bait rod from the soot preforms was achieved. The new handle design is also useful for the original bait rod design made from glass. An example of the alumina bait rod removal is shown in Image 7 the evolution of the deposition step by step as well as the final preform before and after the alumina bait rod removal.

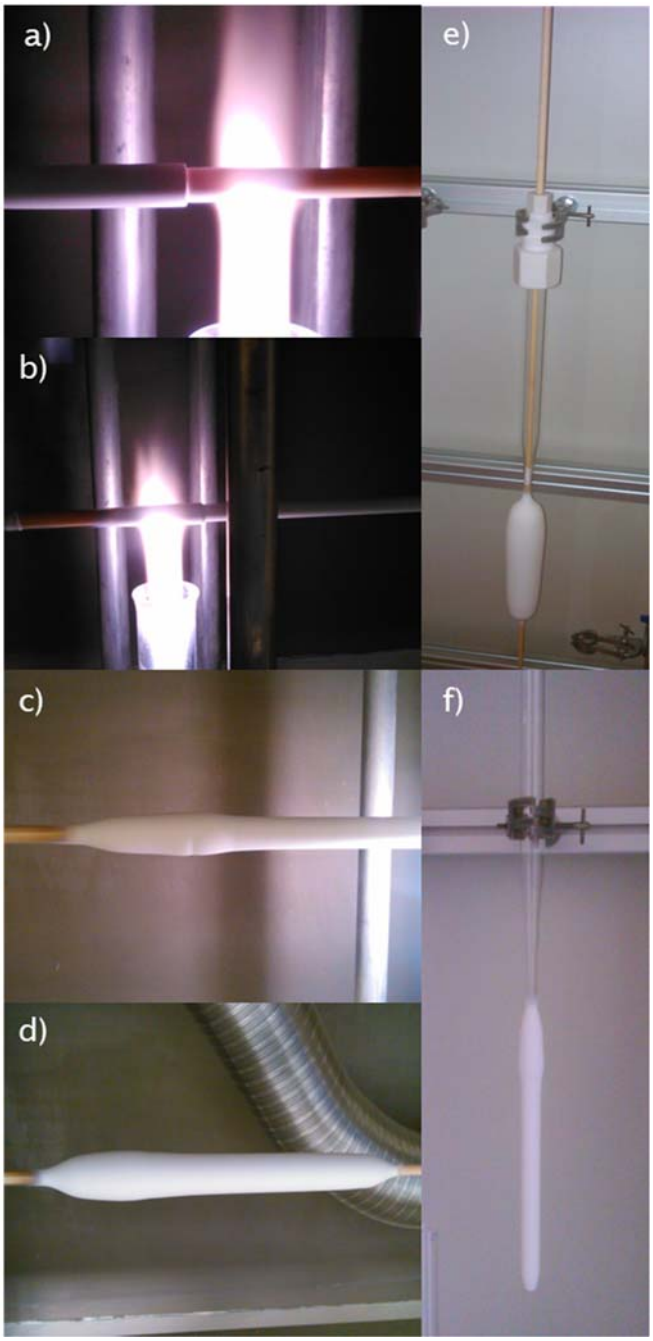

Image 7. Evolution of the preform joint and deposition techniques that enables successful bait rod removal.

The stages shown in Image 7 are as follows: a) first layer; b) the well-executed joint of the preform; c) self-supported preform. At this stage the bait rod can be detached without any risk to the preform or joint; d) final preform; e) preform assembly before removal of the bait rod; f) preform without bait rod. The preform after bait rod removal does not present cracks or fractures.

2.2.3.1 Conclusion

The use of the handle support/seal accessory prevents the escape of deposition gases through the handle tube to the outside. At the same time, it operates as a fixed point for the bait rod. The new handle design allows overcoming the challenges of the bait rod removal, and it can be used with the glass and alumina substrates.

The depositions made using this handle design and following the deposition conditions described in this report can be successfully detached without fissures at the interface between the soot body and the bait rod.

2.2.4 Solution doping apparatus

With the aim of increasing the fabrication capabilities of the OVD process, it is intended to have a solution doping process. The current techniques used for MCVD preforms are not suitable for OVD soot preforms.

Nevertheless, the same principle was used to build-up the first prototype of an apparatus which allows the solution doping technique to be used with OVD soot preforms. Also, the drying process had to be redesigned, enabling all the solvent to evaporate from the soot preform.

The OVD soot preform was soaked inside a tube as shown in Image 8. A peristaltic pump controlled the filling speed of the solution. Once the soot body was soaked, it was possible to observe the volume of the solution being absorbed by the porous soot preform.

A significant reduction (12% - 50%) of liquid volume after draining the solution was noteworthy. The variation of volume absorbed by the soot preform depends on the size of the preforms. The experiments reported in this section were using preforms of 6 and 12 layers of soot deposition.

The amount of solution absorbed is related to the available porous volume inside the soot preforms, with bigger diameters retaining more volume of solution. After soaking an increase of the weight of the preform is noticeable. Also, soot density in the preforms is an additional factor that determines the volume of liquid that can penetrate into the preform.

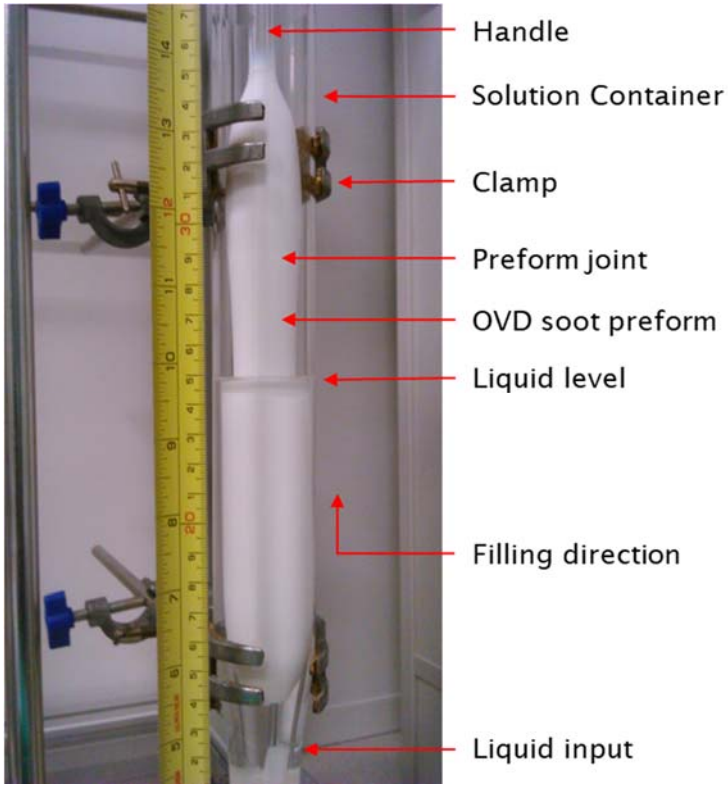

Image 8. Solution doping of OVD porous soot preform.

Preforms were kept in a vertical position to avoid rupture of the joint due to the increased weight of the soaked soot. The preforms were then dried overnight at room temperature under continuous extract flow to evaporate a significant amount of solvent. Nevertheless, an additional controlled heat drying process was required. Therefore, a preform drying apparatus was proposed, which utilised a Heathway MCVD lathe bed for its setup.

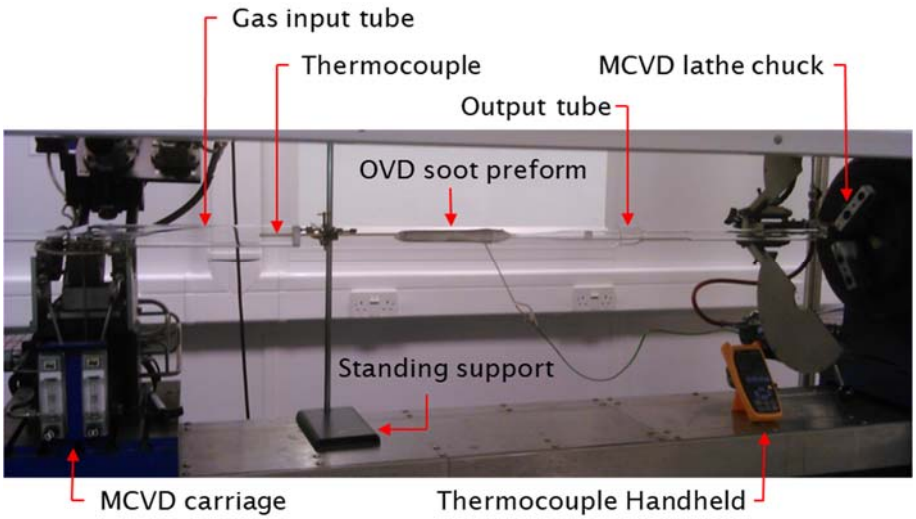

Image 9. Experimental setup for drying apparatus characterisations.

Temperature profile measurements were taken from the drying setup shown in Image 9 by replacing the soot preform with a R-type thermocouple placed in the centre of the lathe axis. Measurements provided information on the gas flow temperature profile along the setup.

A stationary burner with a H_2/O_2 ratio of 2 was used for heating a N_2 flow of 2000 sccm. The temperature was measured with the preheated gas flow at 290 mm from the burner. Graph 6 shows the information obtained after several sampling intervals of 5 minutes. It was possible to observe that the temperature tends to stabilise after 30 minutes to around 314 K. This temperature was too low for the efficient evaporation of the solvents inside the soot preform.

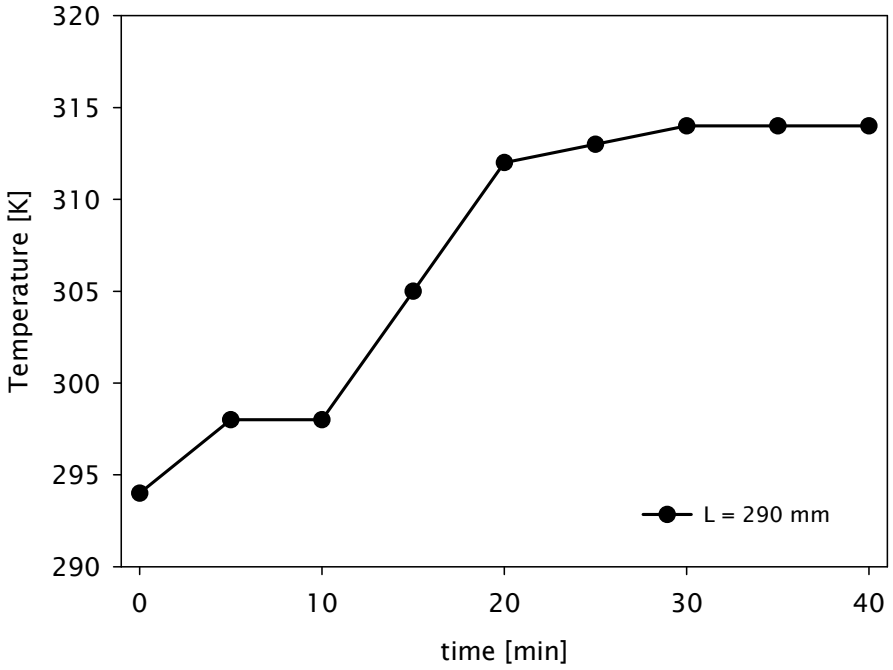

Graph 6. The temperature of gas flow in drying apparatus at L=290mm from burner position.

It was expected that reducing the distance between the burner and the thermocouple would increase the temperature. However, because the solution contains solvents; it was mandatory to identify the real temperatures along the device. It is shown in Graph 7 the temperature behaviour while reducing the distance between the R-type thermocouple and the burner position. Same conditions described before with a stationary burner and a H_2/O_2 ratio of 2 for heating a N_2 flow of 2000 sccm were used. For this part of the characterisation, the thermocouple was the element in motion. Readings were taken at 5 min interval in each position allowing time for the thermocouple measurement to stabilise.

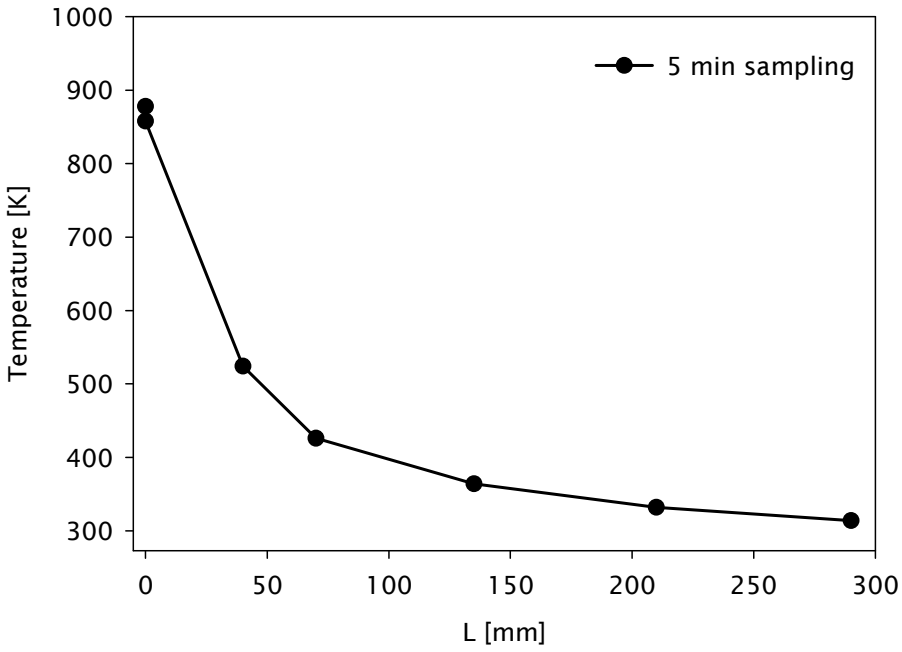

Graph 7. Temperature gradient along the length of the drying apparatus.

Another option for increasing the temperature in the drying process of the soot preform was moving the carriage at a fast speed to provide additional heat for a short period. Temperature measurements with the thermocouple at a fixed point and using the traverse speed of the burner were also performed and are shown in Graph 8.

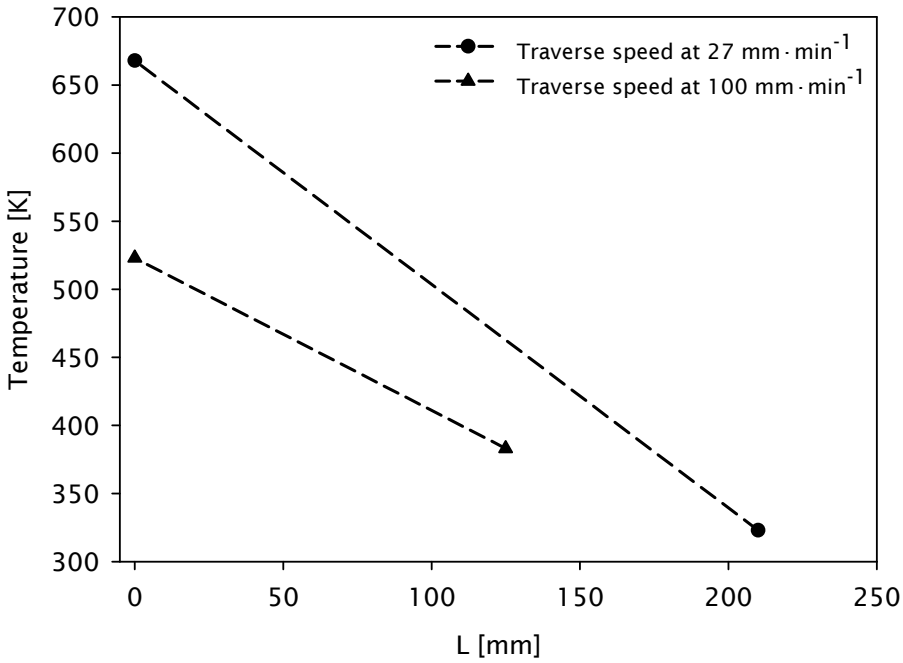

Graph 8. The temperature of gas flow in drying apparatus using burner traverse motion. The lines are drawn as a guide for the eye.

Finally, a horizontal drying setup was established using the information obtained from the drying apparatus characterisation. The drying setup was implemented in one MCVD lathe as shown in Image 10. The setup allows the porous soot preform to dry in a controlled way, using a preheated gas atmosphere. The apparatus enables the use of different lengths of preform/handles sets, which give particular versatility to the process.

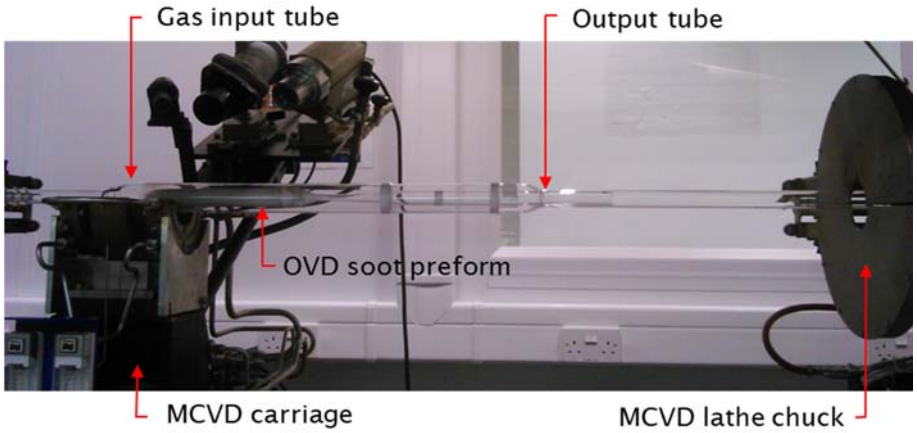

Image 10. OVD solution doping drying setup.

2.2.4.1 Conclusion

The solution doping technique has been successfully demonstrated using the apparatus proposed. The significant solvent volume retained by the porous soot preform is a good indication of the permeability of the soot. The further analysis presented in Chapter 8 shows the incorporation of the dopants added to the preform. The drying apparatus can still be improved in the temperature control. The possibility to use a vertical setup and a more stable heat source is part of the further development required for this technique.

Chapter 3 OVD Process Analysis

The detachable bait rod described in section 2.2.3; and the solution doping described in section 2.2.4 are indeed the result of a long process of establishing the correct parameters for the soot deposition. In this chapter, the analysis of the deposition conditions is discussed.

The initial part of this chapter evaluates the dominant chemical reactions that occur in the OVD. This also, identifies the differences between the ORC system and the equipment that reported in the literature, and how this differences promote different reaction paths, and which parameters require consideration.

After the porous soot preform has been obtained; it is necessary to dehydrate it to remove the OH content, and then the preform can be sintered into a transparent glass. Parameters for the process of dehydration and consolidation are also discussed in this section.

The information contained in this chapter was also essential for the development of the following chapters in this thesis. Notably, the development of germanosilicate glass reported in Chapter 6; Germania glass reported in Chapter 7; and Phosphosilicate glass reported in Chapter 9 were based on the information provided in the following sections of this chapter.

3.1 Characteristics of the deposition

Extensive analysis is required to understand the reactions between the precursors and their dependence on temperature. Parameters such as burner design and stoichiometry of the precursors and fuel modify the reaction conditions.

The incorporation of dopants modifies the thermodynamic reaction parameters, even to the point of suppressing the deposition. Also, different intermediate products may be formed during the process which also requires investigation.

Since the compactness of the soot depends on the deposition parameters[32,43,48,50,51], it is necessary to evaluate the conditions for each of the precursor(s) mixtures and deposition temperatures.

Numerical and experimental studies have reported the hydrolysis and oxidation of silica and germanium-doped silica preforms as the assumed reactions during the external vapour deposition processes such as VAD and OVD; nevertheless, these reports do not explain formally which of the reactions occur or how they occur.

In the literature, the process of heat generation is typically reported including methane oxidation flame; and the chemical delivery systems using O_2 as the carrier gas[5,26,43,47,48,52-56]. For the case of the OVD equipment in the Optoelectronics Research Centre, the heat source is provided by an H_2/O_2 flame and the carrier gas is Ar as described in Chapter 2.

Burner configurations also affect how the reactions undergo. A shield gas between the O_2 and H_2 prevents the premature mixing of the fuel and oxidiser. Likewise, there is no formal explanation about how the reactions undergo in the systems with H_2/O_2 flame burner deposition, or how the use of O_2 as a carrier gas modifies the conditions of the reaction[32,36,44,50,57-63].

A VAD system using argon as a carrier gas was described by Potkay et al.[64]. The system had a specific design for germanium-doped silica soot preforms and used a central tube with a mixture of $SiCl_4$, $GeCl_4$ and argon. It was followed by a secondary tube with a mixture of $SiCl_4$ and argon for the jacketing of the preform core. Unfortunately, there is no information about the reactions and their temperature dependence in the report.

Information obtained from thermodynamic analysis provides critical information for the deposition of SiO_2, SiO_2/GeO_2 and GeO_2 soot porous preforms. The reactions studied are listed below in a stoichiometric reaction followed by their molecular structure[65,66]. Extended data for the $SiCl_4$ reactions described below is available in Appendix B.

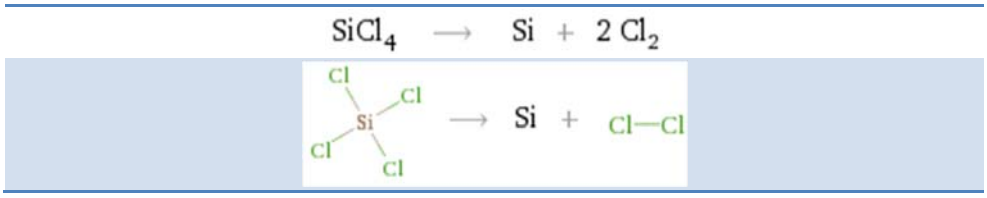

Equation 1. Silicon tetrachloride dissociation.

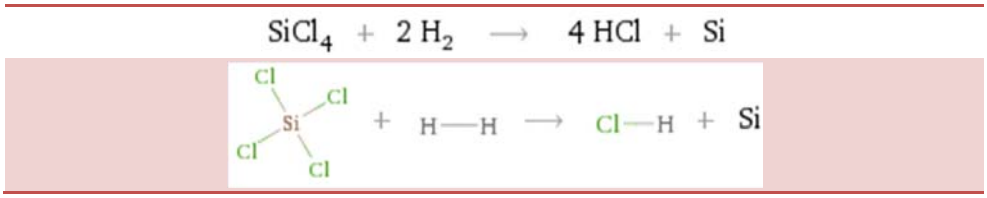

Equation 2. Silicon tetrachloride reduction.

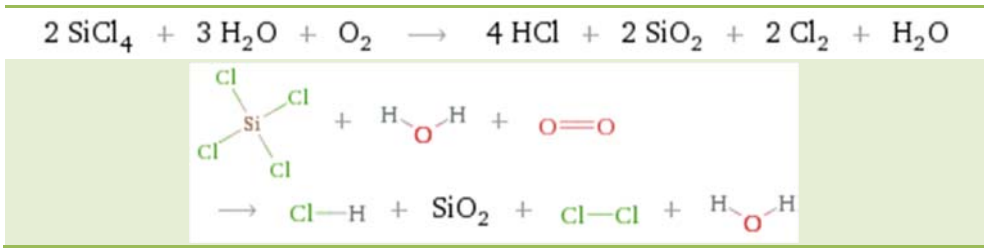

Equation 3. Silicon tetrachloride hydrolysis (1).

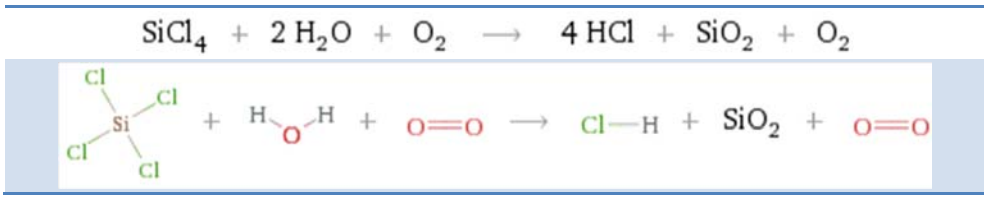

Equation 4. Silicon tetrachloride hydrolysis (2).

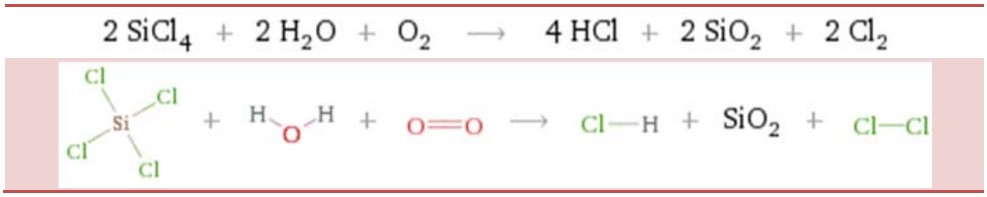

Equation 5. Silicon tetrachloride hydrolysis (3).

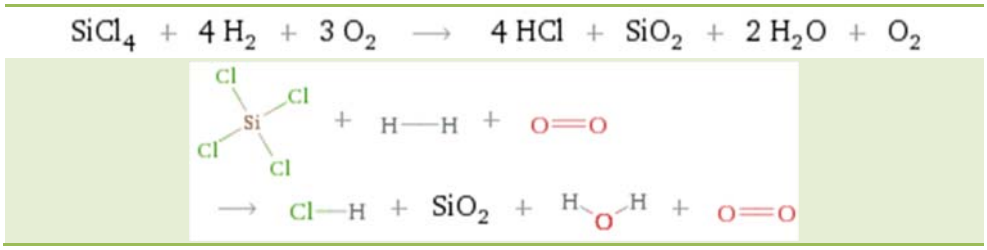

Equation 6. Silicon tetrachloride reduction and oxidation (1).

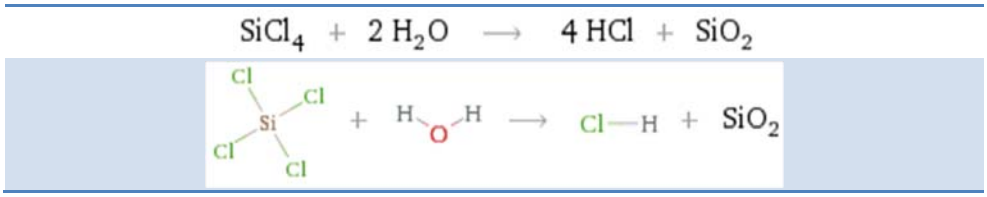

Equation 7. Silicon tetrachloride hydrolysis (4).

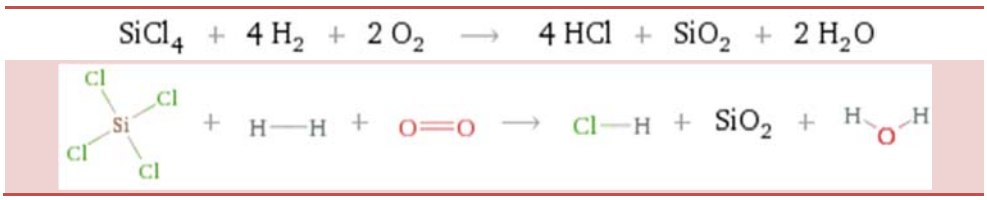

Equation 8. Silicon tetrachloride reduction and oxidation (2).

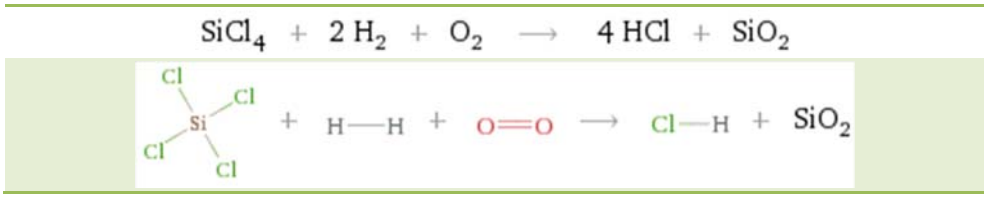

Equation 9. Silicon tetrachloride reduction and oxidation (3).

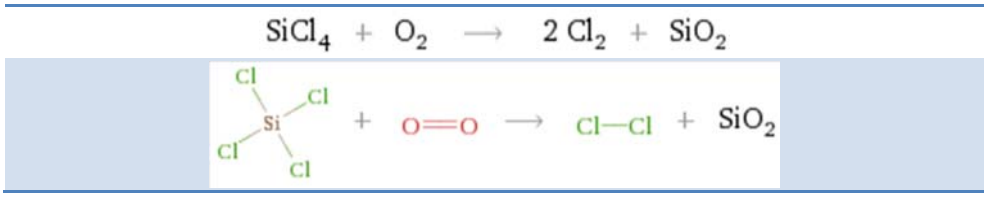

Equation 10. Silicon tetrachloride oxidation.

The changes in the flame happening during the addition of precursors are also essential to understand the behaviour of the temperature with the addition of precursors in the reactants flow. Burner flame studies support the characteristics of the flame temperature and their behaviour along the flame[63,67].

3.1.1 Deposition parameters

Observations during initial test depositions showed a relation between temperature and compactness of the soot. High-temperature depositions resulted in soot more compact, and if the temperature is too high, the deposition can partially sinter.

Based on the fact that the reactions involved are exothermic, a positive change of temperature is expected as a result of adding the precursors to the flow. Thermodynamic analysis of the possible reactions during deposition was performed with the aim of validating the reactions involved and the likelihood of their occurrence.

The author decided, based on his previous research experience, to use the Ellingham diagrams for the thermodynamic calculations. This analytical tool is widely used by materials scientists and has its origins in metallurgy[68]. It is primarily used to evaluate the likeliness of the reduction of metal oxides and sulphides. The Ellingham diagrams assume the thermodynamic principle that any reaction depends on the change of the Gibbs free energy (ΔG). Equation 11 shows the relation between ΔG; the temperature in the system T; the change in Enthalpy (ΔH) and the change in Entropy (ΔS).

$$\Delta G = \Delta H - T\,\Delta S$$

Equation 11. Gibbs free energy change as the principle for Ellingham diagrams.

The Ellingham diagrams plot the ΔG for the reaction as a function of temperature. It is important to mention that this thermodynamic analysis neglects the kinetics of the chemical reaction. Therefore, it is possible that despite having reactions that were predicted as favourable in the Ellingham diagrams; the reactions can happen at a very slow rate. Also, Ellingham diagrams assume certain conditions which may exclude relevant information, such as the melting and boiling point, or crystalline phase transitions of the GeO_2 which needs to be carefully considered. Extended thermodynamic calculations data for the analysis presented in this chapter is available in Appendix C.

Graph 9 shows the Ellingham diagram calculated for the possible reactions involved in the OVD system, accordingly with the precursors and substances available to the process. It shows that the reaction in Equation 1 is endothermic, and it is highly unlikely to happen under the experimental conditions of the OVD process.

Equation 2 also represents an endothermic reaction but turns it into an exothermic reaction at a temperature of ~ 1652 K. The presence of H_2 and high temperatures may result in pure silicon deposition. However, these reactions require the absence of O_2, which is not the case. Both of the previous reactions were analysed to ensure the likeliness of an additional reaction of the gases before its incorporation with the O_2.

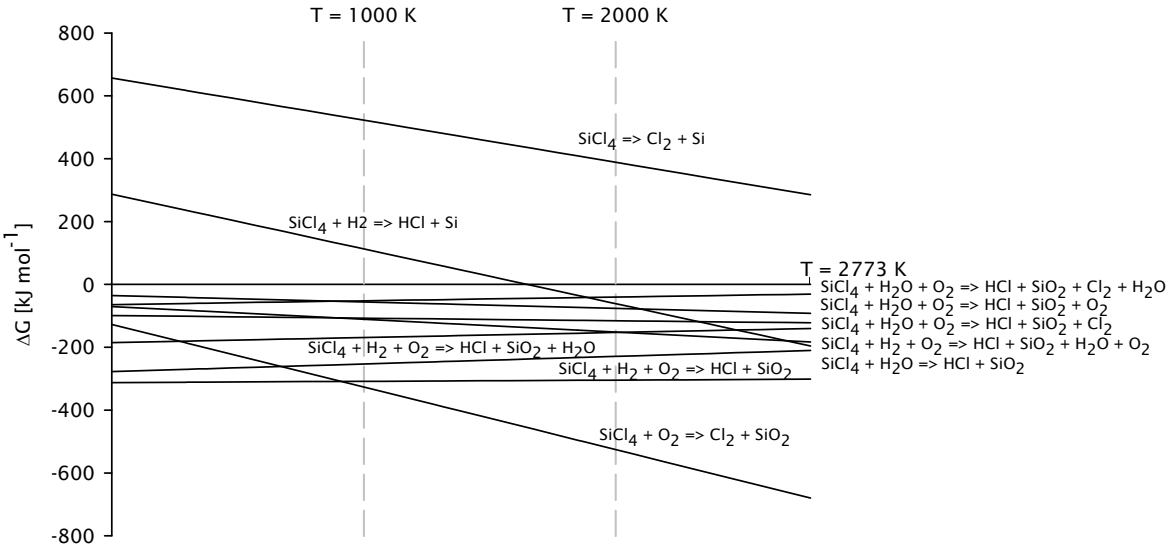

Graph 9. Ellingham diagram for all the reactions identified for the OVD deposition process.

By discarding the endothermic reactions, the Ellingham diagram showed in Graph 10 only considers the exothermic reactions. The reaction from Equation 10 seems

to be the most thermodynamically favourable. However, the conditions for this reaction are given in the case of using O_2 as a carrier gas, as with the MCVD process. Moreover, the presence of H_2 in the reaction zone suppresses this reaction path.

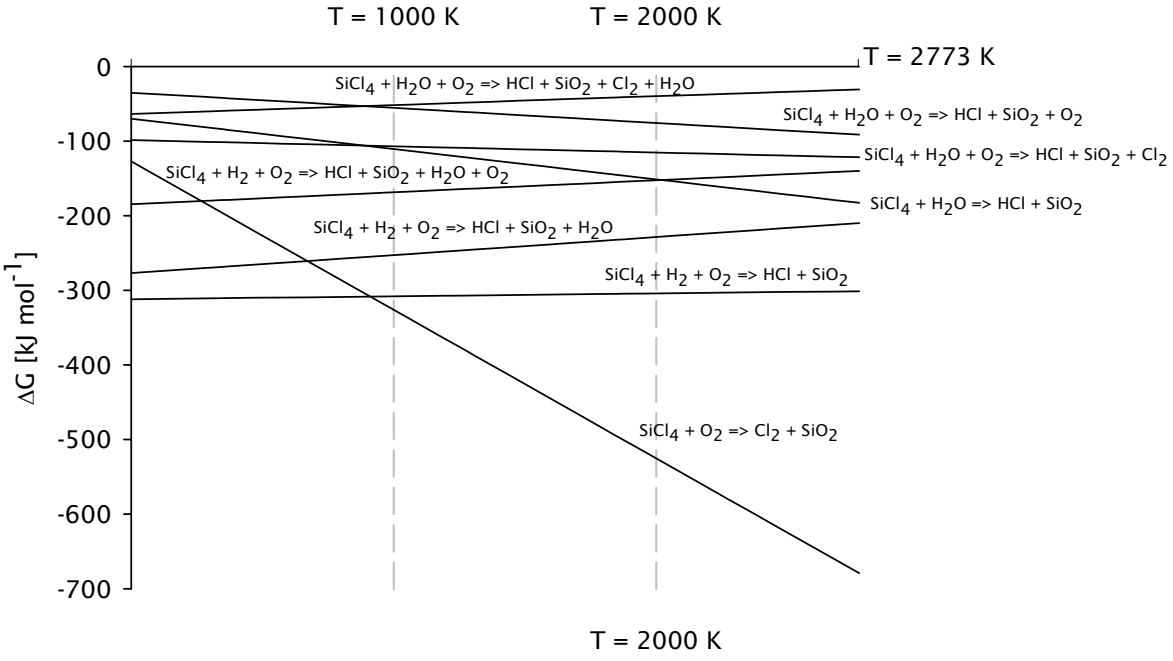

Graph 10. Ellingham diagram for only exothermic reactions identified for the OVD deposition process.

Represented in Graph 11 are the remaining possible reactions to the system. The reactions below satisfy the conditions for the OVD equipment of the ORC. The previous assertion is considering the availability of the substances in the reaction zone, but also the thermodynamic conditions present in the system.

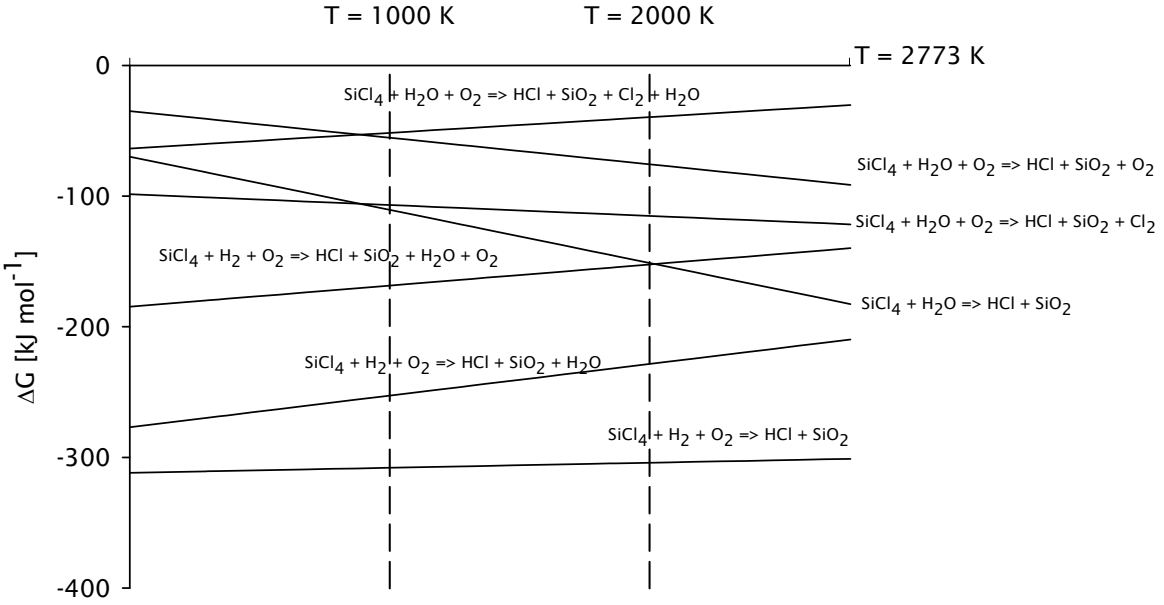

Graph 11. Ellingham diagram for the reaction conditions of the OVD System.

The reactions from Equation 3, Equation 4, Equation 5 and Equation 7 consider H_2O as a reactant. The assumption of having H_2O as a reactant can be correct if the design of the burner combines the mixture of H_2 and O_2 without a shield gas. Alternatively, the burner should have additional fuel/oxidiser outer rings. For both cases, the hydrolysis reaction would happen separately to the oxidation/reduction of the precursors. However, for the OVD burner design that was in use for the experiments in this thesis, this is not the case. The H_2O is not a reactant and therefore is not an input for the chemical reactions.

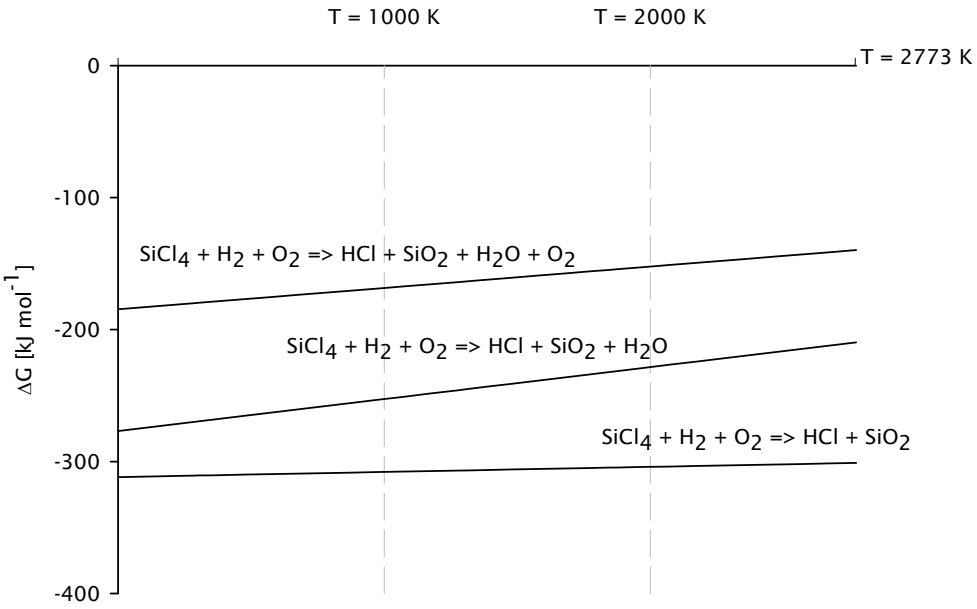

Graph 12. Ellingham diagram for the dominant reactions on the ORC-OVD system.

The three reactions in Graph 12 represent the remaining exothermic reactions which satisfy the thermodynamic requirements. This reactions have a decrease in entropy, as it can be noticed from the slope of the plots. The reaction expressed in Equation 9 is the ideal stoichiometric reaction. However, the reactants flows of the burner at stoichiometric conditions do not reach the temperature required to make a deposition with the desired characteristics.

In fact, reactions from Equation 9, Equation 8 and Equation 6 are the same reactions affected by stoichiometric conditions, and their differences mainly depend on the oxygen availability. Given the conditions required for the depositions, the reaction indicated in Equation 6 is likely to dominate the process.

Based on the previous discussion, the reactions of $SiCl_4/GeCl_4$ and $GeCl_4$ will now be considered taking place in the same reaction path as Equation 6. The reactions for $SiCl_4/GeCl_4$ are conditioned to the molar fraction of the reactants in the flow.

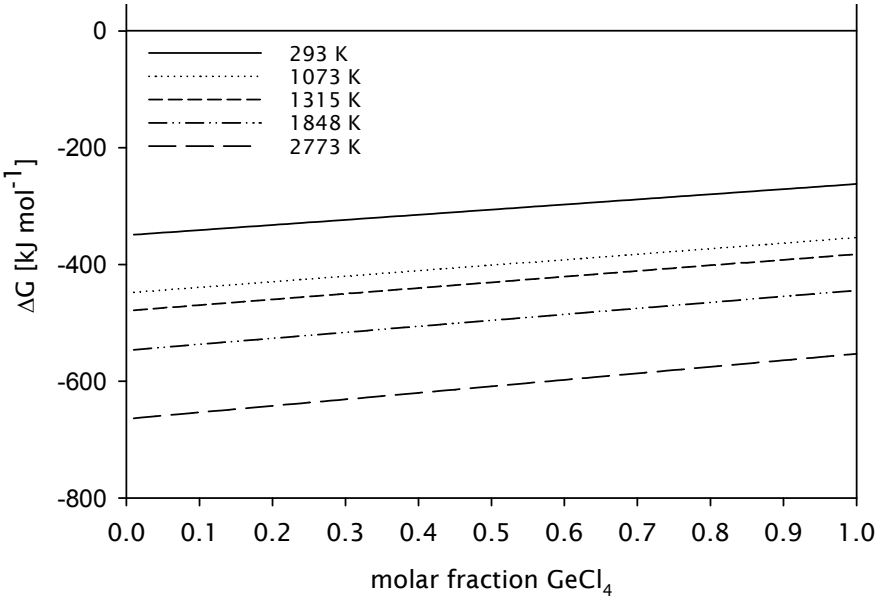

Graph 13. Impact in ΔG by the molar fraction of $GeCl_4$ at different temperatures.

Graph 13 shows how the thermodynamic conditions are less favourable as the amount of $GeCl_4$ is increased. Higher temperatures facilitate the reaction regardless of the molar fraction in the flow composition.

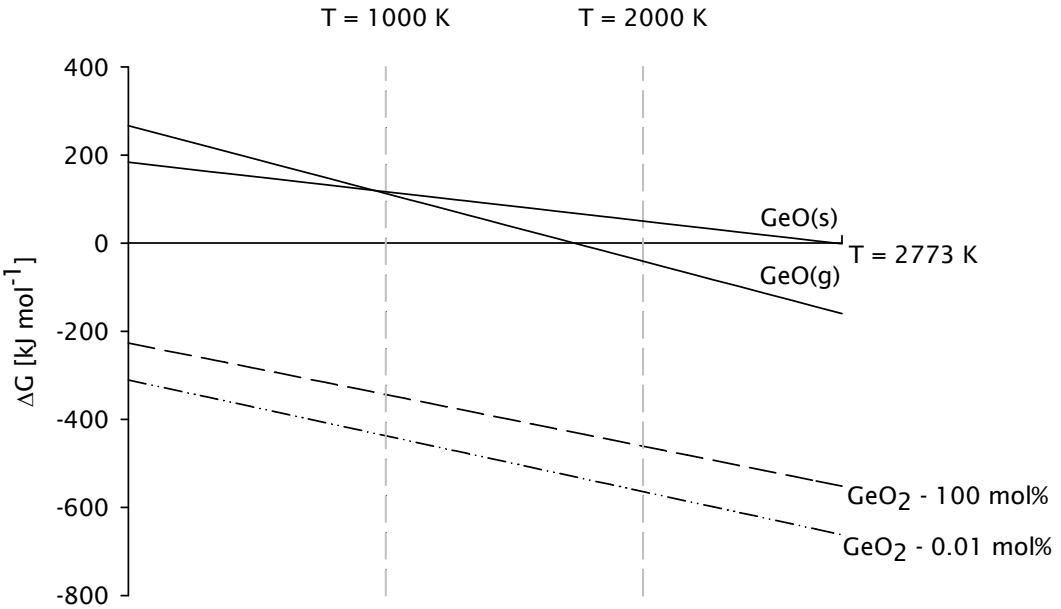

Graph 14. Ellingham diagram for germanium oxides.

The possible reduction of GeO_2 into GeO was analysed. Graph 14 shows the absence of an intersection between the GeO thermodynamic slopes. The GeO_2 reaction conditions, for the range of 0.01% - 100% mol, is also not intersected by the GeO thermodynamic slopes. Moreover, the energies required to reduce the GeO_2 into $GeO_{(g)}$ and $GeO_{(s)}$ are available from temperatures beyond 1735 K and 2754 K respectively. The reduction into pure germanium was not analysed for deposition

condition purposes because the energy in the system during the deposition is not enough to enable these reactions.

3.1.1.1 Conclusion

The deposition parameters for pure silica soot preforms were experimentally demonstrated being less sensitive than the germanium-doped silica preforms. The main difference is due to the thermodynamic and physical property differences between SiO_2 and GeO_2.

Deposition of silica at 1500 K is readily achievable. However, at that temperature, the GeO_2 is evaporated. The reduction of temperature helps the GeO_2 deposition, but it is required in such magnitude that the silica soot starts to lose the density required and fails typically by cracking.

For each SiO_2/GeO_2 ratio, it is necessary to recalculate all the parameters, since there is no real-time temperature measurement which would allow modelling of a parametric relation between mol% and deposition temperature. Pure GeO_2 depositions have been performed successfully; however, the thermodynamic conditions are on the limit, which requires further calculations to modify the system extending the range of deposition operation.

3.2 Dehydration and consolidation

The dehydration process aims to remove the hydroxyl radicals trapped inside the porous soot preform during the deposition by the hydrolysis flame. Nevertheless, when changing the composition of the deposition, it is required to make a thorough analysis of the dehydration process, owing to the possibility of undesirable reactions that may happen at high temperatures[38,69,70]. Similarly, a more meticulous analysis of the consolidation process must be carried out, owing to the possibility of undesirable reactions that may happen at high-temperatures. Also, the influence of different atmospheres is desirable to be studied[39,40].

3.2.1 Dehydration parameters

Dehydration of the porous soot preform is a second step which was carried out, for this study. The process employs a vertical electrical furnace with rotational and

lengthwise feed/retraction options. The process was set on idle mode at a temperature of 1073 K to prevent devitrification and reduce the risk of rupture due to large thermal cycles.

The dehydration process involved placing the preform in the furnace and ramping up the temperature to 1315 K at a controlled rate of 10 $K \cdot min^{-1}$. During the dehydration process, a He/Cl_2 atmosphere flowed inside the liner tube at a ratio of 16.66. Feed speed of 0.010 $m \cdot min^{-1}$ and a retraction speed of 0.025 $m \cdot min^{-1}$ was used to drive the preform lengthwise through the hot zone of the furnace. A rotation speed of 3 RPM was used to enhance the uniformity of the process.

Thermodynamic analysis of the possible reactions during the dehydration process was performed. Following the same methodology previously used to analyse the deposition conditions, all the possible reactants and products will be analysed.

Independent of the molar concentration or phase in which the GeO_2 is deposited in the porous soot preform, the GeO_2 needs to be calculated as a possible reactant, which is counterproductive to the idea of obtaining GeO_2 from the process. Graph 15 describes the GeO_2 stability and its possible reductions. The temperature currently used in the dehydration process is added as a reference in the graph. It is shown that the GeO_2 is stable up to ~1650 K when the reduction into $GeO_{(g)}$ starts to dominate the process.

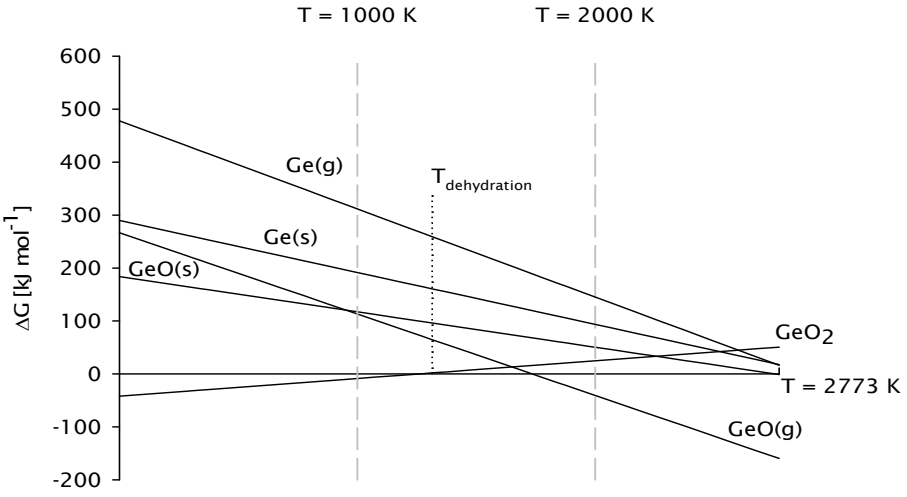

Graph 15. Ellingham diagram for the reduction of GeO_2.

In addition to the thermal reduction, and based on the He/Cl_2 flow during this fabrication step, the halogenation of the GeO_2 was considered as the next principal reaction during the dehydration process.

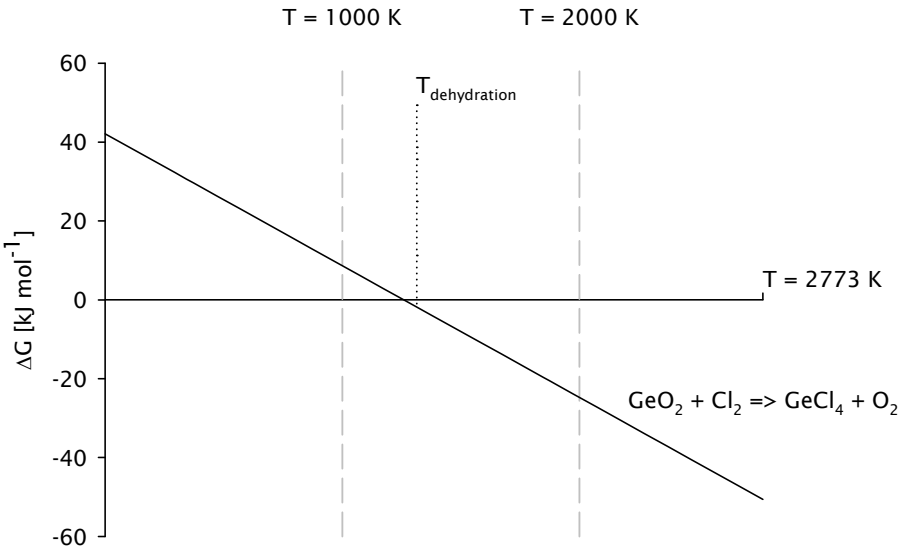

Graph 16. Ellingham diagram for GeO_2 in the Cl_2 atmosphere.

Graph 16 shows the Ellingham diagram for the halogenation of GeO_2 into $GeCl_4$ using the thermodynamic conditions of the dehydration process. It is observed that the formation of $GeCl_4$ is possible under the dehydration conditions.

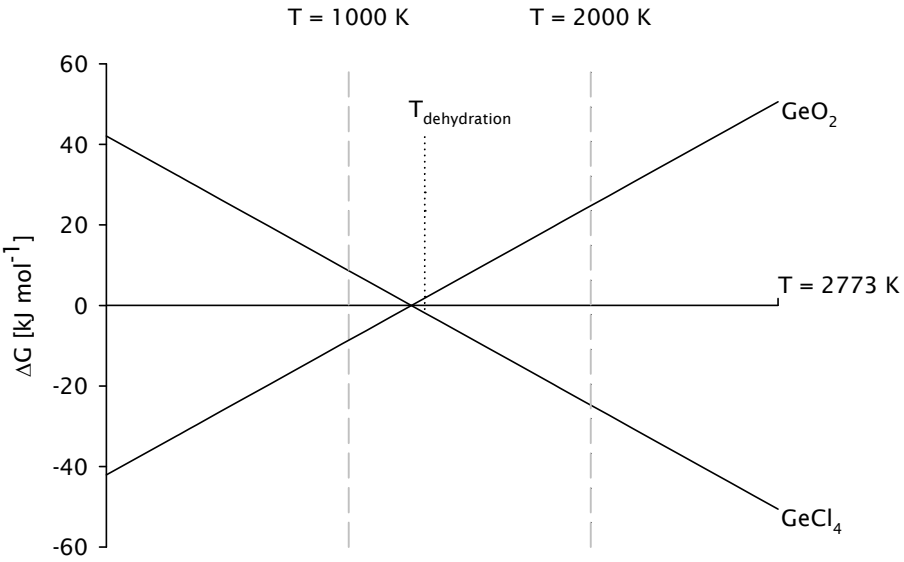

Graph 17. Ellingham diagram for the halogenation of GeO_2.

Graph 17 shows the halogenation reaction of the GeO_2. It is noticeable that the temperature of 1259 K determines the critical point in which the system acquires the amount of energy necessary to proceed with the halogenation.

The information provided by the previous analysis makes clear that the dehydration conditions are not suitable for the germanosilicate preforms. Evidence of the inadequate conditions for the dehydration process in germanosilicate glass is shown in Chapter 6.

The proposed solution to overcome the halogenation of the GeO_2 was to add O_2 flow during the dehydration process. The use of additional O_2 flow in the gas delivery system sets back the halogenation reaction.

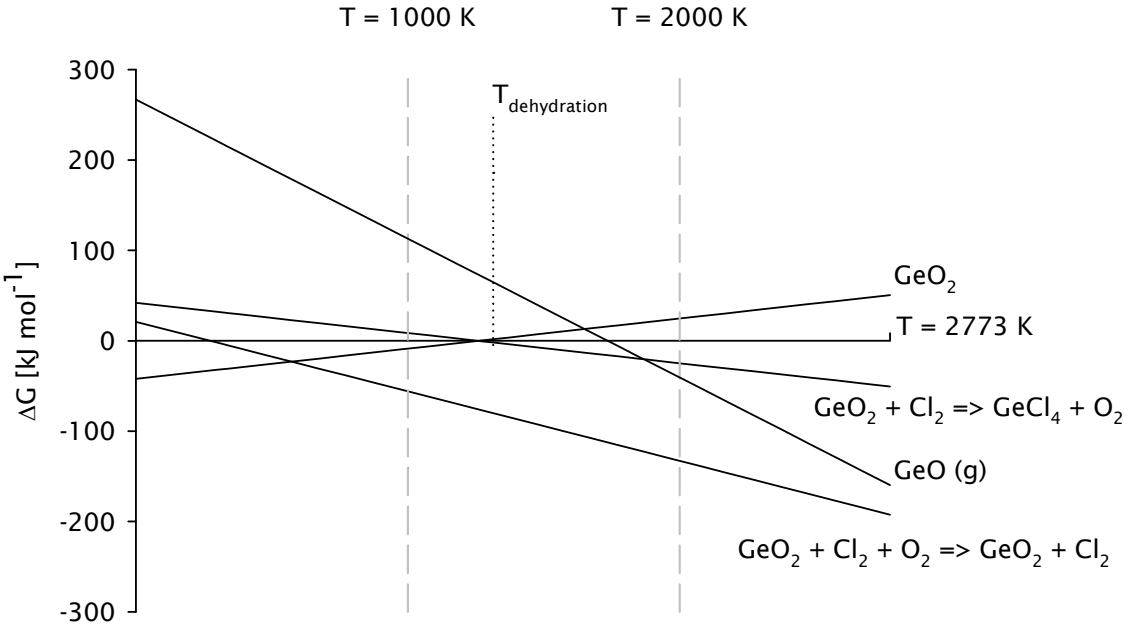

Graph 18. Ellingham diagram for GeO_2 stabilised with a flow of oxygen during the dehydration process.

The calculations for the modified flow conditions are presented in Graph 18. The Ellingham diagram shows that the incorporation of O_2 into the gas flow during the dehydration process is effective, and allows the dehydration of the germanosilicate preforms without reconverting the GeO_2 into halide while still maintaining the dehydration temperature required for the silica. Also, the incorporation of O_2 during the dehydration process sets back the thermal reduction into GeO at high temperatures.

In the interest to understand if any additional reactions were happening with the silicate glass, additional thermodynamic calculations were carried out. The resulting Ellingham diagram for the SiO_2 stability is shown above.

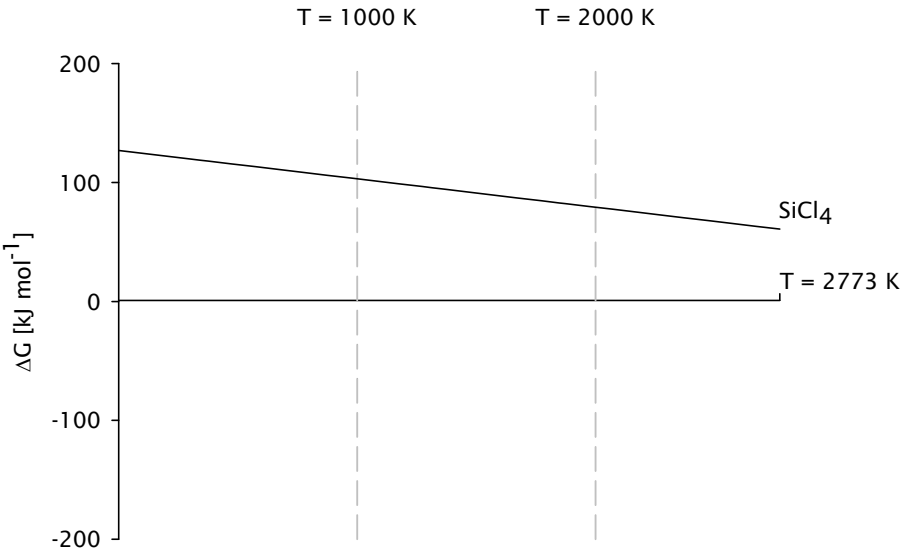

Graph 19. Ellingham diagram for $SiCl_4$.

Graph 19 shows that the formation of $SiCl_4$ by the halogenation of SiO_2 in the Cl_2 atmosphere is not possible. The SiO_2 has high stability during the dehydration process. There is not sufficient energy in the system to enable the halogenation; hence, no further analysis was performed for the pure SiO_2 porous soot preforms.

3.2.1.1 Conclusion

Dehydration conditions for pure silica preforms are suitable, and there are no secondary reactions between the reactants and products as demonstrated by the thermodynamic analysis in this report. However, for the germanosilicate and pure germania soot preforms, the originally proposed dehydration conditions are unsuitable. As a result of the thermodynamic analysis, the halogenation reaction of GeO_2 has been identified as the primary problem. The halogenation of GeO_2 reduces its content inside the porous soot preform, which explains the low content of the compound shown in Chapter 6.

It has been determined that it is compulsory the use of oxygen during the dehydration process to suppress the halogenation. New programs on the electrical dehydration furnace were developed to achieve the correct temperature in the system for each particular case.

3.2.2 Consolidation parameters

The last process of obtaining the clear glass OVD preform is the consolidation. The process was also performed in the vertical electrical furnace. The temperature was

increased to 1848 K at a controlled rate of 10 $K \cdot min^{-1}$. During the consolidation process, a He atmosphere was flowing inside the liner tube. Lower feed speed of 0.005 $m \cdot min^{-1}$ was used during this stage, allowing the preform to turn into a clear glass. Rotation speed remained unchanged. The conditions were experimentally determined using the viscosity curves of the glass as a starting point.

In agreement with Graph 19 from the previous section, the pure silica preforms showed no further reactions due to the consolidation parameters. During consolidation, the SiO_2/GeO_2 and GeO_2 soot preforms are vulnerable to thermal reduction. Considering that helium flows are only used during this fabrication step, there is no other significant reaction during the consolidation process to consider.

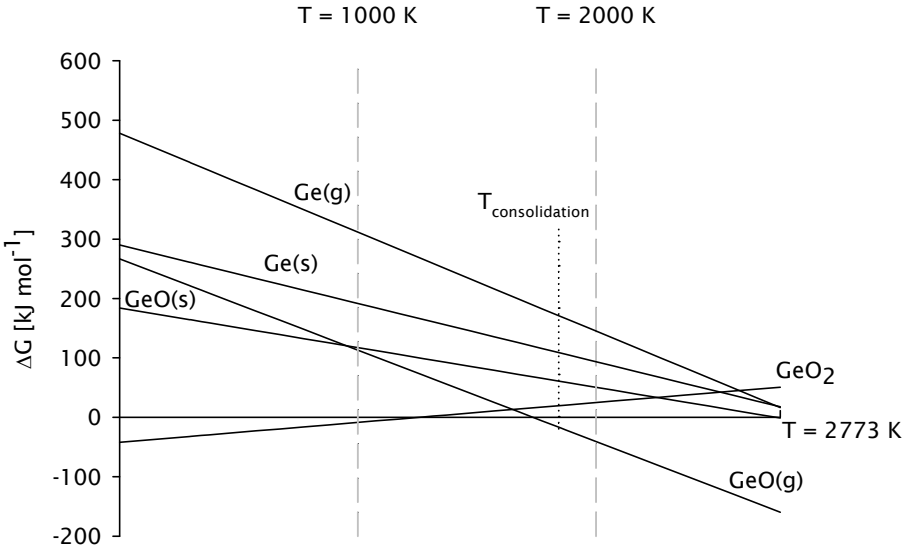

Graph 20. Ellingham diagram for reduction of GeO_2 into $GeO_{(g)}$ during the consolidation process.

Graph 20 shows the temperature of ~1650 K when the reduction into $GeO_{(g)}$ starts to dominate the process; at this temperature, the system acquires the amount of energy necessary to proceed with the reduction. Similarly, than in the case of the halogenation problem faced during the dehydration process, a flow of O_2 can be incorporated to set back the GeO_2 reduction into $GeO_{(g)}$. Unfortunately, as mentioned in section 3.1.1, the Ellingham diagrams not necessarily provide all the relevant information for the reactions. It is important to consider additional properties of the compounds to identify critical points such as phase changes, melting and boiling points.

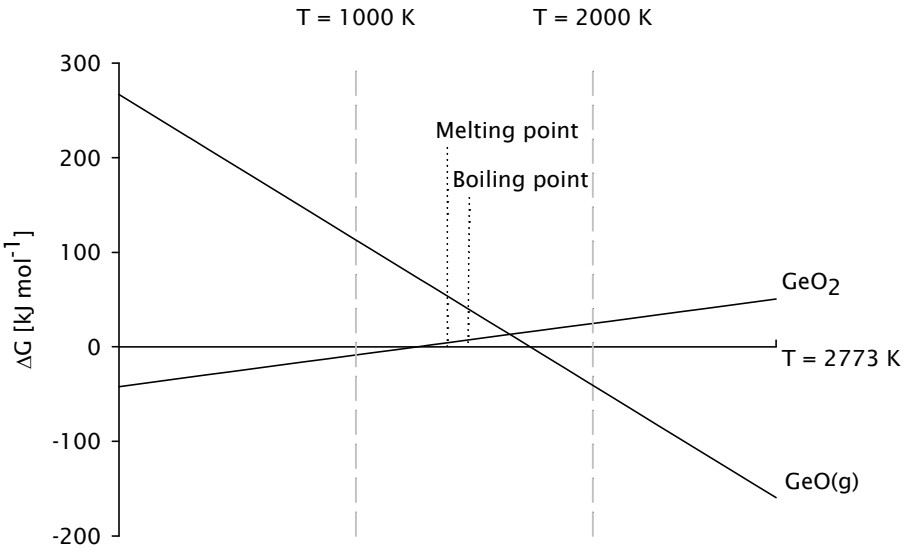

Graph 21. Ellingham diagram for GeO_2 stability including melting and boiling point.

The information of melting and boiling points was added to the GeO_2 Ellingham diagram shown in Graph 21. A thorough analysis of the thermodynamic conditions provided essential information. Calculations suggest that the reduction of GeO_2 into GeO is only possible after the GeO_2 is vaporised. Therefore, it is not expected to have GeO in the soot preform.

The information also revealed that the consolidation parameters require modification for germanosilicate and pure germania soot preforms. Temperature reduction during the consolidation process was performed to avoid evaporation of GeO_2. The higher the concentration of GeO_2 the lower the temperature.

Preforms sintered at lower temperatures exhibit a non-fully transparent appearance, due to the uncompleted sintering of silica. However, an indication to evaluate the correct consolidation process is that the preforms most be translucent. If the preform is opaque, then the consolidation temperature was too low.

3.2.2.1 Conclusion

Consolidation conditions for pure silica preforms are suitable as demonstrated by the thermodynamic analysis in this report. Nevertheless, for the germanium-doped and pure GeO_2 preforms, the consolidation conditions are entirely unsuitable. As a

result of the thermodynamic analysis, the GeO_2 mol% composition of the preforms governs the temperature at which the preform requires to be consolidated.

Chapter 4 Silica Glass

The development of pure silica glass was an essential part of this research project. It is the primary component in the preform fabrication processes. The importance of the silica soot depositions in not only related to the possibility of adding dopants to change its refractive index. It is also the material used as cladding in the optical fibre preforms. High quality glass is required to have an effective waveguide without adding losses due to scattering or absorption in the glass.

The depositions of pure silica can be used for over cladding preforms. Nowadays, this process is achieved by inserting the desired preform inside of a tube made of the same glass. This process is commonly known as sleeving or jacketing. It requires heating the preform and the tube at elevated temperatures and usually the application of vacuum to minimise the bubbles in the interface. The main complication of this process is the preform and tube size availability, which not always match the desired core to cladding ratio of the preform.

Pure silica depositions can satisfy the demand for over cladding the preforms. It is possible to control the thickness of the deposited glass to the desired new outer diameter. Additionally, the interface is not liable to defects such as cracking for stress or bubbles like in the case of the conventional procedures.

In this chapter the characteristics of the pure silica depositions is discussed as well as the properties of the consolidated silica glass. The experimental work in the following sections complements the thermodynamic analysis from the Chapter 3, and it was used as a foundation for the following chapters. Silica glass is also the main component of other types of glass hosts such as germanosilicate, aluminosilicate and phosphosilicate.

4.1 SiO_2 deposition via OVD

Pure silica depositions were performed on CFQ substrates with varying deposition conditions to determine the soot particle size and porosity. Different H_2/O_2 flows at a ratio of 0.466 were used. Samples were prepared for characterisation of SEM and powder diffraction XRD.

The main feature required in the pure silica preforms is to incorporate soot with enough compactness and strength to remain together at the moment of detachment from the bait rod. Also, the control of the porosity in the soot is critical. Depositions too loose tend to crack; on the other hand, depositions too compact may prevent the detachment of the bait rod.

Image 11. Deposition samples for SEM and XRD characterisations.

Pure silica depositions were performed on the edge of CFQ rods with various deposition conditions to determine the particle size and porosity of the soot as shown in Image 11. Micrographs from SEM have been acquired; however, an increase of magnification, tended to produce blurred images because the samples are not conductive, and, even when setting the SEM to variable pressure mode, it was not possible to focus the image on a single aggregate of soot particles. Image 12 shows a low magnification micrograph of the soot; it is possible to appreciate the small particles making up aggregates which at the same time form bigger soot entities.

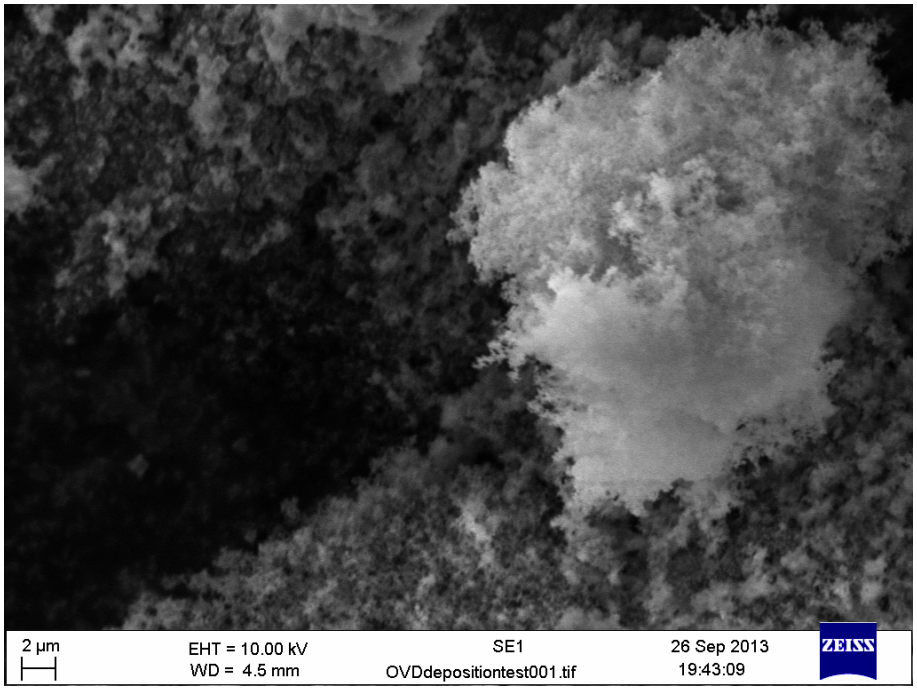

Image 12. Micrograph of a pure silica soot deposition.

A powder diffraction XRD analysis was performed on a pure silica OVD deposition to investigate crystallinity of the soot bodies. Diffractogram presented on Graph 22 shows no evidence of crystalline form in the silica soot deposition.

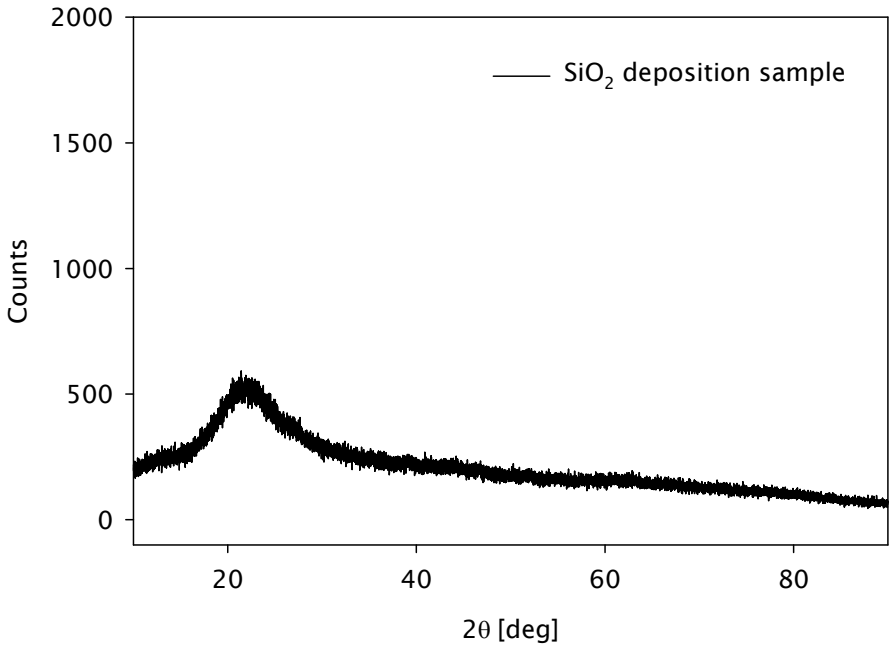

Graph 22. Diffractogram of OVD pure silica soot deposition.

The powder diffraction was measured in the UK National Crystallography Centre. The equipment used was a D2-PHASER from Bruker. The conditions used for the measurement were λ=1.541Å; increments of 0.006; starting 2θ position at 10.002deg and a total of 1364 steps.

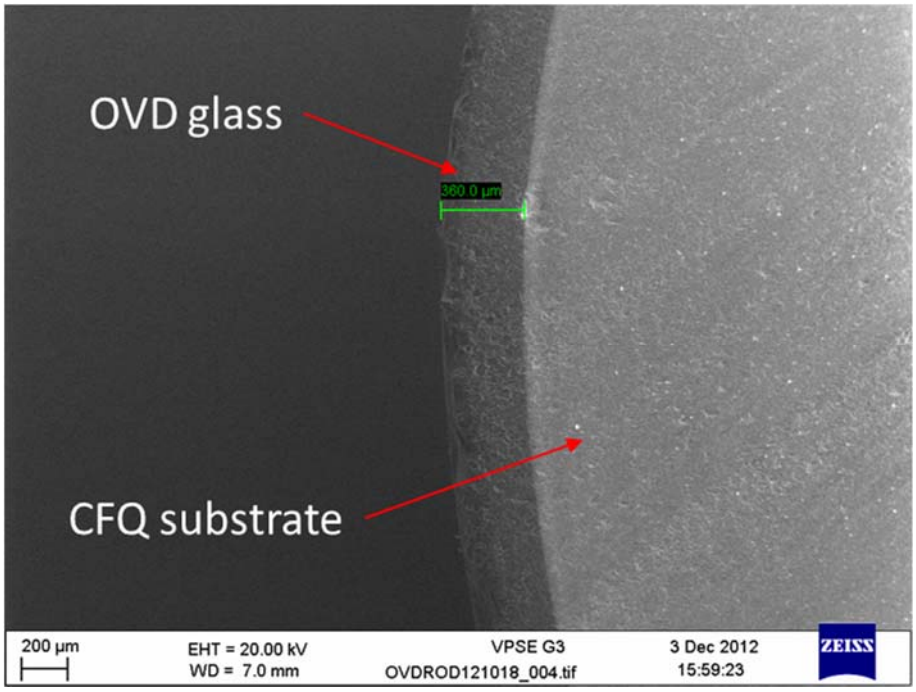

Image 13. Micrograph of a consolidated OVD deposition on top of a CFQ rod.

Initial depositions on CFQ substrates were performed to study consolidation parameters. SEM image in Image 13 shows an OVD deposition consolidated on the surface of a CFQ rod used as a substrate. It is evident the lower density on the outer section of the sample where the OVD deposition was consolidated.

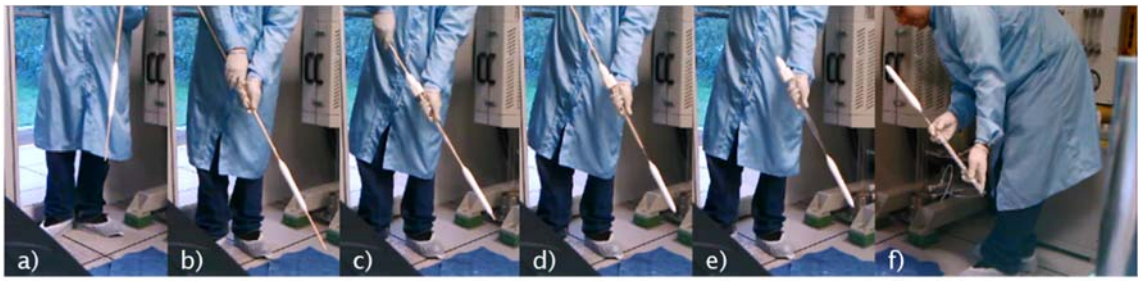

Image 14. Removal procedure of bait rod.

Porous soot preforms with sufficient strength have been successfully detached from the bait rod as shown in Image 14. The removal procedure is as follows: a) the soot preform is grabbed with one hand from the end of the handle; b) the bait rod is held by the other hand; c) the bait rod is pulled out maintaining a straight linear movement; d) the bait rod passes the joint; e) the bait rod has been completely removed; and f) the perform is visually inspected.

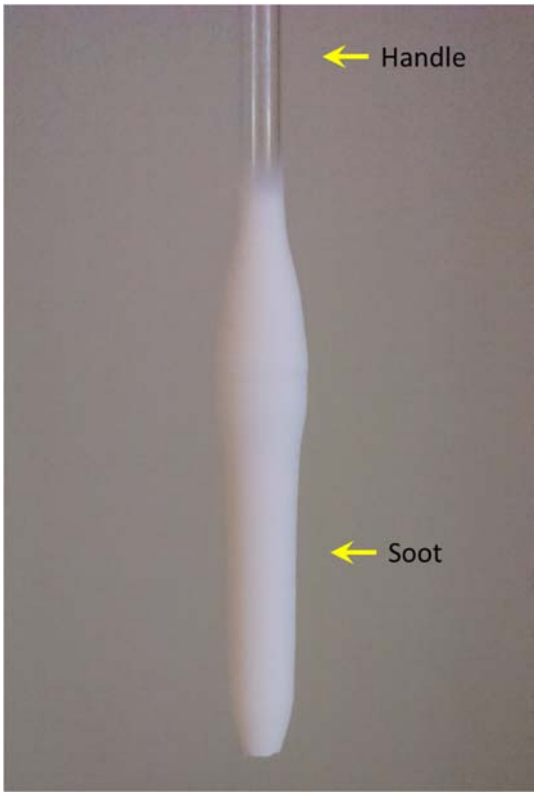

Image 15. Silica soot body attached to its handle.

The density of the soot body depositions was analysed using an indirect technique. Preform attached to its handle and without bait rod as shown Image 15 were used. The external dimensions of the soot body were obtained by projecting the image of the soot body into a fixed background. Since the ratio between the projected image and object were known, then the dimensions from the projected object were calculated. Based on the projected images a 3-D model was built to determine the volume of the irregular shape. The handle is not represented in Figure 6; however, its dimensions were used to reproduce the internal features of the 3-D model.

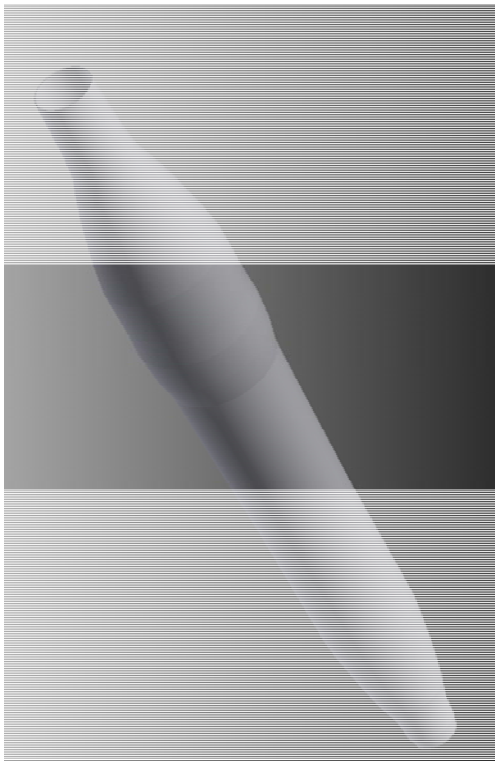

Figure 6. 3-D model of the silica soot body.

By using the volumetric information from the 3-D model and the total soot weight, it was possible to calculate the preform density. The handle and the support base were weighted previously with a standard deviation of 0.0045g and 0.0074g respectively. Table 2 shows the parameters used to calculate the density of the soot body.

	84.923
	63.928
	155.01
	6.16
	19.388
	0.317

Table 2. Silica soot density analysis.

After consolidation preforms fabricated using 6 and 12 layers produce a rod with final diameters of ~6mm and ~12 mm respectively. Image 16 shows the consolidation process of a pure silica preform made in-house.

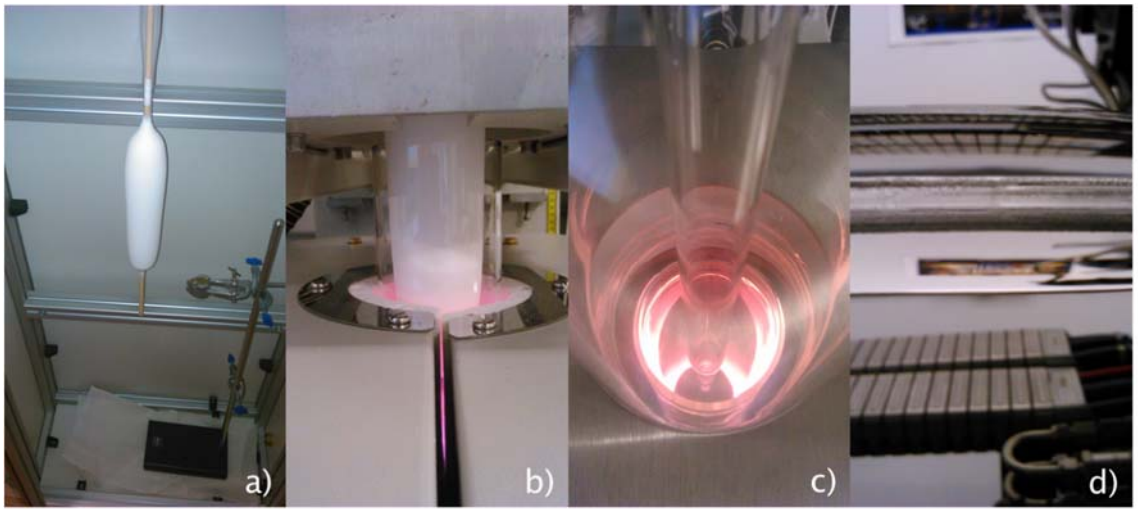

Image 16. Fabrication sequence of transparent silica preform; a) soot preform, b) dehydration process, c) consolidation process, d) transparent glass preform.

The refractive index profile of the fabricated preforms was measured to confirm the OVD glass refractive index. Using a preform profiler PK-2600 the refractive index at λ=633nm is shown on Graph 23. The measured refractive index agrees with the calibrated refractive index for pure silica on the system.

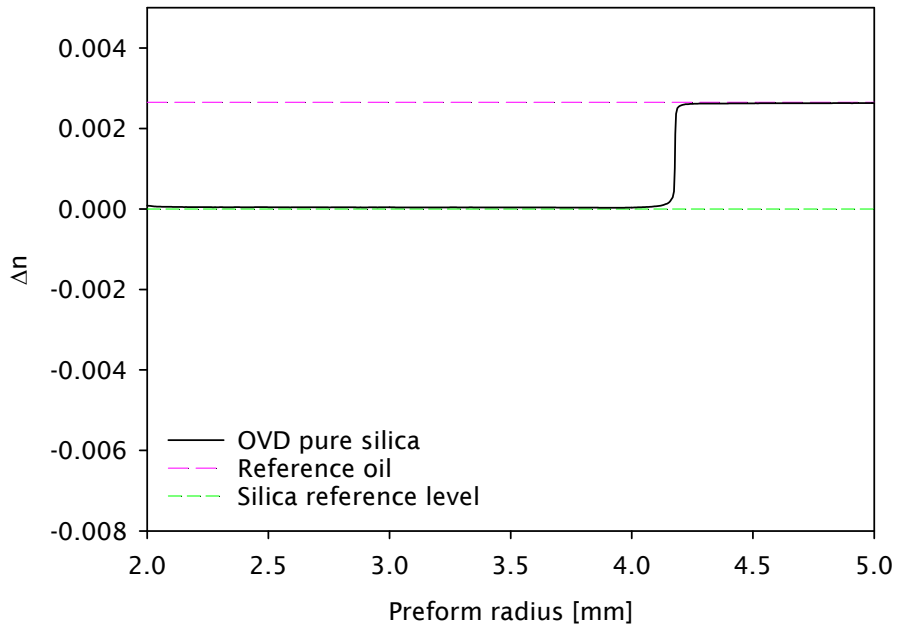

Graph 23. Refractive index profile of an OVD pure silica preform.

4.1.1 Conclusion

The established fabrication conditions allow the Optoelectronic Research Centre to produce high-quality silica preforms up to 25 mm in diameter and 500 mm length. Additionally, outer depositions of pure silica on top of a substrate or a preform can be helpful to avoid multiple operations required for the over cladding of preforms.

An additional advantage of adding pure silica cladding material using the OVD process is to avoid the undesired and inevitable bubbles and scratches that are evident during the sleeving or jacketing process.

The development of the silica glass was fundamental to establish the initial conditions for more complex glass compositions. With the availability of pure silica soot preforms, it was possible to explore the addition of dopants that can be added after the deposition. In the following Chapter 5, it is described the fluorine incorporation into the silica glass for lower the refractive index of the glass. Following chapters used the results of the previous sections for the development of germanosilicate glass; germania glass; aluminosilicate glass and phosphosilicate glass.

Chapter 5 Fluorine-doped Glass

The demand of fluorine doped glass has multiple application such as the over cladding of optical preforms. Nowadays, this process is achieved by a process commonly known as sleeving or jacketing, described in the previous chapter. In addition to the size availability problem, the fluorine-doped tubes have a significant drawback; they are incredibly costly. OVD depositions doped with fluorine can satisfy the demand for over cladding the preforms, minimising the need for costly stocks or long lead times from the suppliers.

5.1 F-doped silica

Fluorine as a dopant reduces the refractive index of the silica glass. In the fibre laser industry, especially for high power applications, F-doped silica substrates are widely used to achieve an outer secondary or a third waveguide structure[71-74], see Graph 24 and Graph 25 respectively. This particular optical fibre configuration is known as cladding pump optical fibre.

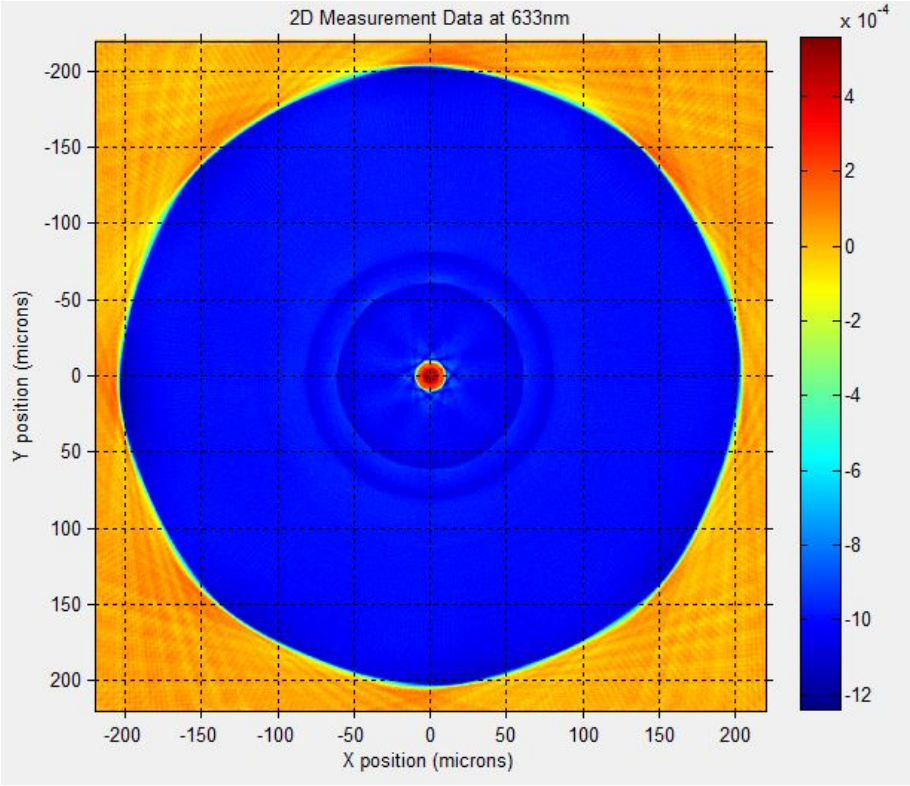

Graph 24. Two-dimensional fibre refractive index profile of a commercial double-clad fibre.

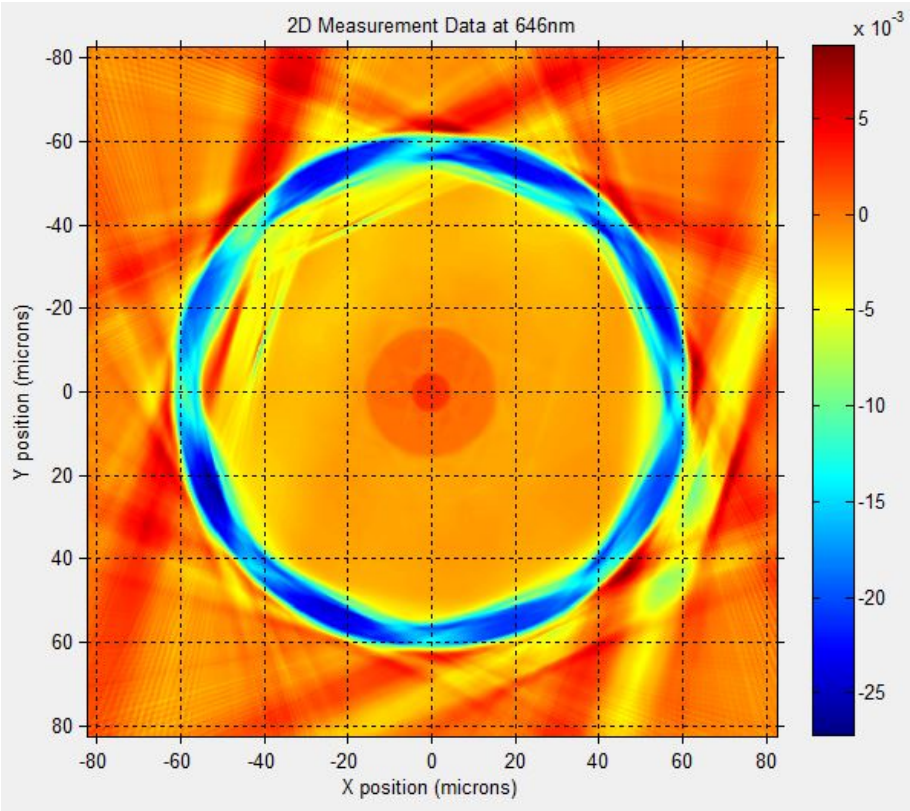

Graph 25. Two-dimensional fibre refractive index profile of a commercial all-glass triple-clad fibre.

Specific applications, mainly in the UV spectral region, also require the incorporation of fluorine into the glass to improve its performance. Alternatively, fluorine-doped silica rods are also used as a core material for a variety of applications in the photonics industry[75-79].

The difference in the refractive index can also be achieved by using a low index polymer such as an acrylate. Nevertheless, specific applications prefer the all-glass structure due to particular absorption of the coating materials or because the glass offers higher mechanical and thermal stability compared to the polymers used for this purpose[80].

Unfortunately, in addition to its lower softening point, the fluorine-doped tubes are considerably more expensive than the high-quality substrates used for the conventional MCVD process. Therefore, this type of tubes is regularly used only as a jacketing material. It is common that these fluorine-doped tubes are processed multiple times to match the desired waveguide characteristics such as core to cladding ratio and final cladding diameter. Conventional processes such as stretching and sleeving can add stresses to the glass making it liable to fail.

One route to achieve a low index cladding is via an OVD silica deposition that can be added on top of a conventional MCVD preform for following treatment in fluorine rich atmosphere to lower the refractive index. The thickness of the desired deposition can be tailored according to the requirements. The approach can potentially prevent the lengthy processes required to match the required specification by using the limited availability of sizes in commercial fluorine-doped glass.

A fluorine incorporation study on pure silica soot bodies was carried out, and the refractive index of the consolidated preforms was measured. Four pure silica soot bodies were fabricated with the same recipe with a porous body made of 6 layers. The consolidation conditions remained constant for all the samples. The experimental run was as described in Table 3.

Preform	SF_6/He ratio	Δn [x10^{-3}]	Thickness loss [mm]
OVD_F0	0.000	0.0	0.0
OVD_F1	0.010	-3.4	-0.292
OVD_F2	0.250	-4.6	-0.310
OVD_F3	0.100	-6.0	-2.432

Table 3. Fluorine incorporation in silica glass.

One of the expected consequences of the fluorine incorporation process is the loss of glass thickness. The loss of glass thickness can also be seen in Table 3. The reason behind the thickness loss is due to the silica etching process, same that happens once the SF_6 is heated to the point of dissociation. The dissociation of SF_6 produces a highly reactive etchant. The fluorine radicals bond with the silicon from the SiO_2 molecules producing the volatile compound SiF_4.

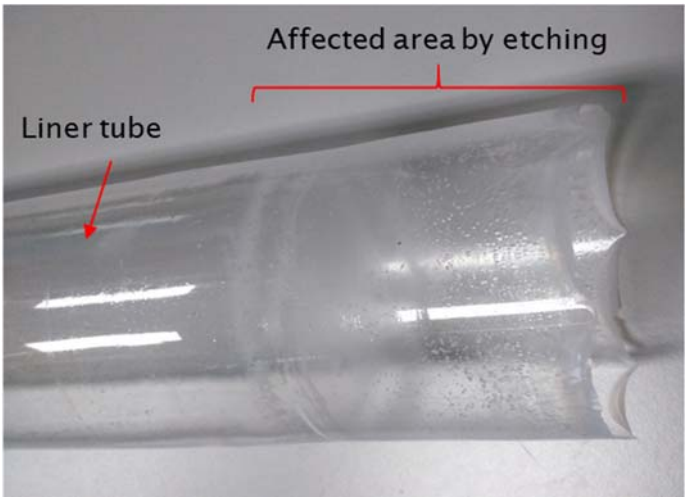

Image 17. Etching on OVD furnace liner tube.

The etching process is not limited to the porous soot body; it also affects the inner liner tube of the OVD dehydration/consolidation furnace. Image 17 shows the effect of etching on tube due to prolonged exposure to fluorine incorporation process.

The damage to the liner tubes is limited and happens after some fluorine-doping processes. However, the replacement of the liner tube is more cost-effective than acquiring the fluorine doped-tubes. Different glass compositions such as 100% GeO_2 have less impact because the process requires lower temperatures minimising the reaction from the SiO_2 substrate. Using lower temperatures neither the glass of the preform nor the liner tube present substantial damages.

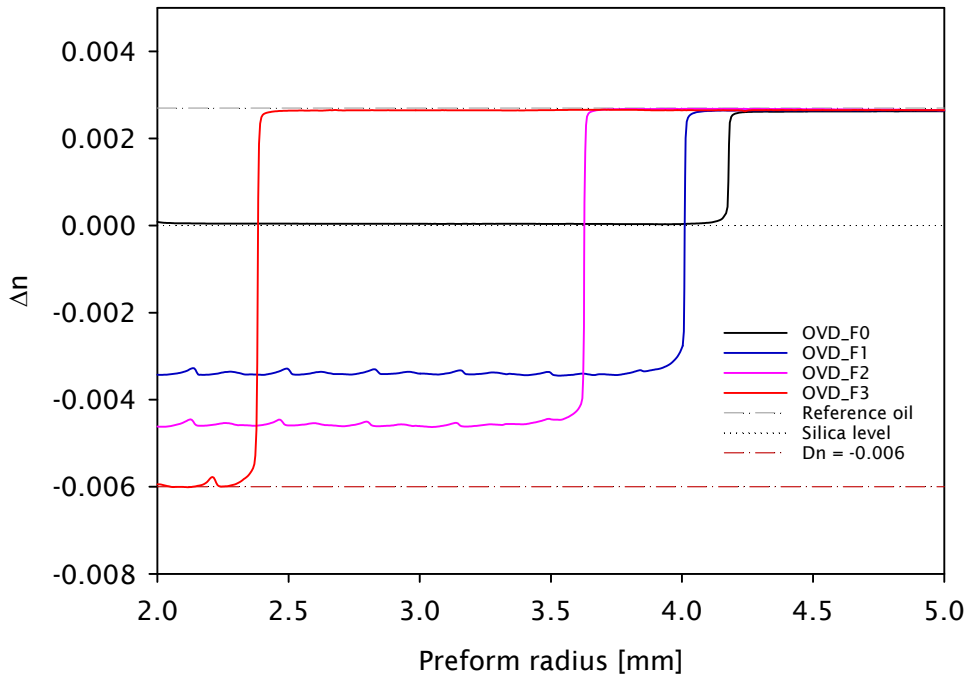

Graph 26. Refractive index profile of OVD fluorine-doped silica preforms.

The change in refractive index and the reduction in thickness is shown in Graph 26. The refractive index profile of the OVD Preform OVD_F0 is consistent with silica reference level as it was a pure silica preform used as a control sample for the experiment. Preforms OVD_F1; OVD_F2 and OVD_F3 present a lower refractive index as a result of the successful fluorine incorporation. The flows used during the dehydration process are described in Table 3. The fluorine doping was performed during the dehydration process.

Image 18 shows preform OVD_F1after the consolidation process. The preform was processed adding a flow of SF_6 described in Table 3 during the dehydration process. The final preform is transparent and defects free.

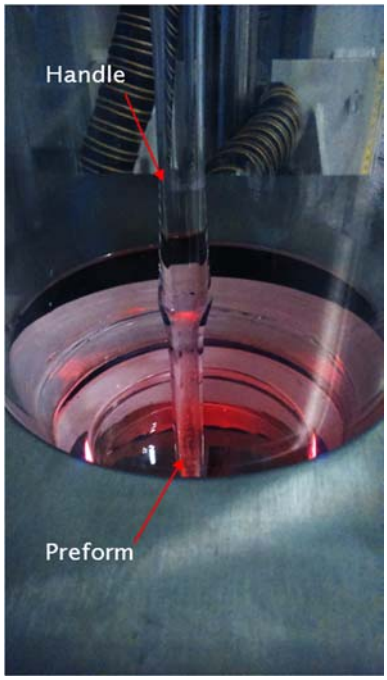

Image 18. Fluorine-doped silica preform.

During these tests, it was found that it is important to keep monitoring the humidity levels on the gas lines. If the gas has traces of moisture, the reaction on the hot-zone changes and unexpected high-risk by-products such as HF can be formed in the process. The adverse effect of HF on the OVD furnace liner tube is similar to the SiF_4 conversion. Nevertheless, the level of risk involved in the operation of the equipment has significant consequences.

An improved recipe was developed to minimise the etching process and favour the fluorine incorporation into the silica glass. An additional preform OVD_F4 was fabricated using the same deposition and consolidation conditions that the previous preforms described in this section.

Preform	SF_6/He ratio	Δn [x10^{-3}]	Thickness loss [mm]
OVD_F0	0.000	0.0	0.0
OVD_F1	0.010	-3.4	-0.292
OVD_F4	0.010	-4.5	-0.091

Table 4. Improved fluorine incorporation in silica glass.

The additional sample was pre-soaked in SF_6 gas flow for 90 minutes before replicating the same process than the preform OVD_F1. Substantial improvements are appreciated with the modified fabrication procedure. The refractive index change is more substantial with the modified recipe as shown in Table 4. Also, the thickness loss is significantly reduced.

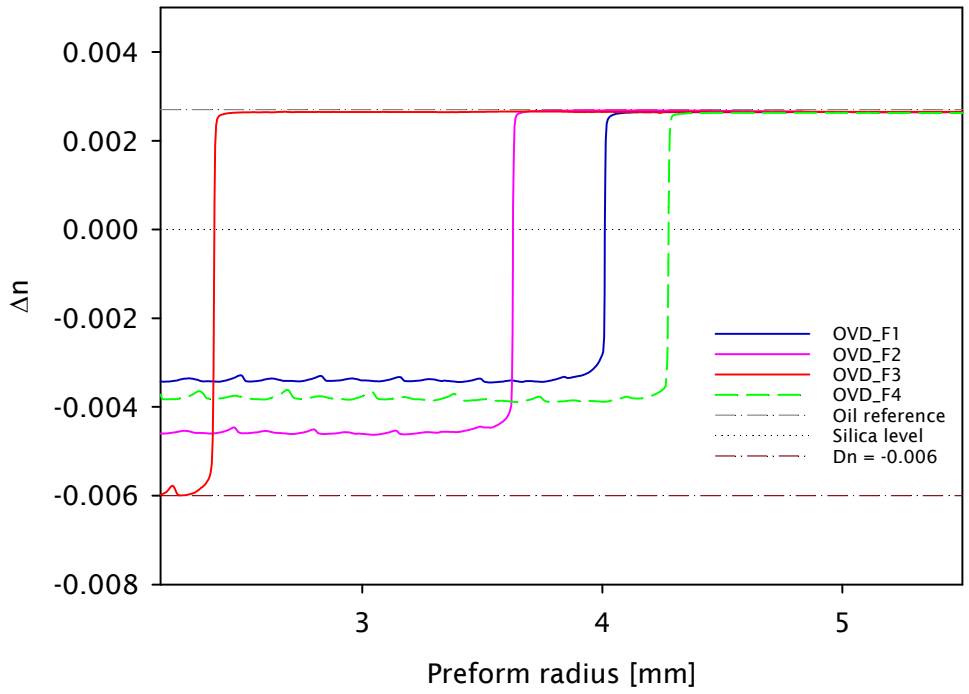

Graph 27. Refractive index profile on OVD fluorine-doped preforms including improved recipe results.

It is shown in Graph 27 the refractive index change due to fluorine incorporation in the OVD preforms. Preform profile from OVD_F4 shows sign of better incorporation of fluorine. Also, the etching process shows less impact on this preform.

Comparison between thickness loss and refractive index change between OVD_F1 and OVD_F4 is described in Table 4.

5.1.1 Conclusion

Incorporation of fluorine into the silica glass has been successfully demonstrated, and the refractive index profile shows the effect of the fluorine content. The development of this process provides the ORC with a new manufacturing capability. Hence, this capability allows fabricating in-house fluorine-doped silica tubes, jacketing material or solid rods with an NA up to 0.13 with respect to silica. The refractive index difference achievable by this process is comparable to the used for double and triple cladding fibres

Higher refractive index change can be achievable replicating the improved recipe with the conditions used for the larger SF_6/He ratio. Ultra low NA changes can also be achievable for particular applications.

The reduction of undesired and inevitable bubbles and scratches that are evident during alternative methods also make attractive the proposed fabrication process. Moreover, highly-doped fluorine tubes are not possible to process by sleeving because the glass starts boiling. Finally, this approach can also be helpful to reduce the processing times of stretch and sleeving when the commercial fluorine-doped rod/tubes have limited existence or size availability.

Chapter 6 Germanosilicate Glass

The germanosilicate glass is a core composition widely used in the photonics industry. It is widely used in telecommunications and also in non-linear devices. The development of the OVD process capability to fabricate germanosilicate glass was of significant interest to the Optoelectronics Research Centre. The information reported in the previous chapters have been of significant relevance, particularly the thermodynamic analysis in Chapter 3.

6.1 SiO_2/GeO_2 glass fabricated via OVD

6.1.1 Germanosilicate preforms

The process to define the correct fabrication parameters was essential to develop the glass. Also, the thermal expansion mismatch is a factor to consider. As the $GeCl_4$ flow is increased, the severity of the incompatibility increases. In addition, the deposition temperature requires adjustment. Otherwise, the deposition tends to sinter, driving preform fissures or total cracking of the soot body.

Preform Number	Substrate	H_2/O_2 ratio	$SiCl_4/GeCl_4$ ratio	Traverse speed [m·min^{-1}]
OVD0001	Bait Rod	0.65	4.44 => pure $SiCl_4$	0.100
OVD0002	Bait Rod	0.65	4.44 => 5.58	0.100
OVD0003	CFQ	0.65	4	0.100
OVD0004	CFQ	0.65	4	0.100
OVD0005	CFQ	0.65	4	0.100
OVD0006	CFQ	0.65	10; 3.33; 2; 2	0.100
OVD0007	CFQ	0.65	20; 10; 6.66; 6.66	0.100
OVD0008	CFQ	1	4	0.100
OVD0010	CFQ	0.8	4	0.100
OVD0011	CFQ	1.33	4	0.100
OVD0012	CFQ	2	4	0.100
OVD0013	CFQ	1.33	4	0.100
OVD0014	CFQ	1.33	2	0.100
OVD0015	F300	1.33	4	0.100
OVD0016	F300	1.33	2	0.100
OVD0017	F300	1.33	4	0.100
OVD0018	F300	2	4	0.100
OVD0019	F300	1	4	0.100
OVD0020	F300	1.33	5; 3.33; 2.5; 2.5	0.100
OVD0029	Bait rod	0.46	1	0.020

OVD0030	CFQ	0.46	1	0.020
OVD0032	CFQ	1.33	5; 3.33; 2.5; 2.5	0.100

Table 5. Deposition parameters of germanium-doped silica OVD preforms.

Depositions with a constant $SiCl_4/GeCl_4$ ratio were performed, and the fabrication conditions are described in Table 5. Different substrates were used such as CFQ and F-300 substrate rods and tubes. Also, in few depositions, the use of the bait rod was incorporated. The experiments on non-removable glass substrates were carried out to understand the deposition behaviour. Hence, the use the refractive index from the substrate as a guide to correlate the $SiCl_4/GeCl_4$ ratio with the refractive index of the deposited glass. This technique was also used to estimate the molar concentration of GeO_2 in the glass.

Depositions with various $SiCl_4/GeCl_4$ ratios were performed using a pure silica layer in between them to prevent undesirable mixtures and for reference. Furthermore, depositions using the bait rods have been successfully achieved. Owing to the different characteristics of the doped soot preforms, a release layer of pure SiO_2 has been used to avoid jamming of the bait rods.

Preform OVD0001 was deposited on a bait rod using a graded index recipe with a $SiCl_4/GeCl_4$ ratio ranging from 4.44 to pure $SiCl_4$. After consolidation, the preform was collapsed into a solid rod. The collapsing process was performed in an MCVD lathe as shown in Image 19.

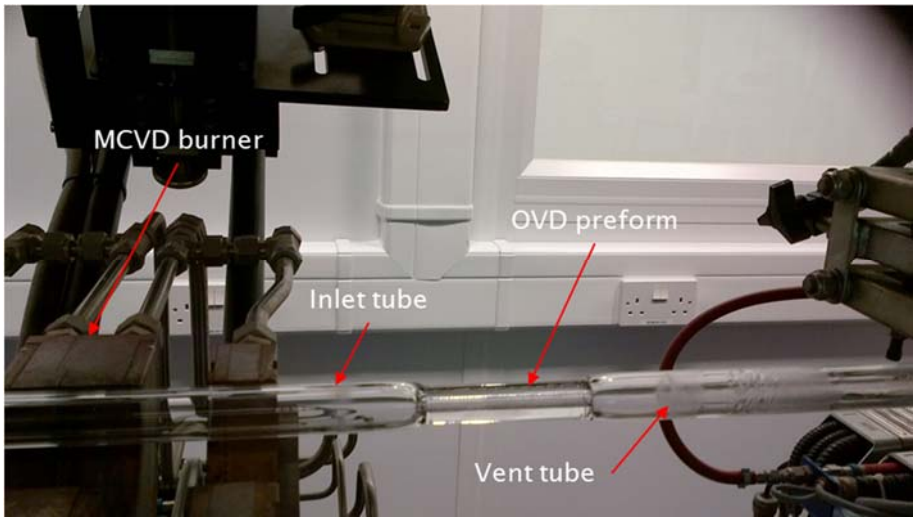

Image 19. Preform OVD0001 during the collapsing process on the MCVD lathe.

The refractive index of the preform was measured after the collapsing process. Graph 28 shows the RIP from preform OVD0001. The maximum Δn of the broad section of the profile is about 0.0032, with two symmetrical peaks reaching Δn =

0.013; the central depth is characteristic of the loss of GeO_2 when collapsing the consolidated tube.

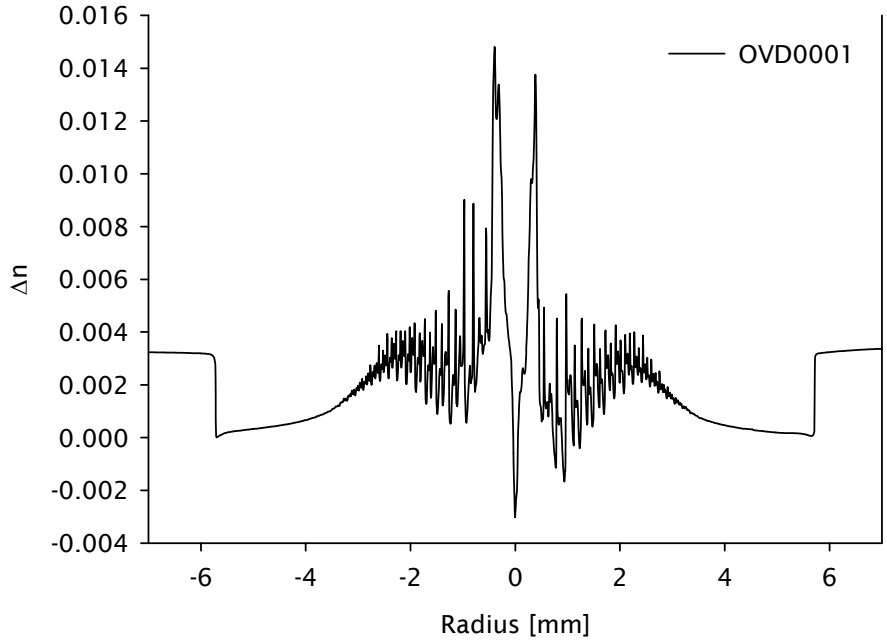

Graph 28. Refractive index profile of preform OVD0001.

The preform OVD0001 was drawn into the fibre A0361, and its refractive index profile is shown in the following section 6.1.2.

Additional depositions were made directly on the surface of two types of glass substrates, CFQ and F-300. Crystallisation in the consolidated deposition started to appear in both substrates.

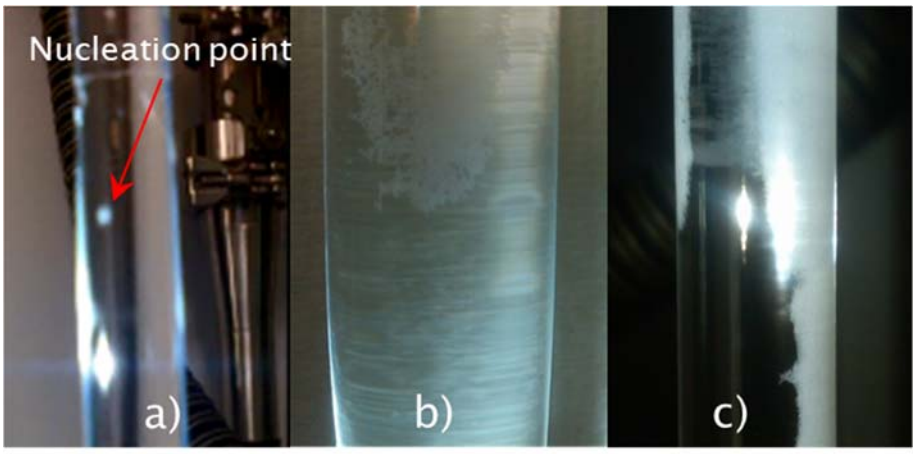

Image 20. The crystallisation of germanosilicate depositions; a) sample nucleation point; b) sample slightly crystallised; c) sample heavily crystallised.

The crystallisation started as small scattered dots on the surface, which resulted from nucleation points where the crystals started growing. Highly germanium-doped preforms (>10 mol%) tended to crystallise readily. Preforms with medium dopant concentration (5 – 10 mol%) required more time to start the nucleation process, and preforms with low dopant concentration (<5 mol%) do not exhibit signs of crystallisation, see Image 20.

The crystallisation of clear and transparent depositions occurred when they had been recently retrieved from the hot zone of the furnace. Crystallisation phenomena were observed during the cooling down process of the preform being exposed to room temperature. Further crystallisation analysis on GeO_2 will be described in section 7.1.4

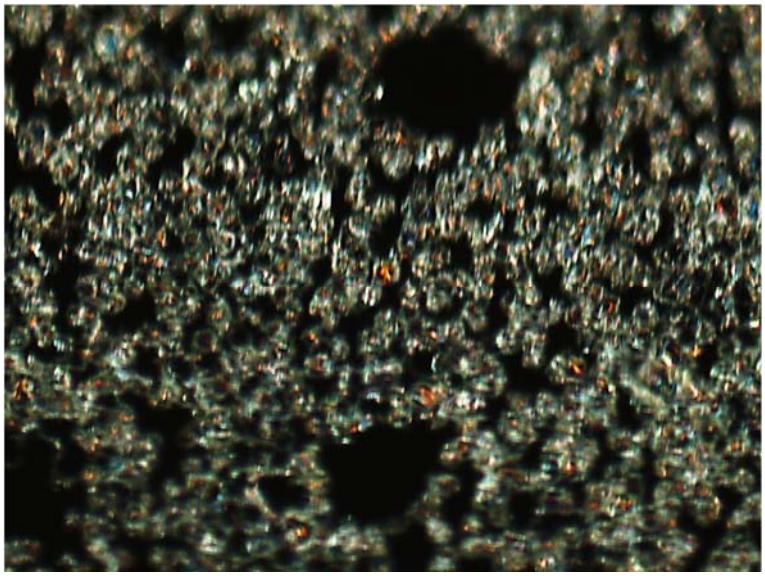

Image 21. Optical Microscope image of crystal growth on OVD preform.

The crystallisation shown in Image 21 was observed on the surface of a CFQ substrate. The experiment was repeated in a different type of glass (F-300) to identify if the substrate was the source of the crystallisation. However, the crystallisation appeared again independently of the type of substrate used for the deposition.

Characterisations of the refractive index were possible in the sections of the preform without crystallisation. Nevertheless, the refractive index profiles presented unusual features shown in Graph 29. Additional depositions were performed using lower concentrations of GeO_2 to investigate if the crystallisation on the preform surface caused the abnormal profiles. The refractive index profiles continued to present the abnormal features independently of the concentration of GeO_2 used during the deposition.

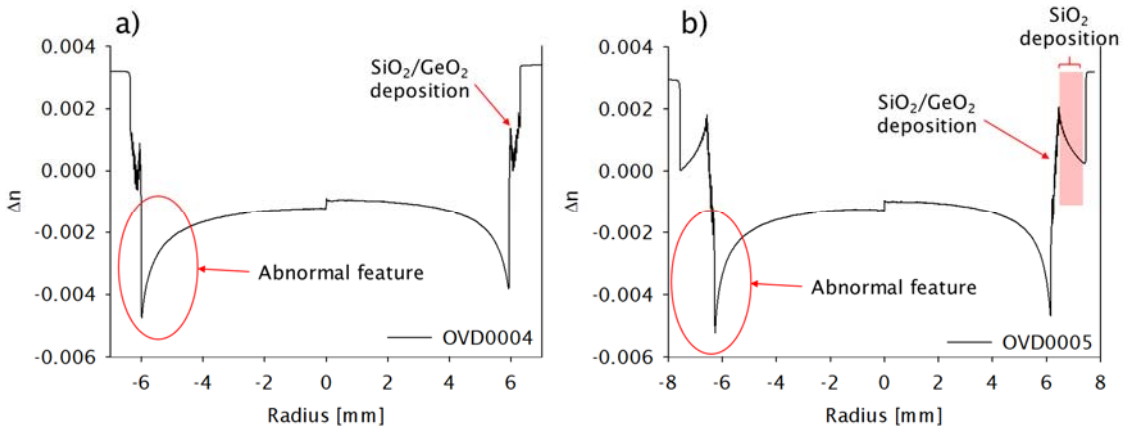

Graph 29. Preforms refractive index profiles of OVD depositions on top of CFQ rod substrates showing unusual features.

The depositions were carried out on top of CFQ rod substrates, the central part of the profile was expected to be flat, and the outer region of the profile was expected to have a higher refractive index due to the germanosilicate composition, see Graph 29 a). An alternative approach to avoid the crystallisation on the surface was adding a pure silica deposition on top of the germanosilicate glass, see Graph 29 b). The crystallisation of the preforms was set back, and the preforms no longer exhibit signs of crystallisation.

The refractive index profile of the preforms fabricated adding pure silica layers on top of the germanosilicate confirmed that the unusual features on the profile are not the effect of the crystallisation. An experiment was carried out exposing the CFQ rod to the same dehydration and consolidation process used during OVD preform fabrication.

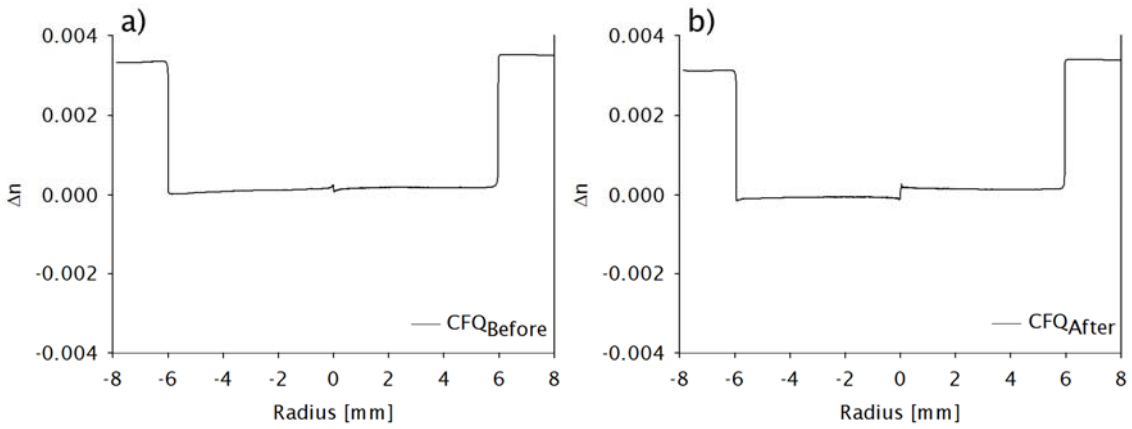

Graph 30. Refractive index profile of CFQ rod; a) before processing and b) after processing.

The preform refractive index presented in Graph 30 a) shows the refractive index profile of the CFQ before processing. Having a reference for the experiment was essential. Graph 30 b) shows the profile after the dehydration and consolidation processes. The resulted refractive index profile did not show any abnormal features as in the RIPs shown in Graph 29.

It was demonstrated that neither the crystallisation nor substrates are the origin of the abnormal features in the RIPs shown in Graph 29. Therefore, an additional experiment was carried out to investigate the effects of the deposition. The previous

experiments shown in this section consisted in depositing germanosilicate or germanosilicate with pure silica on top.

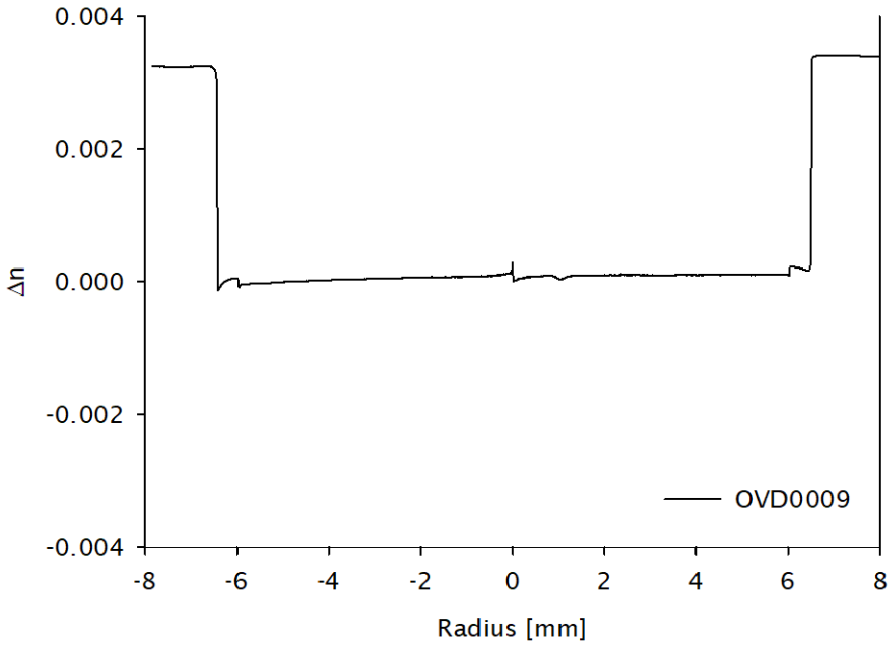

Graph 31. Refractive index profile of SiO_2 deposition on top of CFQ rod substrate.

The refractive index profile shown in Graph 31 is from a deposition of pure silica on top of a CFQ rod substrate. A slight change of the refractive index is noticeable in the region of the deposited glass. Nonetheless, the unusual feature of the refractive index had disappeared. The evidence suggests that the germanosilicate deposited on the outer region of the glass substrates, cannot be appropriately resolved by the preform profiler. Preforms of germanosilicate, glass consolidated without substrate (bait rod removal process), are accurately resolved by the preform profiler software.

It was essential to understand the equipment capabilities and limitations. Hence, a preform that presented the abnormal features in the RIP was drawn into a fibre. The refractive index of the fibre was measured using the fibre profiler S-14. It is shown in Graph 32 the difference between the preform and fibre refractive index.

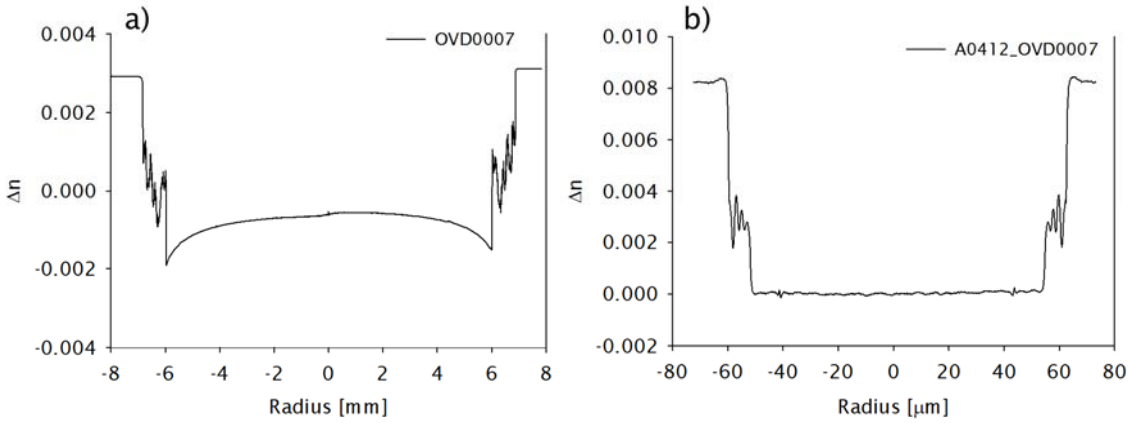

Graph 32. Refractive index profiles of germanosilicate glass; a) preform b) fibre.

The refractive index profile of the fibre shown in Graph 32 b) does not exhibit the abnormal features observed in Graph 32 a). The fibre refractive index has the expected flat profile in the substrate region and a visible refractive index change in the germanosilicate deposition region.

It has been demonstrated that the refractive index profile in the fibres does not show abnormal features. The fibre profiler is capable of providing data correctly for germanosilicate deposition on the outer region of the substrate. Conversely, the preform profiler cannot accurately resolve the refractive index change when this happens in the outer region of the preform. Discussions with the manufacturer (PK- photonics) are proposed to evaluate the possibility of reviewing the algorithm that enables the correct calculation of the mentioned refractive index profiles. Large differences of refractive index and stress are proposed as the main source of the abnormal features.

It was demonstrated that the refractive index of the glass had to be measured after the preform was processed into a fibre due to equipment limitations. Although the refractive index can be measured correctly for the fibres, the refractive index change was lower than expected for the flow composition used during the process of the soot deposition.

The samples of the consolidated preforms were analysed by energy dispersive X-Ray spectroscopy (EDX) to identify their chemical composition. The nature of the EDX analysis identifies the characteristic energy of the X-Rays for each chemical element regardless of the compound in which they are present. Thus, it is essential to identify additional signals that can provide information of the compound in which the element has been detected. It is also important to consider the possible compounds that can be present in the sample by following the information provided in the thermodynamic analysis from Chapter 3.

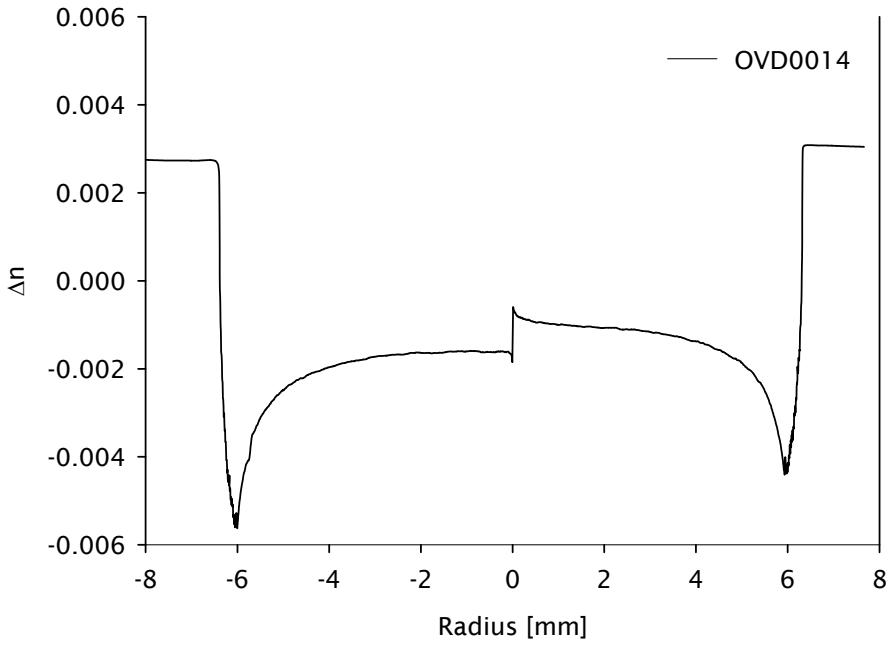

Graph 33. Preform refractive index of germanosilicate glass deposited on top of a CFQ rod substrate.

A germanosilicate OVD deposition was produced on top of a CFQ rod substrate. The preform refractive index profile presented an unusual feature, see Graph 33. Nevertheless, according to the previous analysis of preform to fibre RIP differences, the profile of the fibre was expected to be correct.

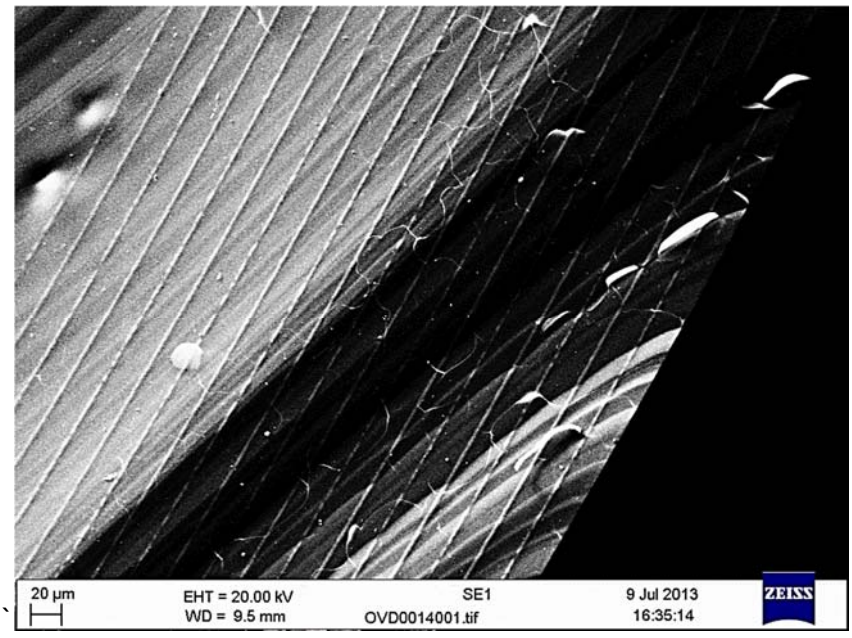

Image 22. Micrograph of consolidated OVD germanosilicate deposition.

Image 22 shows a micrograph obtained by SEM of the same sample. The sample was coated with ~30nm of carbon for conductivity purposes. The different layers of the deposition and contrast lines in between each of the layers can be seen.

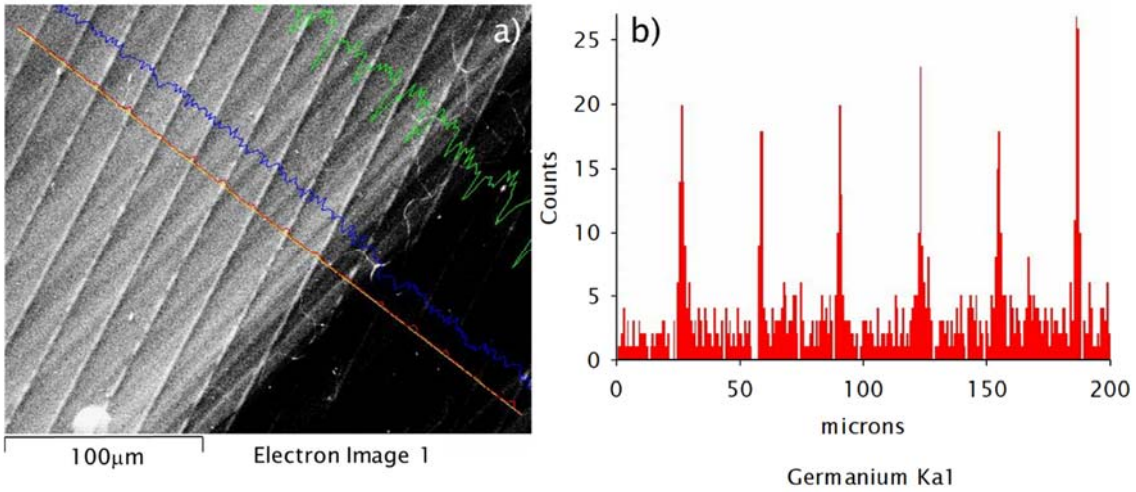

Image 23. EDX analysis of consolidated germanosilicate deposition; a) SEM micrograph with line-scan trajectory and b) signal counting of EDX line-scan measurement.

A line-scan analysis based on EDX was carried out across the deposition layers. The result was the identification of selective higher deposition of GeO_2 in the contrast lines. The lines are the situated in the interface of each of the layers of the deposition forming concentric regions in the preform sample. The EDX scanning along the surface is presented in Image 23 (a) showing the deposition layers and the line-scan position. Image 23 (b) shows the signal counting from germanium at the layers interface.

Also, a complementary single-point EDX measurement was performed on top of an interface line to provide quantitative data on the chemical composition of the interface lines. The resulting EDX spectrum is shown below as well as the SEM micrograph indicating where the spectrum was taken.

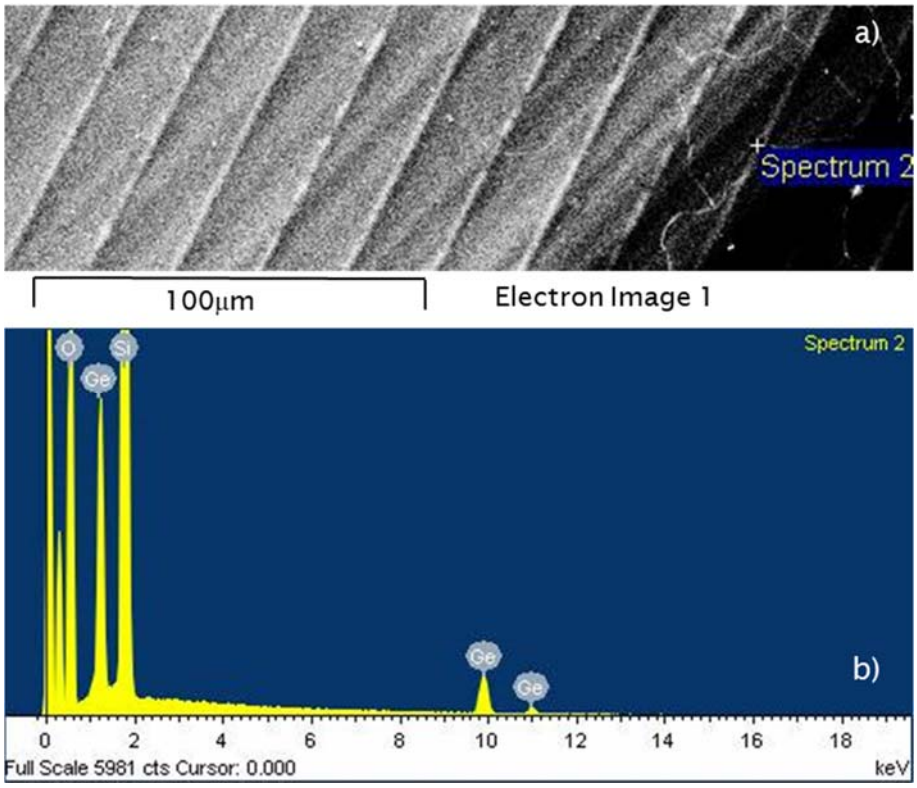

Image 24. Single-point EDX measurement on the interface of the deposited layers: (a) SEM micrograph, (b) EDX spectrum.

High intensities of the germanium energies were recorded in the EDX spectrum represented in Image 24 b). The amount of germanium found in the interface between deposited layers was calculated to be 13.01wt%. Image 24 a) shows an SEM micrograph with the location where the single-point EDX was taken. whereas the typical concentration was ~4wt% between the layers.

The measurement was repeated in additional samples that were fabricated using different H_2/O_2 ratio and various $SiCl_4/GeO_4$ flow compositions. The result of the compositional analysis had minor differences and did not follow the expected refractive index contrast. EDX characterisation carried out is summarised in Table 6. The flow compositions for the preforms fabrication and wt% measured on the preferential zones is also reported in the table below.

Preform Number	H_2/O_2 ratio	$SiCl_4/GeCl_4$ ratio	Germanium wt%
OVD0008	1	4	13.25
OVD0010	0.8	4	11.70
OVD0014	1.33	2	13.01

Table 6. Summary of wt% composition found in preferential deposition zones of germanosilicate glass preforms.

The previous compositional analysis demonstrated the non-uniform distribution of the concentration of germanium in the preform depositions. Moreover, the concentration of germanium apparent to be limited regardless of the flow composition used during the fabrication process. The unknown conditions outlined before led to the thermodynamic analysis presented in Chapter 3. Initially, the lower germanium content was presumed to be a result of the thermal reduction of the GeO_2 into GeO.

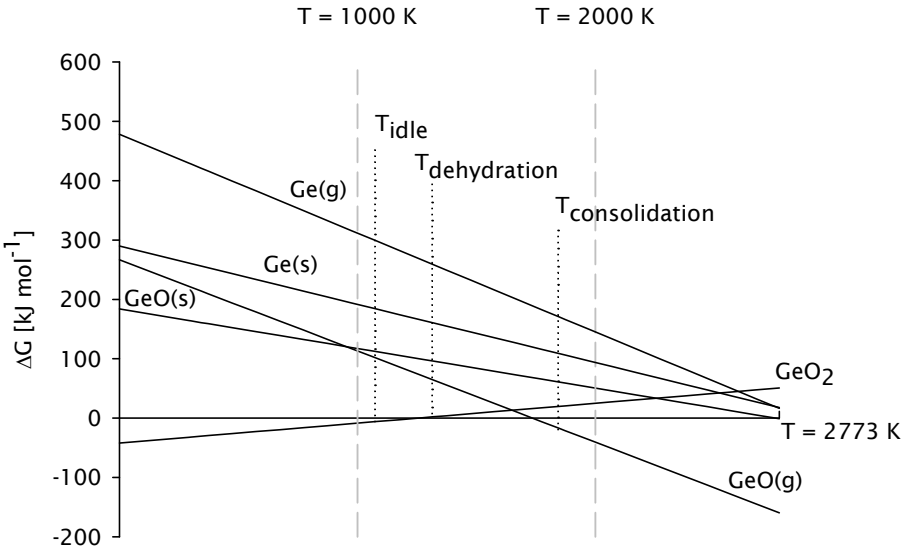

Graph 34. General Ellingham diagram for the thermal reduction of germanium.

The thermodynamic analysis provided evidence that the thermal reduction of the GeO_2 is possible at the consolidation temperature, see Graph 34. However, the loss of germanium was higher than the expected.

The thermodynamic conditions of the consolidation process were close enough to the equilibrium point to expect a minor reduction of the compound. Moreover, the consolidation procedure was not long enough to thermally reduce high volumes of GeO_2 during the processing time. Also, the conversion reaction path for the thermal reduction of GeO_2 into GeO is different. Graph 35 shows that before the thermal reduction can happen, the GeO_2 will undergo a phase transition. It is only then when the vapour of GeO_2 would be thermally reduced to GeO.

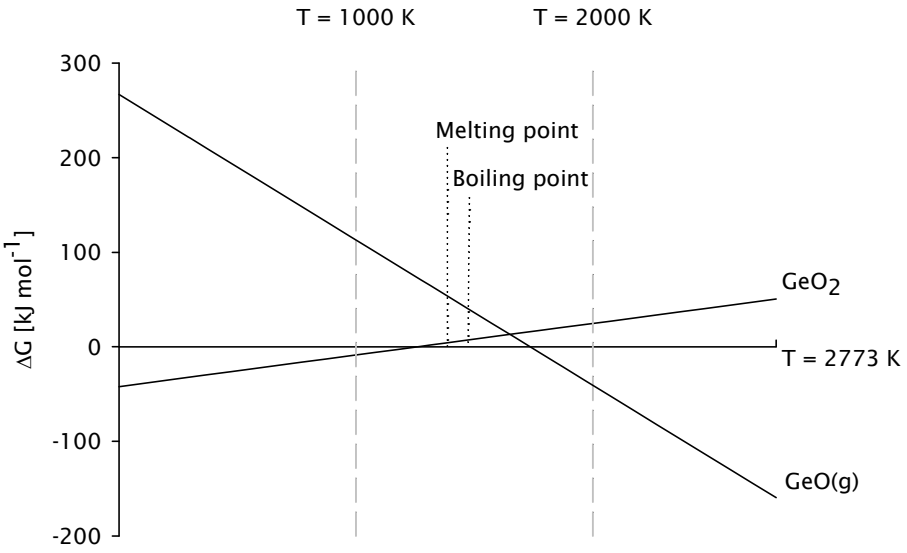

Graph 35. Ellingham diagram for GeO_2 stability including phase transition points.

Evaporation of GeO_2 ocurres at lower temperatures and combined with the possible thermal reduction into GeO could potentially explain the high volume loss of the compound during the fabrication process. Nonetheless, it would be expected to find evidence of the evaporation in the glass. Final preforms did not exhibit any indication of bubbles formed during the GeO_2 evaporation. The lack of evidence indicating boiling of the glass is explained because the depositions are not pure GeO_2. It has a composition of silica that ranges from 50 – 75 % for this samples. Therefore, the phase transition points occur at higher temperatures.

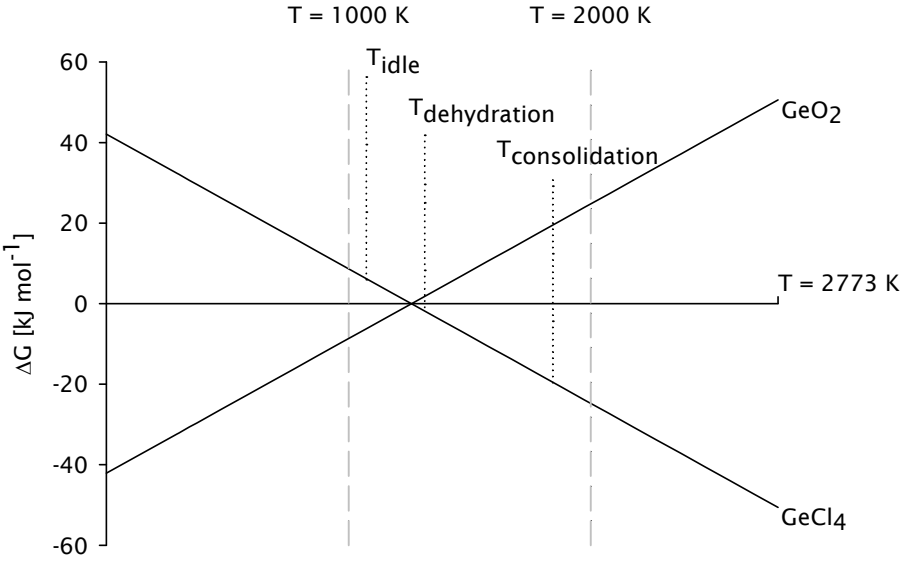

Graph 36. Ellingham diagram for the halogenation process of GeO_2.

The thermodynamic analysis described in Chapter 3, provided the crucial information that explained the loss of germanium. The Ellingham diagram shown in

Graph 36, present the thermodynamic conditions in which the halogenation of germanium oxide can occur. The proposed solution to overcome the halogenation of the GeO_2 is described in section 3.2.1, as well as its impact on the reactions. Adding O_2 flow during the dehydration process in the gas delivery system sets back the halogenation reaction.

The changes to the process were carried out considering the information provided by the thermodynamic analysis. The addition of oxygen to the dehydration process was performed for a preform fabricated using a deposition ratio of two for the $SiCl_4/GeCl_4$ flow. Also, the temperature of the deposition was corrected for the flow composition.

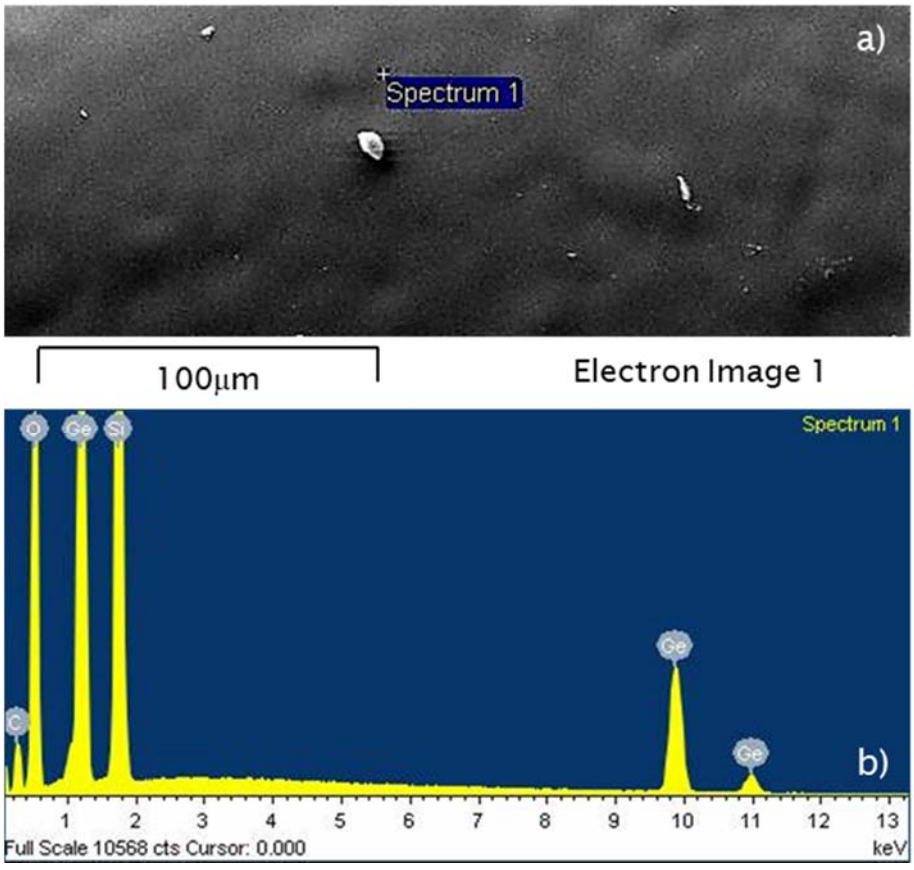

Image 25. Single-point EDX measurement of a germanosilicate glass: (a) SEM micrograph, (b) EDX spectrum

The effects of the modifications to the process were notorious in the germanosilicate glass experiments. The preforms did no longer exhibit preferential deposition zones, and the concentration of germanium followed the expected values. Image 25 b) shows a single-point EDX measurement of a 48.81 mol% of GeO_2. Image 25 a) presents an SEM micrograph of a preform showing the absence of preferential deposition zones. Depositions with germanium oxide concentration of 100 mol% were also achieved and are reported in Chapter 7 of this thesis.

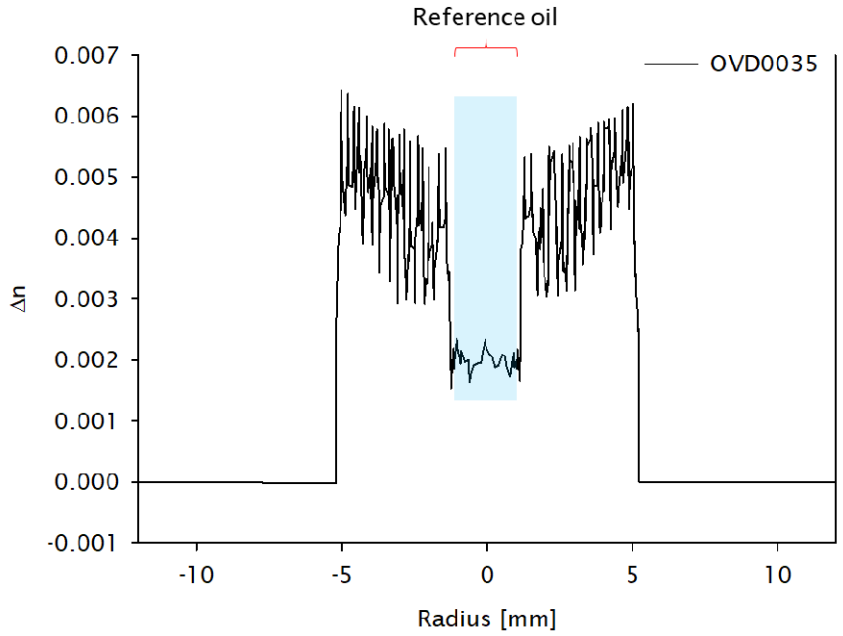

Graph 37. Refractive index profile of an SMF-like preform.

After the previous investigations with high germania concentration, a low NA, SMF-like preforms was fabricated. The preform refractive index profile shown in Graph 37 shows a central region with lower refractive index contrast. The preform was measured before collapsing the preform. The removal of the bait rod leaves the central hole of the OVD preforms. The refractive index profile can be measured if the central void is filled with index matching liquid, also known as reference oil. Also, it is possible to appreciate the twelve layers from the OVD deposition. The refractive index of the fibre drawn from this preform is presented in the following section.

6.1.2 Germanosilicate glass fibres

Consolidated germanosilicate glass preforms were drawn into optical fibres. The fibre refractive index profile was measured to evaluate the differences in the preform profile. It is expected to see evidence of diffusion in the germanosilicate glass due to the additional heating process from the fibre drawing. Diffusion can also be driven by the dimensional change from preform to fibre. Further information on these diffusion mechanisms is explained in section 10.4 for different glass composition. However, the general principle of the diffusion mechanism is the same.

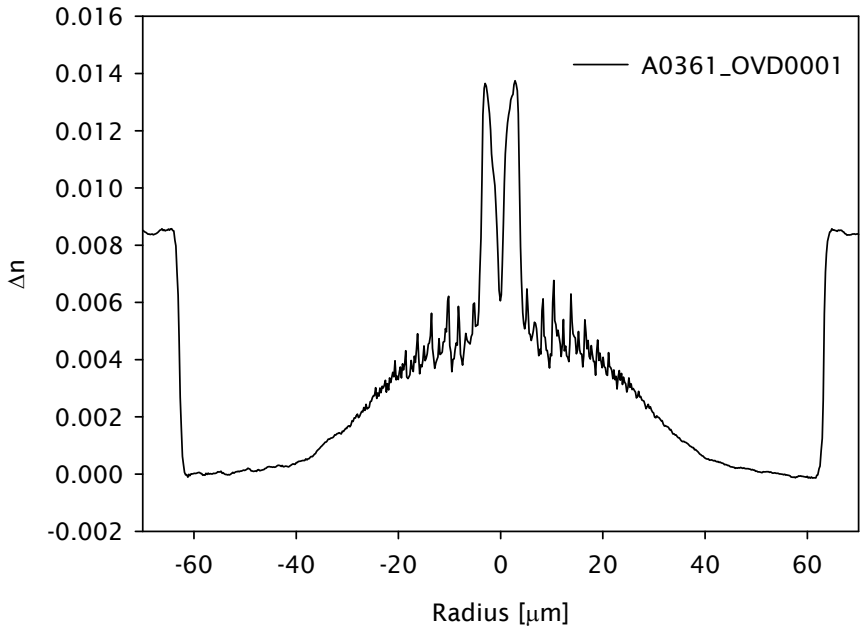

Graph 38. Refractive index profile of fibre A0361_OVD0001.

The fibre refractive index profile (FRIP) of the fibre A0361 is shown in Graph 38. The fibre was drawn from the preform OVD0001 presented in the previous section. The preform was drawn into a 125μm diameter fibre. The FRIP was similar to the RIP of the preform. The central depth is still noticeable, but the profile is more defined and symmetric. The graded profile has also been improved. The maximum Δn of the broad feature of the profile is about 0.005, with two symmetrical peaks reaching Δn = 0.0137.

The difference between the preform and fibre refractive index change in the central region has similar maximum values. Nevertheless, there is a slight increment of the refractive index change at the maximum level of the graded index. The difference in refractive index can be attributable to the diffusion of the graded index towards the centre of the fibre. Inwards diffusion is expected due to the dimensional change occurred when the preform is reduced to the fibre size. A contrast in the core region is noticeable in Image 26 showing the cross-section of the fibre.

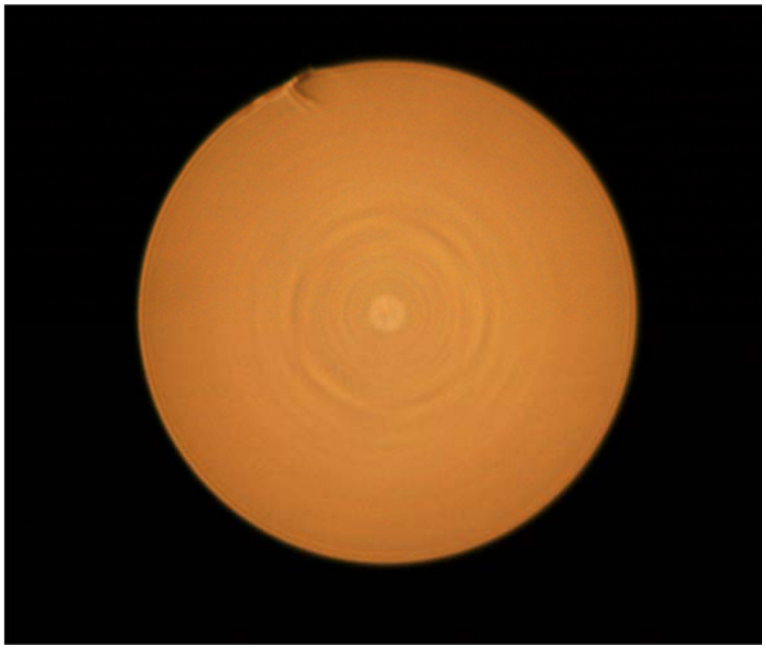

Image 26. Optical microscope image of the cross-section of A0361_OVD0001.

Absorption measurements were carried using a fibre length of ~360m from the fibre A0361_OVD001. The fibre was coated with high index acrylate. The experimental setup is described in Figure 7.

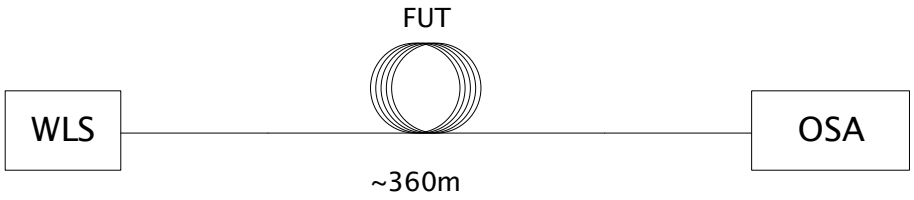

Figure 7. Absorption and loss measurement setup.

Light from a white light source (WLS) was launched into the fibre, an optical spectrum analyser (OSA) was used to measure the light transmission in the fibre. The measurement performed over the range of 600nm – 1200nm wavelength is presented in Graph 39.

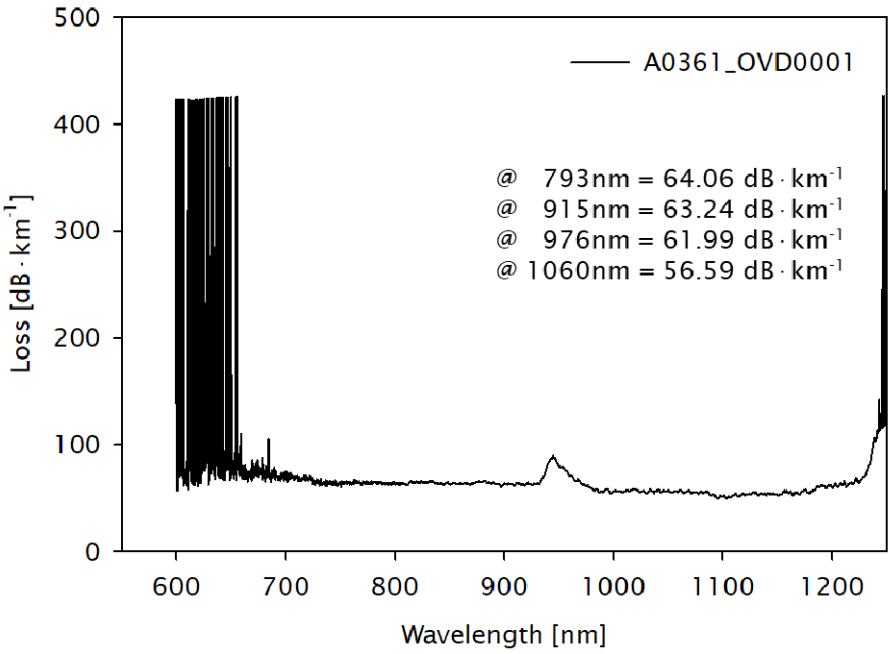

Graph 39. Loss of fibre A0361_OVD0001 (600nm-1200nm).

The fibre exhibits losses in the order of ~60 dB·km^{-1} from 700 nm up to 1200nm, with the exception of the OH absorption band at ~940nm. OH measurement is described below in Graph 41. An additional spectrum was obtained to investigate the losses of the fibre in longer wavelengths.

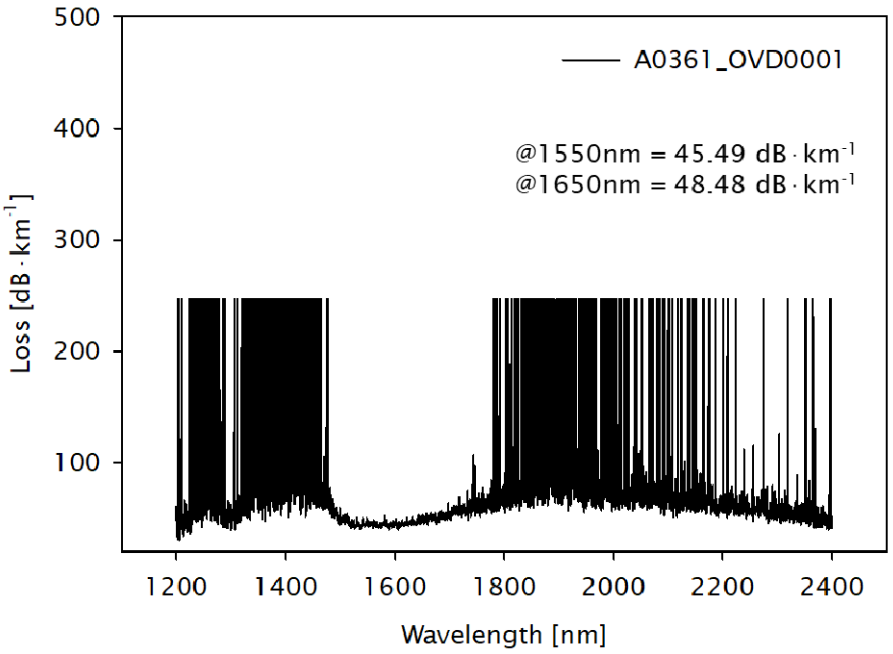

Graph 40. Loss of fibre A0361_OVD0001 (1200nm-2400nm).

The optical spectrum showed in Graph 40 presents the fibre losses, which are in the order of ~50 dB·km^{-1} from 1500 nm to 1700nm. The OH content in the fibre is the principal contributor to the prominent absorptions at these longer wavelengths.

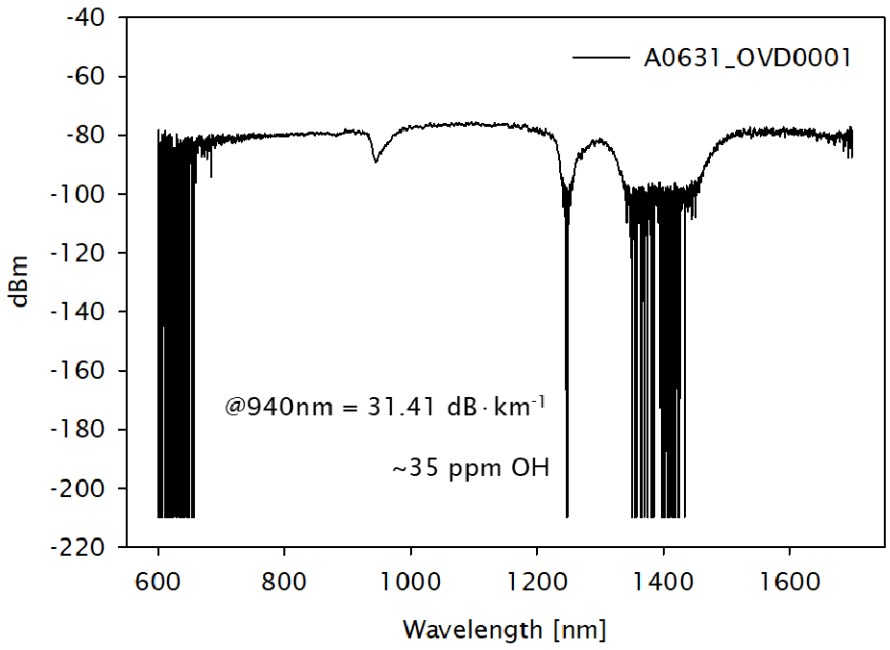

Graph 41. OH absorption measurement of fibre A0361_OVD0001.

The OH in the fibre was measured using the absorption band at ~940nm as it is shown in Graph 41. The length of the fibre and the OH content prevent the use of alternative absorption bands located in 1240nm and 1380nm. A concentration of ~35ppm of OH was calculated for this fibre.

The level of losses in the fibre A0361_OVD0001 is higher compared to commercial graded or step index fibres. Graded index fibres with losses of ~3 $dB \cdot km^{-1}$ are readily available. However, being the first OVD fibre made in-house, the level of losses are reasonable. Though, it is crucial to reduce the level of OH in the fibre and improve the process to enhance the performance of the fibres.

The preform OVD0035 presented in the previous section was drawn into a 125μm fibre. The refractive index profile is presented in Graph 42. The fibre profile maintains the refractive index change. The FRIP has a maximum value of 0.005, and the central hole was fully collapsed during the fibre drawing process. Collapsing the preform during the fibre drawing process minimise the evaporation of the dopants.

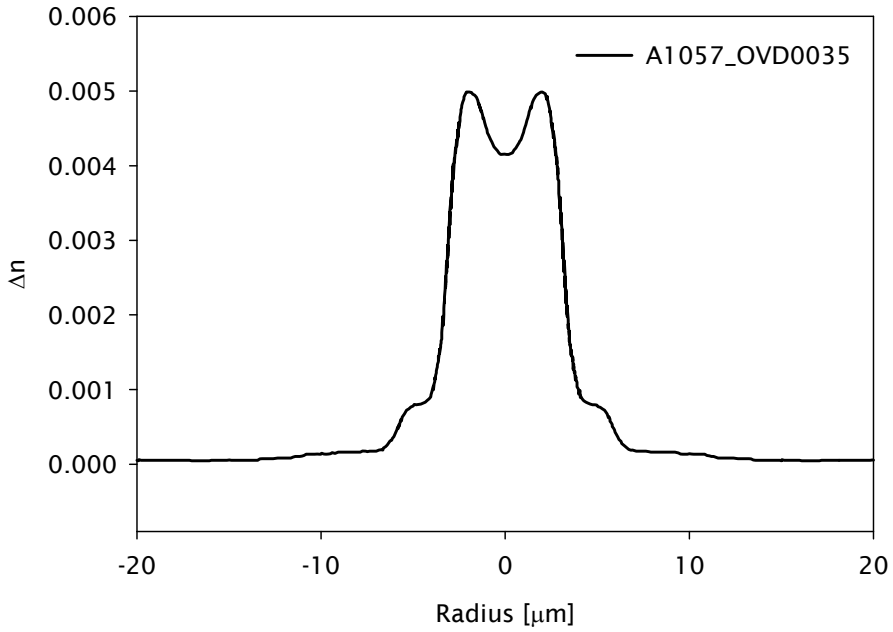

Graph 42. Refractive index profile of fibre A1057_OVD0035.

It is also noticeable that the twelve layers noticeable in the preform refractive index have been diffused into a single profile. The dimensional change during the fibre drawing process was the main contributor to the diffusion of the core layers. It is convenient for the OVD preforms that the core can be fabricated in large diameters. Thus, the fibre profile is refined during the preform conditioning and the fibre drawing process.

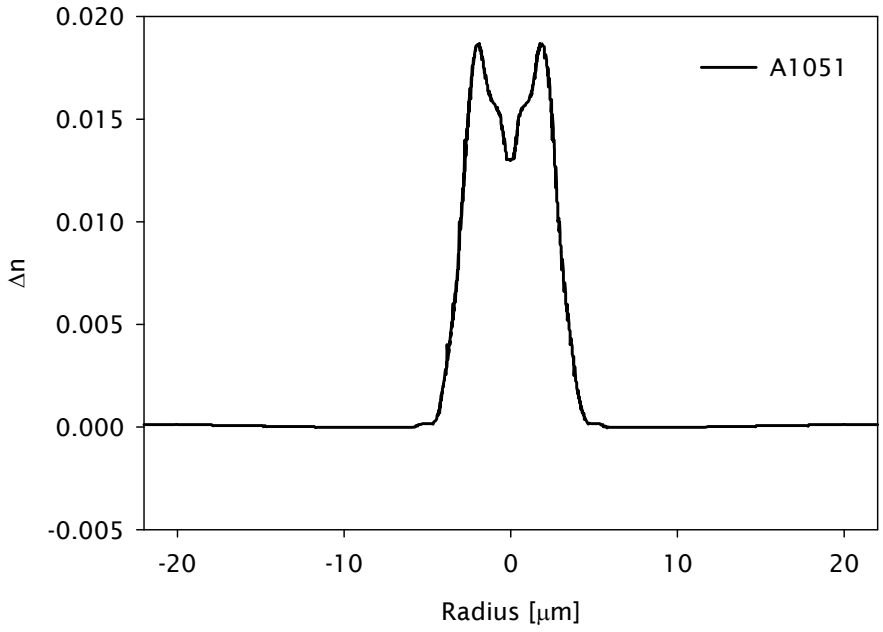

Graph 43. Refractive index profile of fibre A1051.

Similarly to the case of the preform OVD0035 the development of germanium incorporation lead to a more controlled refractive index and higher numerical apertures in the fibre designs, see Graph 43. Increasing the number of layers deposited on the preform also allowed to improve the stability on the profile in the final fibre. Characteristic ripples from the multilayer deposition on the preforms were minimised or eliminated in most of the cases during the drawing process.

6.1.3 Conclusion

The fabrication of germanosilicate preforms encounters particular challenges. Crystallisation on the depositions was found when the concentration of germanium oxide was increased. Adding a pure silica layer on top of the germanosilicate soot helps to prevent the crystallisation.

The preform profiler is not able to accurately process the refractive index changes when the germanosilicate deposition happens in the outer region. The resolved profiles have an unusual feature that shows a concave profile in the substrate. The source of the abnormal profile are the large refractive index profile and the stress in the glass. The fibre profiler can resolve the refractive index profiles of the outer depositions this requires drawing the preforms into fibres to measure the refractive index.

Compositional analysis XRD revealed a non-uniform deposition of germanium in the glass. It was found that a selective deposition zone occurs in the interface between layers. Also, the incorporation of germanium into the glass presented limitations. Thermodynamic conditions were analysed to investigate the source of the germanium incorporation.

It was found that the process of the loss of germanium during the preform fabrication was the halogenation of the GeO_2 during the dehydration process. The thermal reduction of GeO_2 into GeO can only happen after the evaporation of the GeO_2. Dehydration conditions were favourable for the halogenation process. Adding Oxygen to the gas flow during the dehydration process set back the reconversion of GeO_2 into $GeCl_4$.

After the modification of the process conditions, germanosilicate glass with high concentrations of germanium was achievable. Pure germania glass is discussed in Chapter 7. The following preform fabrication were successful and their refractive index profile exhibit the expected index contrast relative to that of the silica.

OVD germanosilicate fibres were drawn from the in-house fabricated preforms. The refractive index profile of the fibres follows the preform profile with evidence of inwards diffusion in the core region. Optical characterisation was performed on the fabricated fibres to investigate the optical loss, and was to be in the order of ~50 – 60 $dB \cdot km^{-1}$. The level of loss is higher compared to commercially available graded and step index fibres. Although further development is required to improve the level of the loss in the fibre, the current attenuation level is reasonable for the first OVD germanosilicate preform and fibre made in the Optoelectronics Research Centre.

Dehydration process requires additional refinement to lower the OH content in the glass. The OH in the fibre was identified as the principal factor for the high absorption in the longer wavelengths during the transmission measurements.

Additional fibres have been produced for demonstration purposes. Fibre A1057 was fabricated to resemble an SMF fibre. Also, the fibre A1051 with NA ~0.22 which is useful as delivery fibre for further experiments.

Chapter 7 Germania Glass

Conventional silica fibres have a theoretical limitation of 0.16 $dB \cdot km^{-1}$, operating at 1550nm. The infra-red (IR) absorption of silica is a fundamental limitation for this glass operating at longer wavelengths. However, the 2-micron spectral region has attracted the attention of research groups around the world. Laser sources at longer wavelengths are currently not easy to obtain, but there are different techniques to generate optical signals at 2-microns, such as optical amplification using TDFA.

Optical transmission at 2-microns is primarily restricted due to limited material availability which sets the challenge of developing a new glass host. Germanium oxide has been investigated as a potential candidate to overcome these current limitations. The fabrication of pure germania glass is discussed in this chapter. 2-micron laser technology has also captured the attention of many research areas, such as biomedical applications, defence systems, and the manufacturing industry. This particular region of the IR spectrum has particular interest due to the hard absorption of some organic molecules. Unfortunately, there is limited availability of literature on this glass. It could be possible that the cost and availability of the chemical precursors had been a factor for the limited research on this glass decades ago.

Nowadays, there is a limited activity on the development of germania glass for optical fibres. What the literature have on this field dates back to the mid-1970's, during the first developments of optical fibre technologies, and continues until the first few of years of the 21st century.

7.1 GeO

7.1.1 Introduction

Germania has been the centre of attraction for many research groups around the world in optical fibre technologies. Not only because of its high non-linear properties; but, also because it is an excellent candidate to transmit with low loss in the 2-micron wavelength region. Graph 44 shows alternative materials to silica and

their theoretical spectral loss. With the incresing data capacity demand due to social networks and mobile technologies the current capacity based on silica Single Mode Fibre (SMF) is reaching its fundamental limit[81,82].

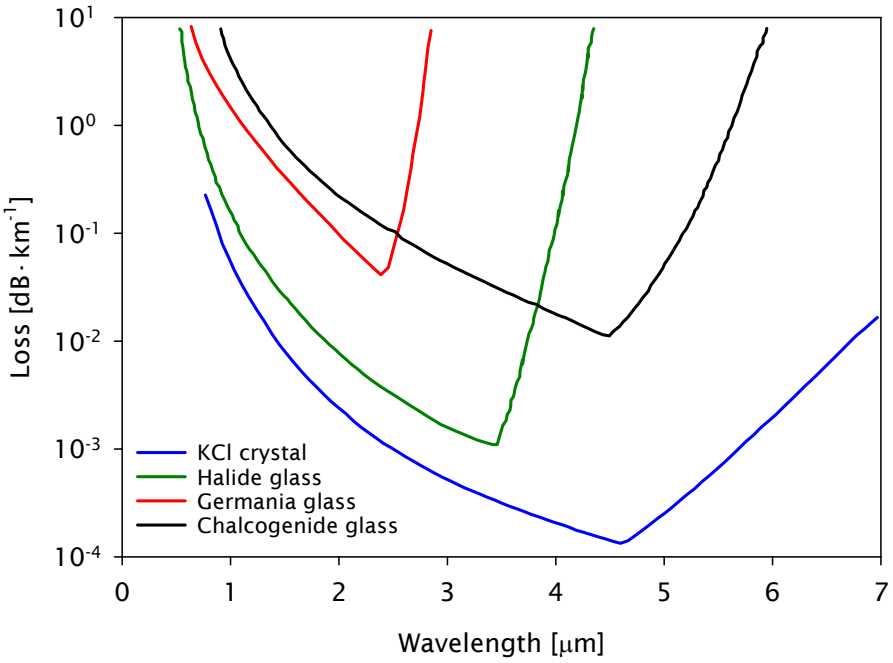

Graph 44. Calculated loss spectra for various materials[83].

The latest activities on germania glass for optical fibres, at the time of this research project, had been using MCVD deposition process. Fabricating cores of GeO_2 in silica or fluorine-doped silica requires heating of the substrate to collapse the tube into a solid rod. The temperatures required to achieve this collapse is higher than the boiling point of the germanium oxide and can reach temperatures that lead into the thermal reduction of the GeO_2 into GeO as discussed in Chapter 3 and Chapter 6.

Recent studies have gained understanding of the Ge-OH bonds, optical losses and Raman amplification in GeO_2 glass and fibres[84,85]. Also, investigations on phase transitions and crystallinity of the germanium oxide had been reported in the last two decades[7,37,58,86,87]. However, fundamental investigations on the deposition and optical properties of the germania glass, as well as demonstrated fabrication of pure germania preforms, had ceased more than 30 years ago[6,29,88-91].

7.1.2 Deposition

The deposition parameters for pure germania soot preforms are very different compared to pure silica. Initial deposition of pure GeO_2 at high temperature causes the immediate evaporation of the soot. On the other hand, medium-high temperatures lead to the deposition of particles in the liquid phase, which cool down rapidly at the moment of impacting on the substrate, leading to its mixing with the substrate surface. Image 27 shows a CFQ rod substrate with the surface removed when a germania glass deposition is peeled off.

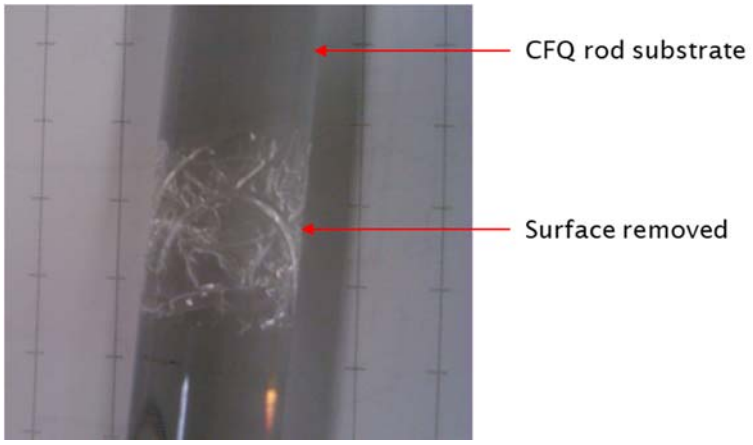

Image 27. Substrate surface removed due to GeO_2 deposition.

The deposited germania glass diffused into the surface of the silica rod, which during the cooling down process, detached the surface of the substrate. The more substantial thermal expansion coefficient from the germania glass lead to the detachment of the silica on the surface. Image 28 shows a different preform using the deposition conditions from the thermodynamic analysis discussed in Chapter 3. It is noticeable that a section of the deposition is detached from the substrate due to the thermal expansion mismatch.

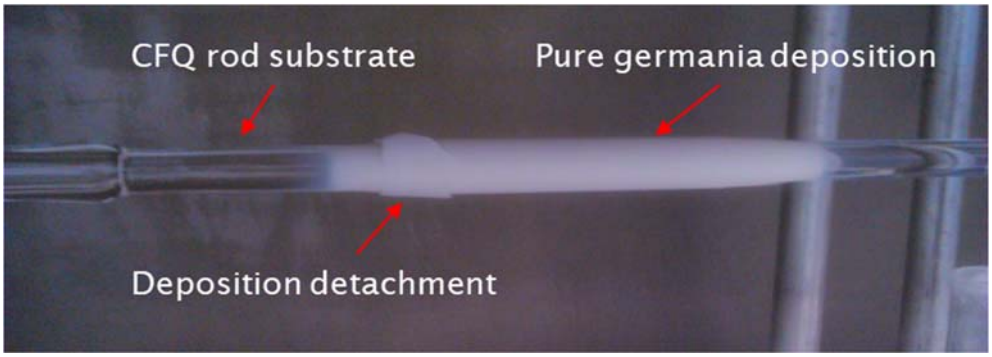

Image 28. Preform OVD0031 deposited outer layer made from 100% GeO_2.

The reduced melting point of the GeO_2 forces a drastic reduction of the temperature of both the OVD deposition and consolidation process. The H_2/O_2 ratio remains unchangeable for flame stability purposes and stoichiometric reactants availability; hence, the gas flows had to be reduced.

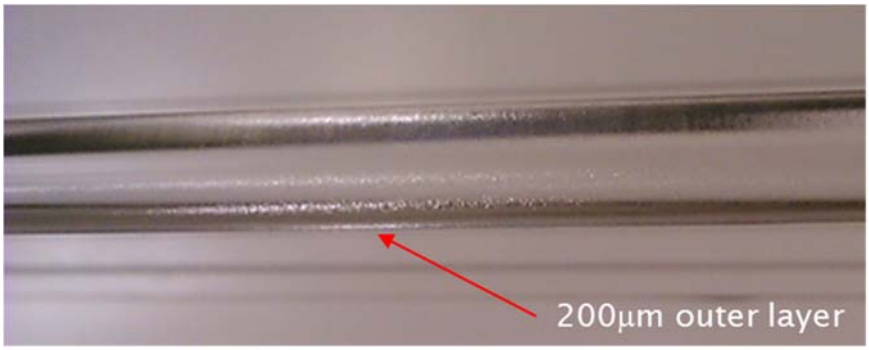

Image 29. Transparent 200μm outer layer of pure GeO_2 after consolidation.

The preform OVD0031 was sintered resulting in a single layer of pure germania glass with a thickness of ~200μm. Image 29 shows a germania deposition on top of a CFQ substrate rod successfully consolidated into a transparent glass. Compositional analysis using EDX presented in Image 30, confirmed that the deposited glass only contains germanium. The glass sample gas coated with ~30nm of carbon for conductivity purposes.

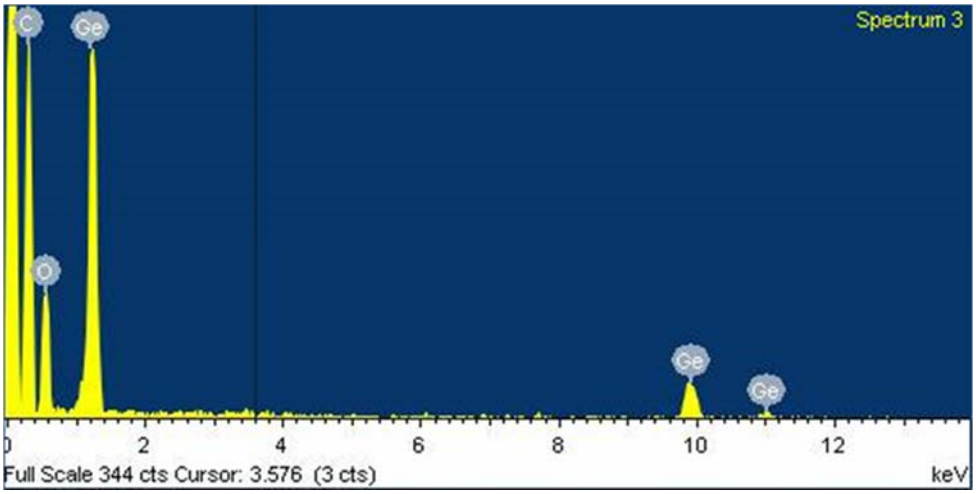

Image 30. EDX analysis of 100% GeO_2 outer deposition

Deposition conditions required improvement to allow the use of a detachable bait rod to proceed with larger volumes. Unfortunately, the thermal coefficient mismatch with silica is the predominant obstacle while processing germania.

Following the procedure used in Chapter 4 for silica deposition conditions, a density study on germania soot depositions was performed. It was essential to identify the conditions that allow the soot body to be successfully detached and processed in the following fabrication stages. Similar to the silica soot behaviour, the depositions at low temperatures produce a fragile soot body due to its low density. Image 31 shows the soot detachment from the carbon-coated substrate.

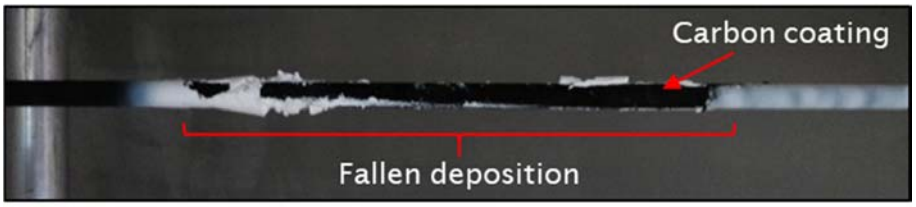

Image 31. Germania density too loose $\rho = 0.196\ g \cdot cm^{-3}$.

Conversely, depositions at high temperatures produce a compact soot body due to its higher density. Nevertheless, if the density is too high the stress in the soot, due to the thermal expansion, might cause the preform to fail. Image 32 shows a soot deposition with a longitudinal fissure due to the stress propagation in a highly dense preform.

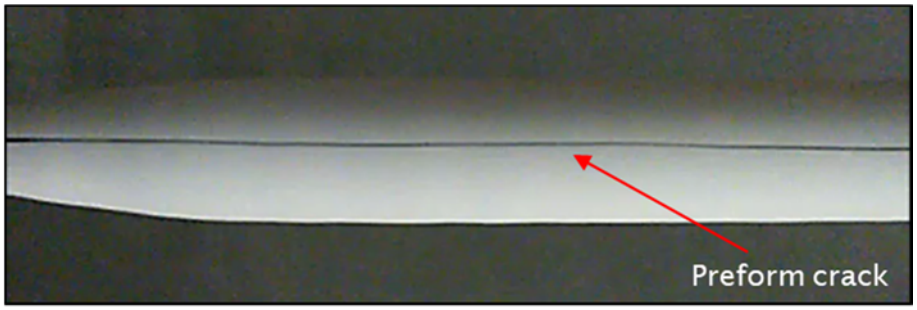

Image 32. Germania density too compact ρ = 1.211 g·cm^{-3}.

Following the procedure from Chapter 4 for the creation of a digital model for the deposition soot, the deposition image was projected into a fixed background. In the case of the low-density soot, it was too fragile to remove it from the OVD lathe. Therefore, both measurement, low and high density, were performed inside the OVD deposition chamber.

The images projected were used as a foundation to build a 3-D model of the volume including the irregular shapes. The substrate is not represented in Figure 8. Nevertheless, its dimensions were used to reproduce the internal geometry of the 3-D model shown below.

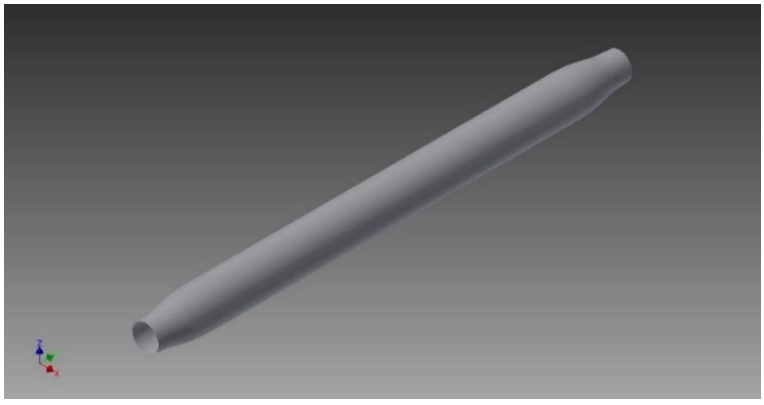

Figure 8. 3-D model of germania deposition soot body.

The germania depositions are exceptionally sensitive to temperature changes compared to silica. For that reason, a characterisation of the soot preform temperature was carried out. Similarly to the temperatures measurement reported in Chapter 2, a thermocouple was inserted into the substrate. Although in this case the temperature measurement was performed during the deposition process, including flows from the reactants. The temperature was measured for the deposition of multiple layers and is shown in Graph 45.

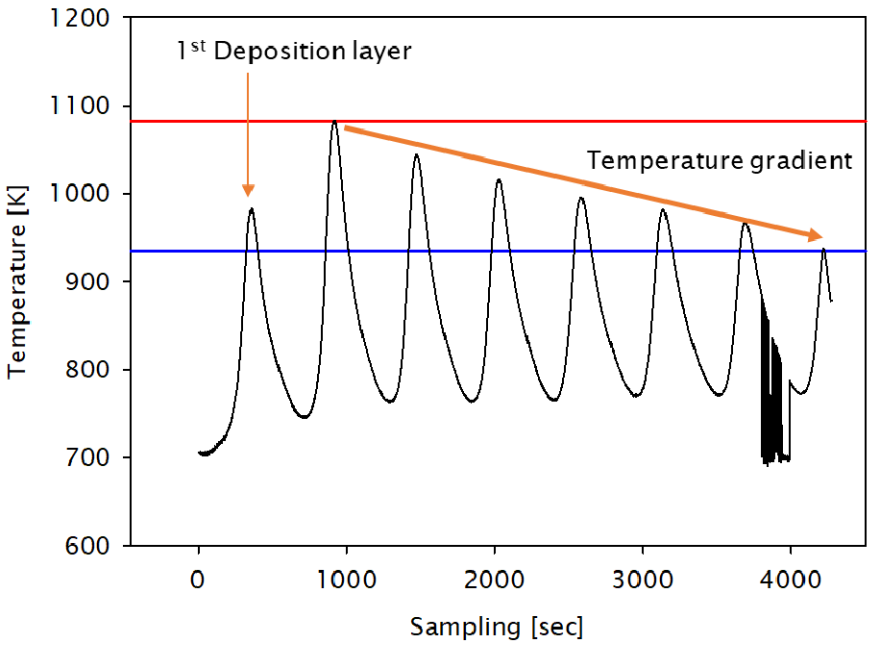

Graph 45. Temperature behaviour during multilayer germania deposition.

Extensive characterisations shown in Graph 45 were carried out during the deposition stage revealing the temperature behaviour on the substrates and its correlation to the preform failure. After the analysis was concluded, an adjustment to the deposition temperatures of the first layer was required.

Image 33. Crack-free germania deposition.

As a result of the density analysis, and the temperature characterisation; it was possible to achieve a crack-free full deposition. Image 33 shows a 100% germania soot body without fissures. The deposition was made on top of an alumina bait rod carbon coated to improve detachment capabilities.

7.1.3 Bait rod removal

For the successful removal of germania soot preforms from the bait rod; it had to have a thermal expansion coefficient higher than GeO_2, i.e. $75x10^{-7} \cdot K^{-1}$. Also, the bait rod needs to have a high tolerance to corrosive environments and a softening point above the deposition temperature. A carbon coating was tested on top of the alumina bait rod as shown in Image 34. The carbon coating was applied by fuming the bait rod with methane reductive flame as a release layer to facilitate the preform removal. The use of carbon was selected as it would be a thin layer that could be converted into CO_2 and evaporated during the dehydration at high temperature with the presence of oxygen in the flow.

Image 34. Carbon coating on an alumina substrate.

Two substrates were satisfactorily tested for germania deposition; both have a higher thermal expansion coefficient compared to germania.

- Alumina: $81x10^{-7} \cdot K^{-1}$
- Soda-lime glass: $85x10^{-7} \cdot K^{-1}$

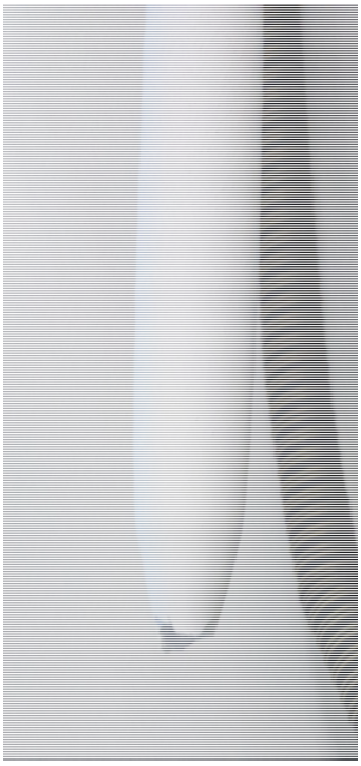

Image 35. Preform removal without soot body cracking

The preform removal process had been successfully established. Image 35 shows a germania soot body removed from the bait rod, crack-free and ready for dehydration and the consolidation processes.

7.1.4 Crystallisation

The first crystallisation occurrence was during the depositions of germanosilicate preforms discussed in Chapter 3. Germanosilicate depositions presented signs of crystallisation when deposited on top of a CFQ substrate. The addition of a silica deposition layer on top prevented the crystallisation. The increase of germanium concentration aggravated the crystallisation.

The silica clad layer used to mitigate the crystallisation in the germanosilicate glass, was not possible to implement for pure germania preforms. The significant thermal expansion mismatch in between the glasses developed cracks in the interface. Also, the dehydration and consolidation conditions are entirely different.

During the initial consolidation experiments of pure germania depositions; inconsistencies in the samples outcome were observed. The samples had unpredictable behaviour during the consolidation process although the fabrication parameters were stable for all the experiments. The alternative possibility was that the samples

were suffering from an unexpected change. Samples from the deposited soot were measured by Thermo Gravimetric Analysis (TGA). The samples were measured with a heating rate of 10K·min^{-1} starting from room temperature up to 1523.15 K. The samples were measured after 0.5, 3.6, 24 and 192 hours after the deposition process.

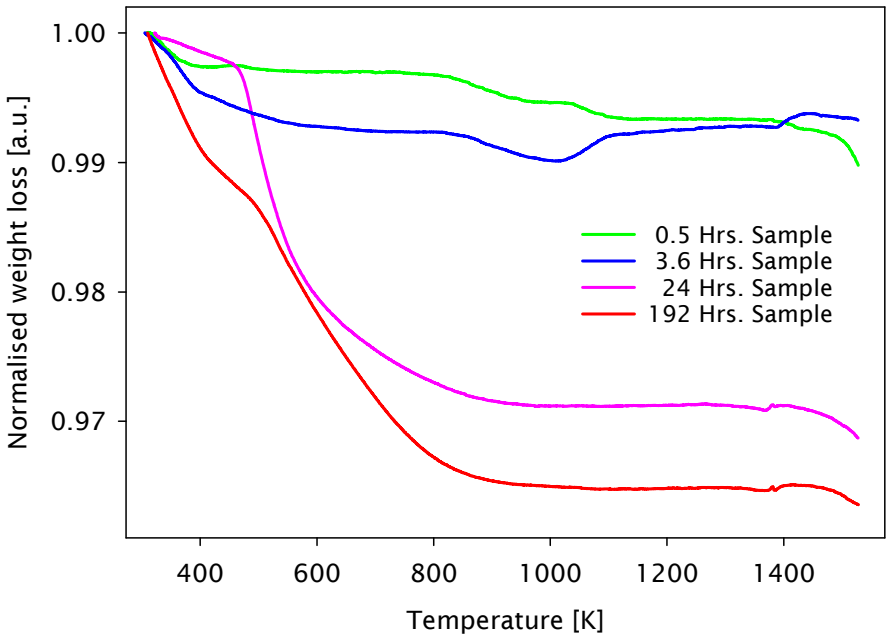

Graph 46. Weight loss of germania soot samples from TGA.

The weight loss of the germania soot samples is shown in Graph 46. The rate of weight loss in the samples increased with the time after the deposition. The amount of weight loss was more substantial in the samples measured after 24 and 192 hours after the deposition. Also, the transition features shown at ~1000 K were not present in the later samples.

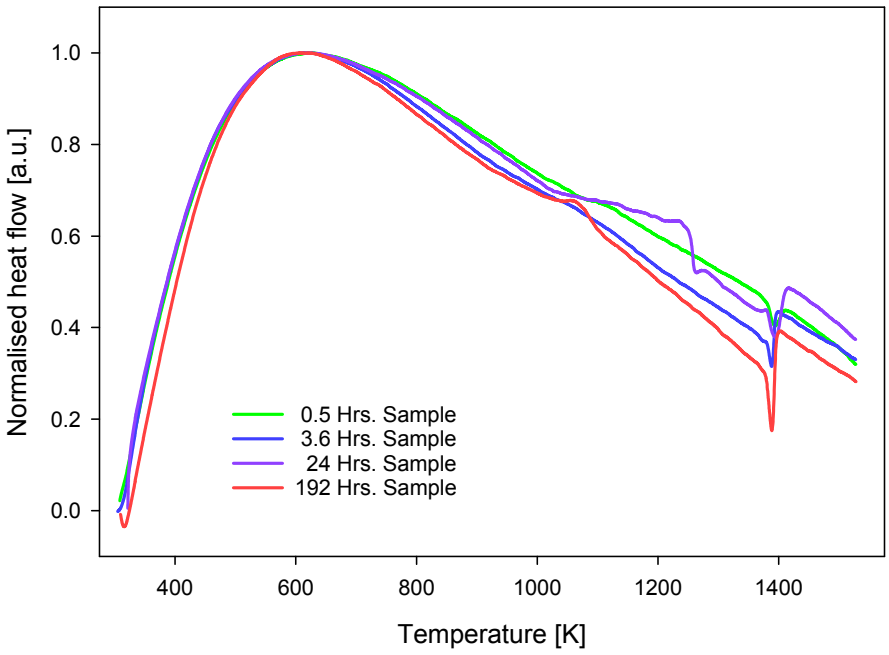

Graph 47. Heat flow of germania soot samples from TGA.

The heat flow of the germania soot samples is shown in Graph 47. The samples measured at 0.5 and 3.6 hours, after the deposition, did not present heat flow events other than the melting point at ~1393 K. Contrarily, the samples measured at 24 and 192 hours, after the deposition, presented a peculiar heat flow event starting at ~1026 K in addition to the melting point at ~1393 K.

Investigations aiming to identify the source of the changes in the samples were carried out. Initially, the samples were put under vacuum to identify any environmental factors, such as moisture that could be affecting the samples. The samples were also shielded from light sources to prevent any potential photo-reaction. Lastly, the samples were dehydrated to remove any potential OH from the deposition that could be driving the sample changes. However, none of these conditions altered the samples.

A final experiment was carried out to corroborate if the OVD process itself had some effect on the samples. Therefore, a sample of germania soot was taken from an MVCD deposition. Since the MCVD deposition follows a different reaction path, it would be possible to identify any associated factors to the process. Unfortunately, the soot from the MCVD suffered from the same atypical behaviour.

During the investigations to identify the source of the changes mentioned before; it was observed that compact and hard soot depositions became soft and loose after few days. Accordingly, a computed tomography (CT) scan was carried out in the μ-VIS X-Ray Imaging Centre to identify potential changes in shape or volume in

the samples. Unfortunately, the change happened on a scale smaller than the equipment resolution. Identification of a barely perceptible shrinkage of the total volume was possible with this technique. Though, the origin of the changes remained without explanation.

Further analysis was carried out using X-Ray diffraction (XRD). Investigations of a crystallisation process within the first 24 to 48 hours were proposed as the source of the changes in the samples. Freshly made deposition samples were prepared and measured by XRD every 12 hours. The powder diffraction was measured in the UK National Crystallography Centre. The equipment used was a D2-PHASER from Bruker. The conditions used for the measurement were λ=1.541Å; increments of 0.022deg; starting 2θ position at 8.002deg and a total of 5027 steps.

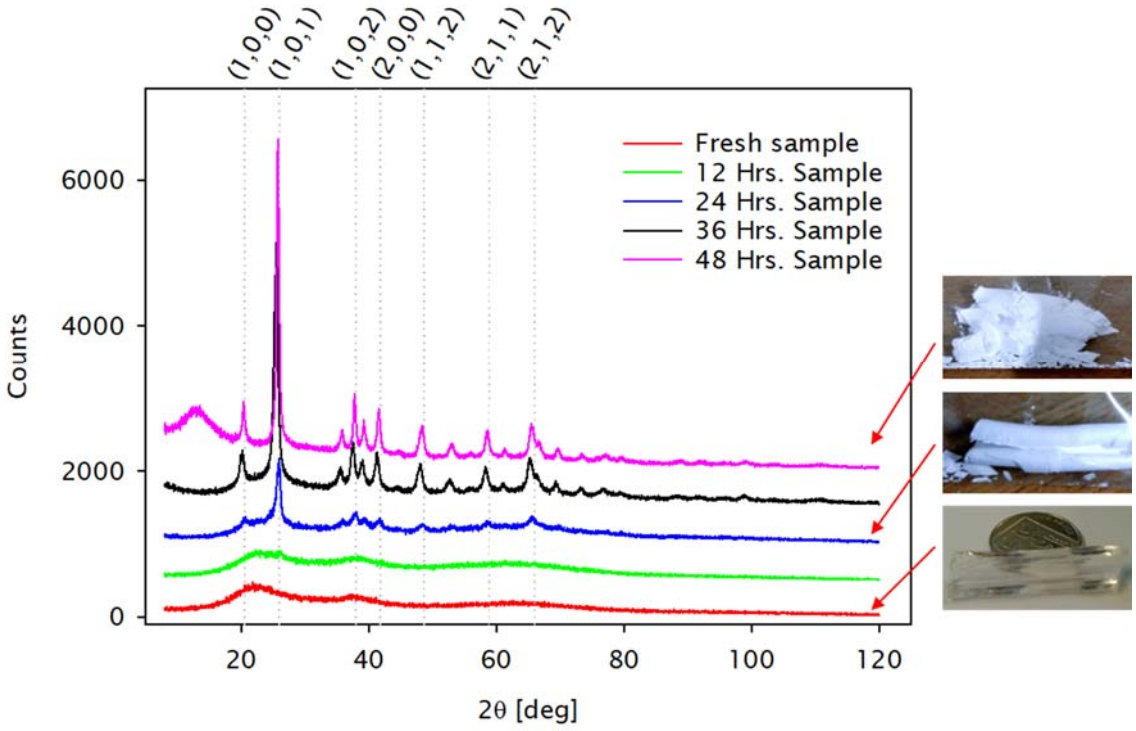

Graph 48. Diffractogram of GeO_2 soot powder.

The diffractogram in Graph 48 shows an evolution of crystal growth on the samples with respect to time. From the lower trace (red) to the top (pink) each trace was taken with ~12 hrs difference. The Miller indexes of the high-intensity crystal planes are annotated with a reference dotted-line on top of Graph 48. The crystallographic information obtained from the XRD measurement is consistent with hexagonal crystalline germania.

A parallel study using the same deposition conditions and consolidation parameters showed that the transparent glass could only be achieved using the freshly made samples. Samples between 12 and 24 hrs can be consolidated as well; but,

the preform is not transparent. If the sample has more than 24 hrs, the powder does not consolidate into a self-supported preform.

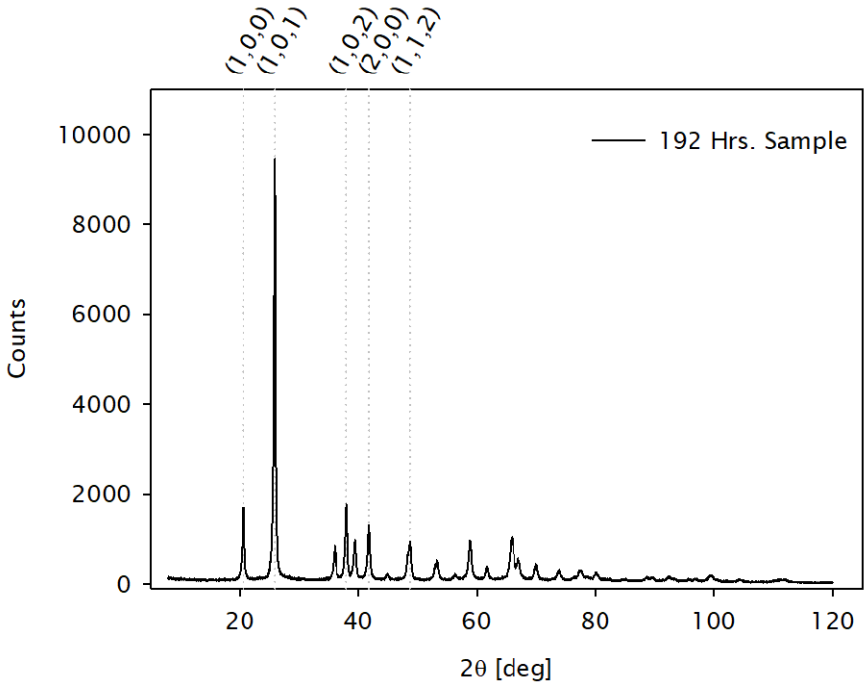

Graph 49. Diffractogram of fully crystallised germania deposition.

The crystallisation process continues until the deposition samples are converted into a fully crystalline powder. Graph 49 shows the diffractogram of the deposition after 192 hours. The Miller indexes of the high-intensity crystal planes were annotated with a reference dotted-line on top of Graph 49.

The information provided from the XRD analysis was essential to modify the deposition process. Also, the entire fabrication process had to be adjusted to complete the deposition to the consolidation process in a few hours.

Image 36. Transparent and defect free 100% GeO_2 preform

Image 36 presents a transparent and fully consolidated 100% GeO_2 preform. The preform was successfully obtained using the modified conditions during the fabrication process. After the consolidation, the germania preforms did not present signs of crystallisation.

7.1.5 Core-cladding structure

Core-cladding structures using single-step fabrication are achievable. However, this approach requires large volumes of cladding deposition to compensate for the thermal stress of the core. Image 37 shows an example of a core-cladding structure in germania preforms.

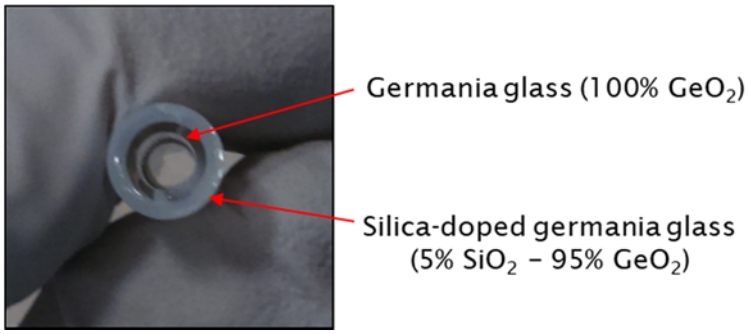

Image 37. Cross-sectional image of a 100% germania core and silica-doped germania cladding (5% SiO_2 / 95% GeO_2).

For high numerical aperture applications or considerable thermal expansion coefficient differences, a two-step fabrication process proved to be more effective. The assembled preform was processed in a glass working lathe (GWL). Image 38 shows a preform with 100% germania core and 100% silica cladding.

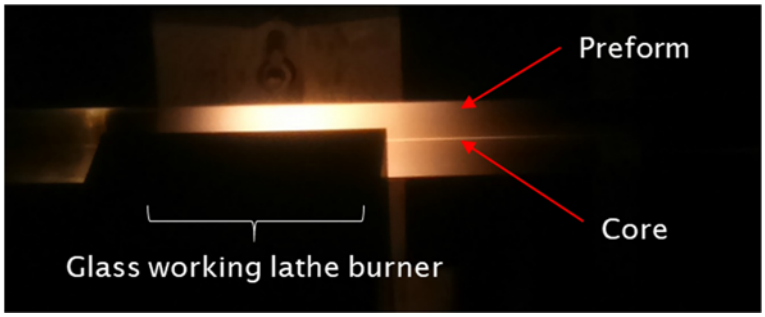

Image 38. Preform assembly for high-NA applications using 100% GeO_2 core and SiO_2 large diameter cladding.

EDX analysis supports the 100% GeO_2 composition in the preform core, see Image 39 a). The profile distribution on the core region is presented in Image 39 b). It is

evident that the diffusion of the core during the preform fabrication did not happen.

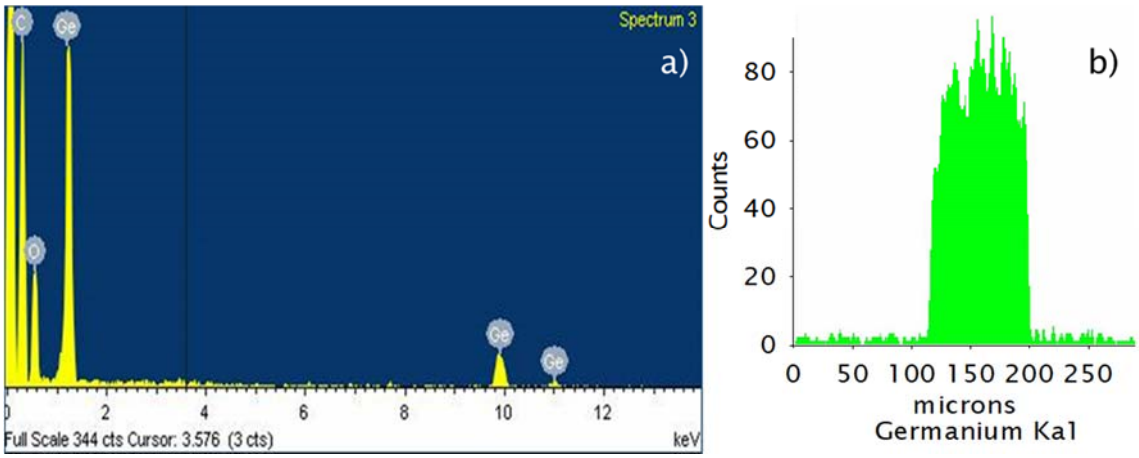

Image 39. a) EDX analysis from the core of germania preform section after drawing; b) profile distribution of Germanium signal Ka1.

7.1.6 Germania glass fibres

An optical fibre with ultra-high numerical aperture using core composition of 100% GeO_2 and cladding of 100% silica was drawn. The first ever 160m of 100% GeO_2 core fibre with silica cladding were drawn with a 3µm core diameter and 200µm cladding diameter. The fibre has a calculated single mode characteristic at ~2400nm.

Graph 50 a) shows the fibre refractive index profile obtained from the IFA. However, the instrument cannot resolve the measurements on small cores, and this is the reason why the profile has a flat top due to the spatial resolution limitation in the instrument.

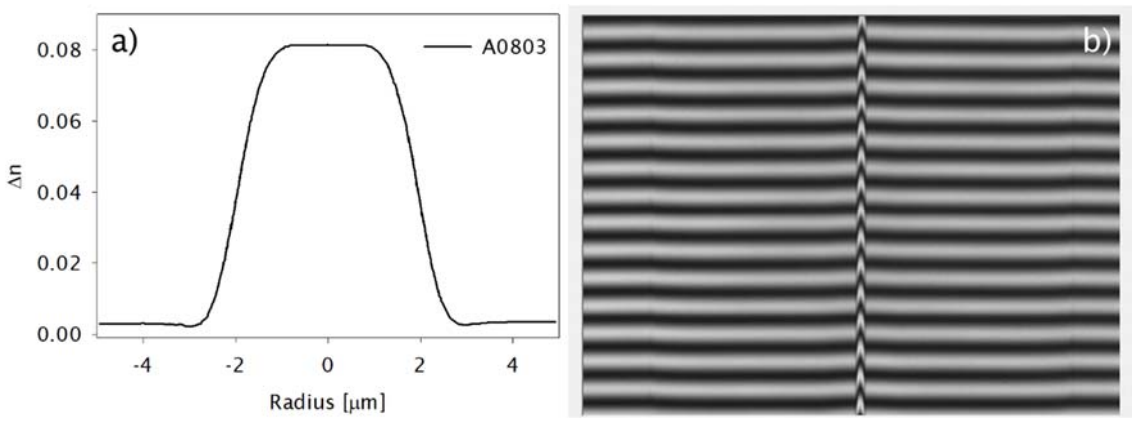

Graph 50. IFA measurement; a) FRIP of 100% GeO_2 fibre with silica cladding and b) IFA interference pattern from 100% GeO_2 fibre.

Graph 50 b) shows the IFA interference pattern. It is possible to appreciate in Graph 50 b) the peak values of the core region reaching the lower values of the upper fringe. Also, the core size of the fibre at the top flat region is below the 3µm, which is the minimum core size that the IFA is capable of resolve. These factors limit the IFA to accurately measure the FRIP of the high-NA 100% GeO_2 fibre.

Fibre Bragg gratings were inscribed to study potential applications for the GeO_2 fibres. The grating shown in Graph 51 was scribed using a femtosecond laser described in section 10.5 with inscription through the coating, and using a point by point technique. The applications for this fs-FBG can be, for instance, Raman lasers to overcome the limitation on wavelength coverage from the rare-earth doped fibres.

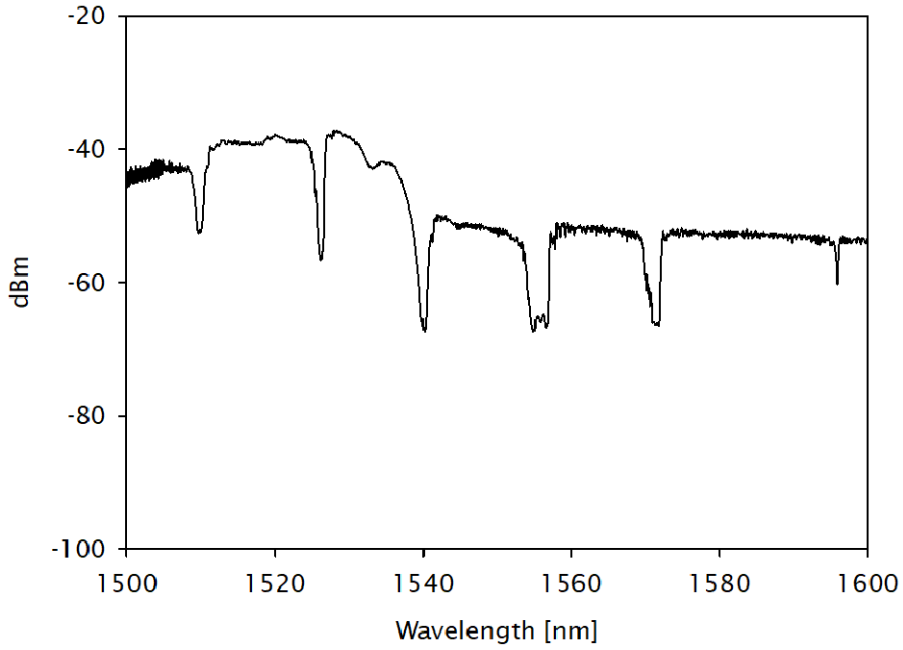

Graph 51. Transmission spectra of FBG inscribed in 100% GeO_2.

7.1.7 Conclusion

Pure germanium depositions at high temperatures result in the deposition of germanium either in the gas or liquid phase, with its corresponding undesirable effects such as low-efficiency deposition. Substrate peeling has been observed during preliminary deposition tests when the deposition is in the liquid phase.

Characterization of deposition conditions have been performed and the deposition process established for preform fabrication. Additionally, the processes for preform removal: deposition parameters and consolidation have been established

The single material composition on the OVD preforms is recommended since the thermal expansion mismatch tends to crack the preform glass. Alternatively, it is possible to make multiple materials in one process. However, the ratio between core and cladding layers must be at least 10, and the concentration difference should not exceed 30%.

Dehydration and consolidation parameters were established. Preforms fully consolidated, bubble and crack free can be obtained. It is essential to review thermodynamic conditions for new compositions to ensure possible reactions and phase changes in the glass.

Optical fibres with core composition of pure germania and cladding of silica have been achieved. Instrument limitations prevent the characterisation of the ultra-high NA difference with a small core. Inscription of fs-FBG in the pure germania core was possible. Investigations on high nonlinear optics and additional applications for the pure germania core optical fibre would be a part of future development.

Chapter 8 Aluminosilicate Glass

Speciality optical fibres for laser applications require the development of the glass host. The incorporation of rare-earth (RE) ions into the glass is essential for the development of fibre laser applications. Aluminium Oxide (Al_2O_3) is a well-known network modifier often used in the glass matrix. Its incorporation to the core material enhances the laser performance and reduces the undesirable clustering of the RE-ions.

Optical fibres with large cores for laser applications are commercially available. However, the current fabrication techniques are mainly limited by the way the glass host is built-up. MCVD preform fabrication, using solution doping technique for aluminium oxide (Al_2O_3) incorporation, present challenges for increasing the number of layers of doped material[23,24].

Novel approaches have been developed based on the same solution doping technique. Developments aiming the increment of dopant incorporation as well as its distribution have been successfully demonstrated[25]. However, the preform core size is limited leading to secondary processes to adjust the core to cladding ratio. A route to obtain a larger core in the final fibre is to reduce the cladding cross-section. The use of hydrofluoric acid etching is a widely adopted process to reduce the cladding of a preform leading to fibres with a large core.

Alternative approaches based on gas phase deposition combined with the MVCD fabrication process have been demonstrated to be useful for large core preform fabrication. Nevertheless, the concentration is still limited by the glass viscosity mismatch between the cladding and the core.

The research presented in this thesis demonstrates that the OVD fabrication technique has the required capabilities for manufacturing large volumes of the preform core materials. Aluminosilicate glass preforms and optical fibres are reported in this chapter. Experiments targeting a change in refractive index and RE-ion incorporation are described in the following sections. These experiments aim to the develop aluminosilicate glass that can have multiple applications such as large-volume core material and substrate tubes that can be used for deposition or as part of pedestal structures on the waveguide for double and triple-clad fibre designs.

8.1 Solution doping

8.1.1 Preforms

To start the solution doping fabrication initial trials focused on well-known doping solutions in pure silica soot preforms. For the initial experimental work, Al and Al+Yb solutions were used. High purity salts dissolved in a volume of MeOH were prepared to be used with the solution doping process. Also, pure MeOH volumes were used as a control to investigate the effects of the soaking process on the OVD porous soot preforms.

OVD0025 and OVD0027, 12 and 6 layers silica soot preforms, respectively, were soaked for 2 hours in 200 cm^3 of MeOH; the solution filling/draining ratio was 2.2. The preforms were kept overnight with a constant extract rate to reduce the solvent content. The drying process conditions are presented in Table 7 and Table 8. The dehydration and consolidation conditions were kept unchanged for both preforms and are described in Table 9.

Number of pass	Gas Flows [sccm]	Rotation [RPM]	H_2/O_2 ratio	Traverse speed [$m \cdot min^{-1}$]	Time [min]
1	N_2 = 2000	1	2	-	30
2-7	N_2 = 2000	1	2	0.100	-

Table 7. Drying conditions of preform OVD0025.

Number of pass	Gas Flows [sccm]	Rotation [RPM]	H_2/O_2 ratio	Traverse speed [$m \cdot min^{-1}$]	Time [min]
1	N_2 = 2000	-	-	-	14
2	N_2 = 2000	-	2	-	24
3-12	N_2 = 2000	1	2	0.200	-
13	N_2 = 2000	1	-	-	11

Table 8. Drying conditions of preform OVD0027.

T [K]	ΔT [$K \cdot min^{-1}$]	Gas Flows	Rotation [RPM]	Feed speed [$m \cdot min^{-1}$]	Retraction speed [$m \cdot min^{-1}$]
1315	10	He/Cl_2 ratio = 16.66	3	0.010	0.025
1848	10	He = 2000 sccm	3	0.005	Up to cool

Table 9. Dehydration and consolidation parameters of preform OVD0025 and OVD0027.

Preform OVD0025 was made from 12 layers of porous soot, and was soaked in MeOH to investigate the effects of the soaking process on the OVD porous soot

preforms, during the solution doping technique. After dehydration and consolidation processes, an opaque preform was obtained. Image 40 shows the roughness in the surface of the consolidated preform.

Image 40. Preform OVD0025 after the consolidation process.

Post-processing of the preform was performed to eliminate the roughness of the surface; Image 41 shows the change to the tip of the preform after exposure to high temperatures. The preform was exposed directly to H_2/O_2 flame using a hand torch.

Image 41. Preform OVD0025 made transparent after heating the tip.

A cross-section of the preform is presented in Image 42. The region between the transparent and rough surface reveals that the opaque undesirable condition is only in the outer layers of the preform. SEM micrographs also confirms the outer location of the defects, see Image 43.

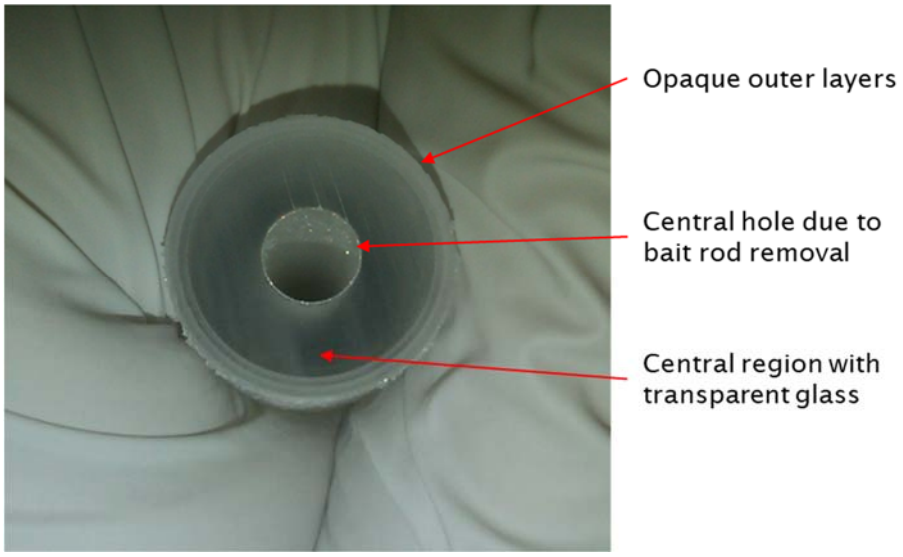

Image 42. OVD0025 cross-section showing opaque layers on the outside.

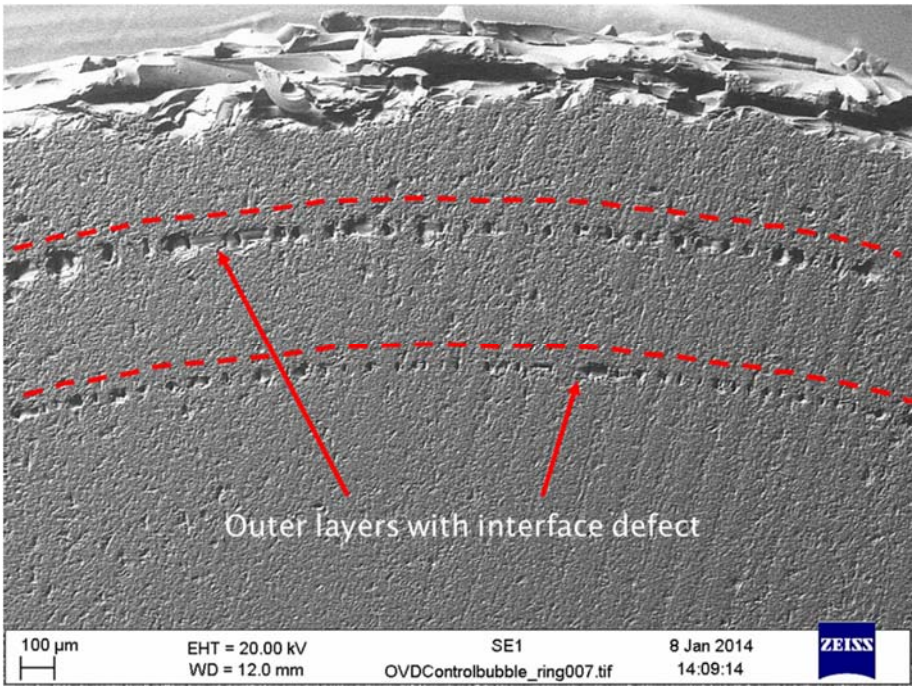

Image 43. Micrograph of defects in outer layers of preform OVD0025.

The entire preform was exposed to high temperatures to make it transparent. A change of the colour flame indicated that the outer layers still had some volatile residues, see Image 44 a). Also, luminescence from the inner layers can be observed in Image 44 b). Sections of the preform deformed due to thermal expansion of the volatile content trapped in the glass.

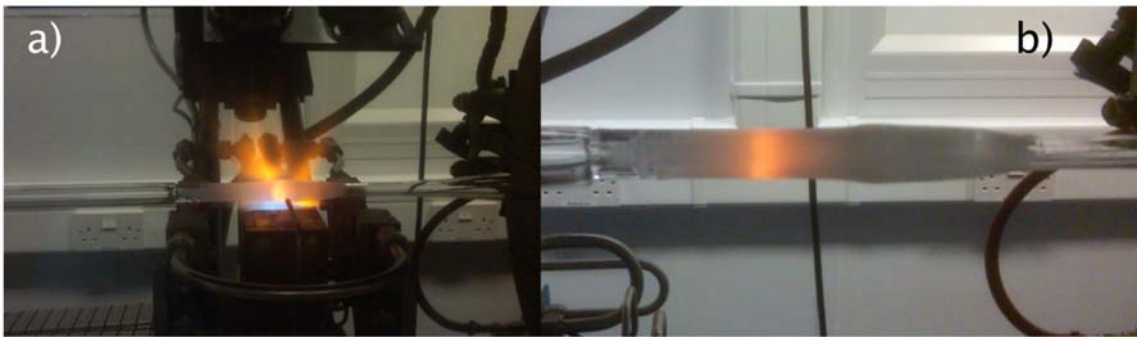

Image 44. Solution doping preform; a) Flame colour change during the heating process, and b) luminescence from the inner layers.

Bubbles started appearing along the preform. After repeated passes at high temperature, the final solid rod was sliced and observed using the SEM. Observations from Image 45 reveal that the bubble sections also correspond to the outer layers, the central part of the preform remained intact. The outer surface was smooth due to the high temperatures, but the bubbles remained inside.

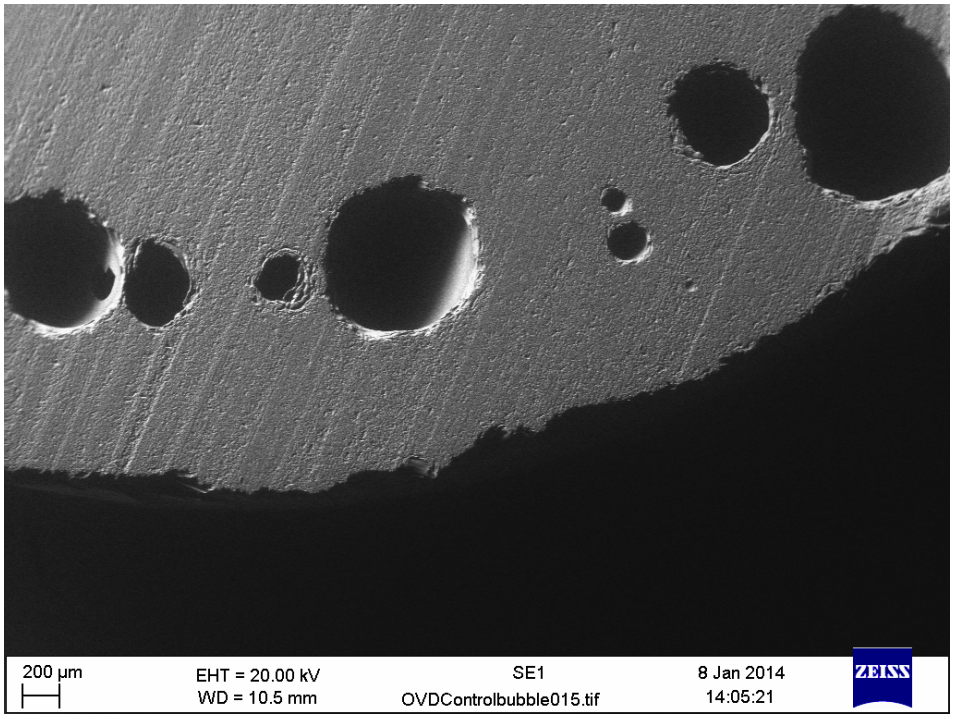

Image 45. Micrograph of bubbles trapped in preform OVD0025.

Preform OVD0027, made from 6 layers of porous soot, was processed in the same way as preform OVD0025 to investigate the correlation between the density of the layers and the effects observed in the 12 layer preform. After dehydration and consolidation processes, an opaque preform was obtained. The same high-temperature treatment was performed for this preform to obtain a transparent glass preform.

8.1.1.1 Aluminium

OVD0026, a 6 layer porous soot preform, was soaked over 2 hours in a 0.0187M solution of $AlCl_3$; the solution filling/draining ratio was 2.2. The preform was kept overnight with a constant extract flow to reduce the solvent content. The drying process conditions are explained in Table 10. Also, the dehydration and consolidation parameters are described in Table 11.

Number of pass	Gas Flows [sccm]	Rotation [RPM]	H_2/O_2 ratio	Traverse speed [m·min^{-1}]	Time [min]
1	N_2 = 2000	1	2	-	17
2-11	N_2 = 2000	1	2	0.200	-
12	N_2 = 2000	-	-	-	63
13-22	N_2 = 2000	1	2	0.200	-

Table 10. Drying conditions of preform OVD0026.

T [K]	ΔT [K·min^{-1}]	Gas Flows	Rotation [RPM]	Feed speed [m·min^{-1}]	Retraction speed [m·min^{-1}]
1315	10	He/Cl_2 ratio = 16.66	3	0.010	0.025
1848	10	He = 2000 sccm	3	0.005	Up to cool

Table 11. Dehydration and consolidation parameters of preform OVD0026.

After dehydration and consolidation processes, an opaque preform was obtained, see Image 46. High-temperature treatment of the preform was performed to obtain a transparent glass preform which was collapsed on an MCVD lathe, obtaining a ~6mm diameter solid rod shown in Image 47. Small bubbles were observed along the preform in the outer layers.

Image 46. Preform OVD0026 after the consolidation process.

Image 47. Preform OVD0026 after the collapsing process.

8.1.1.2 Aluminium - Ytterbium

OVD0023, a 12 layer porous soot preform, was soaked over 2 hours in a 0.2249M solution of $AlCl_3$ in addition to a 0.0536M solution of $YbCl_3$; the solution filling/draining ratio was 2.2. The preform was kept overnight on the solution doping apparatus described in Chapter 2. The drying process conditions are explained in Table 12. Multiple passes of the drying process were required to ensure that all the volatile compounds evaporate completely. Also, the dehydration and consolidation parameters are described in Table 13.

Number of pass	Gas Flows [sccm]	Rotation [RPM]	H_2/O_2 ratio	Traverse speed [m·min^{-1}]	Time [min]
1	N_2 = 1000	-	-	-	300
2	N_2 = 1000	1	2	-	27
3	N_2 = 1000	1	2	-	40
4	N_2 = 1000	1	2	0.027	-
5	N_2 = 1000	-	-	-	835
6	N_2 = 2000	1	2	-	10
7-9	N_2 = 2000	1	2	0.100	-
10-11	N_2 = 2000	1	2	0.075	-
12	N_2 = 2000	-	-	-	1080
13	N_2 = 2000	-	-	-	1020
14	N_2 = 2000	1	2	0.100	-
15	N_2 = 2000 ; O_2 = 50	1	2	0.100	-
16	N_2 = 2000 ; O_2 = 110	1	2	0.100	-
17	N_2 = 2000 ; O_2 = 150	1	2	0.100	-
18	N_2 = 1000 ; O_2 = 150	1	2	0.100	-
19	N_2 = 1000 ; O_2 = 300	1	2	0.100	-
20	N_2 = 1000 ; O_2 = 500	1	2	0.100	-
19	N_2 = 1000 ; O_2 = 1000	-	2	0.100	-
20	N_2 = 500 ; O_2 = 1000	-	2	0.100	-
21	O_2 = 1000	-	2	0.100	-

Table 12. Drying conditions of preform OVD0023.

T [K]	ΔT [K·min^{-1}]	Gas Flows	Rotation [RPM]	Feed speed [m·min^{-1}]	Retraction speed [m·min^{-1}]
1315	10	He/Cl_2 ratio = 16.66	3	0.010	0.025
1848	10	He = 2000 sccm	3	0.005	Up to cool

Table 13. Dehydration and consolidation parameters of preform OVD0023.

EDX analysis of the outer layer of the soot was performed, and it is presented in Image 48. Molar concentrations of the chloride and oxide compounds is not possible to determine since the percentage of chlorine in the sample could be from Al or Yb compounds, in any possible combination with the oxides present.

Nevertheless, it is clear to appreciate the presence of each element by their weight contribution to the sample which was determined to be: Al = 10.71wt% and Yb = 26.64wt%. On the other hand, it was possible to calculate the presence of SiO_2 = 43.55mol%.

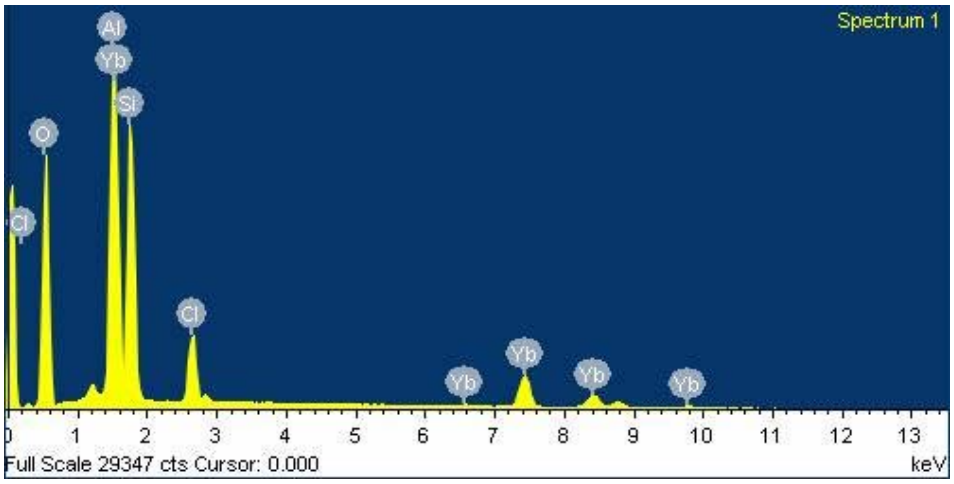

Image 48. EDX spectrum of preform OVD0023 after solution doping.

After dehydration and consolidation processes an opaque preform shown in Image 49 was obtained. EDX analysis of the consolidated preform was carried out on the outer surface of the preform. Molar concentrations were calculated to be: Al_2O_3 = 25.77mol%; Yb_2O_3 = 4.77mol%; and SiO_2 = 69.46mol% (see Image 50).

Image 49. Preform OVD0023 after the consolidation process.

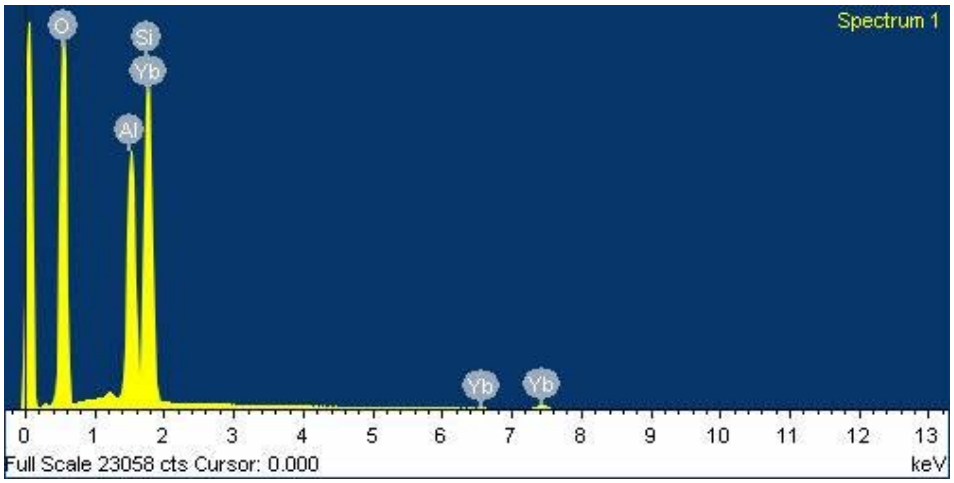

Image 50. EDX spectrum of preform OVD0023 after consolidation.

High-temperature treatment was performed, but the glass preform remained its opaque appearance. The preform was then collapsed at a much higher temperature on an MCVD lathe resulting in an extremely high radiance and finally yielding a ~12mm diameter solid rod shown in Image 51. Bubbles along the preform were observed.

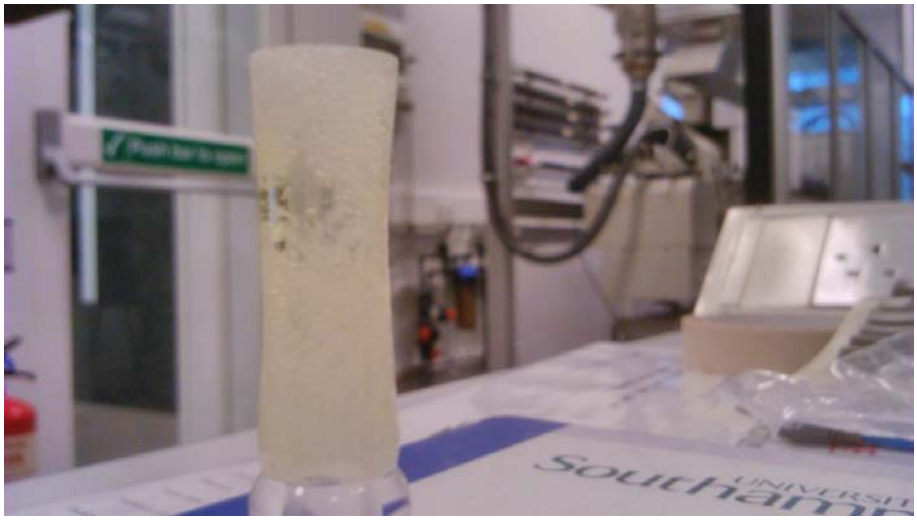

Image 51. Preform OVD0023 after the collapsing process.

EDX analysis of the preform cross-section was carried out on the preform after high temperature treatment. Molar concentrations were calculated to be: Al_2O_3 = 0.84 mol%; Yb_2O_3 = 1.79 mol%; and SiO_2 = 97.37 mol% (see Image 52).

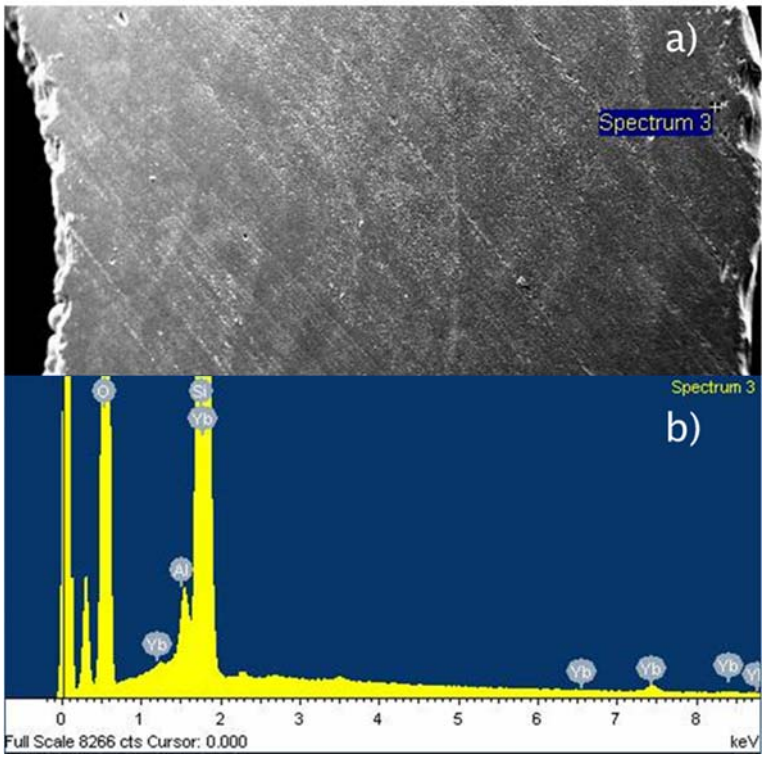

Image 52. Preform OVD0023 after high temperature treatment; (a) SEM micrograph and (b) EDX spectrum.

The preforms were drawn into fibres for their characterisations. The fibre fabrication process is described in the following section.

8.1.2 Aluminosilicate glass fibres

To evaluate the characteristics of a glass preform, a suitable fibre should be fabricated for characterisations such as efficiency, RIP, absorption, OH content, losses, etc.

An ultrasonic drilling process can be used to extract the inner section of the pre-form as shown in Image 53; this process is advantageous when the outside of the preform has some defects or when a specific section of the preform needs to be avoided, e.g. bubbles, scratches and fissures.

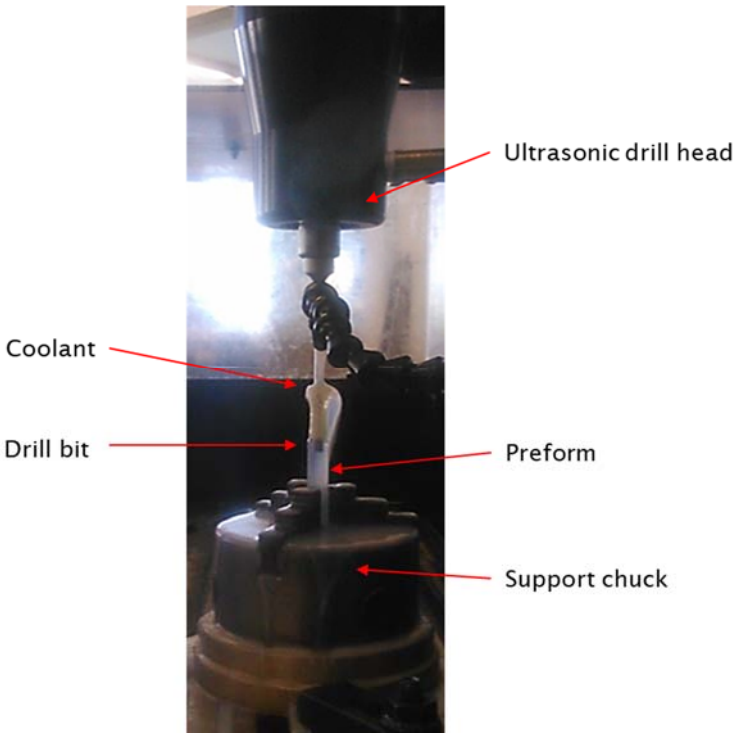

Image 53. Ultrasonic drilling process.

Depending on the final size of the preform, or the size of the central part obtained from the drilling process, a subsequent rod-in-tube process may be required. This operation is carried out by inserting the solid preform into a high-quality substrate tube as shown in Image 54; then, to prevent the preform from falling, a disposable solid rod is attached to the end, working as a bottom seal of the assembly. Finally, the assembly is placed in the fibre drawing tower, and it is processed into a fibre.

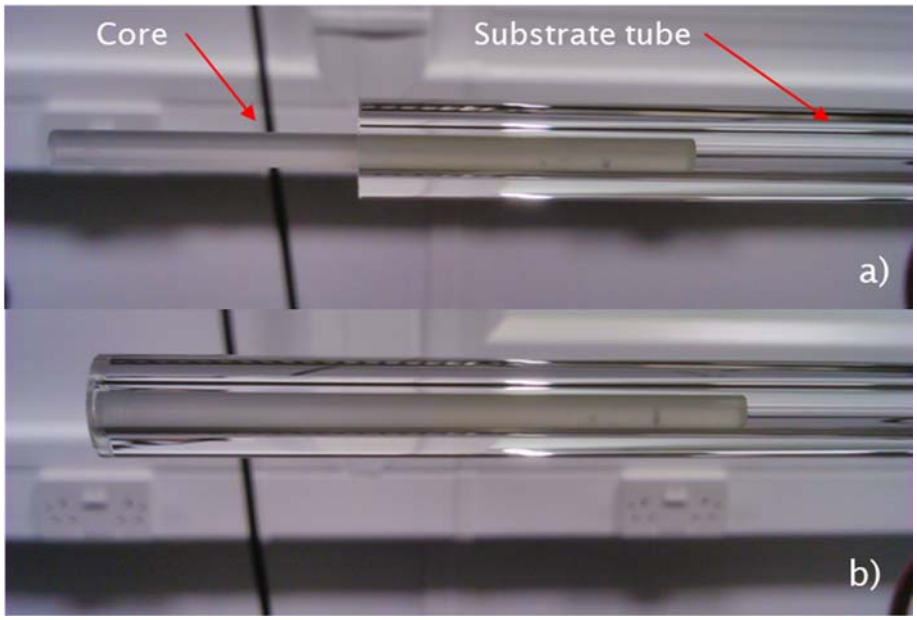

Image 54. Rod-in-tube technique; a) assembly components, and b) final assembly.

8.1.2.1 Aluminium

Core-drilling removed the central region of OVD0026. The Ultrasonic mill was used to remove the central part of the preform and then it was inserted into a high-quality substrate tube. Afterwards, it was drawn into a 125µm diameter fibre, A0519_OVD0026. The refractive index profile of the fibre shown in Graph 52 presents a negative step index change; the value of $\Delta n = -5 \times 10^{-4}$ corresponds to the refractive index contrast of a pure silica deposition made by the OVD process. The diameter of the core section of 37.7 µm is in line with the preform/fibre ratio expected for the 3.5mm OVD deposited core diameter. A difference in the contrast of the cross-section (see Image 55) shows the boundaries of the core region and the F-300 glass used during the rod-in-tube technique.

The evidence suggests that the aluminium chloride used for the doping process was evaporated due to exposure to high temperatures before the oxidation process. Evaporation of dopants can happen if the samples were heated at high temperatures in an inert atmosphere or without enough oxygen flow.

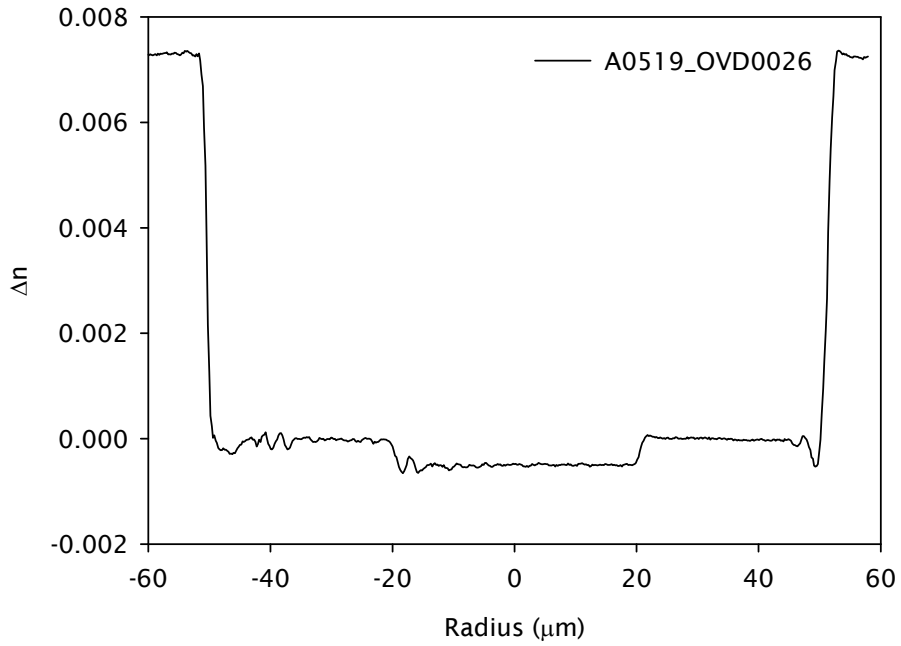

Graph 52. Refractive index profile of fibre A0519_OVD0026.

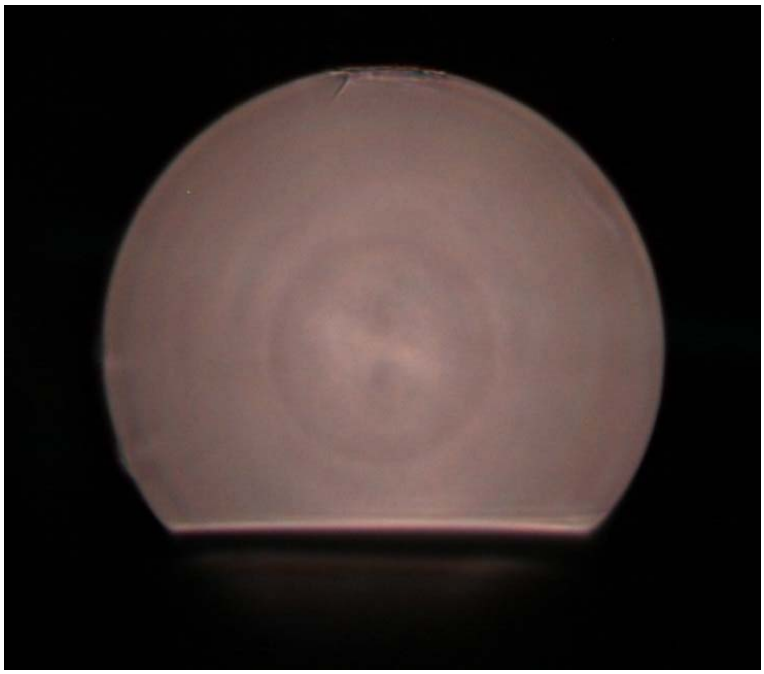

Image 55. Optical microscope image of the cross-section of A0519_OVD0026.

8.1.2.2 Aluminium - Ytterbium

Preform OVD0023 was also processed by ultrasonic drilling and then sleeved in an F-300 tube. Afterwards, it was drawn into a 125μm diameter fibre, A0522_OVD0023. The fibre profiler model S14 measured the refractive index. The

Graph 53 a) presents a value of $\Delta n = 3.6 \times 10^{-4}$, which corresponds to the refractive index contrast of the OVD deposited core. The diameter of the core section of 37.7 μm agrees with the preform/fibre ratio expected for the 3.5mm core diameter.

An off centred peak value of $\Delta n = 14.1 \times 10^{-4}$ is noticeable on the FRIP, corresponding to the refractive index contrast of the central part of the deposited preform. Since the preform was post-processed by ultrasonic drilling, the centre of the original preform is not located in the centre of the fibre.

The fibre profiler S14 software allows the possibility to generate refractive index profiles focusing on the highest Δn. The measurement can be based on the peak value. Graph 53 b) presents the plot generated by this technique; a peak value of $\Delta n = 0.010$ is evident from the FRIP. A difference in the contrast of the cross-section in Image 56 a) shows the boundaries of the deposited core region and the F-300 tube, while Image 56 b) shows the bright spot corresponding to the off-centred Δn peak that was measured.

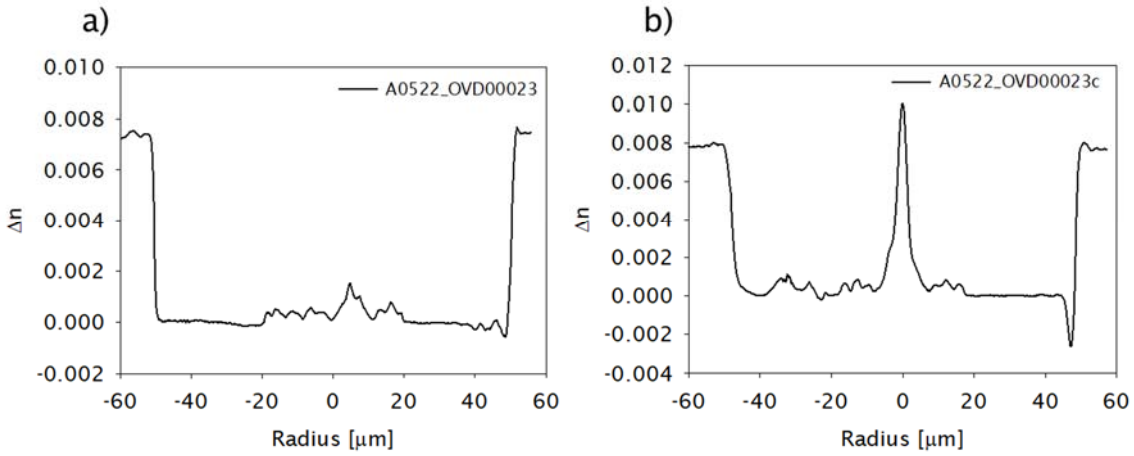

Graph 53. Refractive index profile of fibre A0522_OVD0023; a) profile centred by the diameter and b) profile centred by the highest refractive index change.

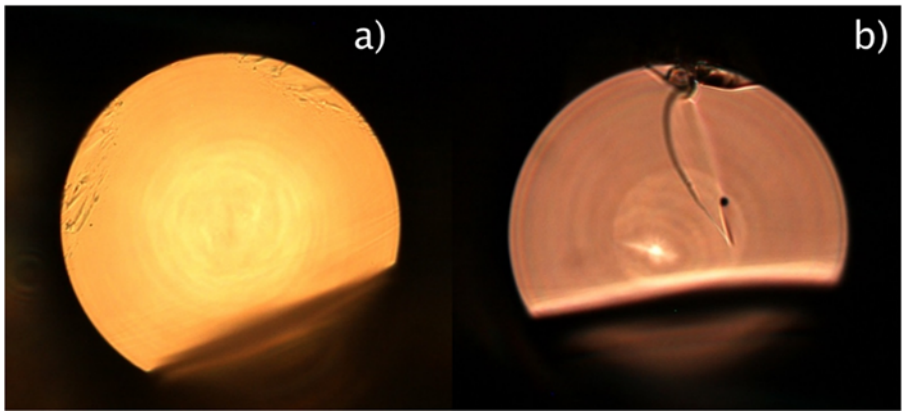

Image 56. Optical microscope image of A0522_OVD0023; a) cross-section and b) shows the bright spot of the high refractive index change peak.

Absorption measurements were carried out using a WLS and an OSA. The spectrum obtained from the wavelength range of 600 nm-1500 nm presented in Graph 54 shows the Yb^{+3} absorption at ~920 nm, and a concentration of ~23,750 ppm has been calculated.

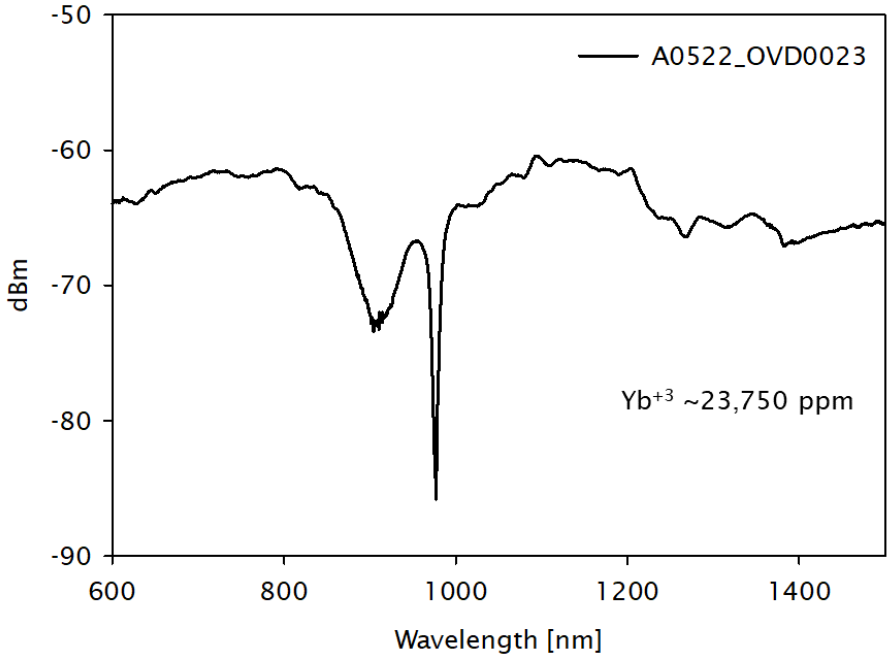

Graph 54. Ytterbium absorption of A0522_OVD0023.

Fibre losses could not be measured due to the cladding pump design of the fibre. The low index coating of the fibre was not suitable for loss measurement. The measurement would capture the transmission characteristics of the cladding and absorptions from the coating. Additional fibre drawing using hi-index coating are desirable in further developments to confirm the loss characteristics of the OVD Yb-doped aluminosilicate glass.

Fluorescence lifetime measurements were carried out using the setup presented in Figure 9. A narrow bandwidth 976nm laser diode with an acoustic optic modulator (AOM) in the laser path, driven by a wave generator attached to an oscilloscope. The fluorescence signal was captured by an InGaAs trans-impedance amplified photodetector.

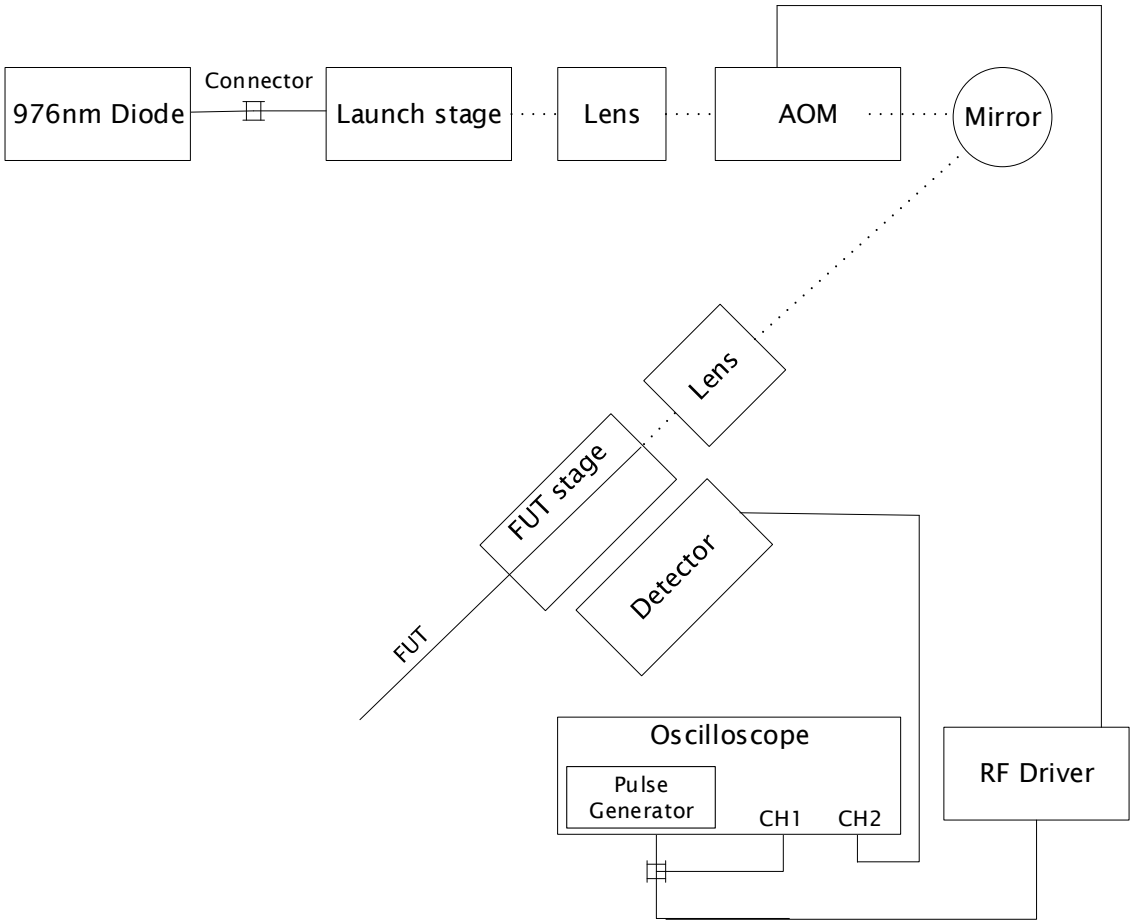

Figure 9. Lifetime free-space setup.

Preliminary lifetime measurements were carried out using a free space setup. An experimentally determined lifetime of ~750μs agrees with the silica fabrication group benchmark values for aluminosilicate Yb-doped fibres fabricated by solution doping technique.

Recent modifications in the OVD system allow the incorporation of Aluminium and RE-dopants offering a more stable process using an OVD modified solution doping technique. Graph 55 shows the FRIP of fibre A1044 using the more controlled and stable doping technique available for OVD preform fabrication.

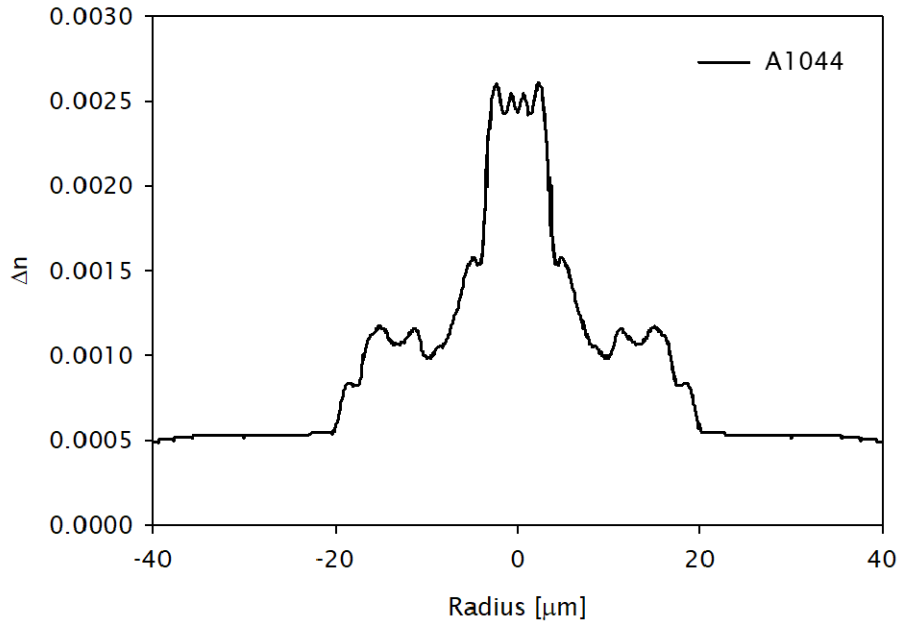

Graph 55. FRIP of OVD aluminosilicate fibre with pedestal.

Fluorescence emission from Yb^{+3} ions is observed when the sample is tested under the IFA-SEM. The fluorescence emission shown in Image 57 is an indication of RE incorporation in the glass matrix.

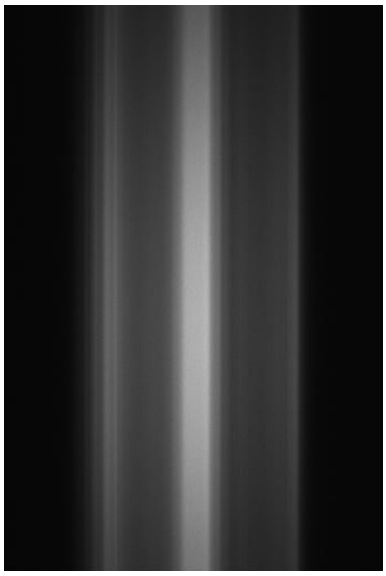

Image 57. IFA-SEM shows fluorescence of Yb^{+3} ions in the aluminosilicate glass.

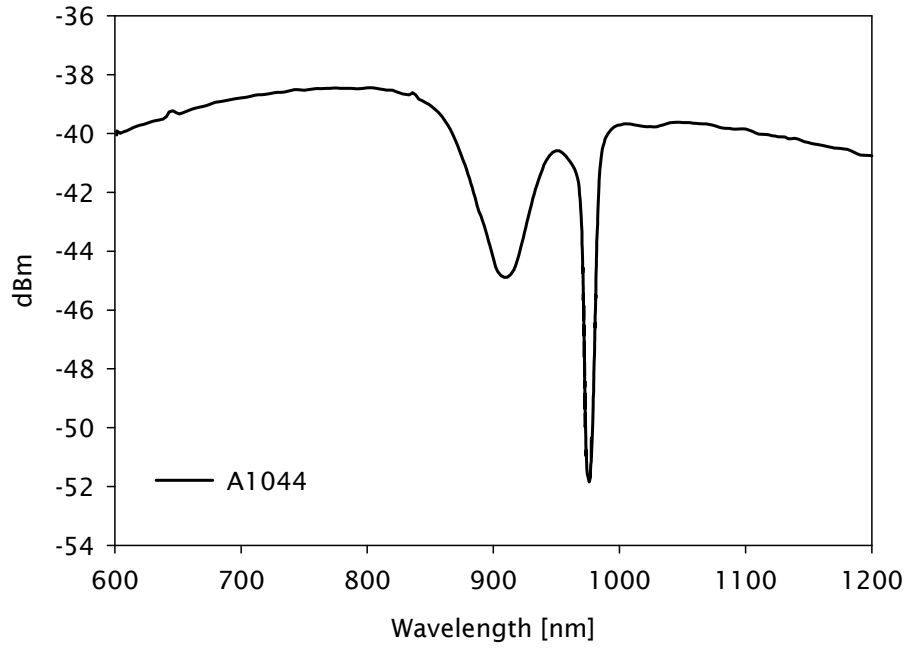

Graph 56. Absorption measurement of Yb^{+3} ions into the aluminosilicate glass.

Initial absorption measurements on the aluminosilicate glass samples shown in Graph 56 presents the characteristic absorption peak of Yb^{+3} at ~920nm and ~976nm wavelength in aluminosilicate glass. It has been demonstrated that the novel approach is effective for the RE dopants incorporation.

8.1.3 Conclusion

Conventional solution doping on OVD preforms still requires refinement. Modified solution doping directly into the torch seems to offer more uniformity on the way the dopants are incorporated. The process still requires minor adjustments to prevent preferential depositions in the layer interfaces. Additional investigations using high index coatings are required to determine the transmission loss of the aluminosilicate glass. This work shows that the OVD process is capable of fabricating aluminosilicate glass in a wide range of compositions either without RE dopant or incorporating RE ions through Solution Doping (SD) or Modified Solution Doping (MSD).

Chapter 9 Phosphosilicate Glass

9.1 SiO_2/P_2O_5

Phosphosilicate glass, when doped with rare earths, is critical in the fibre lasers industry, and especially for high power applications. Perhaps its resistance to photodarkening would be its most significant attractiveness in addition to its broader absorption bands and emission towards longer wavelength compared to aluminosilicate RE-doped fibres. Phosphorus is also frequently added to the silica preforms for improve the transmission characteristics below 1μm or to build up pedestal structures in double and triple clad structures.

Image 58. OVD burner with $POCl_3$ and $SiCl_4$ flows.

It is widely known that incorporating phosphorous into OVD and VAD processes, using a precursor such as $POCl_3$, is challenging to achieve and can also lead to undesired reactions in the flame. The improved OVD process developed during this research project allows the combination of phosphorous and silicon halides as

shown in Image 58. Similar to the depositions mentioned in Chapter 7, the temperature of the burner is required to be reduced minimising the evaporation of phosphorous dopant during the preform build-up process.

Initial experimental work on the phosphosilicate glass was focused on developing the glass. A preform was fabricated using low phosphorous flow to achieve a minimum refractive index contrast. After the consolidation process, the transparent and defect free preform was drawn into a cane. Graph 57 shows the RIP from a cane drawn from a phosphosilicate OVD preform. This deposition presents an ultra-low NA of 0.027. The capability to achieve low and medium refractive index changes open the possibility to use phosphosilicate glass as a substrate for conventional MCVD deposition or to jacket a different glass composition.

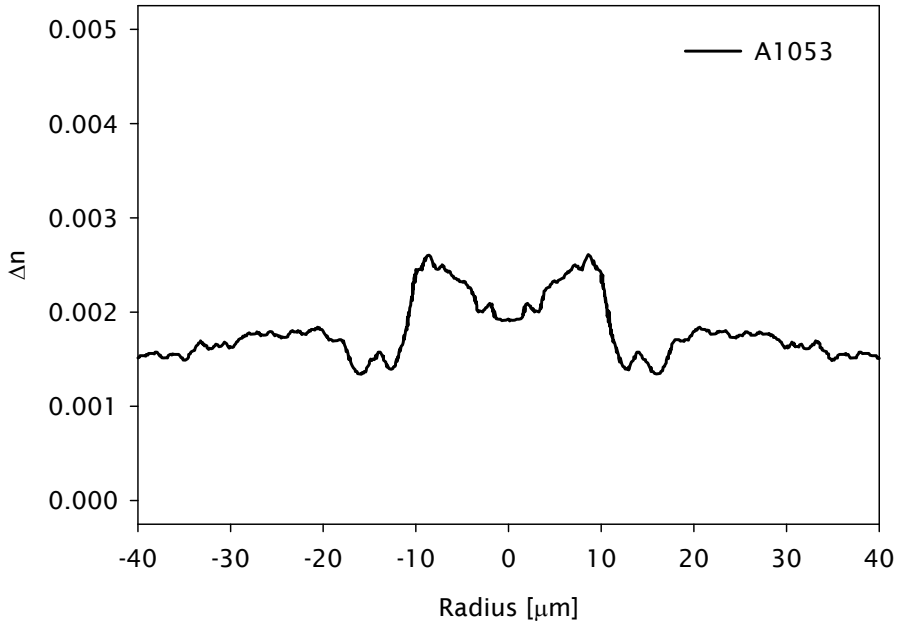

Graph 57. RIP of an ultra-low NA phosphosilicate cane.

The developed capability of using passive phosphosilicate claddings can be a turning point on the way large pedestal preform designs are fabricated. Potentiality using this glass, the cladding can be adjusted to any particular NA, allowing to match the core refractive index and tailor the way the high order modes will be leaked out of the fibre for high power laser applications.

Dehydration and consolidation parameters were also adjusted using the experimental conditions from Chapter 7 as a starting point.

9.2 $SiO_2/P_2O_5/Yb_2O_3$

Adding RE-dopants to phosphosilicate glass fabricated by OVD process is a crucial development in the way optical preforms are currently fabricated. Using the development described in this section, it is possible to tailor pedestal structures and ultra large core fibres which currently cannot be fabricated with the traditional processes. Elliptical cores and limited uniformity are an example of the challenges this improved process can overcome.

As mentioned in section 9.1, the capability of using phosphorous and silicon halides together is a unique capability developed on the ORC system. It gives a competitive advantage in research capabilities, product development and of course collaborative research with the photonics industry.

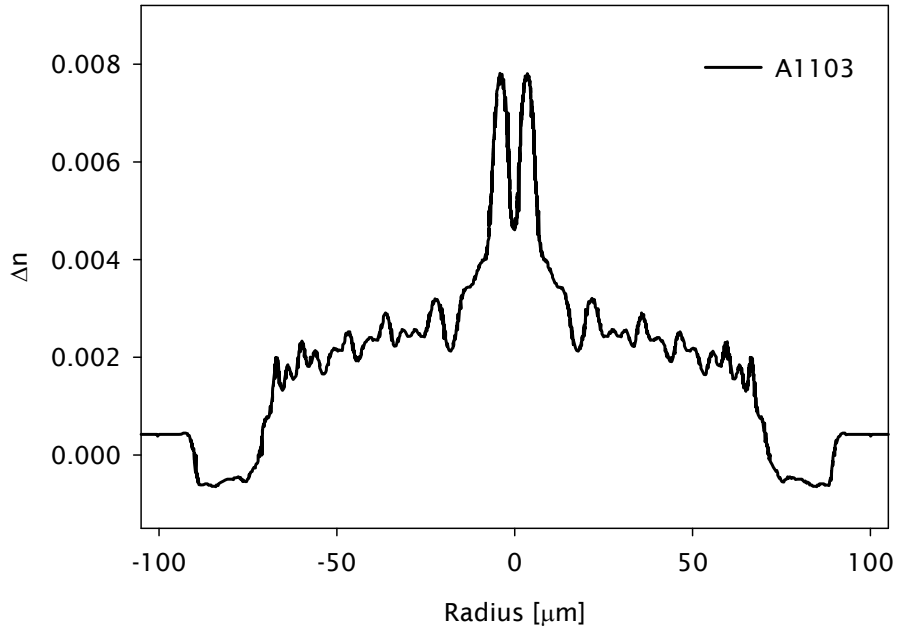

Graph 58. FRIP from an ORC-OVD Yb-doped phosphosilicate sample.

OVD modified solution doping performed the RE incorporation. After consolidation, the transparent and defect free preform was drawn into a fibre. The FRIP shown in Graph 58 was obtained by using the IFA.

This sample has a sizeable pedestal-like feature which demonstrates not only the capability to build the pedestal structure; but, also demonstrates the capability for manufacture large core preforms. For this sample, the pedestal-like area is also doped with RE. At the centre of the profile, the characteristic central dip for phosphosilicate preforms is evident.

The two-dimensional refractive index profile in Graph 59 shows the circularity of the final fibre. The circular profile of a large core/pedestal phosphosilicate fibre is only possible to achieve by using OVD fabrication. Differences between the viscosity of the substrate tube glass and the glass from the deposition layers are the main reason for non-circular cores and pedestal structures when fabricated by MCVD. Since OVD preform growth happens in soot form; in both core/pedestal and cladding, the viscosity difference does not have a significant impact on the circularity of the final preform and fibre.

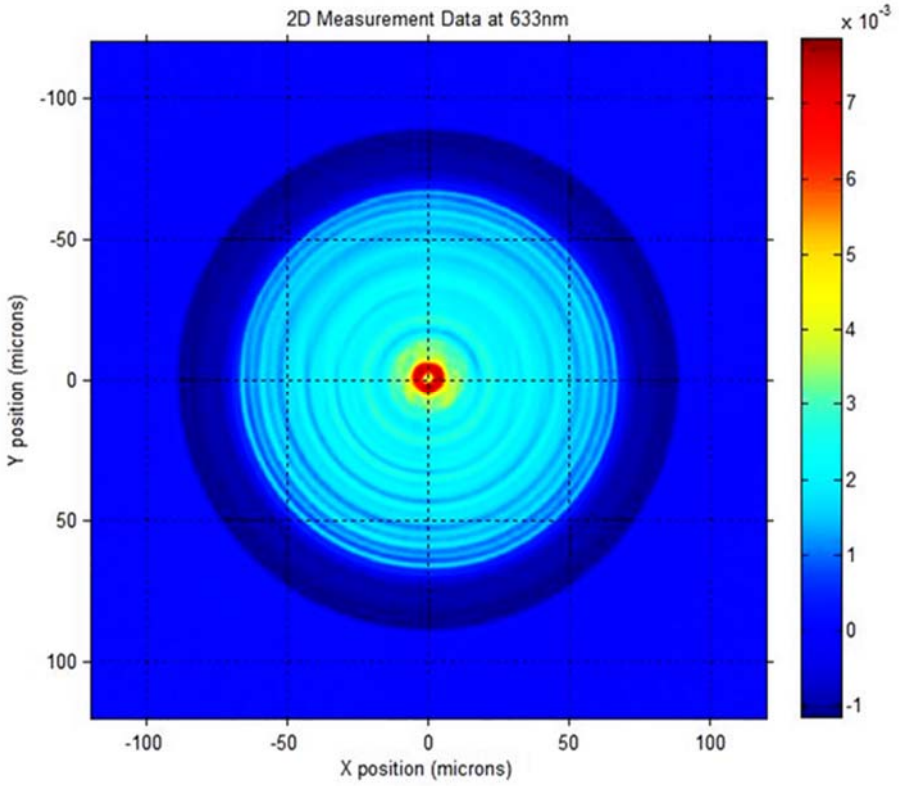

Graph 59. Two-dimensional FRIP of an ORC-OVD Yb-doped phosphosilicate fibre.

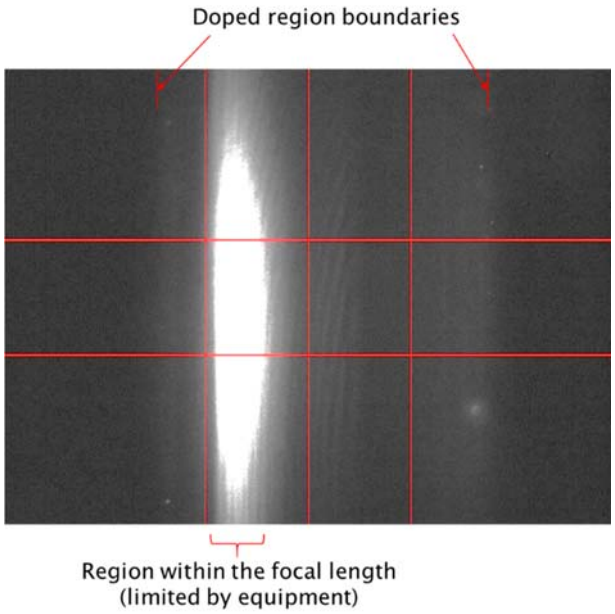

Image 59. Stimulated emission of Yb ions (IFA-SEM) on large core OVD Yb-doped phosphosilicate fibre.

Stimulated emission measurement from the IFA shown on Image 59 cannot resolve the large core measurement due to focal length limitations between the lenses and the CCD camera that collects the emission from the samples. Nevertheless, the fluorescence emission from the Yb^{+3} is a clear indication of the incorporation of Yb into the glass and provide a reference to its distribution.

9.3 $SiO_2/P_2O_5/GeO_2$

Phosphosilicate glass doped with germanium is a typical component of the pedestal structures on the optical preforms and fibres used mainly for high power applications. The use of the pedestal structure allows us to tailor a low NA of the waveguide when the core has a significant refractive index difference with respect to the cladding.

The inner cladding structure enables the possibility of using single-mode conditions on a highly doped fibre. Pedestal structures can also be part of a heat management design by selectively controlling the modal propagation in the fibre.

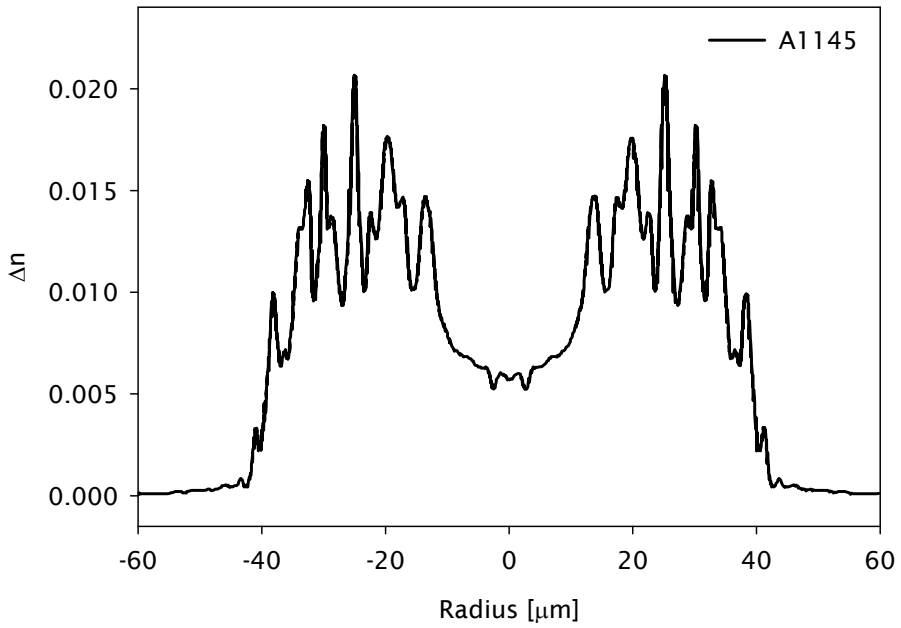

Graph 60. FRIP of a pedestal structure fabricated using $SiO_2/P_2O_5/GeO_2$ glass.

Phosphosilicate glass doped with germanium was successfully deposited and later consolidated to obtain a pedestal structure with pure silica cladding. Preforms were drawn, and its refractive index profile is presented in Graph 60. The ripples in the FRIP are an indication of the multiple layers used during the deposition stage.

Deposition ripples can be reduced by optimising the deposition conditions and when the deposition is drawn into a more significant preform to fibre ratio. The fibre presented on Graph 60 has a central region of approximately 24μm where the core region is expected to be. To obtain the FRIP shown in Graph 60, the central region was filled with index matching oil.

9.4 Conclusion

Phosphosilicate glass fabricated by OVD, either passive or active have a wide range of applications primarily in the fibre laser industry. Large core fibres and higher dopant concentrations can now be achieved, minimising the current limitations faced by other processes such as MCVD-SD or MCVD-CDS. Due to the nature of the OVD process, the viscosity mismatch between materials that provoke elliptical cores has been overcome.

Additionally, it is also possible to eliminate the use of additional phosphorous flow during the MCVD collapsing preform process. This operation is commonly used to compensate for the evaporated phosphorous content. Nonetheless, this is also the

main reason for abnormal distribution on the RE-dopant and unexpected changes on the deposited glass refractive index.

Depositions of pure phosphosilicate glass or doped with germanium have been successfully demonstrated. Also, depositions in the form of pedestal structures using a range of phosphosilicate glass have been successfully demonstrated.

Chapter 10 Additional Projects

10.1 Thulium-doped Fibres Spectroscopy

Investigations of fluorescence lifetime, absorption and fluorescence emission were performed on thulium-doped fibre made in-house. The experimental setups and the parameters used on the spectroscopies are presented in this section. Fibres were fabricated by members of the silica group including Prof. Jayanta Sahu and Deepak Jain. The characterisation and analysis of the fibres were conducted by the author.

Thulium–doped fibres have been studied for its potential application in the 2-micron region. However, the spectroscopy of this rare-earth has unique characteristics. The main feature of the thulium-doped fibres is that they can exhibit a phenomenon known as two-for-one cross-relaxation. The two-for-one cross relaxation happens when one ion is excited to a higher energy level, and a second ion is excited by the energy released during an initial stage of deactivation without fluorescence. Finally, both ions return to the ground state by releasing one photon each and emitting at the same wavelength.

The particular characteristics of the thulium ions had attracted the interest of researchers around the world to understand its spectroscopy and the effect of the glass host and doping concentration[13-15,92,93].

10.1.1 Fluorescence lifetime

The selected pump wavelength for the lifetime measurements was 1565 nm. Two different setups were used: a tuneable laser source (TLS) with an erbium-doped fibre amplifier (EDFA); and a narrow bandwidth laser diode. Both setups use an acoustic optic modulator (AOM) driven by a wave generator attached to an oscilloscope. The fluorescence signal was captured by an InGaAs trans-impedance amplified photo-detector.

Although two different laser sources were used, the fluorescence lifetime measurements from the two measurements did not differ. The same values of fluorescence lifetime were obtained from the setups of Figure 10 and Figure 11.

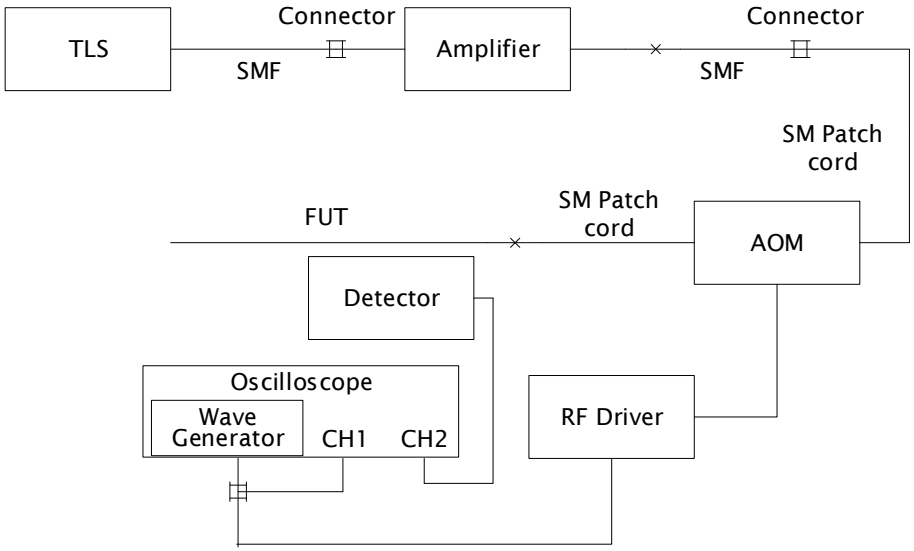

Figure 10. Lifetime setup using a tuneable laser source with an EDFA.

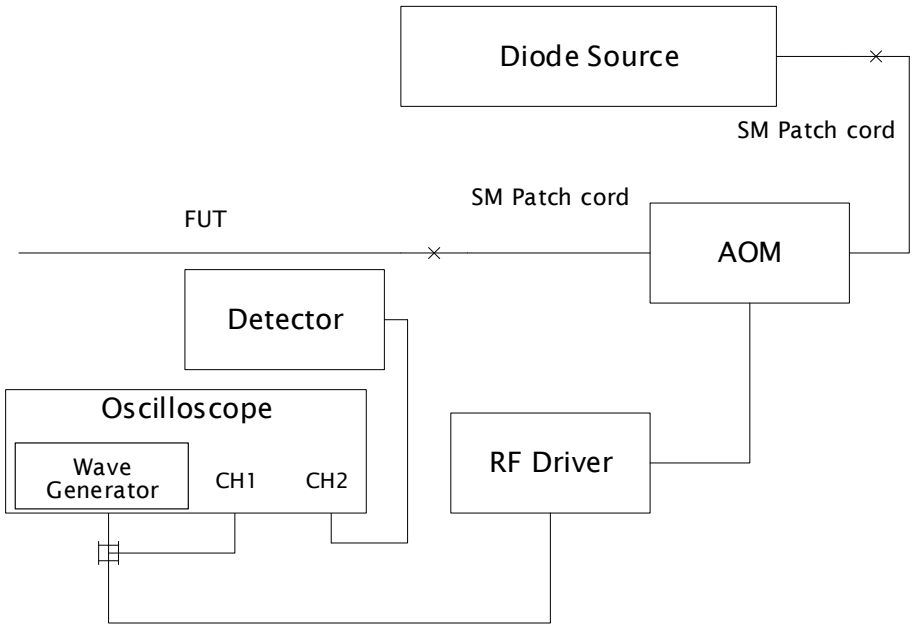

Figure 11. Lifetime setup using a narrow bandwidth laser diode.

The pulse period and pulse width used in the wave generator during the lifetime measurements were 50 ms and 10 ms respectively. The experimental data were processed and fitted into a stretched exponential decay mathematical model expressed by Equation 12.

$$a * exp(-(b * x)\text{^}p\ ) + c$$

Equation 12. Stretched exponential decay.

Due to the experimental setup and electronics limitation, there is an offset between the ground level of the measurements and the ground level of the instrument. Nevertheless, the mathematical model takes this offset into account as a constant term added to the end

The fluorescence lifetime values of the in-house thulium-doped fibres analysed have been summarised in Table 12.

Fibre	Lifetime [µs]
A0017_L30267	366
A0204_L10128	415
A0269_L10164	347
A0275_L10179	350
A0282_L10187	312
A0300_L10191	340
A0331_L30273	582
A0338_L10232	300
A0350_L10232	438
A0352_L10238	334
A0371_L10238	331

Table 14. In-house thulium-doped fibres lifetime values.

The fluorescence lifetime decays of the thulium-doped fibres investigated in this section are shown in Graph 61.

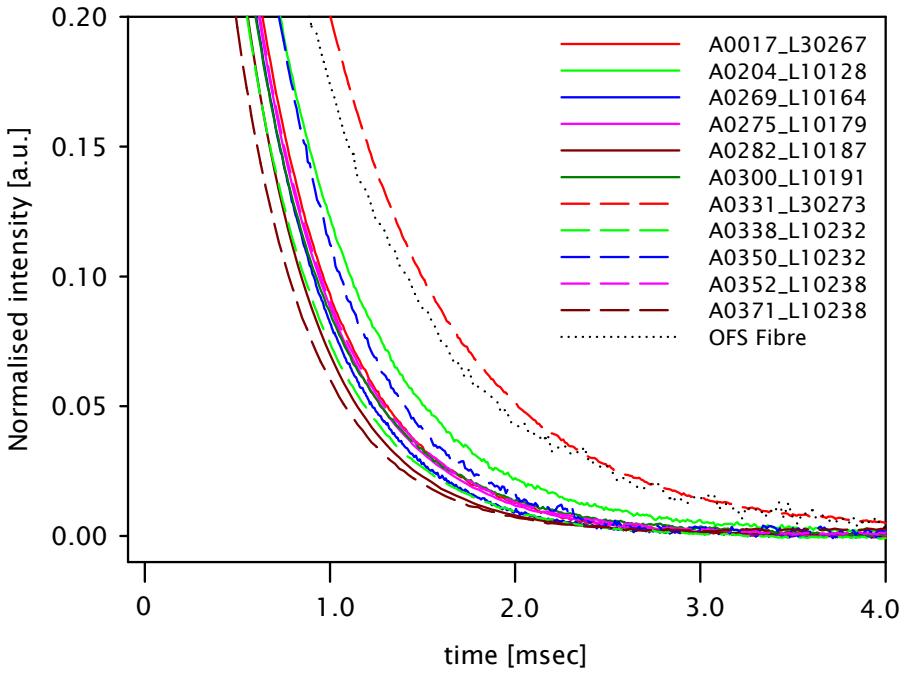

Graph 61. In-house thulium-doped fibres + OFS reference fibre.

The differences in the lifetime values are mainly related to the difference on the amount of dopants fixed into the silica matrix; for the in-house fibres, the dopants

are Al and Tm. Two doping techniques were used during the preform fabrication processes. Table 15 shows which fibres were fabricated with each type of doping technique.

Doping Technique	Fibres
Gas phase + Solution doping	A0017_L30267
	A0338_L10232
Solution doping	A0204_L10128
	A0269_L10164
	A0275_L10179
	A0282_L10187
	A0338_L10232
	A0350_L10232
	A0352_L10238
	A0371_L10238

Table 15. Characterised fibres sorted by doping technique.

Table 16 presents the amount of each dopant in the solution used when the preforms were fabricated.

Fibre	$AlCl_3$ [g]	$TmCl_3$ [g]
A0204_L10128	40	3
A0269_L10164	40	10.25
A0275_L10179	45	6.2
A0282_L10187	45	10.25
A0300_L10191	40	3
A0338_L10232	45	10.2
A0350_L10232	45	10.2
A0352_L10238	45	10.2
A0371_L10238	45	10.2

Table 16. Solutions used in the thulium-doped fibres fabrication.

EDX measurement in the fibres was performed to identify the core composition. The samples were prepared carefully by stripping the coating and cleaving a flat surface in the fibres. The cleaning procedure included the use of acetone, and finally, samples were coated with ~50nm of carbon for conductivity purposes. Table 17 contains the calculated mol% composition of the thulium-doped fibres, in the core region.

Fibre	Core composition [mol%]				
	O	Al	Si	Cl	Tm
A0017_L30267	66.42	2.33	31.06	0.02	0.18
A0204_L10128	67.27	2.96	29.63	-	0.14
A0269_L10164	66.41	3.23	29.91	0.01	0.45
A0275_L10179	66.36	2.48	30.97	-	0.20
A0282_L10187	66.70	1.84	31.51	0.04	0.27
A0300_L10191	63.77	1.08	35.09	-	0.07
A0331_L30273	64.25	6.34	29.29	-	0.13
A0338_L10232	67.03	4.01	29.38	-	0.52
A0350_L10232	68.34	2.68	28.53	0.01	0.44
A0352_L10238	64.04	3.53	31.90	-	0.55
A0371_L10238	65.70	3.11	30.59	0.03	0.58

Table 17. Core region composition in mol% of Thulium-doped fibres.

It is not possible to establish a relationship between the dopant concentrations and the lifetime values independently. Other fabrication parameters were studied as a possible source of the variability observed in the lifetime, but no consistency was found. Graph 62 shows the fluorescence lifetime values obtained.

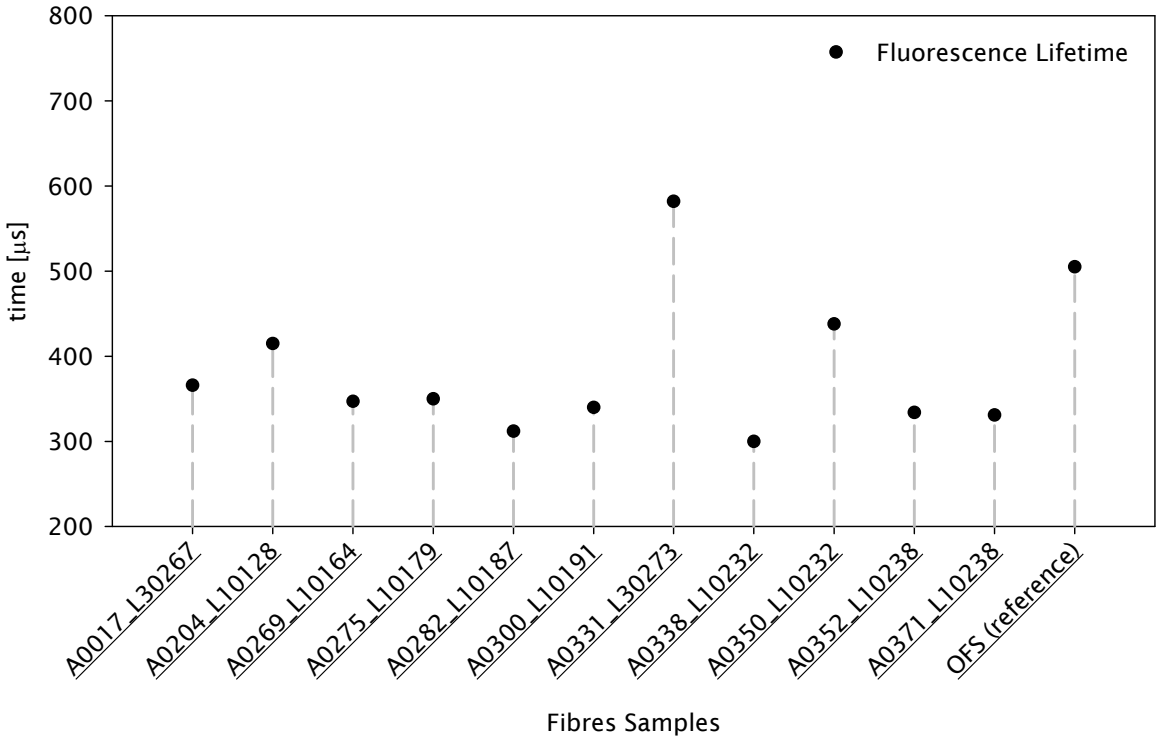

Graph 62. Fluorescence lifetime values.

However, a two variables correlation exhibited in Graph 63 explains the behaviour of the fluorescence lifetimes observed in the in-house thulium-doped fibres.

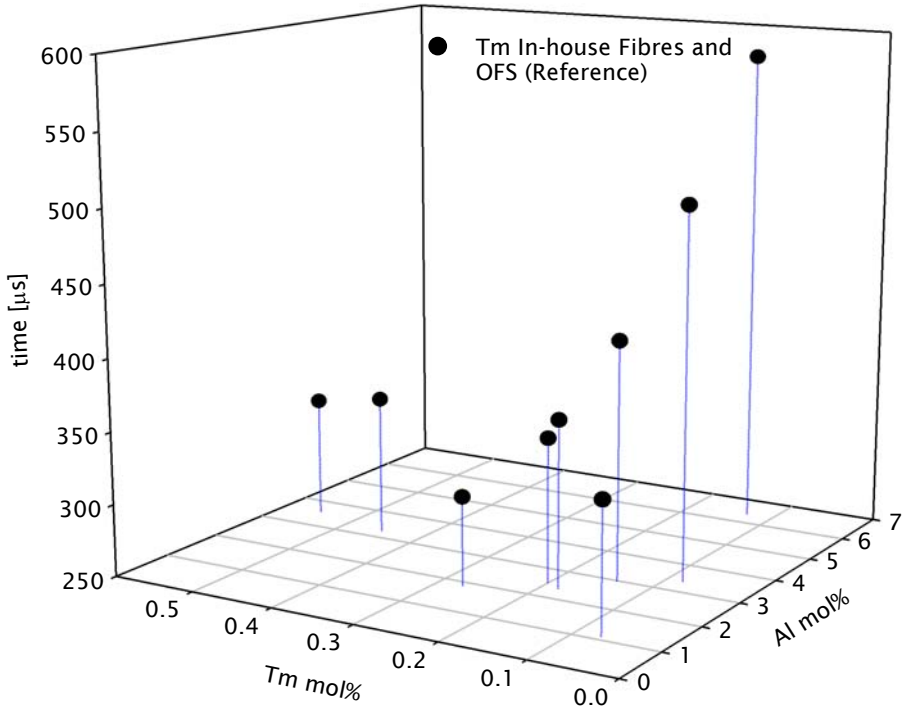

Graph 63. Two variables correlated with the lifetime.

Based on the previous two variables relation, the model proposed in Graph 64 has been established. Nevertheless, the model requires future experimental work to validate the accuracy of the model, since it is only based on the current available data.

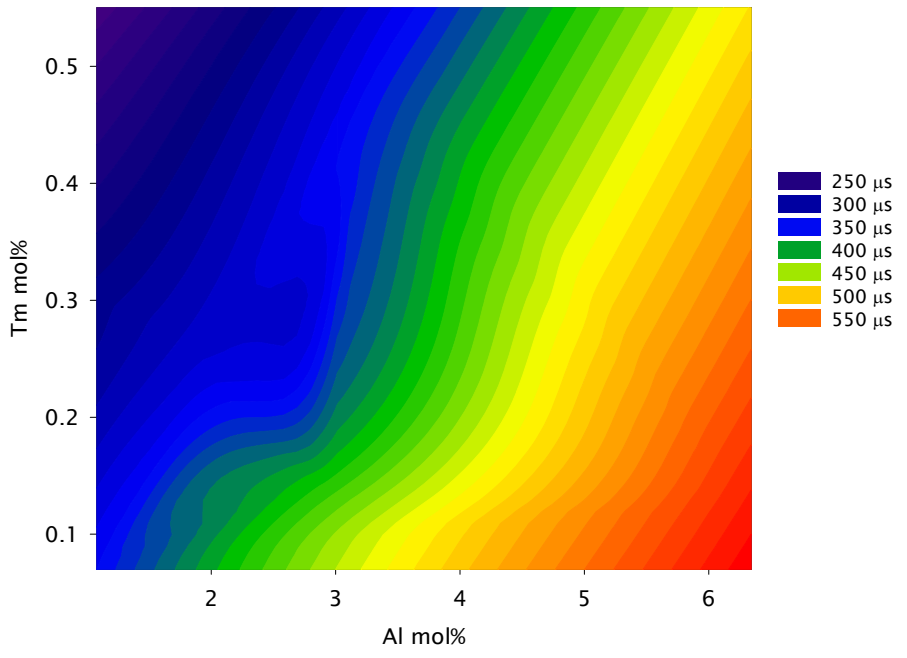

Graph 64. Proposed two variables model for lifetime as a function of Tm and Al.

10.1.2 Absorption

The absorption measurements have been obtained using a WLS and an OSA as described by the setup diagram shown in Figure 12:

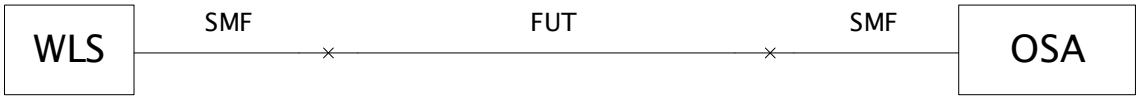

Figure 12. Absorption setup.

The data collected from the OSA has been processed. Graph 65 correlates the absorption values and thulium concentration into the silica matrix within the in-house fibres.

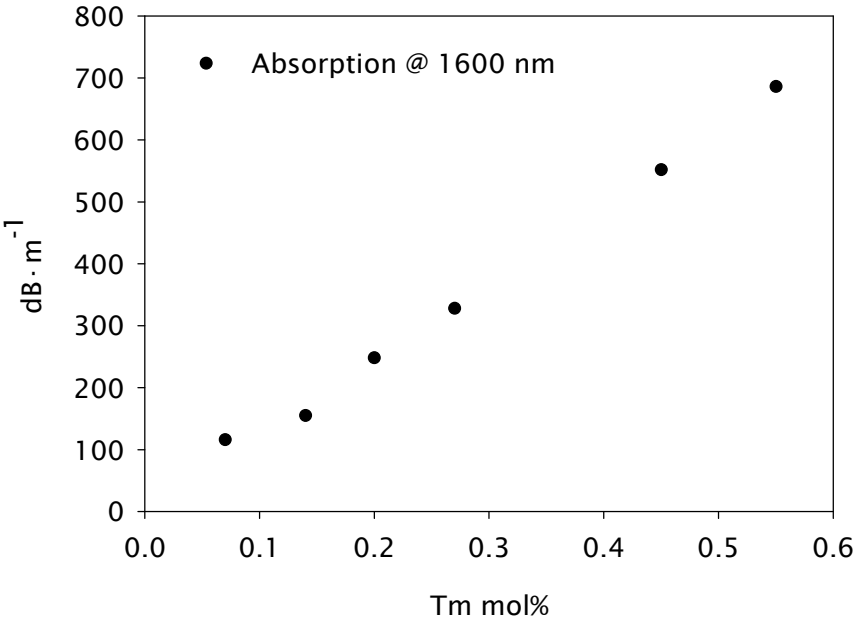

Graph 65. Absorption as a function of thulium concentration.

10.1.3 Emission (fluorescence)

Emission or fluorescence measurements have been obtained using an indirect technique which involves the use of an auxiliary fibre (only glass) to collect the emission around the FUT, then the signal transported by the auxiliary fibre was measured by an OSA.

The same 1565 nm wavelength previously used for the lifetime measurements has been employed for the emission measurements. Two different setups have been utilised: a TLS, followed by an EDFA shown in Figure 13; and a narrow bandwidth laser diode shown in Figure 14.

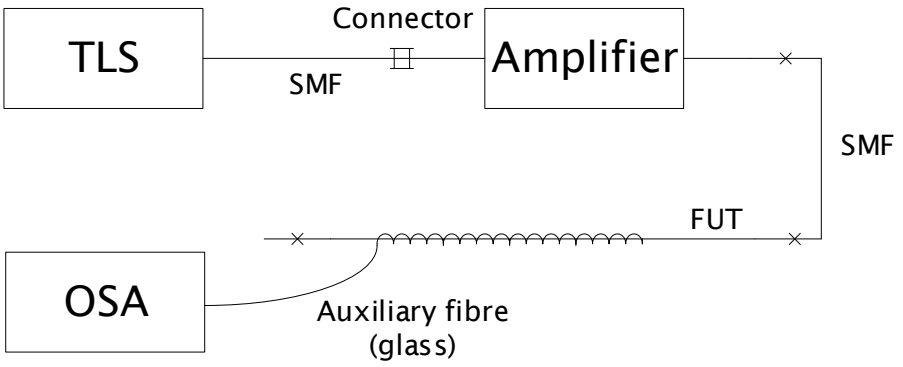

Figure 13. Emission setup using a TLS and an EDFA.

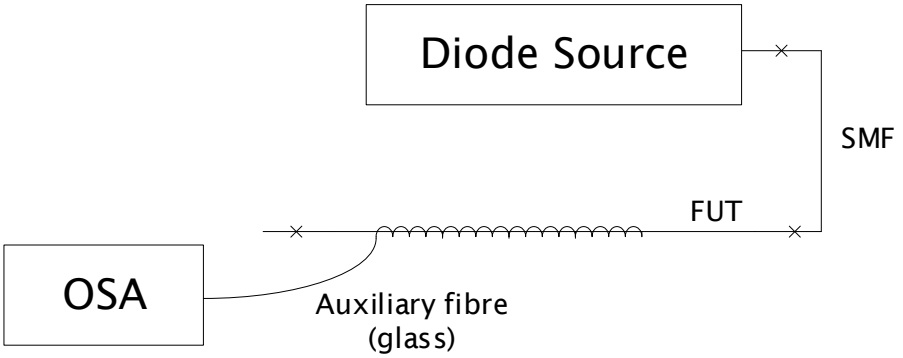

Figure 14. Emission setup using a narrow bandwidth laser diode.

Graph 66 shows the differences in the emission spectra from using the two laser sources, in which the signals acquired from the TLS + EDFA presents a residual lower broader emission due to the EDFA bandwidth. However, those residual signals (<30dB) were neglected for this study.

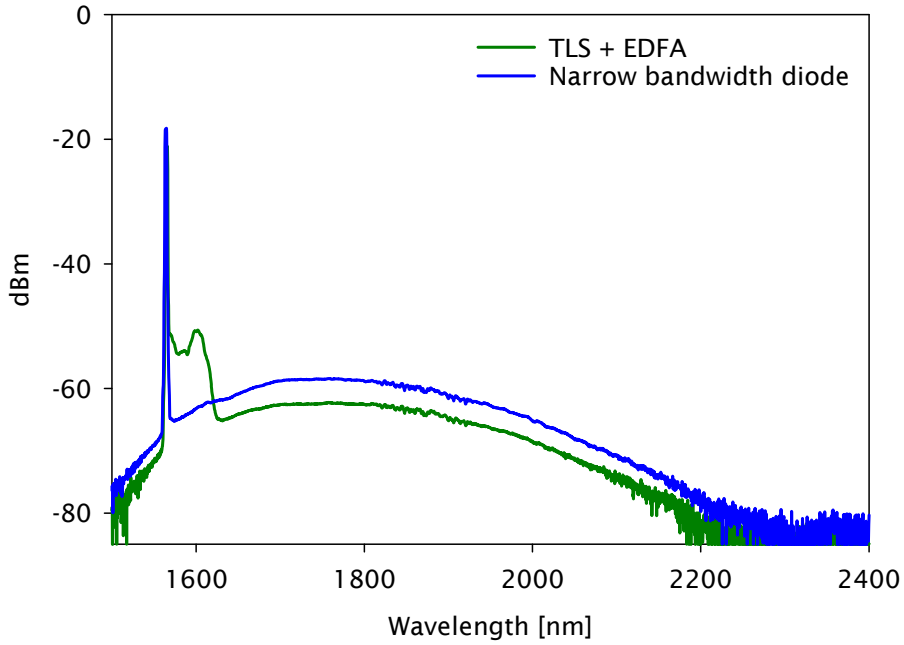

Graph 66. Comparison of emission spectra from different laser sources used for lifetime measurements.

10.1.4 Emission and absorption cross-section

The acquired information has been processed to determine the emission and absorption cross-sections. The method to determine the emission and absorption cross sections used in this work was the F-L equation shown in Equation 13.

The F-L equation is commonly used for calculating the emission and absorption cross-sections of laser gain media.

$$\sigma_{=} \frac{\lambda^5 I(\lambda)}{(8\pi n^2 c \tau_{rad}) \int \lambda I(\lambda) d\lambda}$$

Equation 13. Füchtbauer–Ladenburg equation[94].

Separating the equation into single terms, the numerator factors are already known: λ = wavelength, I = Intensity of the absorption or the emission, depending on the case. The denominator seems to be more complicated, but most of the terms are also known: n = refractive index, c = speed of light in vacuum, τ_{rad} = radiative lifetime, which is constant for these specific fibres with a value of 4.5 ms. Finally, the integral term is based on the intensity measurements of the absorption or the emission, as applicable.

The determined absorption cross-section of the fibre has been plotted in the Graph 67.

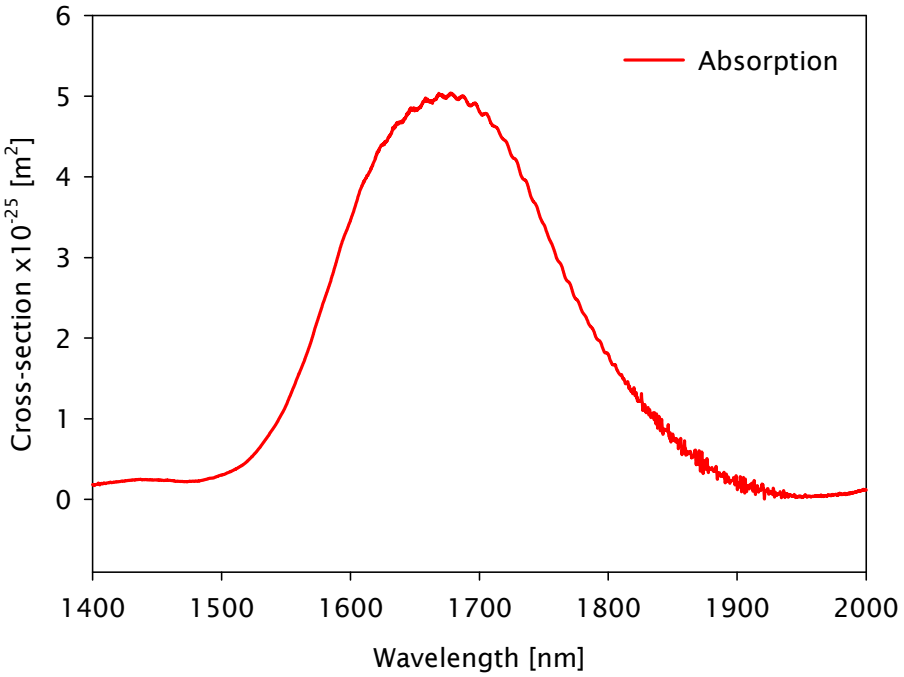

Graph 67. Absorption cross-section.

Once determined the emission cross-section of the fibre, it has been plotted in the Graph 68.

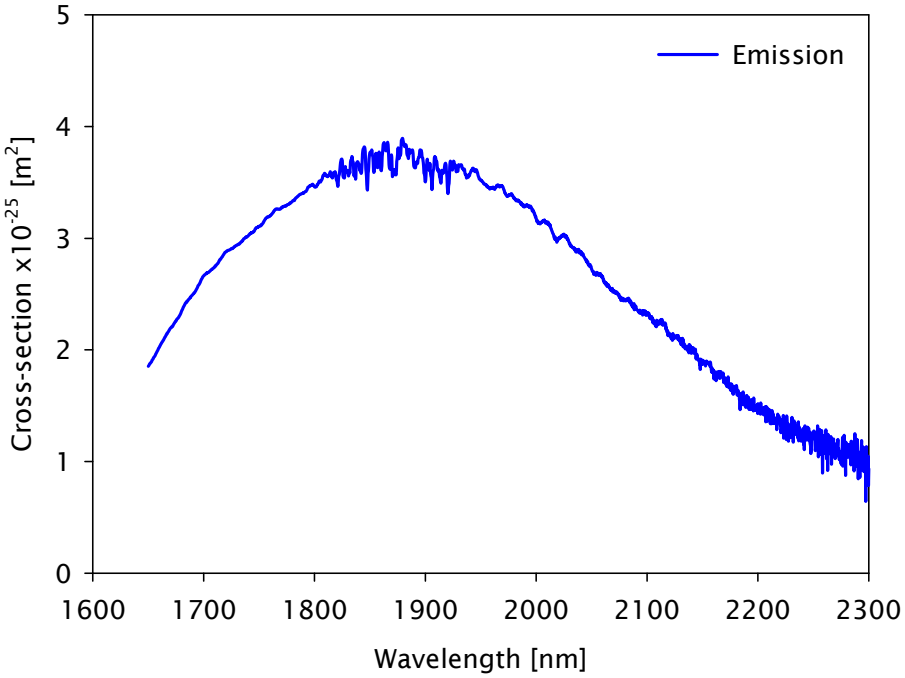

Graph 68. Emission cross-section.

Finally, both graphs are plotted together in Graph 69 where it is possible to appreciate the overlapping between the emission and absorption curves for this experiment.

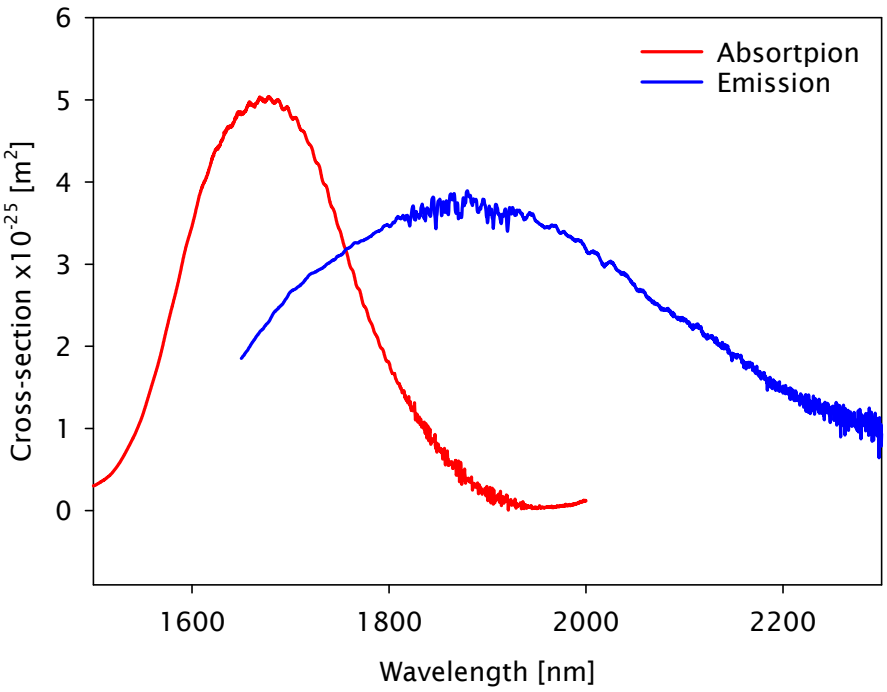

Graph 69. Emission and absorption cross-section.

10.1.5 Conclusion

The information acquired from the spectroscopy study suggests that for a high concentration of thulium, lifetime tends to be limited. It can be explained by the quenching of the thulium ions leading to a non-fluorescence deactivation process.

The samples containing higher aluminium concentration have increased fluorescence lifetime values. It is expected because the aluminium acts as a cluster suppressor allowing a better and more uniform distribution of the dopant into the glass matrix.

In order to achieve high thulium concentrations without suffering from quenching, the core composition must have a high concentration on aluminium and allow a homogenous dispersion of the rare-earth ions.

Further fabrication of thulium doped fibres is required to extend this study by increasing the concentrations of aluminium and keeping the thulium concentration fixed. Conversely, a set of fibres is required using a fixed high concentration of aluminium and varying the concentration of thulium.

10.2 Chelate Deposition System

This section has contributions from Andrey Umnikov and Norberto Ramirez on the MCVD preform fabrication and Pranabesh Barua on the fibre drawings for some of the samples. Additional fibre drawing and the analysis in the section are contributions from the author.

10.2.1 Introduction

The CDS system offers the capability to delivery RE-dopants via gas phase. The system has the capability to be used either in MCVD and OVD processes. The gas phase incorporation of network modifiers can also be achieved by using the CDS. During preform fabrication, substantial incorporation of network modifiers helps to improve the lifetime of the RE dopant. The fibres fabricated through gas phase presented on section 10.1 had improved compared to the traditional solution doping fibres.

Gas phase deposition offers the possibility of increasing the incorporation and therefore the concentration of dopants in the core region in comparison with traditional solution doping.

MCVD is commonly used with standard solution doping allowing the incorporation of glass matrix modifiers such as Al_2O_3 to prevent clustering of the rare earth ions. In order to increase the rare-earth concentration, it is also required to incorporate more Al into the glass.

Unfortunately, the conventional solution doping technique has its limitations. Increasing the concentration of the solution increases its viscosity making it more difficult for the solution to penetrate into de deposited soot. By only using solution doping it is challenging to obtain concentrations above 3.5 – 4 mol%. Moreover, defects in the interface between core and cladding start appearing due to viscosity mismatch between glass compositions[95].

Combining the deposition of Al by gas phase and Tm using solution doping is a feasible approach to overcome this limitation. This approach provides the capability to use high aluminium content and high purity rare-earth precursors for the preform fabrication having a better dispersion of the dopant in the core.

10.2.2 Experimental results

Lifetime measurements on Yb-doped aluminosilicate fibres drawn from preforms fabricated by MCVD-CDS were compared with fibres from preforms fabricated by MCVD-SD. Graph 70 shows the increased lifetime obtained on samples fabricated by CDS compared to conventional SD samples.

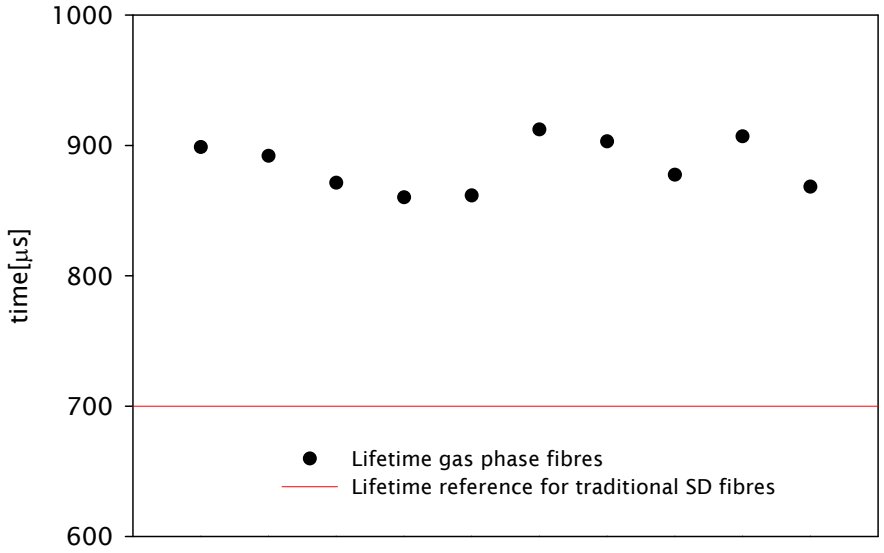

Graph 70. Increased lifetime in Yb:Al fibres fabricated by CDS.

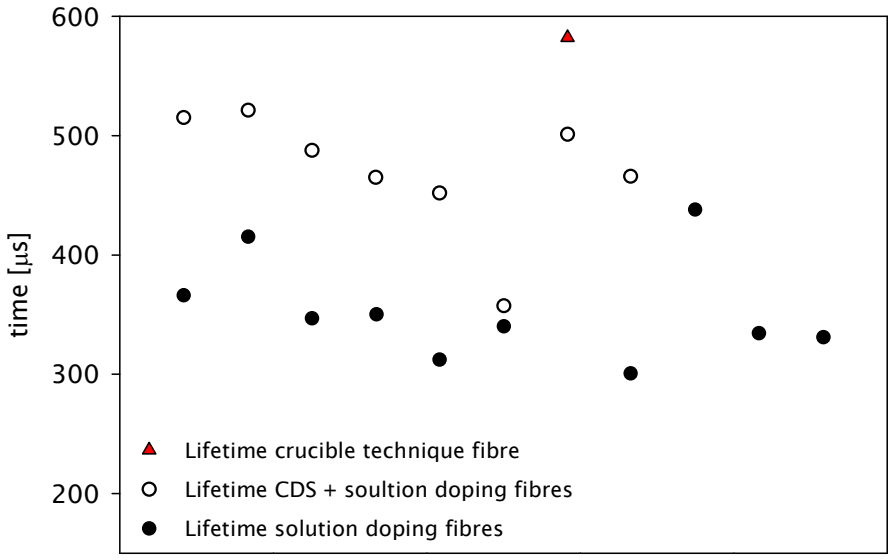

Graph 71. Increased lifetime in Tm:Al fibres fabricated by Hybrid process.

A hybrid process between gas-phase and solution doping has been explored, and it had proved that it also contributes towards longer lifetimes. The approach was experimentally tested on aluminosilicate Tm-doped fibres. Graph 71 shows the

general increment on lifetime values measured in the fibres fabricated using a hybrid process compared to traditional solution doping and crucible technique.

10.2.3 Conclusion

The gas phase deposition using a CDS system still requires refinement. Large core depositions can be achieved. However, the difference in viscosity between the substrate glass and the deposited layers start to be a significant issue as the concentration on aluminium or phosphorous increases.

With high concentrations non-circular and irregular shapes in the core region limit the amount of aluminium or phosphorous that can be incorporated, which also has an impact on the amount of rare earth that can be incorporated without suffering from ion clustering.

Potential cross-contamination between rare-earths at ppm level, in addition to carbon contamination of chelate precursors is an additional drawback of this technology. Precursors used in solution doping are readily available in the market with purity levels of 6N.

The experimental results presented in Chapter 8 and Chapter 9 are feasible alternatives with the potential to overcome the current limitations on large core fabrication. OVD RE-doped preforms can be produced with large core volumes maintaining its circular geometry. Also, it helps to increase the preform to fibre ratio on large core fibres designs.

OVD preforms can be fabricated from a single or multiple glass compositions without suffering from viscosity mismatch. Additionally, if required, single glass core compositions can be over jacketed in a secondary process with pure silica deposition giving the freedom to fabricate almost any core to cladding ratio requirements.

10.3 Hydrogen barrier

This section has contributions from Andrey Umnikov on the MCVD preform fabrication and Austin Taranta in a part of the optical characterisation. The preform assemblies, post-processing, fibre drawing, part of the optical and thermal characterisation as well as preforms and fibre characterisations, data processing and data analysis are from this researcher authorship.

10.3.1 Introduction

A hydrogen diffusion barrier in optical fibres is required to overcome the losses as a result of the absorption band of molecular hydrogen. Absorption band of molecular hydrogen attenuate the signal transmitted through the optical fibre due to wavelength overlapping. Diffusion of molecular hydrogen into the fibre is the identified mechanism for this attenuation to happen. Therefore, a material with a lower hydrogen diffusion is required to protect the optical fibre for this attenuation[96-99].

10.3.2 Fabrication methods

This work proposed an alumina ring as hydrogen diffusion barrier and the four different fabrication approaches were follow to achieve the desired optical fibre design shown in Figure 15 are explained below.

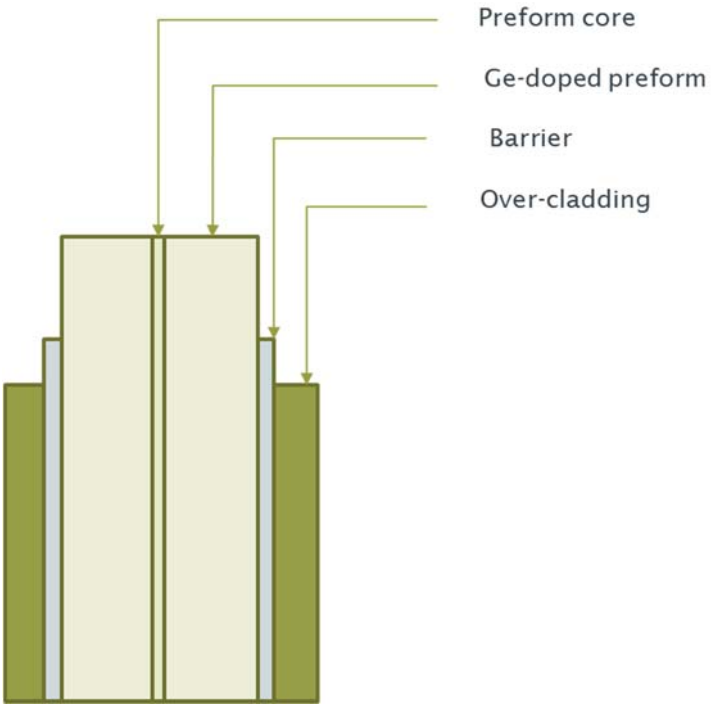

Figure 15. Schematic of fibre design with a diffusion barrier.

10.3.2.1 Alumina rich tube

The approach included a hybrid fabrication method using the conventional Modified Chemical Vapour Deposition (MCVD) system and a gas phase deposition system. The combination of these technologies allowed the deposition of a thin alumina-rich glass using gas phase technique. The amount of alumina was estimated to be ~20mol%, same that was measured by energy dispersive X-ray spectroscopy (EDX) shown on Image 60, assuming all the Al signal is from an oxide form.

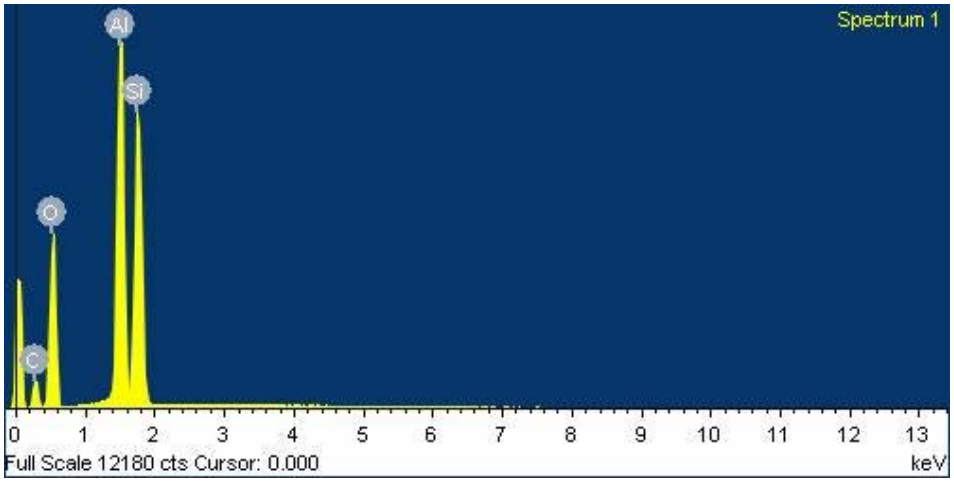

Image 60. EDX spectrum from the inner wall of alumina-rich substrate tube.

Optical measurements such as refractive index profile (RIP) were not possible to use for establishing the alumina content due to the well-known high stress of the layer that interferes with the readings. Graph 72 presents the effect of the stress on the preform refractive index profile

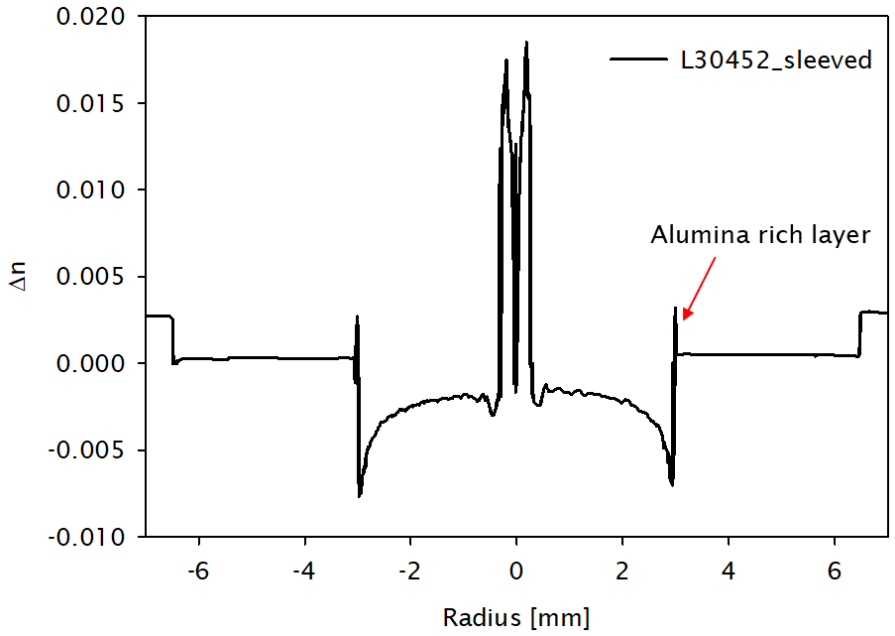

Graph 72. Refractive index profile of germanium-doped preform sleeved inside alumina rich substrate tube.

A subsequent sleeving process was performed inserting the optical preform into the tube with the alumina-rich layer. Finally, the preform was drawn to a standard 125µm fibre coated with acrylate DSM-314. The characteristics of the geometrical uniform ring were: a maximum thickness of 7µm at the base of the optical profile and a maximum change of refractive index of $\Delta n=0.008$; corresponding to a final ~4mol% of alumina content on the ring of the fibre. The fibre refractive index was measured in 1-dimension profile shown in Graph 73 and using de IFA a 2-dimensions profile shown in Graph 74.

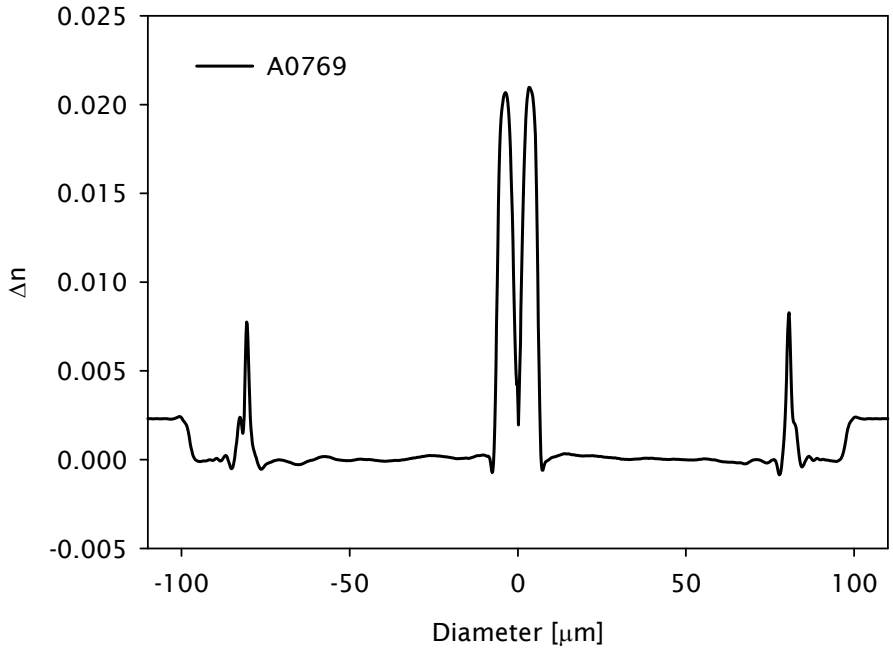

Graph 73. FRIP of single alumina ring fabricated by the gas phase deposition system and Ge-doped core.

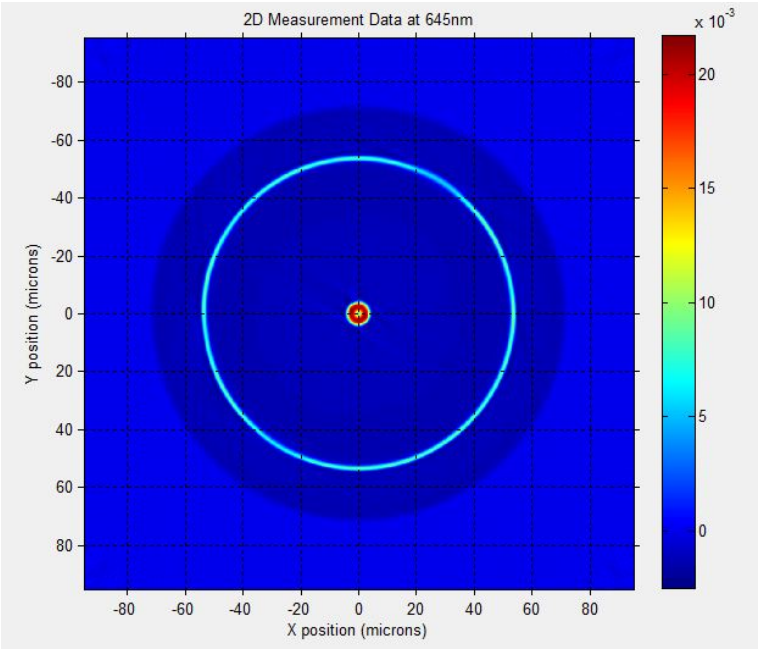

Graph 74. Two-dimensional FRIP of single alumina ring fabricated by the gas phase deposition system.

Unfortunately, by exposing the preform to high temperatures, the concentration of alumina in the interface zone decreases due to the diffusion mechanism into the surrounding silica host. Increasing the alumina content on the substrate tube was explored. However, the stress on the layer started to build up, and the deposited

layer started to shatter, this is due to the mismatch on thermal expansion coefficients between the materials.

10.3.2.2 Sapphire (100% Al_2O_3 single-crystal)

The use of sapphire as a high aluminium oxide source for the hydrogen barrier was explored. Initial experiments using the sapphire tube inserted in a substrate show that the main difficulty with this approach is to prevent the diffusion of the interface. Image 61 a) shows the irregular distribution of alumina-rich regions on initial trials.

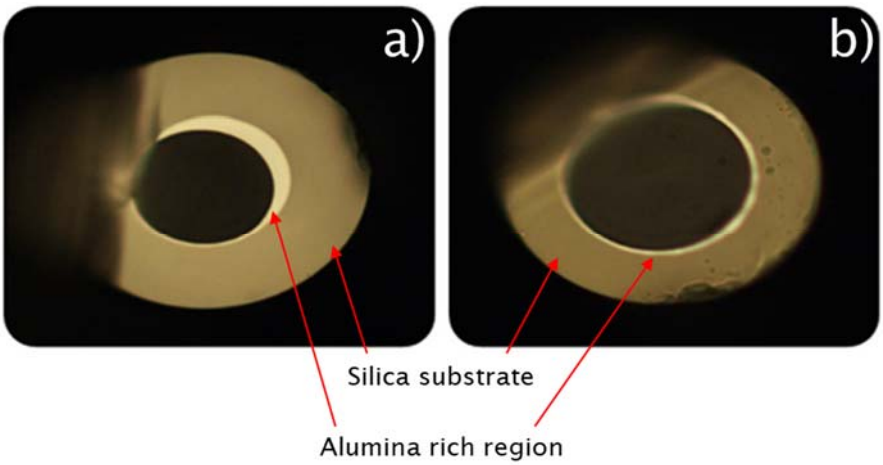

Image 61. Sapphire in silica fibres; a) irregular distribution and b) regular distribution

The irregular distribution of the alumina-rich region was controlled by optimising the drawing conditions, see Image 61 b). The approach involved the use of sapphire crystal substrates that are expensive and has a limitation on delivery time and length availability. Thus, no further experiments were carried out using this approach. Nonetheless, the material behaviour showed promising results that can be a potential alternative to achieve the highest alumina concentrations.

10.3.2.3 Sapphire-like structures

Alternatively, 98% alumina structures, readily available and low-cost ceramic based samples were used trying to achieve higher concentrations of alumina for the hydrogen barrier. This approach was using the sapphire-like structure on the surroundings of an optical preform, giving the structure a single heat exposure, reducing the diffusion mechanism. Nevertheless, the higher the alumina content, the

higher the materials mismatch and if the alumina-rich region is too thick, to the point that the fibre starts presenting signs of stiffness.

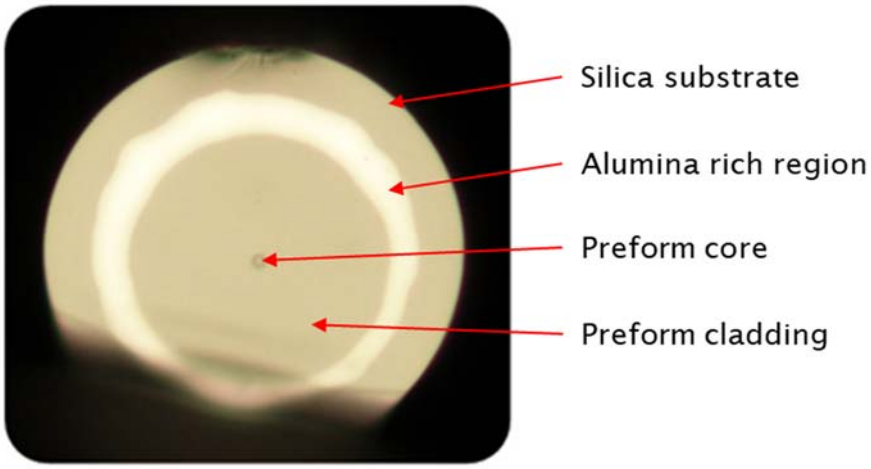

Image 62. Fibre with diffusion barrier fabricated using Sapphire-like structures.

It is important to consider that the diffusion mechanism is a dominant phenomenon in this type of process. The temperatures required for this process provoke a low viscosity silica host at temperatures where the sapphire-like structures start flowing. Increasing the viscosity of the silica glass; allows reducing the diffusion mechanism and increase the concentration where the sapphire-like structure is present, see Image 62.

Fibres obtained through this process achieved the higher alumina concentrations. The higher concentration was calculated to be ~34mol% with a refractive index change of $\Delta n=0.064$ shown in Graph 75.

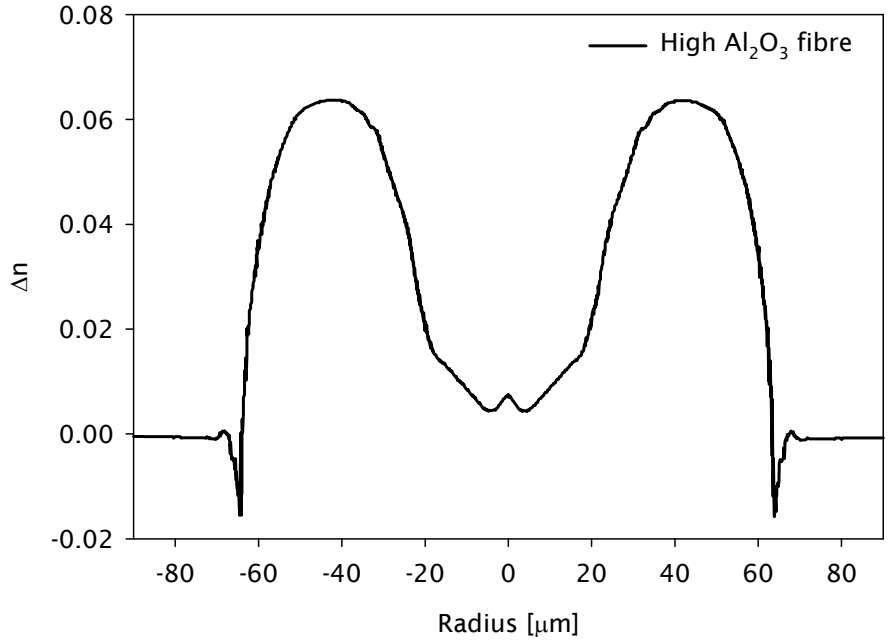

Graph 75. FRIP of high alumina concentration ~34mol%.

The limited viscosity of the sapphire-like material prevent to control the thickness of the ring, and it tends to be irregular in shape across the fibre. These irregularities can allow bubbles to get trapped inside the ring region.

10.3.2.4 MCVD – solution doping

Considering the challenges of the technology transfer, and the challenges faced on the previous fabrication processes; an alternative solution was explored using the fabrication techniques already adopted by the industry. The fibre design was based on the same principle of having an alumina-rich ring to stop or reduce the hydrogen diffusion. However, in this experimental approach, the preform is entirely fabricated by MCVD, without inserting the optical preform after the ring or inside the alumina-rich structure.

The fabrication process comprised the deposition of two barrier rings using the solution doping technique. After the first ring, a few layers of pure silica were deposited to separate the two barrier rings. Subsequently, a broad set of multiple layers of pure silica is deposited, and finally, the germanium doped core is fabricated. This approach involved multiple stages of solution doping aiming to increase the alumina concentration.

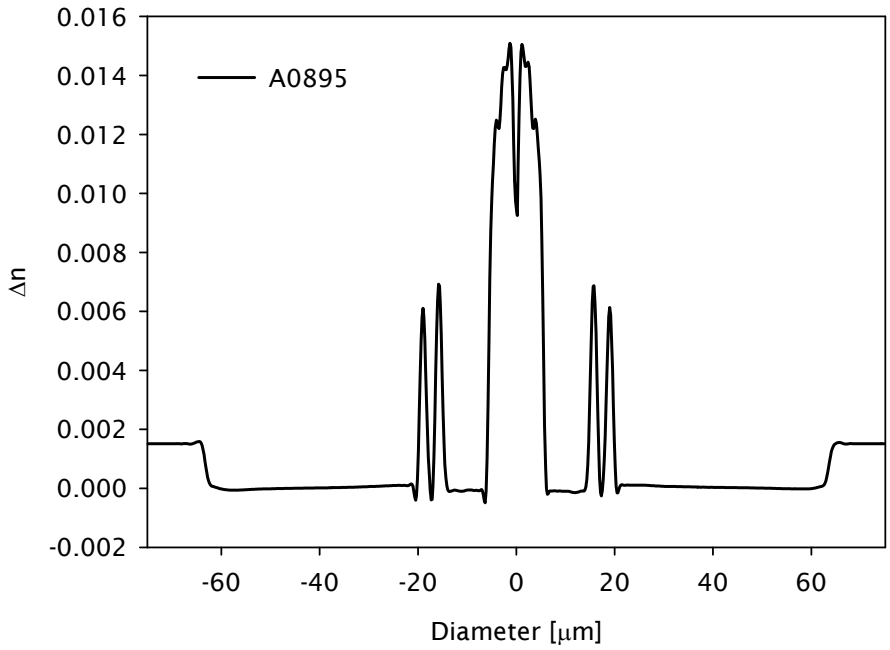

Graph 76. FRIP of dual alumina ring fabricated by multiple solution doping.

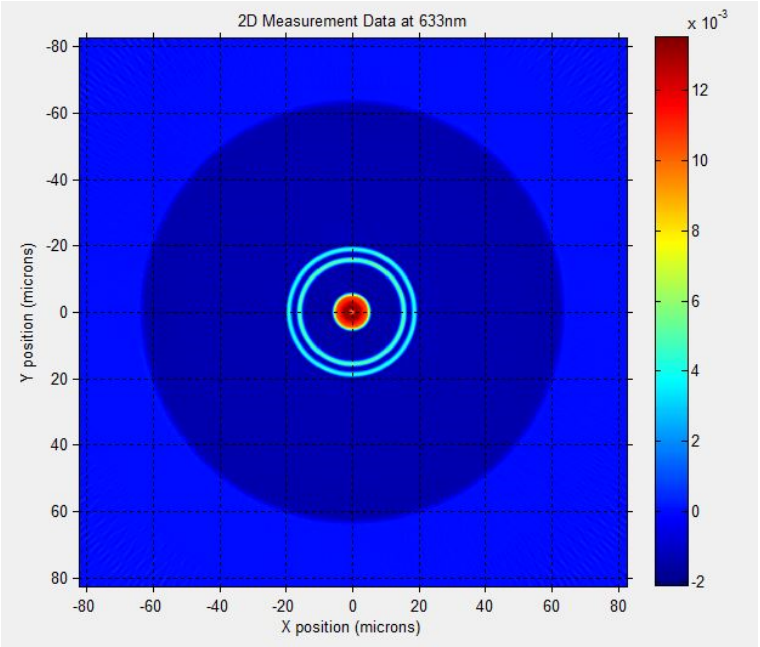

Graph 77. Two-dimensional FRIP of dual alumina ring fabricated by multiple solution doping.

Well-defined and geometrical stable rings were achieved. The concentration of the alumina content on the rings was calculated to be ~3.05mol% for the outer ring and ~3.45mol% for the inner ring. The refractive index changes were $\Delta n=0.0061$ with a maximum thickness of 2.8μm at the base of the profile; and $\Delta n=0.0069$ with a maximum thickness of 2.68μm respectively. The fibre refractive index was measured in 1-dimension as shown in Graph 76 and using the IFA a 2-dimensions FRIP shown in Graph 77.

10.3.3 Performance tests

The performance tests consisted in measuring the absorption of molecular hydrogen into the fibres. The absorption peak at ~1245nm was chosen for this measurement for being the most prominent absorption peak, and it has no substantial overlapping with other absorption wavelength peaks, preventing misleading information or false-positive readings.

10.3.3.1 Experiment 1

The first test was performed using a hydrogen loading cell with a pressure of 120bar and kept at environment temperature. For this test, the selected fibre was fabricated following the alumina-rich tube approach where a single alumina ring was deposited using a gas phase technique. The sample number was A0769_L30404. A control sample was fabricated with the same preform allowing a direct comparison with the same germanium-doped core composition of ~12.5mol%. The control sample number was A0861_L30404.

The samples were measured before and after the hydrogen loading procedure using a white light source (WLS) with a 100W quartz halogen lamp and an optical spectrum analyser (OSA). Samples were kept simultaneously inside the hydrogen loading cell for 10 days, and no additional heat was applied to the chamber.

Fibre	Type	Change @1245nm [dB·km^{-1}]
A0861	Control	986.93
A0769	Single Ring	496.56

Table 18. Experimental results on single-ring diffusion barrier fibre.

After the 10 days, the single-ring fibre showed a ~50% less absorption at 1245nm compared to the control sample. The single ring fibre had an absorption of ~496 dB·km^{-1} whereas the control sample presented an absorption of ~986 dB·km^{-1} at the same wavelength as described in Table 18.

10.3.3.2 Experiment 2

The second set of experiments was carried out using a fibre fabricated by the MCVD with solution doping approach. The conditions of the experiments remained the same using a pressure of 120bar and kept at environment temperature. The fibre for this test was a dual ring fibre, and its number was A0895_L30493. In this occasion, the germanium-doped core of the preform was fabricated with a similar concentration of ~10mol%. The control sample was a new section of the previous fibre A0861_L30404.

Once again, samples were measured before and after the hydrogen loading procedure using a WLS with a 100W quartz halogen lamp and an OSA. Samples were kept simultaneously inside the hydrogen loading cell for 6 days, and no additional heat was applied to the chamber.

Fibre	Type	Change @1245nm [dB·km^{-1}]
A0861	Control	741.48
A0895	Dual Ring	351.19

Table 19. Experimental results on dual-ring diffusion barrier fibre.

After the 6-day period, the dual-ring fibre showed a similar performance of ~53% less absorption at 1245nm compared to the control sample A0861_L30404. The dual-ring fibre had an absorption of ~351 dB·km^{-1} in comparison to the control sample which presented an absorption of ~741 dB·km^{-1} at the same reference wavelength, see Table 19.

10.3.3.3 Experiment 3

Two control samples were used to identify the behaviour of the diffusion related to the doping concentration. Different Germanium doping concentrations on the core were investigated 12.5mol% for a new section of the fibre A0861_L30404, and a 6mol% of a different control sample number A0904_L10464. Experimental conditions were kept constant using a pressure of 120 bar and hydrogen loading cell kept at environment temperature.

Samples were kept simultaneously inside the hydrogen loading cell for 6 days, and no additional heat was applied to the chamber. Measurements from before and after the hydrogen loading were compared. A WLS with a 100W quartz halogen lamp and an OSA were used for the optical characterisation.

Fibre	Type	Change @1245nm [dB·km^{-1}]
A0861 (12.75mol% GeO_2)	Control	741.48
A0904 (6.06mol% GeO_2)	Control	546.48

Table 20. Experimental results of different GeO_2 concentrations on hydrogen diffusion barrier fibres.

As shown in Table 20, sample A0904_L10464 with lower dopant concentration showed ~35% less absorption at 1245nm compared to the higher dopant concentration sample A0861_L30404. The fibre with germanium-doped core composition of ~6mol% had an absorption of ~546 dB·km^{-1}. As to the sample with ~12.5mol% presented an absorption of ~741 dB·km^{-1} at the specified wavelength. The difference in the hydrogen intake is expected due to the higher germanium content in the core of the fibre.

10.3.3.4 Experiment 4

Two hydrogen barrier designs were tested to identify their behaviour under the same conditions. Fibres samples were A0769_L30404 with a single ring and fibre A0895_L30493 with the dual ring. These fibres were fabricated using gas phase technique and MCVD solution doping technique respectively.

Experimental conditions were set using a pressure of 120 bar, and the hydrogen loading cell was kept at constant temperature. Samples were tested for 12 days, and additional heat was applied to the chamber to maintain 333K.

Fibre	Type	Change @1245nm [dB·km^{-1}]

A0769	Single Ring	1122.18
A0895	Dual Ring	1006.30

Table 21. Experimental results on single and dual-ring diffusion barrier fibre.

Both designs show similar performance under extreme conditions with a slight difference of ~10% on the dual-ring design showing less absorption at 1245nm compared to the single-ring fibre. Sample A0895_L30493 had an absorption of ~1006 $dB \cdot km^{-1,}$ and sample A0769_L30404 showed an absorption of ~1122 $dB \cdot km^{-1}$ at a wavelength of 1245nmas shown in Table 21. Samples were also measured before and after using a WLS with a 100W quartz halogen lamp and an OSA.

10.3.4 Conclusions

Experimental results showed that the alumina-rich regions are an effective molecular hydrogen diffusion barrier. Both fibre designs, single and dual-ring, show similar effectiveness reducing by ~50% and 53% respectively the molecular hydrogen absorption at 1245nm compared to the control samples.

There is a relation between the amount of hydrogen diffusion and the germanium doping concentration of the core. Experimental data suggests that higher germanium-doping concentration has higher molecular hydrogen diffusion. Single and dual-ring fibre designs performed similarly under high-temperature and high-pressure conditions with a minor difference of 10% on the absorption at 1245nm peak.

Experimental evidence suggests that the losses at the working wavelength (~1550nm) are due to the increase on multiple absorption peaks on the ~1600nm region. No experimental evidence supports the increase of OH absorption peak at ~1380nm. Using Sapphire as an Al_2O_3 source can be a potential fabrication approach to achieve higher concentrations of alumina. The single crystal based structures have a slightly lower melting temperature than the ceramic based.

Reducing the temperatures required for processing the barrier will help to reduce the viscosity of the silica optical preforms, expecting to eliminate the voids and irregular shapes across the fibre. Unfortunately, limited availability of these materials reduces attractiveness for technological transfer of this fabrication approach.

Hybrid MCVD and CDS fabrication demonstrated being a suitable process for fabrication a hydrogen barrier. Nonetheless, the CDS technology still is not widely

adopted by the industry. It showed a similar final alumina concentration than the conventional MCVD solution doping technique.

The limitation of increasing alumina concentrations for the hydrogen barriers discourages the adoption of this technology. MCVD solution doping technique emerges as the most convenient fabrication approach for being already widely adopted by the industry, and the amount of doping concentration is comparable with the gas phase technique. Future development fabricating preforms using 3 or more rings will be desirable to compare the performance of hydrogen diffusion increasing the amount of alumina-rich regions. Fabrication of preforms with alternative core compositions will be desirable to identify the difference in diffusion changes on different glass compositions.

10.4 Customisable central depth of refractive index profile

The preforms used during this experimental activities were fabricated by Pranabesh Barua. The drawing conditions, characterisations and analysis are from the author.

10.4.1 Introduction

Fibre refractive index profile from preforms with core compositions including germanium and phosphorus have a distinctive feature, also known as central dip. This characteristic is due to the evaporation of the dopant (GeO_2 and P_2O_5) because its lower melting and boiling temperatures compared to silica.

The abovementioned evaporation happens mainly during the collapsing process of the optical preform. The silica glass substrate requires heating to temperatures that can exceed 2,500K. The resultant evaporation of the dopants on the inner layers of the deposition; leads to the decrement of the refractive index change in the central section of the final profile.

A common practice to minimise this problem is to compensate the evaporated dopant by adding it during the collapsing passes. It can be achieved by adding a flow of the reactant into the oxygen stream during the collapsing passes, leading to a second deposition process.

This technique requires a very precise and calibrated amount of reactants flow. When this approach is not followed correctly, the FRIP in the central region can remain lower than expected, or if exceeded; it can result in an undesirable secondary central waveguide profile.

This procedure is much welcome during passive preforms fabrication. Nevertheless, during RE-doped preforms fabrication, this approach is no longer practical. The refractive index profile can be homogenised. However, the RE-dopant distribution profile cannot be compensated. It leaves a central dip on the rare earth distribution profile. For particular applications, the central dip can be beneficial. However, finding the resultant refractive index profile that fits the desired modal propagation properties can be challenging.

Therefore, the possibility of tailoring this profile during the fabrication process would be advantageous for either application that requires a non-central dip profile

and for those that require it, such as high power lasers working on LP_{11} modes or applications requiring to minimise the Gaussian beam profile.

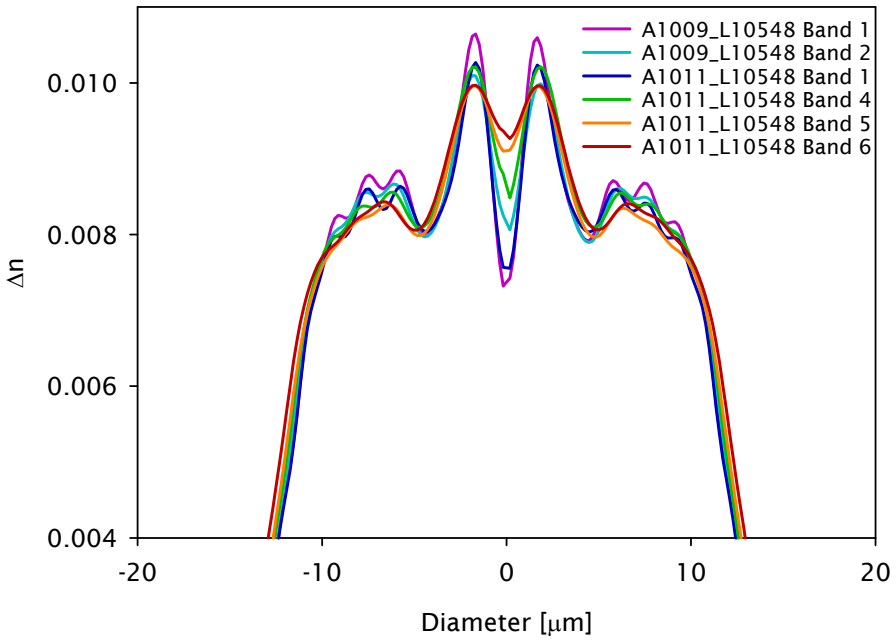

Graph 78. Custom-made central depth on FRIP.

Graph 78 shows how the refractive index profile in the fibre can be custom-made for specific applications. Fibre drawing conditions can be optimised to achieve desired depths on fibre profiles matching specific light propagation conditions.

10.4.2 Refractive index change from preform to fibre

It is important to note that the diffusion phenomenon will dominate the preform refractive index profile change. However, diffusion depends on a number of factors such as preform to fibre ratio; drawing temperature and exposure time to the heat source. These conditions are studied and described in this section.

Graph 79 shows the change in refractive index profile between the preform and fibre in the central region.

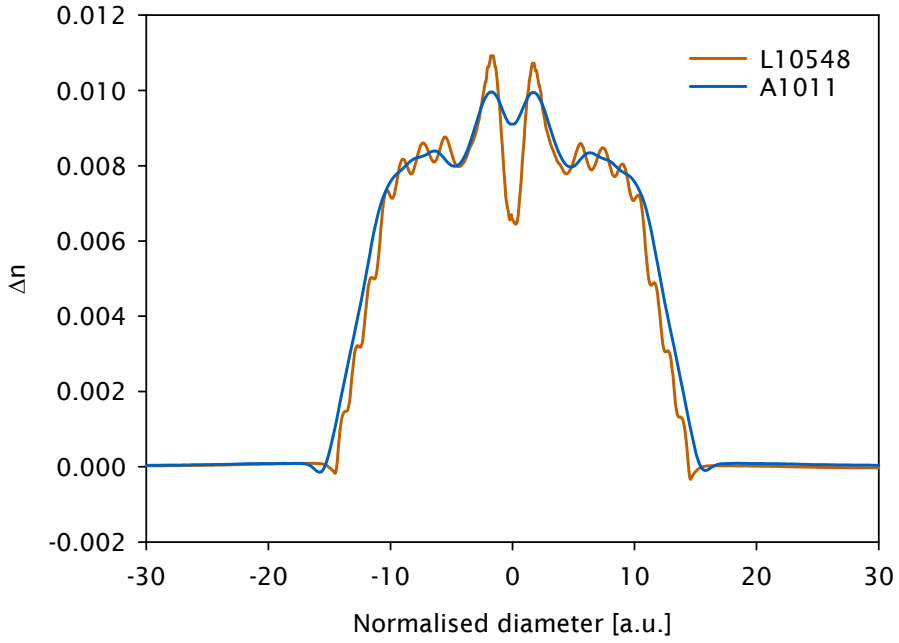

Graph 79. Overlapping between refractive index profiles of preform L10548 and fibre A1011.

10.4.3 Intact dopant distribution

As mentioned in section 10.4, it is required for active preforms and fibre fabrication that the rare-earth distribution remains homogenous across the core region. The change in central depth has been achieved by using the established condition without detrimental effects on dopant distributions as shown in Graph 80.

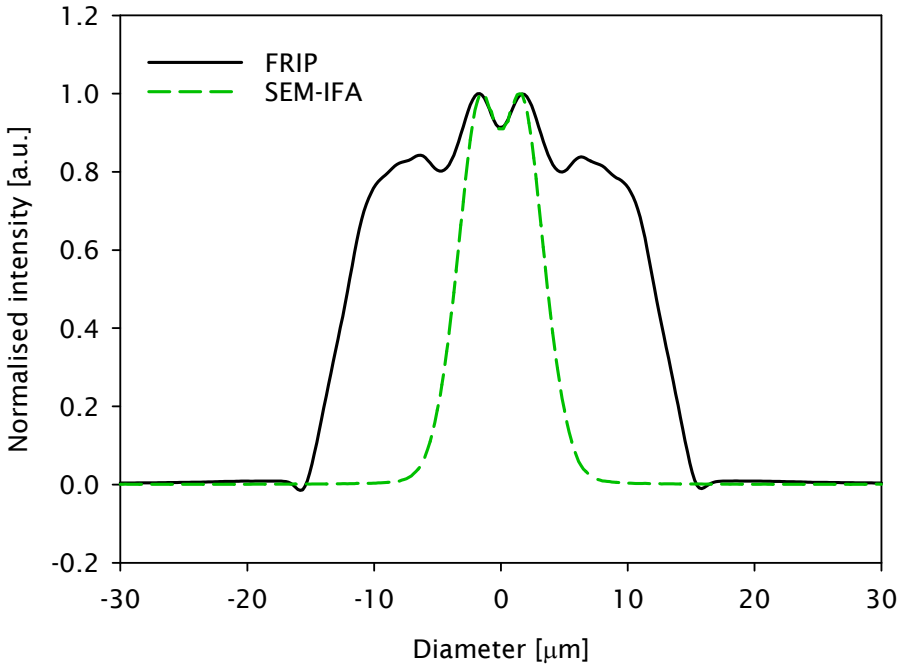

Graph 80. Overlapping between refractive index and dopant distribution profiles.

10.4.4 Implementation

The established conditions do not require any additional devices or processing and are compatible with commercial fibre drawing equipment. Process refinement can achieve further improvements. Graph 81 presents the latest experimental conditions showing additional improvement in minimising the central dip.

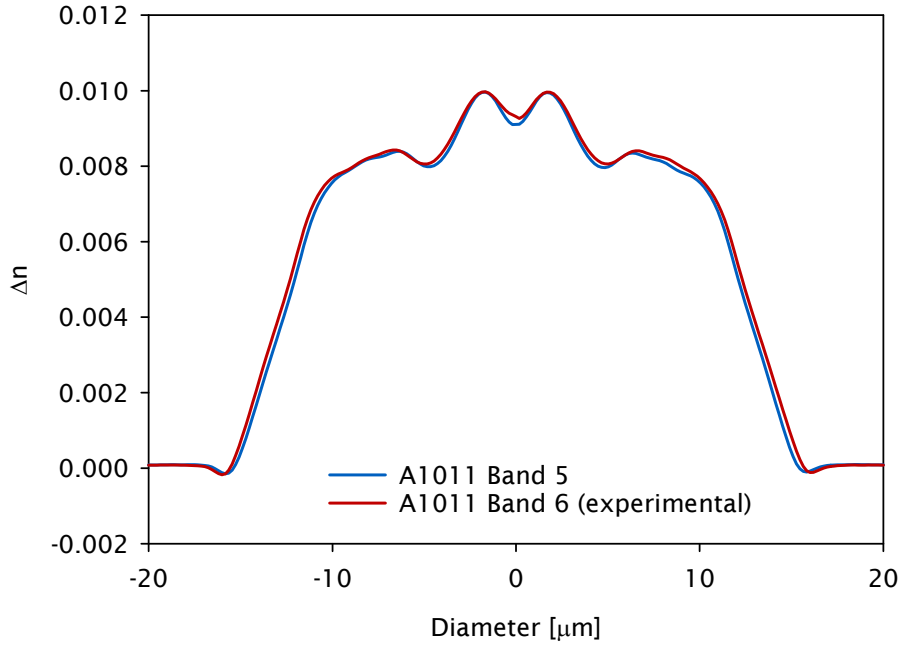

Graph 81. Experimental conditions for minimum central depth on FRIP.

10.4.5 Repeatability of the method

Graph 82 shows repeatability of the established conditions in the alternative preform.

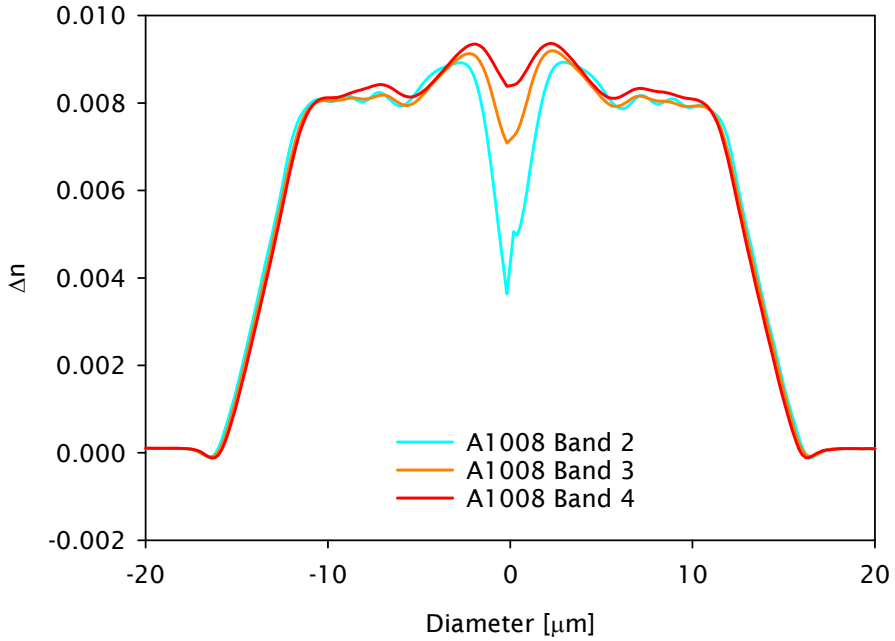

Graph 82. Central depth removal in the additional preform.

The method for tailoring the central depth on the refractive index profile has been successfully implemented, and it has been reproduced in multiple preforms with invariable results.

10.4.6 Impact of preform feed speed

Preform feed speed is the variable that can be modified during the drawing process and it is directly related to the exposure time of the sample to the heat source. It has a significant impact when combined with higher temperatures. However, at normal drawing conditions, the impact is limited.

Graph 83 presents the change on the central dip at different feed speeds from 1.0 to 0.3 $mm \cdot min^{-1}$ at 2,293K without a significant improvement in the fibre refractive index profile.

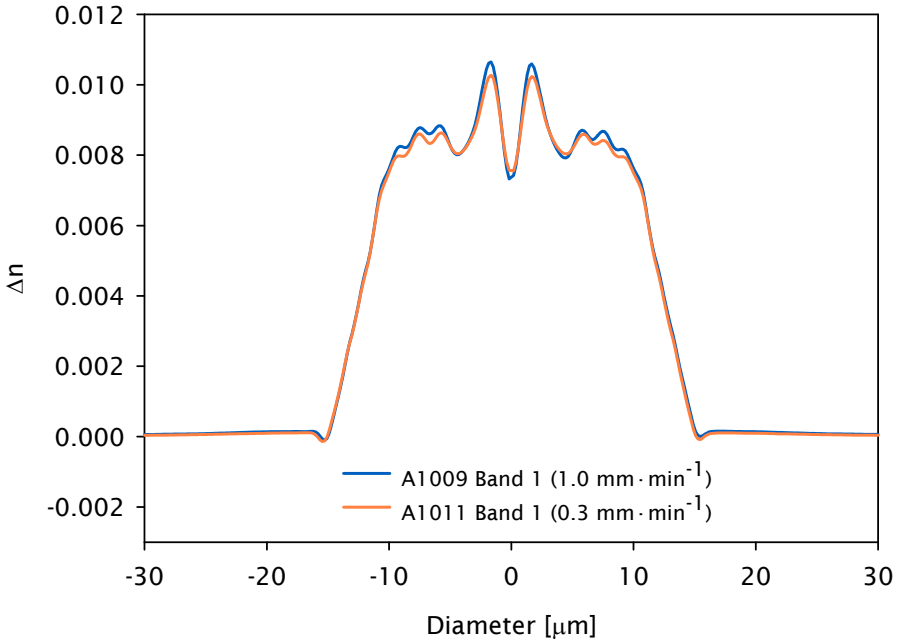

Graph 83. Impact of preform feed speed in tailored FRIP.

10.4.7 Impact of drawing temperature

The impact on drawing temperature was studied by changing the furnace temperature from 2,293K then 2,423K and finally 2,473K. The preform feed was kept unchanged at 0.3 mm · min^{-1} for the three different temperatures. Change in the profile is evident following the increment on drawing temperature as shown above in Graph 84.

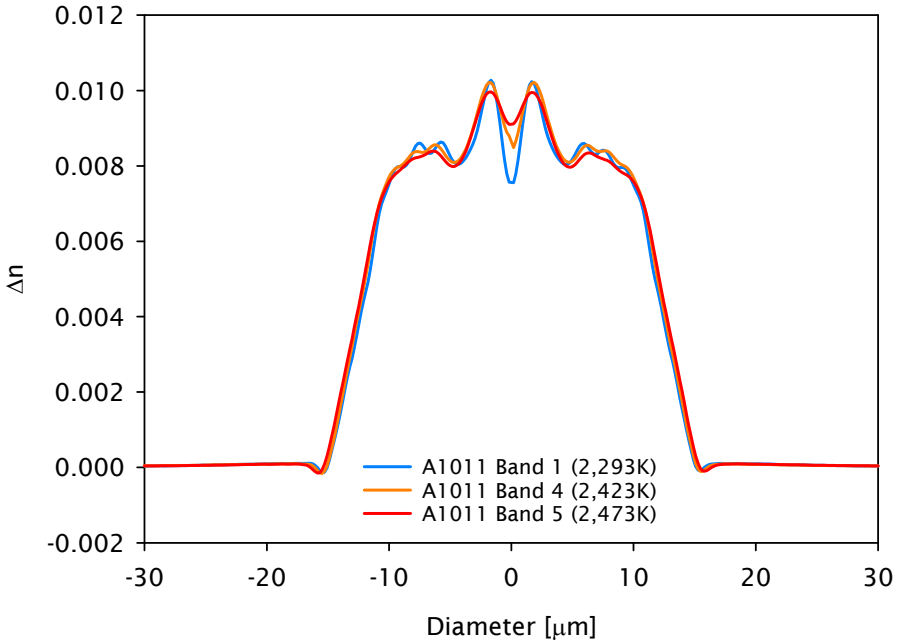

Graph 84. Impact of drawing temperature in tailored FRIP.

10.4.8 Impact of fibre diameter

Fibre diameter is the variable that defines the preform to fibre ratio for this application. It is expected to have an impact on the central dip by scaling down the width of the dip in the FRIP. A demonstrative draw was made to establish the magnitude of this change using the same preform and fibre drawing conditions; the resulted fibres of 125μm and 100μm are shown in Graph 85.

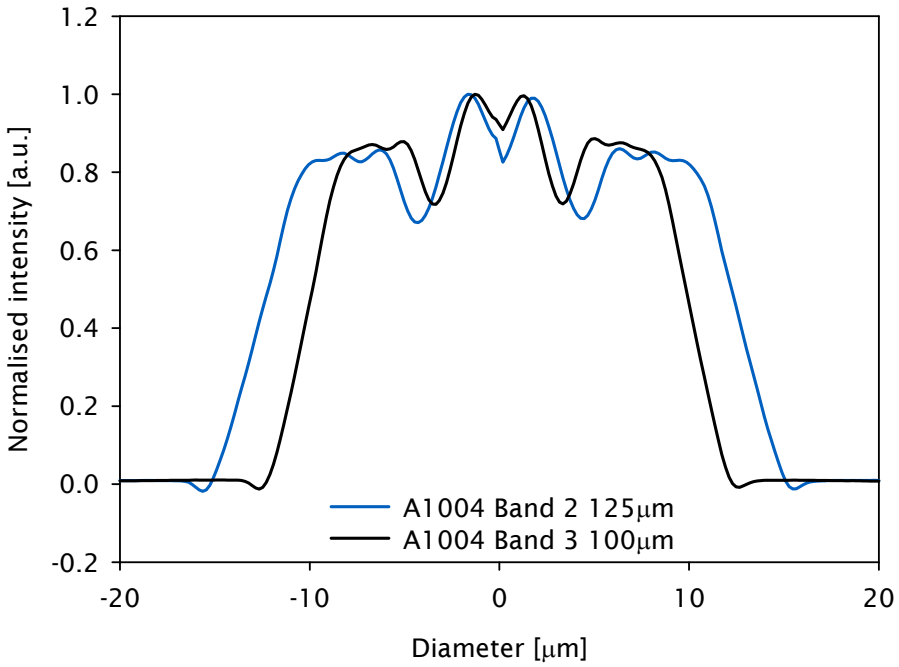

Graph 85. Impact of preform to fibre ratio in tailored FRIP.

10.4.9 Impact in fibre attenuation

It is essential to ensure that the proposed method is not having a detrimental effect regarding attenuation in the final fibre. Extraordinary drawing conditions can introduce defects in the glass.

Graph 86 shows an OTDR trace where no significant increment in losses is evident. The attenuation level of a 125μm fibre, drawn at 2,473K with preform feed speed between 0.3 – 0.2 $mm \cdot min^{-1}$ was ~10 $dB \cdot km^{-1}$ measured at 1285nm.

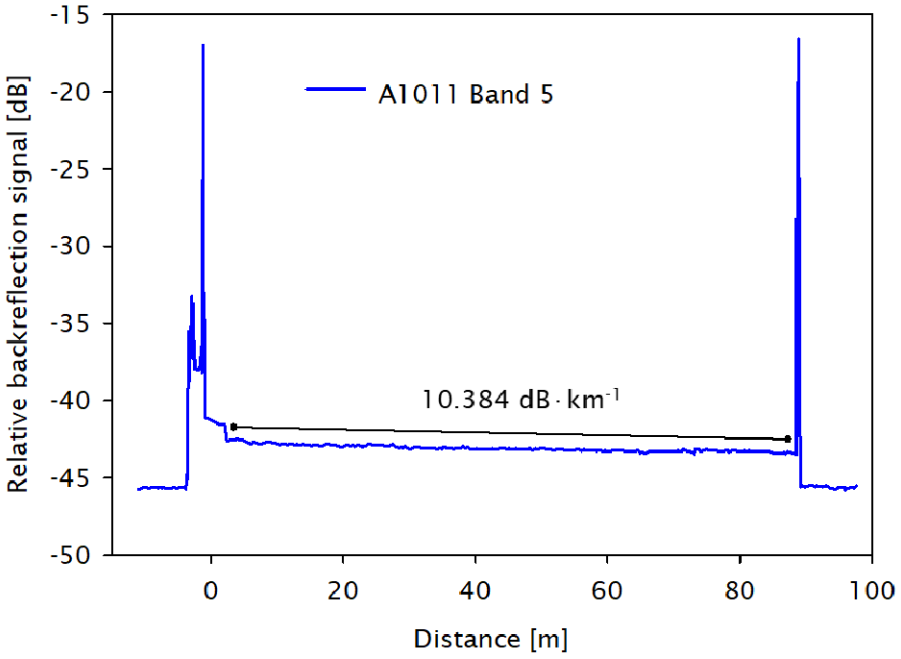

Graph 86. Impact in fibre attenuation by tailored FRIP.

10.4.10 Conclusions

Fabrication conditions were studied to improve the central depth in the refractive index profile of the optical fibres. Factors such as preform to fibre ratio; drawing temperature; and exposure time to the heat source were demonstrated to have a significant impact allowing to tailor the central dip characteristics without detrimental effect in losses and rare-earth dopant distribution.

Increasing the drawing temperature and reducing the preform feed speed faces the challenge of controlling the tension on the fibre during the fibre drawing process. The above is due to the low viscosity of the glass at high temperatures.

The use of the established fabrication parameters is compatible with large-scale fabrication process. For production environment, it is expected to have more substantial preform diameters requiring slower feed speed in the preform. At the same time, it increases the preform to fibre ratio helping the closure of the central dip. Unfortunately, the core size will remain a limitation for the use of this approach. Large core fibres remain a challenge for conventional fabrication process such as conventional MCVD process with solution doping.

The experimental results presented in Chapter 6 and Chapter 9 are feasible alternatives with the potential to overcome the current limitations on the core to cladding ratio.

10.5 Fibre Bragg Gratings

This section has contributions from Andrei Donko on the inscription of the fs-FBG and Pranabesh Barua on the preform and fibre fabrication. The optical and thermal characterisation, as well as the data processing and analysis, are from the author of this thesis.

10.5.1 Introduction

Fibre Bragg gratings are successfully implemented on a wide range of applications and sectors such as automotive, aerospace and energy, among others[100,101]. Fibre gratings are reliable and cost-effective sensors for discrete or quasi-distributed temperature and strain monitoring[102,103]. In the photonics industry, FBG prevails extensively in use in telecommunications for signal filtering, and in the fibre laser technologies, it is a valuable device for customisation of bandwidth and wavelengths.

Femtosecond based FBG successfully overcome the main challenges that traditional UV-scribing technology faces. The main advantage is that the glass host does no longer require being photosensitive[104]. Especially for the fibre laser technologies, it represents the possibility to scribe the gratings directly into the RE-doped fibres eliminating the need of splices in the laser cavity[105-107].

Inscription through the coating is also possible when scribing FBG with femtosecond techniques. That is one of the main drawbacks on the traditional UV-technique due to the high absorption from the polymers used on optical fibre fabrication[108]. High-temperature coatings such as polyimide present detrimental effects when using 800nm radiation. One way to reduce the problem while using that wavelength is loading the samples with hydrogen. Alternatively, the use of higher concentrations of germanium facilitates the inscription[109].

Two different approaches for inscribing fs-FBG are widely in use: phase-mask[107] and direct writing. The direct writing technique offers more flexibility extending the capabilities of inscription by adjusting the period, phase and amplitude to the desired grating[103,110,111].

Only a few authors explored high-NA fibres based on germanium-doped silica fibres. Nevertheless, either the inscription technique is based on UV exposure[112], or they use commercially available fibres with NA<0.358,[113].

The present report explores the characteristics of a femtosecond-IR FBG's through the coating on a speciality optical fibre with NA>0.4. High germanium-doped fibres are especially useful for sensing ionising radiation[114,115], and they are of great interest for laser application due to its high non-linear properties.

10.5.2 Experimental setup

The fibre was fabricated from an MCVD preform made in-house at the ORC. This fibre was coated with a standard acrylate DSM-314 cured by photo-polymerisation. A multi-wavelength optical fibre analyser IFA-100 was used to measure the fibre refractive index profile. As shown in Graph 87, the fibre has a step-index profile with a core size of 3.72μm and a cladding diameter of 106μm.

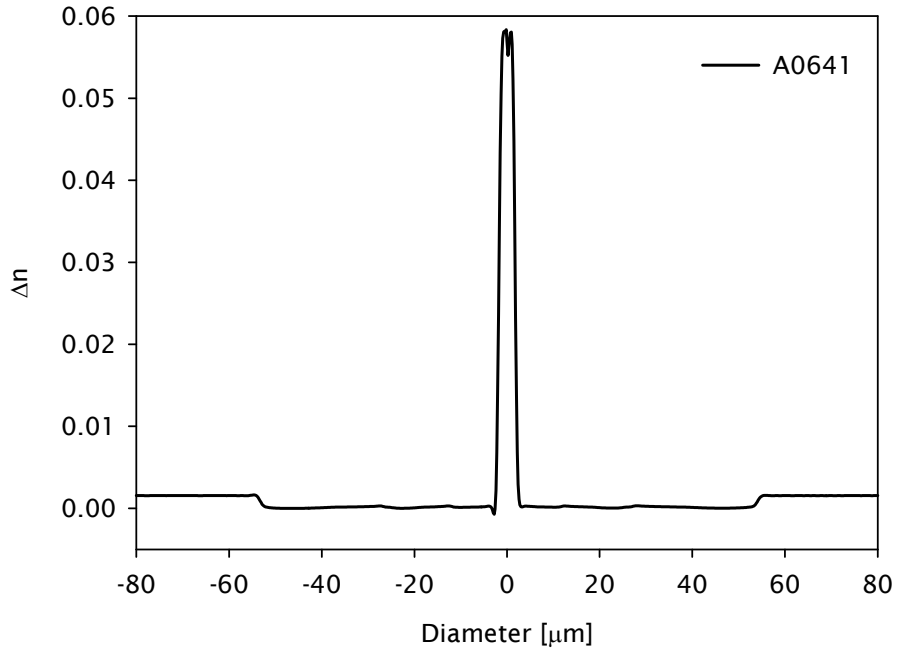

Graph 87. FRIP of high NA germanium-doped silica fibre.

For FBG inscription, a 1030 nm laser system (Pharos, Light Conversion Ltd) was used with a pulse duration of 250 fs. A frequency of 1 kHz was used with a pulse energy of 0.7 μJ. The beam propagated through a 250 μm slit before being focused on the core of the fibre using a 0.65 NA-objective lens. A CCD camera and a dichroic reflector were placed above the writing lens, enabling imaging of the fibre.

Third order gratings of Bragg wavelength λB = 1554nm were inscribed. The transmission spectra of the fibre was monitored continually throughout the writing process using a supercontinuum source and an optical spectrum analyser.

After the grating inscription and initial characterisation of the FBG, the coating on the fibre sample was removed. The setup used for the temperature dependent study on the fibre consisted of installing the fibre through a 400mm tubular furnace with an isochronal change on temperature. The temperature was monitored externally by a thermocouple, to validate the temperature control accuracy showing a deviation of 0.2K after 30 minutes of temperature stabilisation. The transmission spectrum was measured using the same supercontinuum source utilised for the inscription of the grating and an OSA.

10.5.3 Results

An initial measurement on the FBG before the temperature study shows three reflection features. This agrees with the fact that the fibre is few-moded at the λB. This fibre has a normalised frequency V=3.06 which means that the fibre supports up to four modes (HE_{11}, TE_{01}, TM_{01} and HE_{21}) corresponding to the LP_{01} and LP_{11} modes.

The transmission spectra observed in Graph 88 shows the associated depths for the LP_{01} self-coupling, LP_{01}-LP_{11} cross coupling and LP_{11} self-coupling modes. Both modes LP_{01} and LP_{11} present similar power distribution. It is possible to appreciate that the reflections are similar in magnitude (-25dB).

At the shorter wavelengths of the spectrum presented in Graph 88, it is also possible to appreciate the effect of the modes coupling due to the core mismatch between the fibre under test and the standard SMF fibre patch cords used to connect from the SC source and to the OSA.

For this report, only the λB associated with the fundamental mode will be reported for the temperature study. Nevertheless, all the features presented in Graph 88 exhibited the same behaviour during the study.

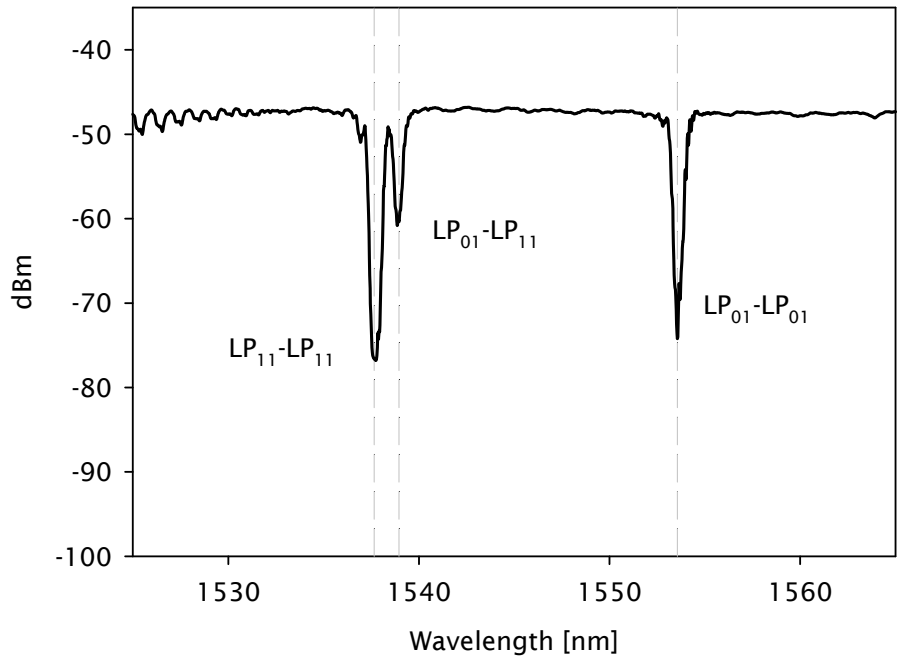

Graph 88. Optical spectrum of FBG in transmission mode before temperature study at 293K without coating.

The FBG was exposed to a range of high temperatures starting from 293K up to 773K. Graph 89 shows the temperature profiles of λB at 323K and 773K. It is evident that the intensity of the grating background loss and the profile of the grating do not present signs of detrimental effects after being exposed to 773K.

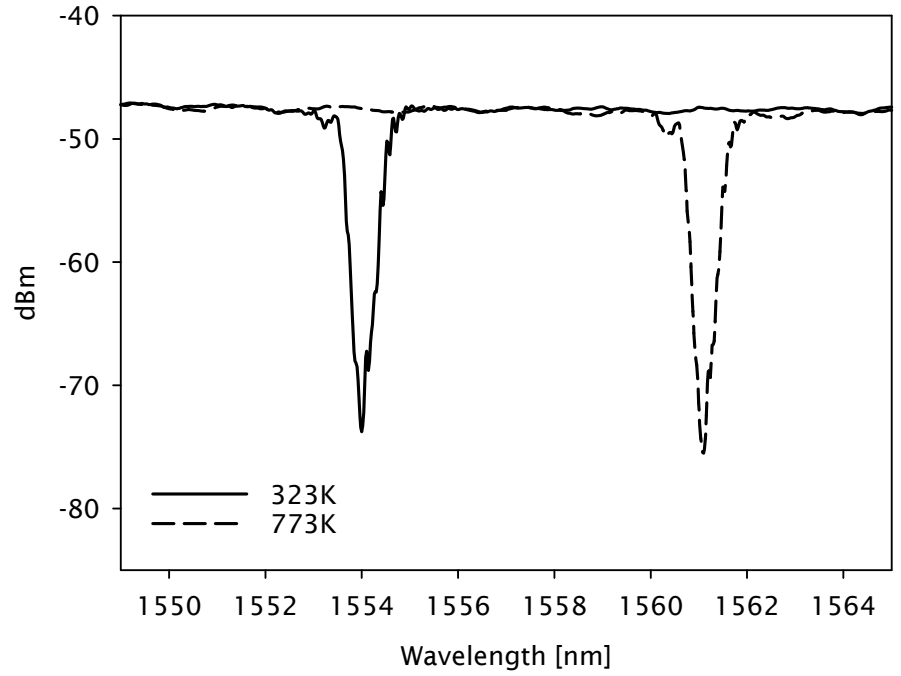

Graph 89. Transmission spectra of FBG reflection shows no signs of detrimental effects on the intensity with temperature up to 773K.

The sensitivity of the FBG has an overall response of 15.7pm/K calculated from $\Delta\lambda/\Delta T$ with the FBG response from 293K to 773K shown in Graph 90.

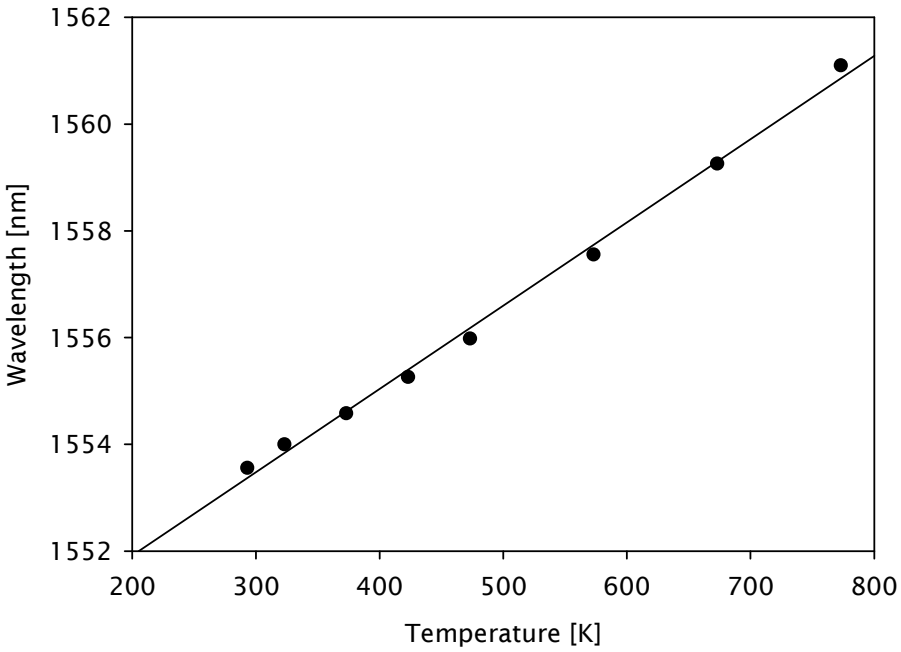

Graph 90. The variation of Bragg wavelength against temperature has an overall sensitivity of 15.7pm/K.

The FBG was exposed at 773K for 10 hours with the aim to investigate the temperature stability of the FBG due to the prolonged exposure to high temperatures.

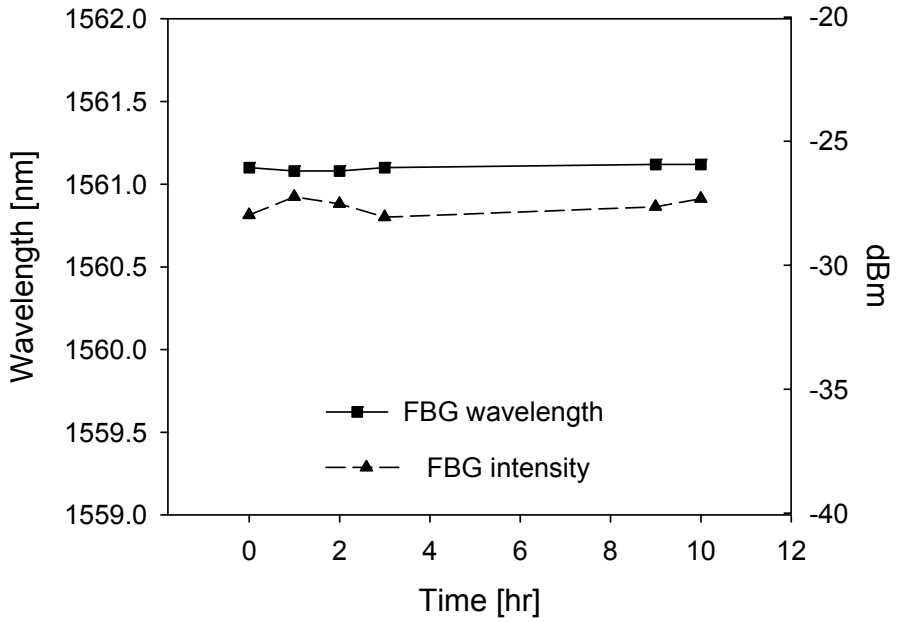

Graph 91. FBG wavelength and intensity changes during 10hrs exposure at 773K.

Graph 91 shows the effects of long-term exposure at 773K. Neither the FBG wavelength nor the intensity of the grating were affected by the 10hrs exposure to high temperature as reported in this study.

10.5.4 Conclusions

FBG's were successfully inscribed through the fibre coating with the fs-IR radiation at 1030nm using the point-by-point technique. The temperature study shows that this type of FBG can withstand temperatures exceeding 773K. That makes this FBG a potential candidate for temperature sensors that can be used by energy, gas and oil industries. Additional applications such as ionisation radiation sensors are yet to be investigated.

Finally, the high content of germanium oxide in these speciality fibres together with the inscription of FBG opens the door for further studies based on non-linear phenomena, especially for Raman laser applications to overcome the limitations in wavelength coverage from its RE-doped counterparts.

10.6 Multi-Element Fibre

This section complements the study reported by Saurabh Jain in his PhD thesis and also has a contribution from Pranabesh Barua in the fabrication of few fibres. The characterisations reported in this section, the analysis and part of the preforms and fibre fabrication are contributions from this author.

10.6.1 Introduction

In recent years the growth of Internet users and services requiring the web for transmitting information has exponentially increased as shown Graph 92. The system capacity has grown trying to meet the demand.

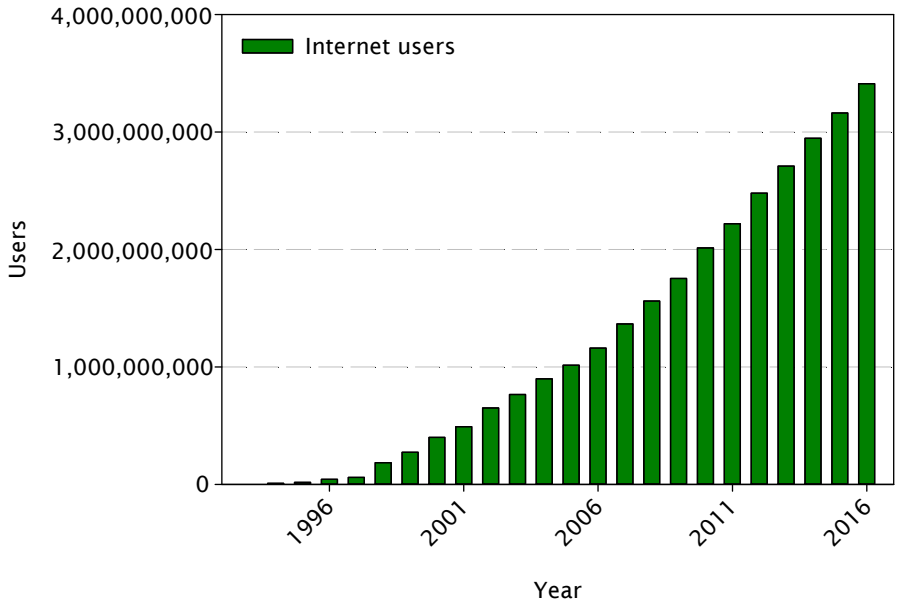

Graph 92. Internet users around the world[81].

With the constant data capacity demand increasing at a rapid pace due to social networks, mobile technologies and big-data application, the current capacity based on SMF is reaching its fundamental limit[81,82]. Different multiplexing approaches had been proposed trying to satisfy the demand. Almost all the non-physical multiplexing approaches had been exhausted leaving the space division multiplexing (SDM) as one of the last resources to cope with the rampant increase in demand.

Within the SDM approach exists three main routes that researcher across the globe have been following. Perhaps multi-mode fibres are the easiest solution from the

fabrication perspective. Few-mode fibres supporting 2 or 3 spatial modes are easy to achieve by conventional fabrication methods.

Nevertheless, challenges such as complex multiple-input and multiple-output (MIMO) processing required for larger number of modes, and equalisation requirements for amplification purposes conflict with the attractiveness of this option.

Multi-core fibres (MCF) have been explored in recent years. The main challenges of this alternative are the limitations of the outer diameter which is usually restricted to ~225μm. The diameter restriction tends to increase the level of cross-talk between the cores, forcing to implement more complex preforms designs and therefore more expensive and complex fabrication processes.

Selective core designs to minimise the cross-talk also implies that the original preform cannot be the same for all the cores. Different preforms add costs and require special care on how the cores are assembled to prevent the undesired cross-talk. Finally, another major problem is the splicing and the connection of MCF's into single fibres.

Multi-element fibre (MEF) share the basic principle of the MCF, except for the fact that the cores do not share the same cladding. In MEF design the fibres come from individual preforms as shown in Image 63; but, they are drawn simultaneously and coated together in a wet-on-wet dual coating process.

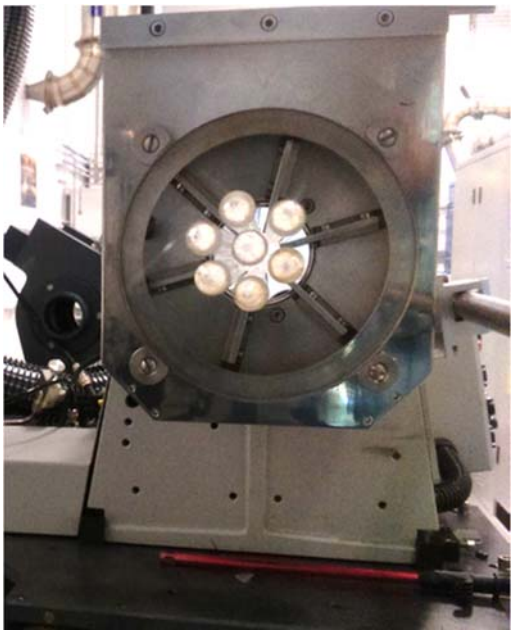

Image 63. 7-MEF preform shown before preparation for fibre drawing process.

Multi-element fibre does not suffer from cross-talk, and neither requires sophisticated signal processing nor special equipment for splicing and connection

into the current systems. Being individual fibres, after coating removal, its implementation is straightforward.

10.6.2 Experimental results

Seven-element MEF preform was drawn into 80µm diameter fibres and characterised to investigate the attenuation of the individual fibres. Image 64 shows the cross-sectional image of the 7-MEF. Table 22 presents the attenuation values measured by OTDR at 1550nm on a single layer configuration with a rewinding tension of 10g.

Image 64. Cross-sectional OM image from 80µm 7-MEF.

From the attenuation values, the location of each element was estimated with the premise that the closest the elements the higher the attenuation.

Fibre element	Attenuation [dB · km^{-1}]
1	0.374
2	0.410
3	0.483
4	0.331
5	0.685
6	0.381
7	0.278

Table 22. Attenuation of 7-MEF with 80µm fibre diameter.

A comparative study between 80µm single-fibre and 7-MEF with 80µm fibre diameter was performed to investigate the effect of the rewinding-tension on the attenuation levels of the fibres. Graph 93 shows the relation between the tension and the attenuation at different wavelengths for the 80µm single-fibre.

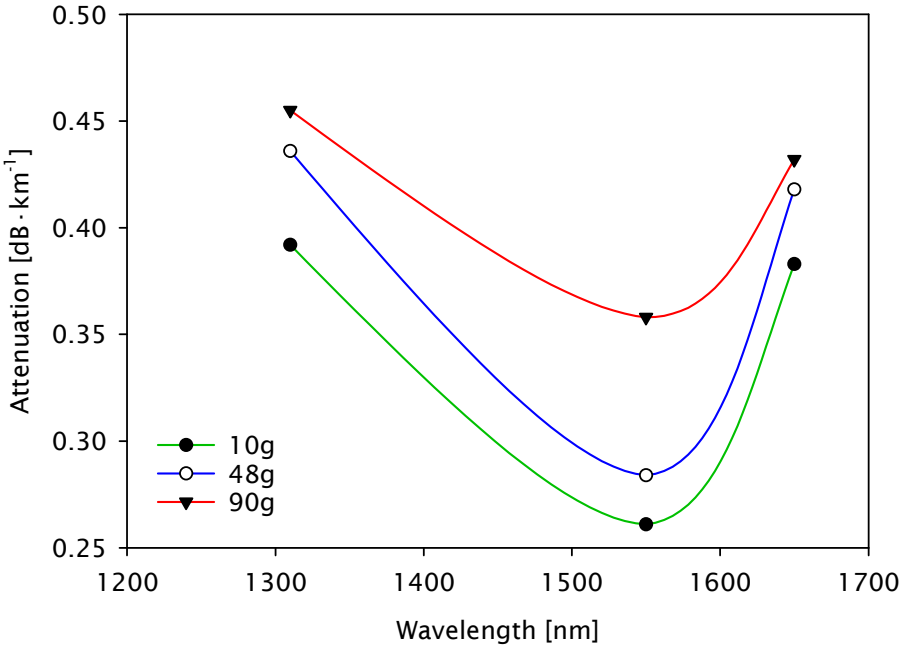

Graph 93. Tension-dependent attenuation in 80µm single-fibre

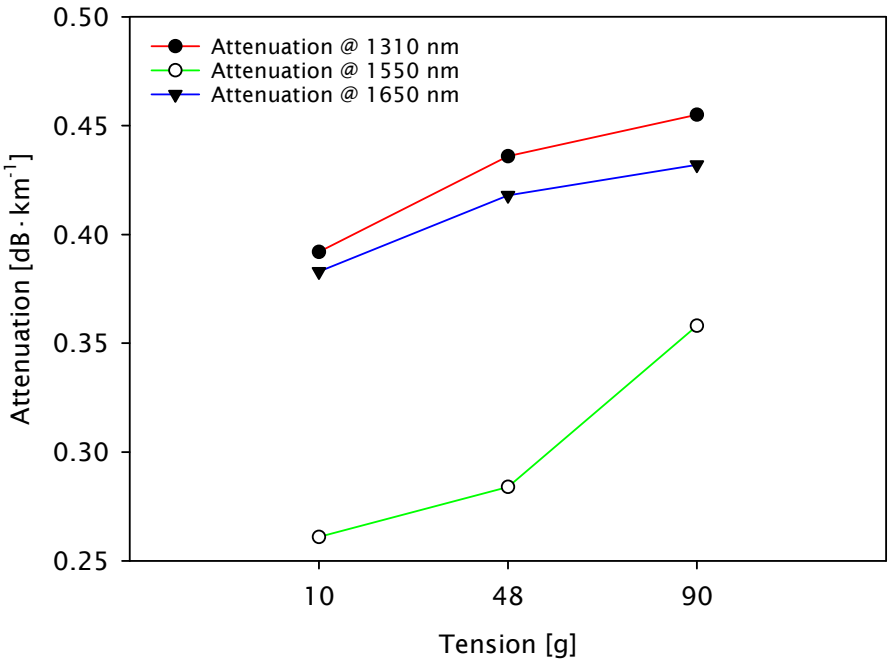

Graph 94. Wavelength-dependent attenuation in 80µm single-fibre.

Graph 94 shows that 80µm single fibre presents a strong relation between attenuation levels and rewinding-tension. Graph 95 compares both 80µm fibre designs

and demonstrate the negligible effect on attenuation from the rewinding-tension in the 7-MEF configuration.

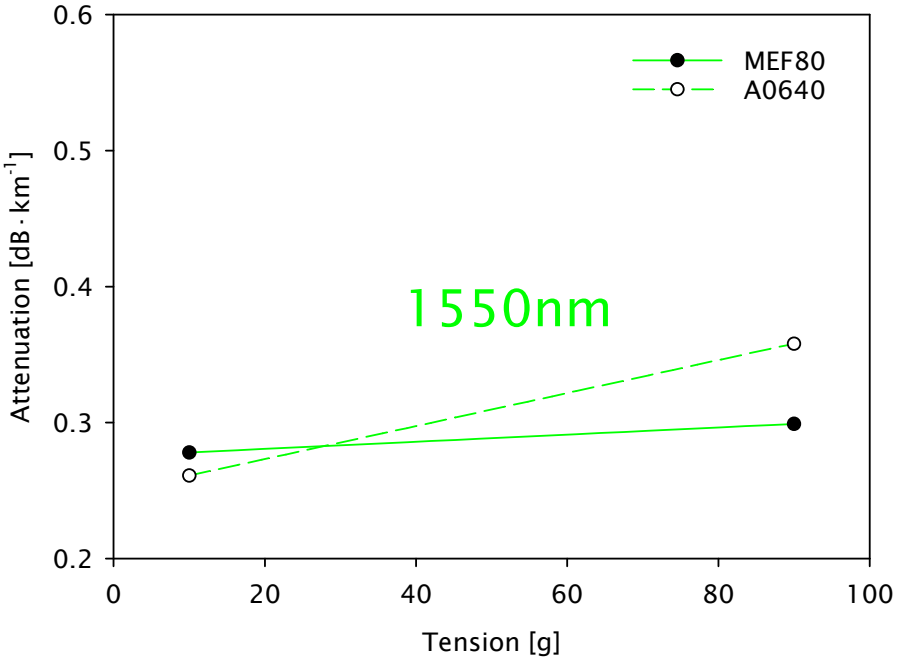

Graph 95. Tension-dependent attenuation in 7-MEF and 80µm single-fibre.

Further fabrication of 60µm 7-MEF was performed. However, due to limited preform availability, only 3 elements were germanium-doped preforms and 4 elements were coreless rods. Seven-elements MEF drawn into 60µm diameter fibres was characterised to investigate its attenuation. Image 65 shows the cross-sectional image of the 7-MEF. Table 23 presents the attenuation values measured by OTDR at 1310nm on a single layer configuration with a rewinding tension of 10g.

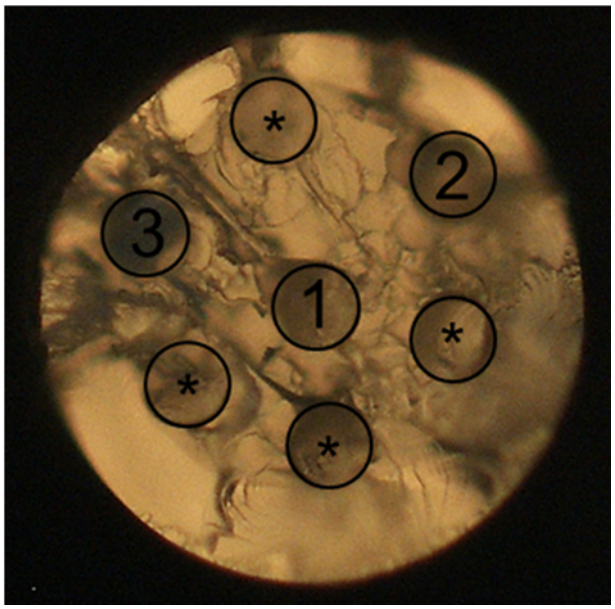

Image 65. Cross-sectional OM image from 60µm 7-MEF.

From the attenuation values, the location of each element was estimated with the premise that the closest the elements the higher the attenuation

Fibre element	Attenuation [dB·km^{-1}] @ 1310nm
1	0.356
2	0.303
3	0.473

Table 23. Attenuation of 7-MEF with 60µm fibre diameter.

Attenuation obtained in the 60µm 7-MEF have a similar level than the 80µm 7-MEF and 80µm single fibre measured at 1310nm. Graph 96 presents a comparative study between 60µm 7-MEF and different fibres from the same preform drawn into different diameters and configurations in 7-MEF and single fibres. This comparison shows that the measured attenuation in 60µm 7-MEF is similar to the other fibres in the study.

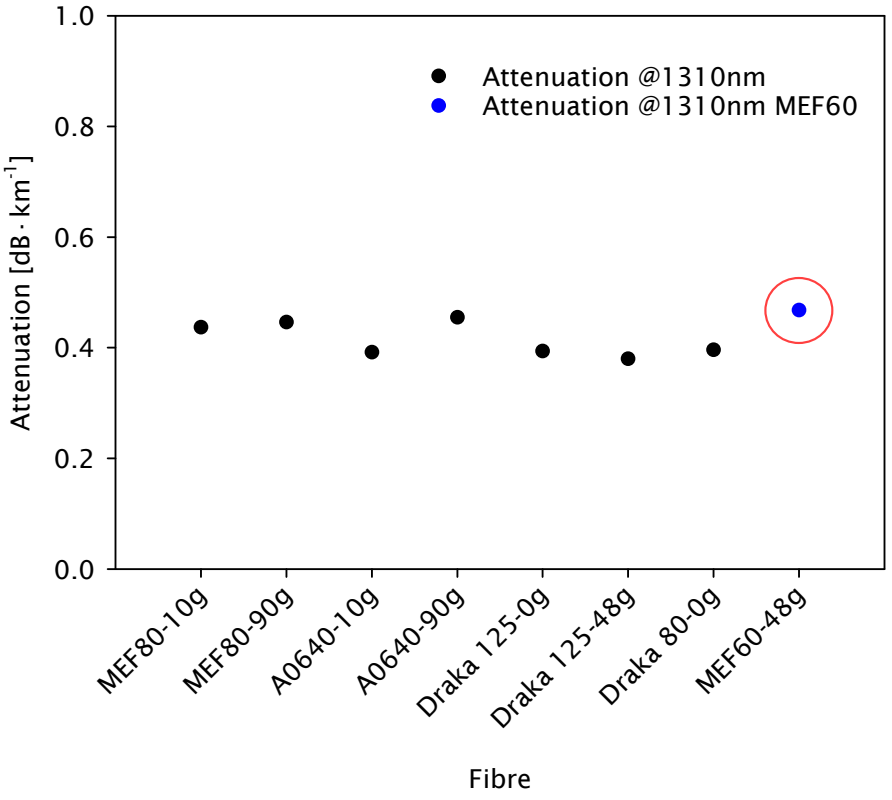

Graph 96. Attenuation comparison between 60µm 7-MEF and different fibres at 1310nm.

10.6.3 Fibre degradation with rewinding process.

During the 7-MEF fibres characterisations, it was observed that the attenuation levels increased every time the fibre was transferred from one bobbin to another. By taking samples in different positions, it was possible to observe that the geometry of the fibre elements has been modified.

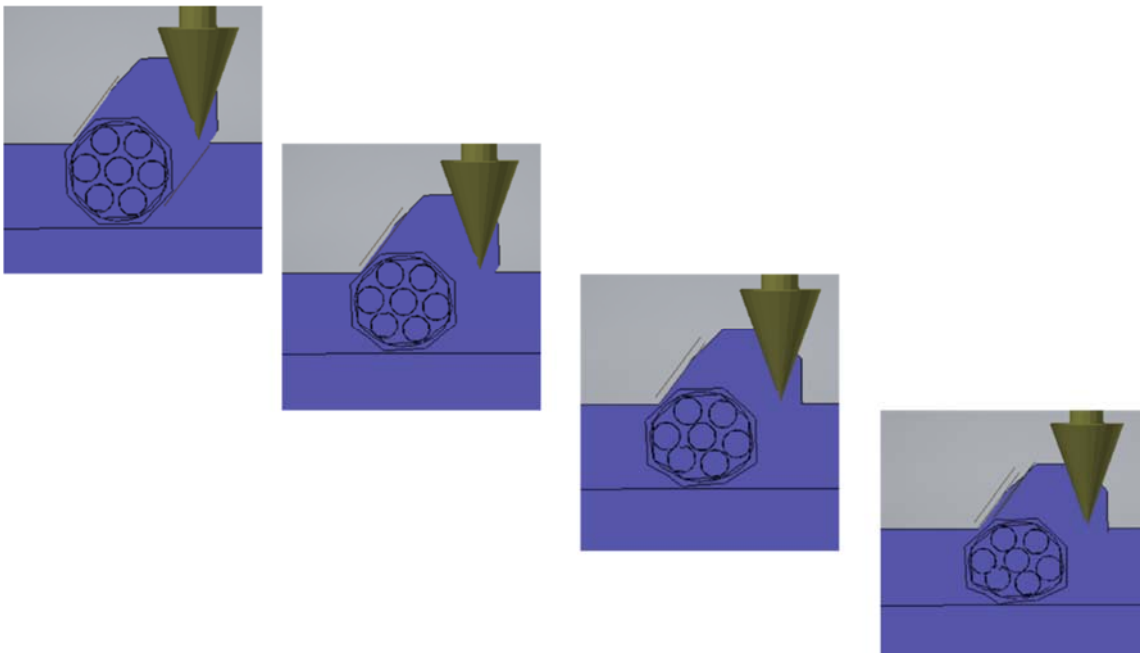

Figure 16. The detrimental effect of rewinding process on MEF.

Figure 16 shows a computational modelling using experimental data for the effect of the compression on the fibre during the rewinding process. The tractor belt provides the compression on the fibre on the rewinding machine; this pressure especially affects the MEF design due to the softness of the primary (inner) coating. The soft coating allows the fibres to be displaced from its original position. When the elements of the fibre come closer, the attenuation levels increase.

10.6.4 Conclusions

Multi-element fibre is a practical SDM solution that has the capability to be escalated and be integrated in the current telecommunications infrastructure. Characterisations on 80µm 7-MEF do not present evidence of tension-dependent attenuation at 1310, 1550 or 1650nm.

It is imperative to maintain the geometry and separation between elements during the fabrication process as well as avoid unnecessary handling that can lead to displacements of the fibre elements. Improvements on the rewinding process can be made to avoid the excessive compression force that deteriorates the fibre characteristics.

Experimental results on 60µm 7-MEF reveal similar attenuation level as compared to 80µm single-fibre and 80µm 7-MEF at 1310nm. The specific cut-off design on the preform fabrication can improve the attenuation levels for 1550 and 1650 nm. This practice of cut-off design is currently used by other SDM approaches such as MCF's.

Chapter 11 Overall Conclusions

The OVD system requires a comprehensive characterisation of the temperatures in the system. Thermodynamic analysis is fundamental to ensure that the processes conditions fit for the desired composition. Fabrication parameters for transparent and bubble free preforms and fibres have been developed for:

- pure silica
- fluorine-doped silica
- germanium-doped silica
- pure germania
- aluminosilicate
- rare-earth aluminosilicate
- phosphosilicate
- rare-earth phosphosilicate
- phosphogermanate silica

It is essential to validate the deposition, dehydration and consolidation parameters for the desired glass composition. It is expected that novel compositions require a calibration process. The temperature in the reaction zone and the deposition layers are the primary parameter to monitor.

OVD deposition system opens the door for a new way of fabricating optical preforms for the photonics industry. In the high power lasers, a direct contribution of this manufacturing process could be the aluminosilicate and phosphosilicate passive glass. These types of glass can match the doped-core refractive index and reduce the amount of high order modes confined to the waveguide.

Active preforms fabricated by OVD offers a more reliable and stable fabrication process compared to traditional MCVD. Preform repeatability and large volumes of doped core material can be a turning point for the current laser technologies.

Germanate glass can also be used for high non-linear applications, where the current systems depend on the commercially available fibres. However, since the manufacturing of 100% GeO_2 has been demonstrated, further development of the current technologies is expected.

The Optoelectronics Research Centre has now the manufacturing capability to fabricate its own types of glass in a wide range of compositions for applications ranging from the UV to the IR.

It has been demonstrated that the current technologies face challenges that can be overcome using the OVD for fabrication of optical preforms. A selection of additional projects carried out during the research programme showed the limitations and potential implementation of the OVD technology as a novel route to tackle the drawbacks of the conventional fabrication processes.

Chapter 12 Future Work

The following section describes the activities that had been identified as potential future developments for further research projects or improvement on the processes described in this thesis.

The solution doping apparatus can use a vertical setup and a more stable heat source. The development of the solution doping technique in OVD preforms can offer an alternative fabrication method for large core preforms.

Optical fibres from germanosilicate glass require further development to improve the propagation losses in the fibre. The dehydration process requires additional refinement to lower the OH content in the glass. The contribution towards a joint technology development with the PK supplier is proposed to overcome current equipment limitations.

Speciality optical fibres with compositions >50% of GeO_2 and up to pure germania glass require investigations on high non-linear optics. Also, it is required to explore additional applications such as Raman lasers, sensors or components for the photonics industry.

Aluminosilicate glass preforms doped by solution doping require further development to achieve a uniform dopant distribution and minimise defects on the final glass. The process still requires minor adjustments to prevent preferential depositions in the layer interfaces. Additional investigations using high-index coating are required to determine the transmission loss of the aluminosilicate glass. Also, evaluation of the laser performance of the optical fibres manufactured by this process is desired.

Phosphosilicate glass fabricated by OVD require further development and optical characterisations for loss and performance in laser configuration are part of the pending activities with this novel glass.

Optimisation of deposition conditions for aluminosilicate and phosphosilicate preforms is required to investigate a novel route to fabricate active preforms by combining the OVD process with a liquid phase deposition of rare earth ions. An additional benefit of the proposed approach is that it does not require the use of high-temperature RE delivery lines, as required for MCVD-CDS or gas phase deposition system.

Further fabrication of thulium doped fibres is required to extend this study by increasing the concentrations of aluminium and keeping the thulium concentration fixed. Conversely, a set of fibres is required using a fixed high concentration of aluminium and varying the concentration of thulium.

The gas phase deposition using a CDS system still requires refinement to incorporate high dopant concentrations and maintain the geometry of the core. Also, it is required a comprehensive study on the precursors decomposition mechanism to reduce the carbon impurities and reduce the losses in the fibre.

Hydrogen diffusion barrier fibres fabricating preforms using 3 or more rings will be desirable to compare the performance of hydrogen diffusion increasing the amount of alumina-rich regions. Fabrication of preforms with alternative core compositions will be desirable to identify the difference in diffusion changes on different glass compositions. Also, investigations in CH_4 molecular absorption would be desired to investigate absorption in the 1550nm wavelength region.

Validation of the customisable central depth refractive index profile experiments using a large core preform made by OVD would be ideal to demonstrate the effect of preform to fibre ratio and to show the potentiality of the OVD to overcome the current limitation faced by traditional fabrication processes.

Further experiments in 100% germania fibres using FBG's inscribed by femtosecond and by UV are desirable for demonstrations of applications in sensing and laser devices.

Fabrication of multi-element fibre with specific cut-off design can improve the attenuation levels for 1550 and 1650 nm. This practice of cut-off design is currently used by other SDM approaches such as MCF's. Also, a research for extending this investigations in the number of elements and multi-core-multi-element configuration is still not demonstrated.

Appendix A

A.1 Method of fabricating handles for OVD deposition

Material: 890 mm length of CFQ tube with ∅ = 20 mm, 2 mm wall thickness, previously drilled as shown in Figure 17.

- Burner speed = 0.027 [m·min^{-1}]
- H_2/O_2 ratio = 2

Conditions: The distance between the end of the tube and the end of the setup end position is required to be 280 mm. Table 24 shows the end position referred from the desired starting point, which is recommended to be 250 mm on the Heathway MCVD lathe using absolute values for carriage positions.

Number of pass	$V_{tailstock}$ [m·min^{-1}]	H_2 Flow [slm]	End position
1	6.33	20	373
2	7.16	19	406
3	8.25	18	453
4	9.72	17	527
5	3.27	16	560

Table 24. Fabrication conditions for OVD handles.

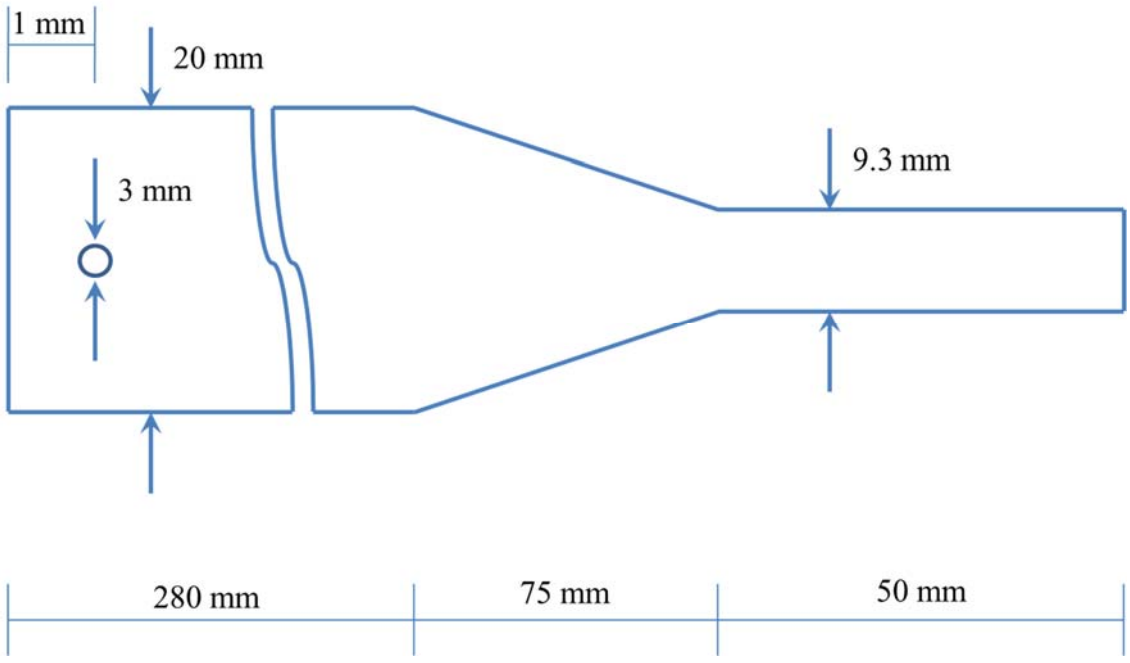

Figure 17. Schematic of OVD handle.

Appendix B

B.1 Extended data for $SiCl_4$ chemical reactions

B.1.1 Reaction 1:

$$SiCl_4 \longrightarrow Si + 2\,Cl_2$$

Structures:

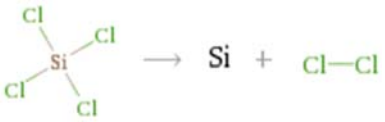

Equilibrium constant:

$$K_c = \frac{[Cl_2]^2[Si]}{[SiCl_4]}$$

B.1.2 Reaction 2:

$$SiCl_4 + 2\,H_2 \longrightarrow 4\,HCl + Si$$

Structures:

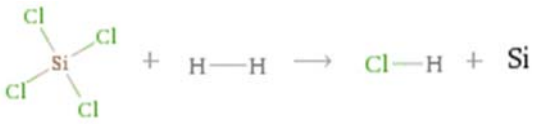

Equilibrium constant:

$$K_c = \frac{[HCl]^4[Si]}{[H_2]^2[SiCl_4]}$$

B.1.3 Reaction 3:

$$2\,SiCl_4 + 3\,H_2O + O_2 \longrightarrow 4\,HCl + 2\,SiO_2 + 2\,Cl_2 + H_2O$$

Total ionic equation:

$$2\,SiCl_4 + 3\,H_2O + O_2 \longrightarrow 4\,H^+ + 4\,Cl^- + 2\,SiO_2 + 2\,Cl_2 + H_2O$$

Net ionic equation:

$$2\,SiCl_4 + O_2 + 2\,H_2O \longrightarrow 4\,H^+ + 4\,Cl^- + 2\,SiO_2 + 2\,Cl_2$$

Structures:

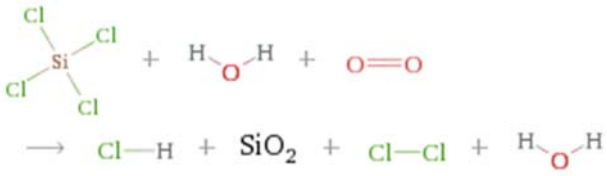

Equilibrium constant:

$$K_c = \frac{[HCl]^4[Cl_2]^2[SiO_2]^2[H_2O]}{[O_2][SiCl_4]^2[H_2O]^3}$$

B.1.4 Reaction 4:

$$SiCl_4 + 2\,H_2O + O_2 \longrightarrow 4\,HCl + SiO_2 + O_2$$

Total ionic equation:

$$SiCl_4 + 2\,H_2O + O_2 \longrightarrow 4\,H^+ + 4\,Cl^- + SiO_2 + O_2$$

Net ionic equation:

$$SiCl_4 + 2\,H_2O \longrightarrow 4\,H^+ + 4\,Cl^- + SiO_2$$

Structures:

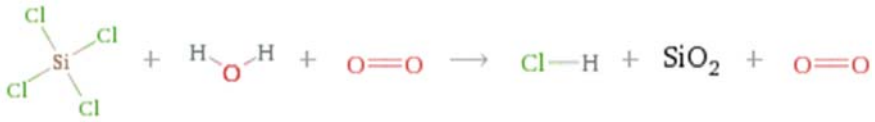

Equilibrium constant:

$$K_c = \frac{[HCl]^4[SiO_2]}{[SiCl_4][H_2O]^2}$$

B.1.5 Reaction 5:

$$2\,SiCl_4 + 2\,H_2O + O_2 \longrightarrow 4\,HCl + 2\,SiO_2 + 2\,Cl_2$$

Total ionic equation:

$$2\,SiCl_4 + 2\,H_2O + O_2 \longrightarrow 4\,H^+ + 4\,Cl^- + 2\,SiO_2 + 2\,Cl_2$$

Structures:

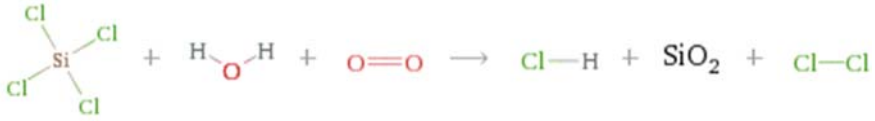

Equilibrium constant:

$$K_c = \frac{[HCl]^4[Cl_2]^2[SiO_2]^2}{[O_2][SiCl_4]^2[H_2O]^2}$$

B.1.6 Reaction 6:

$$SiCl_4 + 4\,H_2 + 3\,O_2 \longrightarrow 4\,HCl + SiO_2 + 2\,H_2O + O_2$$

Total ionic equation:

$$SiCl_4 + 4\,H_2 + 3\,O_2 \longrightarrow 4\,H^+ + 4\,Cl^- + SiO_2 + 2\,H_2O + O_2$$

Net ionic equation:

$$SiCl_4 + 4\,H_2 + 2\,O_2 \longrightarrow 4\,H^+ + 4\,Cl^- + SiO_2 + 2\,H_2O$$

Structures:

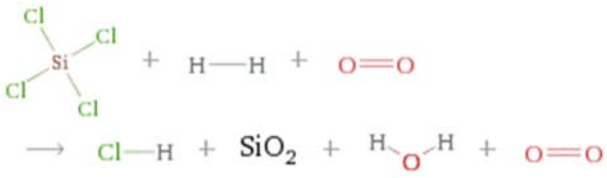

Equilibrium constant:

$$K_c = \frac{[HCl]^4[O_2][SiO_2][H_2O]^2}{[H_2]^4[O_2]^3[SiCl_4]}$$

B.1.7 Reaction 7:

$$SiCl_4 + 2\,H_2O \longrightarrow 4\,HCl + SiO_2$$

Total ionic equation:

$$SiCl_4 + 2\,H_2O \longrightarrow 4\,H^+ + 4\,Cl^- + SiO_2$$

Structures:

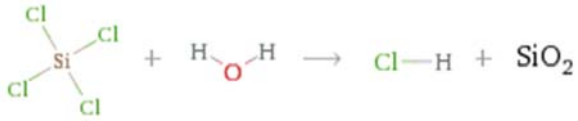

Equilibrium constant:

$$K_c = \frac{[HCl]^4[SiO_2]}{[SiCl_4][H_2O]^2}$$

B.1.8 Reaction 8:

$$SiCl_4 + 4\,H_2 + 2\,O_2 \longrightarrow 4\,HCl + SiO_2 + 2\,H_2O$$

Total ionic equation:

$$SiCl_4 + 4\,H_2 + 2\,O_2 \longrightarrow 4\,H^+ + 4\,Cl^- + SiO_2 + 2\,H_2O$$

Structures:

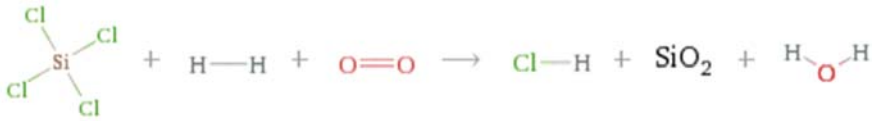

Equilibrium constant:

$$K_c = \frac{[HCl]^4[SiO_2][H_2O]^2}{[H_2]^4[O_2]^2[SiCl_4]}$$

B.1.9 Reaction 9:

$$SiCl_4 + 2\,H_2 + O_2 \longrightarrow 4\,HCl + SiO_2$$

Total ionic equation:

$$SiCl_4 + 2\,H_2 + O_2 \longrightarrow 4\,H^+ + 4\,Cl^- + SiO_2$$

Structures:

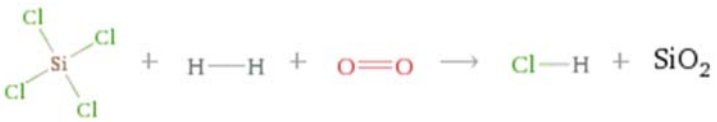

Equilibrium constant:

$$K_c = \frac{[HCl]^4[SiO_2]}{[H_2]^2[O_2][SiCl_4]}$$

B.1.10 Reaction 10:

$$SiCl_4 + O_2 \longrightarrow 2\,Cl_2 + SiO_2$$

Structures:

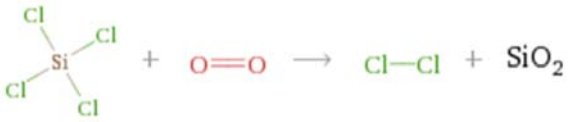

Equilibrium constant:

$$K_c = \frac{[Cl_2]^2[SiO_2]}{[O_2][SiCl_4]}$$

Appendix C

C.1 Thermodynamic calculations for $SiCl_4$ chemical reactions

C.1.1 Reaction 1

$$G=H-TS$$

$$\Delta G=\Delta H-T\Delta S$$

$$\Delta H=\Sigma H_{f(prod)}-\Sigma H_{f(React)}$$

1	$SiCl_4$	+			+			=	2	Cl_2	+		Si	Unbalanced
1	$SiCl_4$	+			+			=	2	Cl_2	+	1	Si	Balanced
1	-657	+	0	0	+	0	0	=	2	0	+	1	0	All data in $kJ \cdot mol^{-1}$ @ 298K
	-657			0			0			0			0	Subtotal
	$\Sigma H_{f(React)}$				=		-657			$\Sigma H_{f(prod)}$	=		0	
	ΔH				=		0	-		-657				
	ΔH				=		657			$kJ \cdot mol^{-1}$ @ 298K				

$$\Delta S=\Sigma S_{(prod)}-\Sigma S_{(React)}$$

1	$SiCl_4$	+			+			=	2	Cl_2	+	1	Si	Balanced
1	330.86	+	0		+	0	0	=	2	222.97	+	1	18.83	All data in $J \cdot mol^{-1} K^{-1}$
	330.86			0			0			445.94			18.83	Subtotal
	$\Sigma S_{(React)}$				=		330.86			$\Sigma S_{(prod)}$	=		464.77	
	ΔS				=		464.77	-		330.86				
	ΔS				=		133.91			$J \cdot mol^{-1} K^{-1}$				
	ΔS				=		0.13391			$kJ \cdot mol^{-1} K^{-1}$				

C.1.2 Reaction 2

$G=H-TS$

$\Delta G=\Delta H-T\Delta S$

$\Delta H=\Sigma H_{f(prod)}-\Sigma H_{f(React)}$

1	$SiCl_4$	+	2	H_2	+		=	4	HCl	+		Si	Unbalanced
1	$SiCl_4$	+	2	H_2	+		=	4	HCl	+		Si	Balanced
1	-657	+	2	0	+	0	=	4	-92.31	+	0	0	All data in $kJ\cdot mol^{-1}$ @ 298K
	-657			0		0			-369.24			0	Subtotal

$\Sigma H_{f(React)}$	=	-657		$\Sigma H_{f(prod)}$	=	-369.24
ΔH	=	-369.24	-	-657		
ΔH	=	287.76	$kJ\cdot mol^{-1}$ @ 298K			

$\Delta S=\Sigma S_{(prod)}-\Sigma S_{(React)}$

1	$SiCl_4$	+	2	H_2	+		=	4	HCl	+		Si	Balanced
1	330.86	+	2	130.7	+	0	=	4	186.902	+	0	18.83	All data in $J\cdot mol^{-1}\ K^{-1}$
	330.86			261.4		0			747.608			18.83	Subtotal

$\Sigma S_{(React)}$	=	592.26		$\Sigma S_{(prod)}$	=	766.438
ΔS	=	766.438	-	592.26		
ΔS	=	174.178	$J\cdot mol^{-1}\ K^{-1}$			
ΔS	=	0.174178	$kJ\cdot mol^{-1}\ K^{-1}$			

C.1.3 Reaction 3

$G=H-TS$

$\Delta G=\Delta H-T\Delta S$

$\Delta H=\Sigma H_{f(prod)}-\Sigma H_{f(React)}$

1	$SiCl_4$	+	1	H_2O	+	1	O_2	=	4	HCl	+	1	SiO_2	+	1	Cl_2	+	1	H_2O	Unbalanced
0.3	$SiCl_4$	+	0.5	H_2O	+	0.3	O_2	=	0	HCl	+	0.3	SiO_2	+	0.5	Cl_2	+	0.5	H_2O	Balanced
0.3	-657	+	0.5	-241.82	+	0.3	0	=	0	-92.31	+	0.3	-911	+	0.5	0	+	0.5	-241.82	All data in $kJ\cdot mol^{-1}$ @ 298K
	-164.25			-120.91			0			0			-227.75			0			-120.91	Subtotal

$\Sigma H_{f(React)}$	=	-285.16		$\Sigma H_{f(prod)}$	=	-348.66
ΔH	=	-348.66	-	-285.16		
ΔH	=	-63.5	$kJ\cdot mol^{-1}$ @ 298K			

$\Delta S=\Sigma S_{(prod)}-\Sigma S_{(React)}$

0.3	$SiCl_4$	+	0.5	H_2O	+	0.3	O_2	=	0	HCl	+	0.3	SiO_2	+	0.5	Cl_2	+	0.5	H_2O	Balanced
0.3	330.86	+	0.5	188.72	+	0.3	205.07	=	0	186.902	+	0.3	42		0.5	222.97		0.5	188.72	All data in $J\cdot mol^{-1}\ K^{-1}$
	82.715			94.36			51.2675			0			10.5			111.485			94.36	Subtotal

$\Sigma S_{(React)}$	=	228.3425		$\Sigma S_{(prod)}$	=	216.345
ΔS	=	216.345	-	228.3425		
ΔS	=	-11.9975	$J\cdot mol^{-1}\ K^{-1}$			
ΔS	=	-0.012	$kJ\cdot mol^{-1}\ K^{-1}$			

C.1.4 Reaction 4

$G=H-TS$

$\Delta G=\Delta H-T\Delta S$

$\Delta H=\Sigma H_{f(prod)}-\Sigma H_{f(React)}$

1	$SiCl_4$	+	1	H_2O	+	1	O_2	=	4	HCl	+	1	SiO_2	+	1	O_2	Unbalanced
0.3	$SiCl_4$	+	0.5	H_2O	+	0.3	O_2	=	1	HCl	+	0.3	SiO_2	+	0.3	O_2	Balanced
0.3	-657	+	0.5	-241.82	+	0.3	0	=	1	-92.31	+	0.3	-911	+	0.3	0	All data in $kJ\cdot mol^{-1}$ @ 298K
	-164.25			-120.91			0			-92.31			-227.75			0	Subtotal

$\Sigma H_{f(React)}$	=	-285.16		$\Sigma H_{f(prod)}$ =	-320.06
ΔH	=	-320.06	-	-285.16	
ΔH	=	-34.9	$kJ\cdot mol^{-1}$ @ 298K		

$\Delta S=\Sigma S_{(prod)}-\Sigma S_{(React)}$

0.3	$SiCl_4$	+	0.5	H_2O	+	0.3	O_2	=	1	HCl	+	0.3	SiO_2	+	0.3	O_2	Balanced
0.3	330.86	+	0.5	188.72	+	0.3	205.07	=	1	186.902	+	0.3	42		0.3	205.07	All data in $J\cdot mol^{-1} K^{-1}$
	82.715			94.36			51.2675			186.902			10.5			51.2675	Subtotal

$\Sigma S_{(React)}$	=	228.3425		$\Sigma S_{(prod)}$ =	248.6695
ΔS	=	248.6695	-	228.3425	
ΔS	=	20.327	$J\cdot mol^{-1} K^{-1}$		
ΔS	=	0.020327	$kJ\cdot mol^{-1} K^{-1}$		

C.1.5 Reaction 5

$G=H-TS$

$\Delta G=\Delta H-T\Delta S$

$\Delta H=\Sigma H_{f(prod)}-\Sigma H_{f(React)}$

1	$SiCl_4$	+	1	H_2O	+	1	O_2	=	4	HCl	+	1	SiO_2	+	1	Cl_2	Unbalanced
0.5	$SiCl_4$	+	0.5	H_2O	+	0.3	O_2	=	1	HCl	+	0.5	SiO_2	+	0.5	Cl_2	Balanced
0.5	-657	+	0.5	-241.82	+	0.3	0	=	1	-92.31	+	0.5	-911	+	0.5	0	All data in $kJ\cdot mol^{-1}$ @ 298K
	-328.5			-120.91			0			-92.31			-455.5			0	Subtotal

$\Sigma H_{f(React)}$	=	-449.41		$\Sigma H_{f(prod)}$ =	-547.81
ΔH	=	-547.81	-	-449.41	
ΔH	=	-98.4	$kJ\cdot mol^{-1}$ @ 298K		

$\Delta S=\Sigma S_{(prod)}-\Sigma S_{(React)}$

0.5	$SiCl_4$	+	0.5	H_2O	+	0.3	O_2	=	1	HCl	+	0.5	SiO_2	+	0.5	Cl_2	Balanced
0.5	330.86	+	0.5	188.72	+	0.3	205.07	=	1	186.902	+	0.5	42		0.5	222.97	All data in $J\cdot mol^{-1} K^{-1}$
	165.43			94.36			51.2675			186.902			21			111.485	Subtotal

$\Sigma S_{(React)}$	=	311.0575		$\Sigma S_{(prod)}$ =	319.387
ΔS	=	319.387	-	311.0575	
ΔS	=	8.3295	$J\cdot mol^{-1} K^{-1}$		
ΔS	=	0.00833	$kJ\cdot mol^{-1} K^{-1}$		

C.1.6 Reaction 6

$G=H-TS$

$\Delta G=\Delta H-T\Delta S$

$\Delta H=\Sigma H_{f(prod)}-\Sigma H_{f(React)}$

1	$SiCl_4$	+	2	H_2	+	1	O_2	=	4	HCl	+	1	SiO_2	+	1	H_2O	+	1	O_2	Unbalanced
0.2	$SiCl_4$	+	0.7	H_2	+	0.5	O_2	=	0.7	HCl	+	0.2	SiO_2	+	0.3	H_2O	+	0.2	O_2	Balanced
0.2	-657	+	0.7	0	+	0.5	0	=	0.7	-92.31	+	0.2	-911	+	0.3	-241.82	+	0.2	0	All data in $kJ\cdot mol^{-1}$ @ 298K
	-109.5			0			0			-61.54			-151.833			-80.6067			0	Subtotal

$\Sigma H_{f(React)}$	=	-109.5		$\Sigma H_{f(prod)}$	=	-293.98
ΔH	=	-293.98	-	-109.5		
ΔH	=	-184.48	$kJ\cdot mol^{-1}$ @ 298K			

$\Delta S=\Sigma S_{(prod)}-\Sigma S_{(React)}$

0.2	$SiCl_4$	+	0.7	H_2	+	0.5	O_2	=	0.7	HCl	+	0.2	SiO_2	+	0.3	H_2O	+	0.2	O_2	Balanced
0.2	330.86	+	0.7	130.7	+	0.5	205.07	=	0.7	186.902	+	0.2	42		0.3	188.72	+	0.2	205.07	All data in $J\cdot mol^{-1}\,K^{-1}$
	55.14333			87.13333			102.535			124.60133			7			62.90667			34.17833	Subtotal

$\Sigma S_{(React)}$	=	244.8117		$\Sigma S_{(prod)}$	=	228.6863
ΔS	=	228.6863	-	244.81167		
ΔS	=	-16.1253	$J\cdot mol^{-1}\,K^{-1}$			
ΔS	=	-0.01613	$kJ\cdot mol^{-1}\,K^{-1}$			

C.1.7 Reaction 7

$G=H-TS$

$\Delta G=\Delta H-T\Delta S$

$\Delta H=\Sigma H_{f(prod)}-\Sigma H_{f(React)}$

1	$SiCl_4$	+	1	H_2O	+			=	4	HCl	+	1	SiO_2			Unbalanced
0.5	$SiCl_4$	+	1	H_2O	+			=	2	HCl	+	0.5	SiO_2			Balanced
0.5	-657	+	1	-241.82	+	0	0	=	2	-92.31	+	0.5	-911			All data in $kJ\cdot mol^{-1}$ @ 298K
	-328.5			-241.82			0			-184.62			-455.5			Subtotal

$\Sigma H_{f(React)}$	=	-570.32		$\Sigma H_{f(prod)}$	=	-640.12
ΔH	=	-640.12	-	-570.32		
ΔH	=	-69.8	$kJ\cdot mol^{-1}$ @ 298K			

$\Delta S=\Sigma S_{(prod)}-\Sigma S_{(React)}$

0.5	$SiCl_4$	+	1	H_2O	+			=	2	HCl	+	0.5	SiO_2			Balanced
0.5	330.86	+	1	188.72	+	0	0	=	2	186.902	+	0.5	42			All data in $J\cdot mol^{-1}\,K^{-1}$
	165.43			188.72			0			373.804			21			Subtotal

$\Sigma S_{(React)}$	=	354.15		$\Sigma S_{(prod)}$	=	394.804
ΔS	=	394.804	-	354.15		
ΔS	=	40.654	$J\cdot mol^{-1}\,K^{-1}$			
ΔS	=	0.040654	$kJ\cdot mol^{-1}\,K^{-1}$			

C.1.8 Reaction 8

$$G=H-TS$$

$$\Delta G=\Delta H-T\Delta S$$

$$\Delta H=\Sigma H_{f(prod)}-\Sigma H_{f(React)}$$

1	$SiCl_4$	+	2	H_2	+	1	O_2	=	4	HCl	+	1	SiO_2	+	1	H_2O	Unbalanced
0.3	$SiCl_4$	+	1	H_2	+	0.5	O_2	=	1	HCl	+	0.3	SiO_2	+	0.5	H_2O	Balanced
0.3	-657	+	1	0	+	0.5	0	=	1	-92.31	+	0.3	-911	+	0.5	-241.82	All data in $kJ{\cdot}mol^{-1}$ @ 298K
	-164.25			0			0			-92.31			-227.75			-120.91	Subtotal

$\Sigma H_{f(React)}$	=	-164.25		$\Sigma H_{f(prod)}$	=	-440.97
ΔH	=	-440.97	-	-164.25		
ΔH	=	-276.72		$kJ{\cdot}mol^{-1}$ @ 298K		

$$\Delta S=\Sigma S_{(prod)}-\Sigma S_{(React)}$$

0.3	$SiCl_4$	+	1	H_2	+	0.5	O_2	=	1	HCl	+	0.3	SiO_2	+	0.5	H_2O	Balanced
0.3	330.86	+	1	130.7	+	0.5	205.07	=	1	186.902	+	0.3	42	+	0.5	188.72	All data in $J{\cdot}mol^{-1}\,K^{-1}$
	82.715			130.7			102.535			186.902			10.5			94.36	Subtotal

$\Sigma S_{(React)}$	=	315.95		$\Sigma S_{(prod)}$	=	291.762
ΔS	=	291.762	-	315.95		
ΔS	=	-24.188		$J{\cdot}mol^{-1}\,K^{-1}$		
ΔS	=	-0.02419		$kJ{\cdot}mol^{-1}\,K^{-1}$		

C.1.9 Reaction 9

$$G=H-TS$$

$$\Delta G=\Delta H-T\Delta S$$

$$\Delta H=\Sigma H_{f(prod)}-\Sigma H_{f(React)}$$

1	$SiCl_4$	+	2	H_2	+	1	O_2	=	4	HCl	+	1	SiO_2	Unbalanced
0.5	$SiCl_4$	+	1	H_2	+	0.5	O_2	=	2	HCl	+	0.5	SiO_2	Balanced
0.5	-657	+	1	0	+	0.5	0	=	2	-92.31	+	0.5	-911	All data in $kJ\cdot mol^{-1}$ @ 298K
	-328.5			0			0			-184.62			-455.5	Subtotal

$\Sigma H_{f(React)}$	=	-328.5		$\Sigma H_{f(prod)}$ =	-640.12
ΔH	=	-640.12	-	-328.5	
ΔH	=	-311.62	$kJ\cdot mol^{-1}$ @ 298K		

$$\Delta S=\Sigma S_{(prod)}-\Sigma S_{(React)}$$

0.5	$SiCl_4$	+	1	H_2	+	0.5	O_2	=	2	HCl	+	0.5	SiO_2	Balanced
0.5	330.86	+	1	130.7	+	0.5	205.07	=	2	186.902	+	0.5	42	All data in $J\cdot mol^{-1}\ K^{-1}$
	165.43			130.7			102.535			373.804			21	Subtotal

$\Sigma S_{(React)}$	=	398.665		$\Sigma S_{(prod)}$ =	394.804
ΔS	=	394.804	-	398.665	
ΔS	=	-3.861	$J\cdot mol^{-1}\ K^{-1}$		
ΔS	=	-0.00386	$kJ\cdot mol^{-1}\ K^{-1}$		

C.1.10 Reaction 10

$$G=H-TS$$

$$\Delta G=\Delta H-T\Delta S$$

$$\Delta H=\Sigma H_{f(prod)}-\Sigma H_{f(React)}$$

0.5	$SiCl_4$	+			+	0.5	O_2	=	2	Cl_2	+ 0.5	SiO_2	Unbalanced
0.5	$SiCl_4$	+			+	0.5	O_2	=	2	Cl_2	+ 0.5	SiO_2	Balanced
0.5	-657	+	0	0	+	0.5	0	=	2	0	+ 0.5	-911	All data in $kJ \cdot mol^{-1}$ @ 298K
	-328.5			0			0			0		-455.5	Subtotal
	$\Sigma H_{f(React)}$				=		-328.5			$\Sigma H_{f(prod)}$	=	-455.5	
	ΔH				=		-455.5	-		-328.5			
	ΔH				=		-127			$kJ \cdot mol^{-1}$ @ 298K			

$$\Delta S=\Sigma S_{(prod)}-\Sigma S_{(React)}$$

0.5	$SiCl_4$	+			+	0.5	O_2	=	2	Cl_2	+ 0.5	SiO_2	Balanced
0.5	330.86	+	0		+	0.5	205.07	=	2	222.97	+ 0.5	42	All data in $J \cdot mol^{-1} K^{-1}$
	165.43			0			102.535			445.94		21	Subtotal
	$\Sigma S_{(React)}$				=		267.965			$\Sigma S_{(prod)}$	=	466.94	
	ΔS				=		466.94	-		267.965			
	ΔS				=		198.975			$J \cdot mol^{-1} K^{-1}$			
	ΔS				=		0.198975			$kJ \cdot mol^{-1} K^{-1}$			

Appendix D

D.1 List of publications

2018

- Shoulin Jiang, Lin Ma, Martin Nunez Velazquez, Zuyuan He and Jayanta Kumar Sahu, Design of 125-μm Cladding Diameter Multicore Fibers with High Core Multiplexing Factor for Wideband Optical Transmission, Journal of Lightwave Technology, 2018 (Manuscript submitted).
- N.J. Ramirez-Martinez, M. Nunez Velazquez, A.A. Umnikov and J.K. Sahu, Efficient Thulium-doped Fiber Laser Operating in the 1890 – 2080nm Wavelength Band, Advanced Photonics Congress, Zurich, Switzerland, 2018.
- Shoulin Jiang, Lin Ma, Martin Nunez Velazquez, Zuyuan He and Jayanta Kumar Sahu, Optimized design of 125-μm 6-core fiber with large effective area for wideband optical transmission, Conference on Lasers and Electro-Optics – Pacific Rim, Hong Kong, 2018.
- Halder, Di. Lin, A. A. Umnikov, N.J. Ramirez- Martinez, M. Nunez-Velazquez, P. Barua, S. Alam and J.K. Sahu, Picosecond Yb-doped alumino-phospho-silicate fiber MOPA with >35kW peak power, Advanced Photonics Congress, Zurich, Switzerland, 2018.
- N.J. Ramirez-Martinez, M. Nunez Velazquez, A.A. Umnikov and J.K. Sahu, Novel Fabrication Technique for Highly Efficient Tm-doped Fibres, Conference on Lasers and Electro-Optics, San Jose California, United States, 2018.
- Halder, Di. Lin, A. A. Umnikov, N.J. Ramirez- Martinez, M. Nunez-Velazquez, P. Barua, S. Alam and J.K. Sahu (2018) Yb-doped Large-Mode-Area Al-P-Silicate Laser Fiber fabricated by MCVD, Conference on Lasers and Electro-Optics, San Jose California, United States, 2018
- Angeles Camacho, Martin Nunez, Jayanta Sahu, Additive Manufacturing Towards Fabrication of the Next Generation of Optical Fibres, SPIE Focus, Trento Italy, 2018.

2017

- Donko, M. Nuñez-Velazquez, P. Barua, F. Guzman Cruz, R. Ismaeel, T. Lee, J.K. Sahu, M. Beresna, and G. Brambilla, Femtosecond inscription and thermal testing of Bragg gratings in high concentration (40 mol%) Germania-doped optical fibre, Optics Express 25, 32879-32886, 2017.
- Donko, A., Nuñez Velazquez, M., Barua, P., Sahu, J., Beresna, M. and Brambilla, G., Point-by-point femtosecond laser inscription of Bragg gratings in high NA (>0.4) germania-doped optical fibre At WSOF 2017, Limassol, Cyprus. 11 - 13 Oct 2017. 3 pp.

2016

- Thipparapu, Naresh, Umnikov, Andrey, Barua, Pranabesh, Nuñez Velazquez, Martin and Sahu, Jayanta, A review on our latest amplifier and laser demonstrations by Bi-doped fibers At International Training School on Fiber Lasers & Optical Fiber Technology 2016, Czech Republic. 30 Aug - 01 Sep 2016.
- Sahu, Jayanta, Thipparapu, Naresh, Umnikov, Andrey, Barua, Pranabesh and Nuñez Velazquez, Martin, Amplifier and laser demonstrations in Bi-doped silica optical fibers At International Conference on Fibre Optics and Photonics 2016, India. 04 - 08 Dec 2016.
- Thipparapu, Naresh, Umnikov, Andrey, Barua, Pranabesh, Nuñez Velazquez, Martin and Sahu, Jayanta, Bi-doped fiber amplifiers: optical properties, challenges and applications At XXIst International Krutyn Summer School 2016, Poland. 04 - 10 Sep 2016.
- Posner, Matthew, John, Pearl, Wong, Nicholas, Heng Loong, Mittal, Vinita and Nuñez Velazquez, Martin, From school classes to UNESCO: IYL-enabled environments for tackling the STEM skills shortage through student-led outreach At SPIE Optical Engineering + Applications Symposium, United States. 28 Aug - 01 Sep 2016. 10 pp. (doi:10.1117/12.2238222).
- Jain, Deepak, Alam, Shaif-ul, Jung, Yongmin, Barua, Pranabesh, Nuñez Velazquez, Martin and Sahu, Jayanta, Highly efficient Yb-free Er-La-Al doped ultra-low Na large mode area single-trench fiber laser At SPIE LASE 2016, United States. 13 - 18 Feb 2016. (doi:10.1117/12.2211336).

2015

- Berendt, M.O., Spurrell, J., Barua, P., Umnikov, A.A., Nuñez Velazquez, M., Sahu, J.K., Alam, S.U. and Richardson, D.J., 5mJ pulsed Yb-doped all-fiber MOPA seeded by 0.2nm spectrally sliced super luminescent diode At

CLEO/Europe 2015 - European Conference on Lasers and Electro-Optics, Germany. 21 - 25 Jun 2015.

- Serrano Perez, Edgar, Nuñez Velazquez, Martin and Juárez Lopez, Fernando (2015) A numerical analysis of a MOCVD process for the growth of GaN nanowires using GaCl3 and NH3 Physica Status Solidi (c), 12, (4-5), pp. 389-393.
- Jain, Deepak, Alam, Shaif-ul, Sahu, Jayanta, Jung, Yongmin, Barua, Pranabesh and Nuñez Velazquez, Martin (2015) Highly efficient Yb-free Er-La-Al doped ultra low NA large mode area single-trench fiber laser Optics Express, 23, (22), pp. 28282-28827.

2014

- Tománek, Pavel, Senderáková, Dagmar, Páta, Petr, Cajzl, Jakub, Peterka, Pavel, Honzátko, Pavel, Mrázek, Jan, Podrazký, Ondřej, Todorov, Filip, Gladkov, Petar, Sahu, Jayanta, Nuñez Velazquez, Martin, Nekvindová, Pavla and Kašík, Ivan (2014) Characterization of fluorescence lifetime of Tm-doped fibers with increased quantum conversion efficiency At SPIE Photonics, Devices, and Systems VI, Czech Republic. 27 - 29 Aug 2014. (doi:10.1117/12.2070425).
- Jain, D., Jung, Y., Nuñez Velazquez, M. and Sahu, J.K. (2014) Extending single mode performance of all-solid large-mode-area single trench fiber Optics Express, 22, (25), pp. 31078-31091.
- Nuñez Velazquez, Martin and Lopez, Fernando Juárez (2014) Investigations into the growth of GaN nanowires by MOCVD using azidotrimethylsilane as nitrogen source Advanced Materials Research, 875-877, pp. 1483-1489. (doi:10.4028/www.scientific.net/AMR.875-877.1483).
- Jain, S., Duchez, J.B., Mebrouk, Y., Nuñez Velazquez, M., Mady, F., Dussardier, B., Benabdesselam, M. and Sahu, J.K. (2014) Thermally-stimulated emission analysis of bismuth-doped silica fibers Optical Materials, 4, (7), pp. 1361-1366. (doi:10.1364/OME.4.001361).

D.2 List of conferences

- Optical fibres for distributed sensors for real-time monitoring for detection of leakages and mechanical integrity of fuel lines, Innovation Match MX 2016-2017; Ciudad de Mexico, Mexico, May 31st – June 2nd 2017.
- Importance and contributions of the Mexican diaspora in Europe for the economic growth and technological development, Innovation Match MX2016-2017; Ciudad de Mexico, Mexico, May 31st – June 2nd 2017.
- New Generation of Optical Fibres, XIV Symposium of Mexican Students and Studies; University of Edinburgh, United Kingdom, June 2016.
- Speciality Optical Fibre Fabrication using Outside Vapour Deposition Process, XIII Symposium of Mexican Students and Studies; University College London, United Kingdom, July 2015.
- Two-Micron Optical Fibres, XII Symposium of Mexican Students and Studies; University of Leeds, United Kingdom, July 2014.
- Two Micron lasers, III Symposium of CONACyT Scholars in Europe; European Parliament, Strasburg, France, November 2013
- Manufacture of optical fibre using OVD technique for applications at 2 microns wavelength, XI Symposium of Mexican Students and Studies; University of Sheffield, United Kingdom, July 2013.
- Thulium doped fibres, spectroscopies and dopants behaviour modelling, XI Symposium of Mexican Students and Studies; University of Sheffield, United Kingdom, July 2013.
- Aluminosilicate Optical Fibres, dopants distribution and their impact in the refractive index profile, XI Symposium of Mexican Students and Studies; University of Sheffield, United Kingdom, July 2013.
- Synthesis of GaN nanowires by MOCVD using azidotrimethylsilane as Nitrogen precursor, XI Symposium of Mexican Students and Studies; University of Sheffield, United Kingdom, July 2013.
- Investigations into the growth of GaN nanowires by MOCVD using azidotrimethylsilane as nitrogen source, “International Conference on Frontiers of

Mechanical Engineering, Materials and Energy (ICFMEME 2012)", December 20-21, 2012, Beijing, China.

- Photoluminescence characterization of ZnS nanowires grown via colloidal suspension, Symposium 9, Photovoltaics, Solar Energy Materials & Technologies at the XX International Materials Research Congress, Cancun Mexico, August 14 - 19, 2011.
- Growth of ZnS nanowires using Zn[TMHD]2 as low-temperature precursor, Symposium 9, Photovoltaics, Solar Energy Materials & Technologies at the XX International Materials Research Congress, Cancun Mexico, August 14 - 19, 2011

List of References

1 Schultz, P. C. Fabrication of Optical-Waveguides by the Outside Vapor-Deposition Process. *Proc. IEEE* **68**, 1187-1190, doi: 10.1109/Proc.1980.11828 (1980).

2 Vandewoestine, R. V. & Morrow, A. J. Developments in Optical Wave-Guide Fabrication by the Outside Vapor-Deposition Process. *J. Lightwave Technol.* **4**, 1020-1025, doi: 10.1109/Jlt.1986.1074844 (1986).

3 Li, T. *Optical fiber communications*. (Academic Press, 1985).

4 Tsujikawa, K., Tajima, K. & Zhou, J. Intrinsic loss of optical fibers. *Optical Fiber Technology* **11**, 319-331, doi:http://dx.doi.org/10.1016/j.yofte.2005.04.003 (2005).

5 Tandon, P. & Murtagh, M. Particle–vapor interaction in deposition systems: influence on deposit morphology. *Chem. Eng. Sci.* **60**, 1685-1699, doi:10.1016/j.ces.2004.10.027 (2005).

6 Takahashi, H., Sugimoto, I. & Sato, T. Germanium-oxide glass optical fibre prepared by VAD method. *Electron. Lett* **18**, 398-399, doi:10.1049/el:19820272 (1982).

7 Sakaguchi, S. & Todoroki, S. Optical properties of GeO_2 glass and optical fibers. *Appl. Opt.* **36**, 6809-6814 (1997).

8 Higby, P. L., Aggarwal, I. D. & Friebele, E. J. Low Loss Glass And Optical Fibers Therefrom. United States patent US5305414 (1994).

9 Micoulaut, M., Cormier, L. & Henderson, G. S. The structure of amorphous, crystalline and liquid GeO_2. *J. Phys.: Condens. Matter* **18** (2006).

10 Luu-Gen Hwa, C.-C. C., Shin-Lang Hwang. Optical Properties of Calcium-Aluminate Oxide Glasses. *Chinese Journal of Physics* **35**, 78-89 (1997).

11 Sakamoto, A., Asano, H., Wada, M., Yamamoto, S. & Nishii, J. Mechanical and optical properties of silica glass optical fiber with low-expansion glass-ceramic jacket. *J. Ceram. Soc. Jpn.* **111**, 640-644, doi: 10.2109/jcersj.111.640 (2003).

12 Higby, P. L. & Aggarwal, I. D. Properties of barium gallium germanate glasses. *J. Non-Cryst. Solids* **163**, 303-308, doi:http://dx.doi.org/10.1016/0022-3093(93)91308-P (1993).

13 Simpson, D. A. *Spectroscopy of Thulium Doped Silica Glass* PhD thesis, Victoria University, (2006).

14 Agger, S. D. & Povlsen, J. H. Emission and absorption cross section of thulium doped silica fibers. *Opt. Express* **14**, 50-57 (2006).

15 Gebavi, H. *et al.* Spectroscopy and optical characterization of thulium doped TZN glasses. *J Phys D Appl Phys* **43**, 135104, doi:Artn 135104 Doi 10.1088/0022-3727/43/13/135104 (2010).

16 Judd, B. R. Optical Absorption Intensities of Rare-Earth Ions. *Phys. Rev.* **127**, 750-761 (1962).

17 Ofelt, G. S. Structure of the f^6 Configuration with Application to Rare-Earth Ions. *J. Chem. Phys.* **38**, 2171-2180 (1963).

18 Turri, G. *et al.* Temperature-dependent spectroscopic properties of Tm^{3+} in germanate, silica, and phosphate glasses: A comparative study. *J. Appl. Phys.* **103**, 093104-093107 (2008).

19 Pal, M. *et al.* Investigation of the deposition of porous layers by the MCVD method for the preparation of rare-earth doped cores of optical fibres. *Opt. Commun.* **254**, 88-95, doi:10.1016/j.optcom.2005.05.022 (2005).

20 Dhar, A. *et al.* An improved method of controlling rare earth incorporation in optical fiber. *Opt. Commun.* **277**, 329-334, doi:10.1016/j.optcom.2007.05.053 (2007).

21 Tang, F. Z., McNamara, P., Barton, G. W. & Ringer, S. P. Nanoscale characterization of silica soots and aluminium solution doping in optical fibre fabrication. *J. Non-Cryst. Solids* **352**, 3799-3807, doi: 10.1016/j.jnoncrysol.2006.06.014 (2006).

22 Dhar, A., Das, S., Paul, M. C., Pal, A. & Sen, R. Study of incorporation efficiency of different precursor salts in fabrication of rare-earth doped optical fibers. *physica status solidi (a)*, doi:10.1002/pssa.201330315 (2013).

23 Tang, F. Z., McNamara, P., Barton, G. W. & Ringer, S. P. Multiple solution-doping in optical fibre fabrication I - Aluminium doping. *J. Non-Cryst. Solids* **354**, 927-937, doi: 10.1016/j.jnonerysol.2007.08.020 (2008).

24 Tang, F. Z., McNamara, P., Barton, G. W. & Ringer, S. P. Multiple solution-doping in optical fibre fabrication - II - Rare-earth and aluminium co-doping. *J. Non-Cryst. Solids* **354**, 1582-1590, doi: 10.1016/j.jnoncrysol.2007.10.006 (2008).

25 Webb, A. S. *et al.* MCVD in-situ solution doping process for the fabrication of complex design large core rare-earth doped fibers. *J. Non-Cryst. Solids* **356**, 848-851, doi:10.1016/j.jnoncrysol.2010.01.008 (2010).

26 Blankenship, M. G. & Deneka, C. W. The Outside Vapor Deposition Method of Fabricating Optical Waveguide Fibers. *IEEE Trans. Microwave Theory Tech.* **30**, 1406-1411, doi:10.1109/tmtt.1982.1131273 (1982).

27 James, F. H. Method of making a transparent article of silica. US2272342 (1942).

28 Hanawa, F., Inagaki, N., Nakahara, M., Suda, H. & Suto, S. Fabrication methods of doped silica glass and optical fiber preform by using the doped silica glass. Japan patent US4414012 (1983).

29 Fukuda, O., Inada, K., Sanada, K. & Takahashi, S. Method for producing multi-component glass fiber preform. Japan patent US4336049 (1982).

30 Schultz, P. C. Method of producing glass by flame hydrolysis. US3859073 (1975).

31 Bartholomew, R. F. & Sadd, A. L. Solution Doping of Porous Preforms. US005151117A (1992).

32 Petit, V., Le Rouge, A., Béclin, F., El Hamzaoui, H. & Bigot, L. Experimental Study of SiO_2 Soot Deposition using the Outside Vapor Deposition Method. *Aerosol Sci. Technol.* **44**, 388-394, doi:10.1080/02786821003671315 (2010).

33 Kakuzen, H., Kurosaki, S. & Usui, Y. Process for producing glass member. Japan patent US4225330 (1980).

34 Macedo, P. B., Murai, S. & Simmons, J. H. Method of producing a glass article having a graded refractive index profile of a parabolic nature. Japan patent US4302231 (1981).

35 Baret, G., Madar, R. & Bernard, C. Silica‐Based Oxide Systems: I . Experimental and Calculated Phase Equilibria in Silicon, Boron, Phosphorus, Germanium, and Arsenic Oxide Mixtures. *J. Electrochem. Soc.* **138**, 2830-2835, doi:10.1149/1.2086066 (1991).

36 Cuevas, R. F., Sekiya, E. H., Garcia-Quiroz, A., Da Silva, E. C. & Suzuki, C. K. Dependence of H_2/O_2 ratio and GeO_2 content on the enhancement of second-order non-linearity related defects in Ge-doped optical fiber preforms. *Materials Science and Engineering: B* **111**, 135-141, doi:10.1016/j.mseb.2004.04.010 (2004).

37 Deringer, V. L., Lumeij, M., Stoffel, R. P. & Dronskowski, R. Ab initio study of the high-temperature phase transition in crystalline GeO_2. *J. Comput. Chem.* **34**, 2320-2326, doi:10.1002/jcc.23387 (2013).

38 Sanada, K., Moriyama, T. & Inada, K. Chlorination and vaporization of GeO_2 component in SiO_2:GeO_2 porous preform in dehydration process by VAD method and spontaneous formation of SiO_2 cladding layer during the dehydration by selective vaporization of GeO_2. *J. Non-Cryst. Solids* **194**, 163-172, doi: 10.1016/0022-3093(95)00481-5 (1996).

39 Jetschke, S. *et al.* Photodarkening in Yb-doped silica fibers: influence of the atmosphere during preform collapsing. *Fiber Lasers V: Technology, Systems, and Applications* **6873**, U286-U295 (2008).

40 Kirchhof, J., Unger, S., Schwuchow, A., Grimm, S. & Reichel, V. Materials for high-power fiber lasers. *J. Non-Cryst. Solids* **352**, 2399-2403, doi: 10.1016/j.jnoncrysol.2006.02.061 (2006).

41 Ainslie, B. J. A Review of the Fabrication and Properties of Erbium-Doped Fibers for Optical Amplifiers. *J. Lightwave Technol.* **9**, 220-227, doi: 10.1109/50.65880 (1991).

42 Ainslie, B. J., Craig, S. P., Wyatt, R. & Moulding, K. Optical and structural analysis of neodymium-doped silica-based optical fibre. *Mater. Lett.* **8**, 204-208, doi:http://dx.doi.org/10.1016/0167-577X(89)90104-3 (1989).

43 Tsai, H. C., Greif, R. & Joh, S. A Study of Thermophoretic Transport in a Reacting Flow with Application to External Chemical-Vapor-Deposition Processes. *Int. J. Heat Mass Transfer* **38**, 1901-1910, doi: 10.1016/0017-9310(94)00265-W (1995).

44 Cho, J., Kim, J. & Choi, M. An experimental study of heat transfer and particle deposition during the outside vapor deposition process. *Int. J. Heat Mass Transfer* **41**, 435-445, doi: 10.1016/S0017-9310(97)00139-7 (1998).

45 Tandon, P. & Balakrishnan, J. Predicting heat and mass transfer to a growing, rotating preform during soot deposition in the outside vapor deposition process. *Chem. Eng. Sci.* **60**, 5118-5128, doi: 10.1016/j.ces.2005.04.043 (2005).

46 Kang, S. H. & Greif, R. Thermophoretic Transport in the Outside Vapor-Deposition Process. *Int. J. Heat Mass Transfer* **36**, 1007-1018, doi: 10.1016/S0017-9310(05)80285-6 (1993).

47 Wu, C. K. & Greif, R. Thermophoretic deposition including an application to the outside vapor deposition process. *Int. J. Heat Mass Transfer* **39**, 1429-1438, doi: 10.1016/0017-9310(95)00180-8 (1996).

48 Tandon, P., Terrell, J. P., Fu, X. D. & Rovelstad, A. Estimation of particle volume fraction, mass fraction and number density in thermophoretic deposition systems. *Int. J. Heat Mass Transfer* **46**, 3201-3209, doi: 10.1016/S0017-9310(03)00117-0 (2003).

49 Hong, K. H. & Kang, S. H. Three-dimensional analysis of heat transfer and thermophoretic particle deposition in OVD process. *Int. J. Heat Mass Transfer* **41**, 1339-1346, doi: 10.1016/S0017-9310(97)00200-7 (1998).

50 Cho, J. & Choi, M. Determination of number density, size and morphology of aggregates in coflow diffusion flames using light scattering and local sampling. *J. Aerosol Sci* **31**, 1077-1095, doi: 10.1016/S0021-8502(99)00574-1 (2000).

51 Choi, M., Park, K. S. & Cho, J. Modeling of Chemical-Vapor-Deposition for Optical-Fiber Manufacture. *Opt Quant Electron* **27**, 327-335, doi: 10.1007/Bf00563567 (1995).

52 Graham, G. M. & Alam, M. K. Experimental Study of the Outside Vapor Deposition Process. *Aerosol Sci. Technol.* **15**, 69-76, doi:10.1080/02786829108959514 (1991).

53 Bautista, J. R. & Atkins, R. M. The Formation and Deposition of SiO_2 Aerosols in Optical Fiber Manufacturing Torches. *J. Aerosol Sci* **22**, 667-675, doi: 10.1016/0021-8502(91)90019-E (1991).

54 Tandon, P. Fundamental Understanding of Processes Involved in Optical Fiber Manufacturing Using Outside Vapor Deposition Method. *International Journal of Applied Ceramic Technology* **2**, 504-513, doi:10.1111/j.1744-7402.2005.02051.x (2005).

55 James David Greaves, J. *Numerical Analysis of the Outside Vapor Deposition Process* Master of Science thesis, Ohio University, (1990).

56 Janakiraman, V. *Computer Simulation of Material Processing By Outside Vapor Deposition* Master of Science thesis, Ohio University, (1990).

57 dos Santos, J. S., Ono, E., Gusken, E. & Suzuki, C. K. Correlation study between VAD preform deposition surface and Germanium doping profiles. *J. Lightwave Technol.* **24**, 831-837, doi:10.1109/jlt.2005.861936 (2006).

58 Sekiya, E. H. *et al.* Crystalline and amorphous phases of GeO_2 in VAD silica-germania soot preform. *J. Non-Cryst. Solids* **273**, 228-232, doi: 10.1016/S0022-3093(00)00131-9 (2000).

59 Horender, S., Lipowsky, J., Sommerfeld, M., Schwerin, M. & Badeke, K. U. Deposition of SiO_2 Nanoparticles Produced in a Turbulent H_2/O_2 Flame. *Aerosol Sci. Technol.* **42**, 873-883, doi:10.1080/02786820802350766 (2008).

60 Kawachi, M., Sudo, S., Shibata, N. & Edahiro, T. Deposition Properties of SiO_2-GeO_2 Particles in the Flame Hydrolysis Reaction for Optical Fiber Fabrication. *Jpn. J. Appl. Phys.* **19**, L69-L71, doi: 10.1143/Jjap.19.L69 (1980).

61 Linow, S. *et al.* Experimental study of the synthesis of fused silica by direct combustion hydrolysis. *Exp. Fluids* **32**, 66-75, doi: 10.1007/s003480200007 (2002).

62 Cheng, S. C. & Liu, J. TEM Investigation of GeO_2 Concentration Profiles in GeO_2-SiO_2 Soot Particles from Preforms of Outside Vapor Deposition. *Microsc. Microanal.* **11**, doi:10.1017/s1431927605500783 (2005).

63 Muller, D. *et al.* Two-dimensional concentration and temperature measurements in extended flames of industrial burners using PLIF. *P Soc Photo-Opt Ins* **5191**, 66-74 (2003).

64 Potkay, E., Clark, H. R., Smyth, I. P., Kometani, T. Y. & Wood, D. L. Characterization of soot from multimode vapor-phase axial deposition (VAD) optical fiber performs. *J. Lightwave Technol.* **6**, 1338-1347 (1988).

65 (eds P. J. Linstrom & W. G. Mallard) (National Institute of Standards and Technology, 2005).

66 Kots, J. C., Treichel, P. M. & Weaver, G. C. *Chemistry & Chemical Reactivity*. (Brooks Cole, 2006).

67 Schefer, R. W., Kulatilaka, W. D., Patterson, B. D. & Settersten, T. B. Visible emission of hydrogen flames. *Combust. Flame* **156**, 1234-1241, doi:http://dx.doi.org/10.1016/j.combustflame.2009.01.011 (2009).

68 Ellingham, H. J. T. Reducibility of oxides and sulphides in metallurgical processes. *Journal of the Society of Chemical Industry*, 125-133 (1944).

69 Keck, D. B., Maurer, R. D. & Schultz, P. C. On the ultimate lower limit of attenuation in glass optical waveguides. *Appl. Phys. Lett.* **22**, 307-309, doi:http://dx.doi.org/10.1063/1.1654649 (1973).

70 Sanada, K. *et al.* Behavior of GeO_2 in dehydration process of VAD method. (1982).

71 Po, H. *et al.* in *Optical Fiber Communication Conference.* PD7 (Optical Society of America).

72 Kawakami, S. & Nishida, S. Characteristics of a Doubly Clad Optical Fiber with a Low-Index Inner Cladding. *IEEE J. Quantum Electron.* **Qe10**, 879-887, doi: 10.1109/Jqe.1974.1068118 (1974).

73 Kouznetsov, D. & Moloney, J. V. Efficiency of pump absorption in double-clad fiber amplifiers. II. Broken circular symmetry. *J. Opt. Soc. Am. B* **19**, 1259-1263, doi:10.1364/JOSAB.19.001259 (2002).

74 Filippov, V. *et al.* Double clad tapered fiber for high power applications. *Opt. Express* **16**, 1929-1944, doi:10.1364/OE.16.001929 (2008).

75 Oto, M., Kikugawa, S., Sarukura, N., Hirano, M. & Hosono, H. Optical fiber for deep ultraviolet light. *IEEE Photonics Technology Letters* **13**, 978-980, doi:10.1109/68.942666 (2001).

76 Hosono, H., Mizuguchi, M., Kawazoe, H. & Ogawa, T. Effects of fluorine dimer excimer laser radiation on the optical transmission and defect formation of various types of synthetic SiO_2 glasses. *Appl. Phys. Lett.* **74**, 2755-2757, doi:10.1063/1.124004 (1999).

77 Matthijsse, P., Gooijer, F., Flammer, I., Regnier, E. & Kuyt, G., Patent, 2009.

78 Sanada, K., Shamoto, N. & Inada, K. Radiation resistance of fluorine-doped silica-core fibers. *J. Non-Cryst. Solids* **179**, 339-344, doi:https://doi.org/10.1016/0022-3093(94)90714-5 (1994).

79 Kyoto, M., Ohoga, Y., Ishikawa, S. & Ishiguro, Y. Characterization of fluorine-doped silica glasses. *Journal of Materials Science* **28**, 2738-2744, doi:10.1007/bf00356211 (1993).

80 Gao, Y., Feng, G., Liu, Y., Zhou, S. & Zhu, S. The Loss of Optical Fiber with Pure Quartz Core and Fluorine—Doped Glass Cladding. *Optics and Photonics Journal* **03**, 117-121, doi:10.4236/opj.2013.31019 (2013).

81 <http://www.internetlivestats.com/internet-users/>

82 Richardson, D. J., Fini, J. M. & Nelson, L. E. Space-division multiplexing in optical fibres. *Nat Photon* **7**, 354-362, doi:10.1038/nphoton.2013.94 (2013).

83 Miyashita, T. & Manabe, T. Infrared optical fibers. *Quantum Electronics, IEEE Journal of* **18**, 1432-1450, doi:10.1109/jqe.1982.1071428 (1982).

84 Mashinsky, V. M. *et al.* Germania-glass-core silica-glass-cladding modified chemical-vapor deposition optical fibers: optical losses, photorefractivity, and Raman amplification. *Opt. Lett.* **29**, 2596-2598, doi:10.1364/OL.29.002596 (2004).

85 Plotnichenko, V. G. *et al.* Hydroxyl groups in germania glass. *J. Non-Cryst. Solids* **296**, 88-92, doi:http://dx.doi.org/10.1016/S0022-3093(01)00887-0 (2001).

86 Sakaguchi, S. Consolidation of GeO_2 soot body prepared by flame hydrolysis reaction. *J. Non-Cryst. Solids* **171**, 228-235, doi:http://dx.doi.org/10.1016/0022-3093(94)90191-0 (1994).

87 Imai, M., Mitamura, T., Yaoita, K. & Tsuji, K. Pressure-induced phase transition of crystalline and amorphous silicon and germanium at low temperatures. *High Pressure Research* **15**, 167-189, doi:10.1080/08957959608240470 (1996).

88 Hiroshi, T. & Iwane, S. Decreased Losses in Germanium-Oxide Glass Optical Fiber Prepared by VAD Method. *Jpn. J. Appl. Phys.* **22**, L139 (1983).

89 Takahashi, H. & Sugimoto, I. A Germanium Oxide Glass Optical Fiber Prepared by a Vad Method. *J. Lightwave Technol.* **2**, 613-616, doi: 10.1109/Jlt.1984.1073663 (1984).

90 Takahashi, H. & Sugimoto, I. Preparation of Germanate Glass by Vapor-Phase Axial Deposition. *J. Am. Ceram. Soc.* **66**, C-66-C-67, doi:10.1111/j.1151-2916.1983.tb15698.x (1983).

91 Atkins, R. M. & Hohan, V. A. Reactions of silicon tetrachloride and germanium tetrachloride with oxygen and oxides of nitrogen. *J. Mater. Res.* **4**, 641-650, doi:10.1557/JMR.1989.0641 (1989).

92 Cajzl, J. *et al.* in *Photonics Prague 2014.* 8 (SPIE).

93 Richards, B., Shen, S., Jha, A., Tsang, Y. & Binks, D. Infrared emission and energy transfer in Tm^{3+}, Tm^{3+}-Ho^{3+} and Tm^{3+}-Yb^{3+}-doped tellurite fibre. *Opt. Express* **15**, 6546-6551 (2007).

94 Pollnau, M. & Eichhorn, M. 387-404 (Springer Netherlands).

95 Khopin, V. F. *et al.* Effect of core glass composition on the optical properties of active fibers. *Inorg. Mater.* **41**, 434-437, doi:10.1007/s10789-005-0148-3 (2005).

96 Bonnell, E. A. *Temperature Dependent Behavior of Optical Loss from Hydrogen Species in Optical Fibers at High Temperature* Master of Science thesis, Virginia Polytechnic Institute and State University, (2015).

97 Mochizuki, K., Namihira, Y., Kuwazura, M. & Iwamoto, Y. Behavior of Hydrogen Molecules Adsorbed on Silica in Optical Fibers. *IEEE J. Quantum Electron.* **20**, 694-697, doi: 10.1109/Jqe.1984.1072462 (1984).

98 Orcel, G., Dubois, S. & Campion, J. F., Patent, 2002.

99 Stone, J. & Walrafen, G. E. Overtone vibrations of OH groups in fused silica optical fibers. *The Journal of Chemical Physics* **76**, 1712-1722, doi:http://dx.doi.org/10.1063/1.443210 (1982).

100 Lamberti, A. *et al.* Dynamic Strain Measurements on Automotive and Aeronautic Composite Components by Means of Embedded Fiber Bragg Grating Sensors. *Sensors* **15**, 27174 (2015).

101 Foote, P. D. in *IEE Colloquium on Optical Fibre Gratings and Their Applications.* 14/11-14/16.

102 Echevarria, J., Quintela, A., Jauregui, C. & Lopez-Higuera, J. M. Uniform fiber Bragg grating first- and second-order diffraction wavelength experimental characterization for strain-temperature discrimination. *IEEE Photonics Technology Letters* **13**, 696-698, doi:10.1109/68.930418 (2001).

103 Mihailov, S. J. Fiber Bragg Grating Sensors for Harsh Environments. *Sensors* **12**, 1898 (2012).

104 Dong, L. *et al.* Efficient single-frequency fiber lasers with novel photosensitive Er/Yb optical fibers. *Opt. Lett.* **22**, 694-696, doi:10.1364/OL.22.000694 (1997).

105 Jovanovic, N. *et al.* Narrow linewidth, 100 W cw Yb^{3+}-doped silica fiber laser with a point-by-point Bragg grating inscribed directly into the active core. *Opt. Lett.* **32**, 2804-2806, doi:10.1364/OL.32.002804 (2007).

106 Lai, Y., Martinez, A., Khrushchev, I. & Bennion, I. Distributed Bragg reflector fiber laser fabricated by femtosecond laser inscription. *Opt. Lett.* **31**, 1672-1674, doi:10.1364/OL.31.001672 (2006).

107 Mihailov, S. J. *et al.* Bragg grating inscription in various optical fibers with femtosecond infrared lasers and a phase mask. *Opt. Mater. Express* **1**, 754-765, doi:10.1364/OME.1.000754 (2011).

108 Martinez, A., Khrushchev, I. Y. & Bennion, I. Direct inscription of Bragg gratings in coated fibers by an infrared femtosecond laser. *Opt. Lett.* **31**, 1603-1605, doi:10.1364/OL.31.001603 (2006).

109 Mihailov, S. J. *et al.* Bragg grating writing through the polyimide coating of high NA optical fibres with femtosecond IR radiation. *Opt. Commun.* **281**, 5344-5348, doi:https://doi.org/10.1016/j.optcom.2008.07.056 (2008).

110 Williams, R. J., Krämer, R. G., Nolte, S. & Withford, M. J. Femtosecond direct-writing of low-loss fiber Bragg gratings using a continuous core-scanning technique. *Opt. Lett.* **38**, 1918-1920, doi:10.1364/OL.38.001918 (2013).

111 Marshall, G. D., Williams, R. J., Jovanovic, N., Steel, M. J. & Withford, M. J. Point-by-point written fiber-Bragg gratings and their application in complex grating designs. *Opt. Express* **18**, 19844-19859, doi:10.1364/OE.18.019844 (2010).

112 Medvedkov, O. I., Vasiliev, S. A., Gnusin, P. I. & Dianov, E. M. Photosensitivity of optical fibers with extremely high germanium concentration. *Opt. Mater. Express* **2**, 1478-1489, doi:10.1364/OME.2.001478 (2012).

113 Mihailov, S. J., Grobnic, D., Smelser, C. W. & Walker, R. B. 73160B-73160B-73113.

114 Avino, S. *et al.* Ionizing radiation detectors based on Ge-doped optical fibers inserted in resonant cavities. *Sensors (Basel, Switzerland)* **15**, 4242-4252, doi:10.3390/s150204242 (2015).

115 Grobnic, D. *et al.* 73160C-73160C-73169.